ABSTRACT

Title of Document: Electronic Structure of SiC/SiO_2 by Density Functional Theory

Shahrzad Salemi, PhD, 2012

Directed By: Prof. Neil Goldsman, Reliability Engineering

Silicon carbide (SiC) is a promising semiconductor material with desirable properties for many applications. SiC-based electronic devices and circuits are being developed for use in high-temperature, high-power, and high-radiation conditions under which conventional semiconductors cannot function. Additionally, it has the advantage of growing a native oxide, SiO_2, by simple thermal oxidation. Despite all desirable properties, SiC-based devices still face major challenges.

The main problem of SiC-based devices is the great density of imperfections at the SiC/SiO_2 interface, which not only degrades the device performance but also causes reliability problems coming from the extreme operating conditions. The quality of the interface affects the channel mobility of MOSFETs, which is the most critical parameter of devices.

In this work a hybrid functional density functional theory framework is employed to model the (0001)4H-SiC/SiO_2 abrupt interface. Using this, defect energy levels in the bandgap have been calculated through the total and projected density of states. There is experimental evidence for improvement of the quality of the interface after passivation, However the atomic mechanisms of the improvement are not yet clear., Thus, the impact of various passivations on the potential defects has also been studied.

Since the interface of SiC/SiO_2 is not perfectly abrupt, several atomic configurations for (0001)4H-SiC/SiO_2 transition layers have also been modeled, and their effect on the bandgap, and the near interface trap density has been studied.

A DFT-based Monte Carlo carrier transport simulation technique is employed to compute the average velocities, phonon-limited and ionized-impurity-limited mobilities of the most probable transition layer structures.

Finally, since low frequency noise calculation is a powerful tool to diagnose quality and reliability of semiconductor devices, a DFT-based method is presented to calculate the current spectral noise density of the (0001)4H-SiC/SiO_2 transition layers.

ELECTRONIC STRUCTURE OF SiC/SiO_2 BY DENSITY FUNCTIONATHEORY

By

Shahrzad Salemi

Dissertation submitted to the Faculty of the Graduate School of the
University of Maryland, College Park, in partial fulfillment
of the requirements for the degree of
Doctor of Philosophy
2012

Advisory Committee:
Professor Neil Goldsman, Chair/Advisor
Professor Martin Peckerar
Professor Aris Christou
Professor Peter Sandborn
Professor Loudres Salamanca-Riba

© Copyright by
Shahrzad Salemi
2012

Acknowledgements

I would like to express my greatest gratitude and special thanks to Prof. Neil Goldsman for giving me the opportunity to study and work on a very interesting and challenging topic. He has been supportive and provided insightful discussions about the research. He provided the vision, encouragement and advice necessary for me to proceed the doctoral program and complete my dissertation.

I am also very grateful to Dr. Akin Akturk, and Dr Siddharth Potbhare for their scientific advice, many suggestions, and friendly help. Dr. Akturk's extensive discussions and encouragement have been very helpful for this study.

I wish to express my sincere gratitude to Dr. Aivars Lelis for supporting the research; I felt motivated and encouraged every time I attended his meetings.

I owe my gratitude and appreciation to Prof. Martin Peckerar, and Prof. Aris Christou for their generosity in sharing their profound knowledge with me.

I would like to acknowledge and extend my heartfelt gratitude to Prof. Hugh Bruck, and Prof. Mohammad Modarres for their constant support in every aspects of my study.

I would like to thank Prof. Christou, Prof. Peckerar, Prof. Salamanca-Riba, and Prof. Sandborn for taking time off their busy schedules and serving my dissertation committee.

Many thanks to the ENME/UMD staff who always kindly provide me with necessary assistance.

Table of Contents

Acknowledgements ii

Table of Contents iii

List of Tables ix

List of Figures x

Chapter 1: Introduction 1

1.1. History of SiC 1

1.2. SiC Crystals Structure 1

1.3. SiC Properties, and Applications 6

1.3.1. Electronic Structure of SiC/SiO_2 8

1.4. SiC/SiO_2 Interface 9

1.5. SiC Oxidation 11

1.6. Defect at SiC/SiO_2 Interface, and Defect Classifications 13

1.7. Transition Layer 17

1.8. Passivation, and Annealing of Interface Defects 18

1.9. SiC Mobility 20

1.10. Dissertation Goal, and Outline 21

1.11. Contributions 24

Chapter 2: Theoretical Background; From Schrodinger Equation to Density Functional Theory Calculation of Semiconductors 26

2.1. Introduction 26

2.2. Many-Body Schrodinger Equation 27

2.3. Born Oppenheimer/ Classical Nuclei Approximation 30

2.4. Mean-Field Theories/ Non-Interacting Electrons 31

2.5. Hartree Approximation 31

2.6. Hartree-Fock Approximation... 34

2.7. Introduction to Density Functional Theory.. 36

2.7.1. Electron Density.. 37

2.7.2. Hohenberg-Kohn Theorems.. 39

2.7.2. Kohn-Sham Formalism 42

2. 8. Solving Kohn-Sham Equation/ DFT in Practice... 47

2.8.1. Exchange-Correlation Functionals... 49

2.8.2. The Choice of Basis 51

2.8.2.1. Periodic Supercells/ Solid State Basis Functions.. 52

2.8.2.2. Bloch's Theorem.. 52

2.8.2.3. k-Point Sampling 54

2.8.2.4. Plane Wave Basis and Plane-Wave Representation of Kohn-Sham Equation

.... 57

2.8.2.5. Cut-off the Basis Set 60

2.8.3. The Supercell Approximation.. 61

2.8.4. Pseudopotential 62

2.8.5. The Calculation of Coulomb Term in General 67

2.9. Application of Density Functional Theory to Semiconductors 68

2.9.1. Bulk Semiconductors 68

2.9.1.1. Band Gap Calculation with Density Functional Theory............................... 69

2.9.1.2. Density of States in Bulk Semiconductors 72

2.10. Geometric Optimization 74

2.10.1. Hellmann-Feynman Theorem 75

2.11. Algorithm for Solving Kohn-Sham Equation, and Geometric Relaxation 76

2.12. Summary 78

Chapter 3: From Bulk to (0001)4H-SiC/SiO_2 Interfacial Mode 79

3.1. Introduction 79

3.2. SiC Bulk Simulation 80

3.2.1. Effective Masses for 4H-SiC 89

3.3. The SiO_2 Bulk Model 92

3.4. Toward Modeling the (0001)4H-SiC/SiO_2 Interface 94

3.4.1. The Evolution of Bandgap 98

3.5. Summary 103

Chapter 4: The Effect of Defects, and their Passivation on the Density of States of 4H-SiC(0001)/SiO_2 Interface 105

4.1. Introduction 105

4.2. Introduction to SiC/SiO_2 Defects 105

4.3. Introduction to Passivation 108

4.3.1. Hydrogen Passivation 109

4.3.2. Nitrogen Passivation 111

4.3.3. Phosphorus Passivation 113

4.4. Methodology 113

4.5. Defect Level at SiC Side of the (0001)4H-SiC/SiO_2 Interface, and their Passivation 116
4.5.1. Neutral Silicon vacancy 116
4.5.1.1. Passivation of Silicon Vacancy 119
4.5.1.2. Negatively Charged Silicon Vacancy 122
4.5.2. Carbon Contaminations in SiC Side of SiC/SiO_2 124
4.5.2.1. Carbon Interstitials in SiC Side of SiC/SiO_2 125
4.5.2.1.1. Passivation of Carbon Interstitials in SiC Side of SiC/SiO_2 126
4.5.2.2. A Pair of Carbon Interstitials in SiC Side of SiC/SiO_2 129
4.5.2.2.1. Passivation of a Pair of Carbon Interstitials in SiC Side of SiC/SiO_2 131
4.6.1. Carbon Excess in Oxide Side 133
4.6.2. Oxygen Deficiency at the Interface 134
4.7. Silicon Dangling Bonds, and their Passivations 136
4.8. Conclusion and Discussion 140
Chapter 5: DFT Prediction, and DFT-Based Carrier Transport Simulation of 4H-SiC(0001)/SiO_2 Interface 143
5.1. Introduction 143
5. 2. SiC/SiO_2 Transition Layer 145
5. 3. Experimental Evidences for, and Atomic Structure of the SiC/SiO_2 Transition Layer 146
5.4. Introduction to Mobility Calculation 147
5.4.1. Monte Carlo Bulk Transport Calculation in 4H-SiC 149
5.4.2. Scattering Mechanisms 151

5.4.3. Monte Carlo Calculation Methodology for Bulk 4H-SiC.............................. 154

5. 5. Density Functional Theory Methodology... 157

5. 6. DFT and DFT-Based Monte Carlo Calculations for Transition Layer............. 159

5. 6.1. $Si_{1-x}C_xO_2$ Structures in SiO_2.. 159

5. 6.2. SiO_xC_y Structures in SiO_2.. 160

5. 6.2.1. Monte Carlo Mobility Calculations for SiO_xC_y Structures in SiO_2............ 163

5. 6.3. SiO_xC_y Structures in SiC... 164

5. 6.3.1. Monte Carlo Mobility Calculation for SiO_xC_y Structures in SiC 167

5. 6.3.2. Passivation of SiO_xC_y Structures in SiC 169

5.7. Formation of Nitrogen Epi-Layer at the Interface 171

5.8. Conclusion 173

Chapter 6: Flicker Noise in MOSFET 175

6.1. Introduction... 175

6.2. Introduction: Noise Definition and Classification 175

6.3. The Estimation of Spectral Noise Density as a Function of Frequency by Unified Model 178

6.3.1. Estimation of Spectral Noise Density as a Function of Frequency by Unified Model for SiC_xO_y in SiC side of Interface.. 181

6.4. Estimation of Spectral Noise Density as a Function of Frequency by Statistical Method 183

6.4.1. Estimation of the Number of Traps 186

6.4.2. Estimation of the Trap Location 188

6.4.3. Estimation of the Trap Occupency 188

6.4.4. Spectral Noise Density Simulation for SiC_xO_y Transition Layer in a Statistical Model 189
6.5. Summary 191
Conclusion and Future Work 192
Appendices 196
A.1. Exchange-Correlation Hole 196
A.2. Functional 198
A.3. Thomas-Fermi Approximation 199
A.4. N- and V- Representability 202
A.5. Local Density Approximation (LDA) 203
A.5.1. Generalized Gradient Approximation (GGA) 207
A.5.2. Meta-GGA 211
A.5.3. Hybrid Functionals 213
A.6. Crystal Structure; Real and Reciprocal Lattice 215
A.7. Basic Ideas of Pseudopotential/ Frozen-Core Approximation 217
A.7.1. Pseudopotential Construction and Classifications 221
A.7.2. Norm-Conservative Pseudopotential 222
A.7.3. Troullier-Martins Pseudopotential 225
A.7.4. Kleinman and Bylanber Pseudopotential 225
A.7.5. Structure Factor and Total Nuclear Potential 227

List of Tables

Table 1.1: The properties of the most important technological SiC polytypes [11, 12].

Table 1.2: Electric properties of 4H-, and 6H-SiC.

Table 5.1: 4H-SiC electron-phonon coupling parameters.

List of Figures

Figure 1.1: Atomic structure of SiC: tetrahedrally bonded Si-C_4 cluster.

Figure 1.2: Crystal of difference polytypes displayed to the $(11\bar{2}0)$ plane: from left to right: Zinc blend (cubic 3C-SiC), hexagonal 4H-SiC and hexagonal 6H-SiC [11].

Figure1.3: Energy gaps and relative band-offsets of Si, SiO_2, and common SiC polytypes [13].

Figure 1.4: Hexagonal unit cell, and common orientations used to grow oxides on SiC [14].

Figure1.5: Schematic of the interface trap density in SiC/SiO_2 for several SiC polytypes [18].

Figure 1.6: Flow chart as a guideline for the dissertation simulations, and calculations.

Figure 2.1: Supercell approximation for a single defect, a surface area and a molecule.

Figure 2.2: Comparison of a wave function in the potential of the nucleus to the one in the pseudopotential. The real and pseudo wave function and potentials match above a certain radius r_c.

Figure 2.3: Algorithm for Solving Kohn-Sham equation, geometric relaxation, and bandgap correction.

Figure 3.1: Two-dimensional views of primitive hexagonal cells for 4H-SiC and 6H-SiC [99, 101].

Figure 3.2: Theoretical determination of the 4H-SiC equilibrium lattice constant in PBE calculations through the minimization of total energy vs. lattice constant a.

Figure 3.3: The unit cell of: a) 4H-SiC, b) 6H-SiC (xcrysden); the blue large, and the yellow small spheres are silicon, and oxygen atoms, respectively.

Figure 3.4: Convergence with respect to total cutoff energy for 4H-SiC.

Figure 3.5: a) DOS, and b) Band diagram of 4H-SiC along A L M Γ A H K Γ.

Figure 3.6: Band diagram of 4H-SiC along Γ M K Γ A L H A.

Figure 3.7: a) DOS, and b) Bandstructure of 6H-SiC along A L M Γ A H K Γ̃

Figure 3.8: The shape of the lowest conduction band branch in 4H-SiC along a) MΓ, b) MK.

Figure 3.9: α-quartz unit cell; the large blue spheres are silicon, and the small red spheres are oxygen atoms by xcrysden.

Figure 3.10: a) DOS, and b) Band structure of α-quartz.

Figure 3.11: The interface of the (0001) 4H-SiC/SiO_2, used in the abrupt model; in this model three Si atoms of 4H-SiC are saturated with three oxygen atoms of SiO_2.

Figure 3.12: The atomic structure of abrupt structure.

Figure 3.13: The evolution of bandgap of the interface obtained by the total and projected DOS, corrected by hybrid functionals. The DOS contributions of Si, C, and O atoms are light blue, yellow, and red, respectively. The total DOS of SiC (figure a)), and SiO_2 (figure e)) in general are shown in navy. The pDOS figures between SiC, and SiO_2 are the pDOS of almost 4.5 angstrom (from figure b) to figure e)), each.

Figure 3.14: The total DOS of the abrupt structure.

Figure 3.15: The bandgap evolution of (0001)4H-SiC/SiO2 abrupt model at the interface; the top line shows the evolution of the minimum of the conduction band edge, while the bottom line represents the the evolution of the maximum of the valence band edge.

Figure 4.1: Algorithm for energy calculation of defects, and their passivations.

Figure 4.2: a) The atomic structure with silicon vacancy, and schematic of silicon vacancy and four carbons with four dangling bonds around it; b) pDOS of four carbon atoms around Si vacancy; c) total DOS of the abrupt structure (dotted line), and pDOS of carbon atoms around silicon vacancy (solid line).

Figure 4.3: a) Atomic structure of the carbon atoms around silicon vacancy passivated by four hydrogen atoms. b) pDOS of C atoms around silicon vacancy before passivation (solid line), pDOS of all carbon atoms together with hydrogen atoms after 4H (dotted circle line).

Figure 4.4: a) Atomic structure of the structure with Si vacancy; b) pDOS of four atoms around the Si vacancy (solid line), and pDOS of all C atoms together with N after N passivation (dotted triangle line).

Figure 4.5: pDOS of the carbon atoms around Si vacancy for neutral (red), and one negatively charged structure (purple).
Figure 4.6: Comparison between the pDOS of all four C atoms around Si vacancy, and the total DOS of the whole structure with a Si vacancy.
Figure 4.7: a) atomic structure with a carbon interstitial in SiC side, b) pDOS of carbon interstitial.
Figure 4.8: a) Atomic configuration of the abrupt structure with a carbon interstitial in SiC side; b) pDOS of carbon interstitial (solid line), carbon and hydrogen atoms after H (dotted circle line), and carbon atom plus nitrogen atom after N (dotted triangle line) passivation.
Figure 4.9: a) pDOS of carbon interstitial before passivation (solid line), pDOS of nitrogen replacing carbon interstitial (dotted triangle line), and pDOS of phosphorus replacing the carbon interstitial (dotted square line).
Figure 4.10: a) atomic configuration of a pair of carbon interstitials in SiC side of interface, b) pDOS of a pair of C atoms in SiC side of SiC/SiO_2.
Figure 4.11: a) atomic structure of a pair of carbon atoms passivated by two hydrogen atoms; b) pDOS of a pair of carbons before (solid line), and after hydrogen passivation (dotted circle line).
Figure 4.12: pDOS of a Pair of Carbon atoms (solid line) before, and after C removal by a pair of Nitrogen atoms (dotted triangle line).
Figure 4.13: pDOS of carbon interstitial in oxide side of the structure.
Figure 4.14: a) Atomic configuration of an O deficiency at the interface, and the resulting Si-Si bond; b) pDOS on all Si atoms with an oxygen deficiency at the interface (solid line), pDOS on all Si atoms after N passivation (dotted triangle line).
Figure 4.15: The contribution of all silicon atoms with three dangling bonds on the surface of SiC side of SiC/SiO_2.
Figure 4.16: Total DOS of the structure with unpassivated three Si dangling bonds perpendicular to the interface (solid line), and after N Passivation (dotted triangle line), after P passivation (dotted circle line), and H passivation (open circle line).
Figure 4.17: Total DOS of the structure with silicon dangling bonds (blue), and after arsenic passivation (orange).

Figure 4.18: The relative Dit of the structures with three silicon dangling bonds (blue), and after nitrogen (brown), and phosphorous (green) passivation.
Figure 5.1: Conduction band DOS as a function of energy away from the conduction band minimum.
Figure 5.2: Average velocity versus field for 4H-SiC.
Figure 5.3: Mobility versus field for 4H-SiC.
Figure 5.4: Algorithm of electronic calculation of transition layers, and the related passivations.
Figure 5.5: b) Comparison between the pDOS of C-Si-O_C SiO_xC_y formed in SiO_2 with one C atom replacing oxygen in the oxide side of the interface with and C-Si-C of the abrupt structure. We represent carbon substituted for or replacing oxygen as C(O).
Figure 5.6: a) Super cell used in DFT calculations for SiO_xC_y structures with three C (O) in oxide side; b) Comparison between all the C-Si-C(O) bridges in SiO_xC_y formed in the oxide side with three C(O) and all C-Si-C bridges in the abrupt structure.
Figure 5.7: Electron-phonon limited bulk mobility for bulk SiC, and SiO_xC_y structures with various concentrations of C_O in the oxide side.
Figure 5.8: a) Super cell used in DFT calculations for SiO_xC_y structure with one O_C substitution; b) Comparison between pDOS of C-Si-C, and O-Si-C bridges in abrupt, and SiO_xC_y structure with one O_C in SiC side.
Figure 5.9: a) Super cell used in DFT calculations for SiO_xC_y structure with three O(C) substitutions; Comparison between pDOS of all C-Si-C bridges in abrupt and O-Si-C bridges in a SiO_xC_y structure with three O(C) in SiC side.
Figure 5.10: Electron-phonon limited bulk mobility for bulk SiC, and SiO_xC_y structures with several concentrations of O(C) in SiC.
Figure 5.11: Electron-phonon and ionized impurity limited mobility as a function of ionized impurity for SiO_xC_y structures with various concentrations of O(C) in SiC side.
Figure 5.12: Projected density of states of C-Si-O_C bridge in SiC formed in SiC side with one O(C) (solid line), and the C-Si-N_O after N passivation (dotted circle).

Figure 5.13: Total density of states of SiO_xC_y with 6O(C) in SiC side before (solid line), and after N passivation (dollted line).

Figure 5.14:a) Atomic configuration of the structure with nitrogen epi-layer in SiC side; b) The total DOS of abrupt structure (solid line), and the epi-layer structure.

Figure 6.1: Noise versus frequency in an electrical component [167].

Figure 6.2: The cross-section of a MOSFET device with random traps distributed in different locations of the oxide from the interface.

Figure 6.3: The algorithm for estimation the Current spectral noise density as a function of frequency calculated by MATLAB program according to the Unified or Correlated flicker noise model .

Figure 6.4: Current spectral noise density versus the frequency (between 1Hz to 100Hz), for Si SiC_xO_y in SiC with 1O(C) (blue), 2O(C) (Pink), 3O(C) (yellow), 6O (Brown).

Figure 6.5: Cumulative of Ntr and (Ntr-1) vs. Average Number trap (Navg) with their difference as a poisson distribution.

Figure 6.6: The algorithm for calculating current spectral noise density with statistical model.

Figure 6.7: Current spectral noise density versus the frequency (between 1Hz to 100Hz), for Si SiC_xO_y in SiC with 1O(C) (blue), 2O(C) (Pink), 3O(C) (yellow), 6O (Brown).

Chapter 1: Introduction

1.1. History of SiC

"My Invention relates to the production of artificial crystalline carbonaceous materials; Acheson [1]"

The invention of Silicon Carbide (SiC) goes back to 1893, when E.G. Acheson [1] patented a method for making the powder. It has been used as an abrasive and cutting tool until 1907, when the first SiC light emitting diode (LED) was discovered by H. J. Round [2].

The difficulty of crystal properties, and purity, to some extent, was solved by Lely's method, in which SiC powder is evaporated at elevated temperature in a graphite crucible, and then sublimes on a porous graphite wall inside the crucible, forming hexagonal platelets [3].

In 1978, Tairov, and Tsvetkov introduced the seeded sublimation method, known as physical vapor transport, to have better control over the polytypes by spontaneous nucleation on the graphite walls. Nowadays, 4H-, and 6H-SiC wafers of several inches in diameter are available commercially by modified physical vapor transport, and step controlled epitaxy [4, 5], and several groups world wild have the ability of making high quality SiC wafers [6-8].

1.2. SiC Crystals Structure

SiC is a wide band-gap semiconductor with high breakdown voltage and high saturation electron drift velocity. It is composed of carbon and silicon in a stoichiometric ratio of 1:1. Each atom is bonded to four atoms of the other element.

Silicon carbide can exist under various crystal structures called polytypes. They all have a common building block: the Si-C tetrahedron. It consists of one Si atom bonded to four C atoms (or one C bonded to four Si). The Si-C bond length is 1.89 ˚A, indicating a stronger atomic interaction than in silicon crystals in which the Si-Si bond length is 2.35 ˚A [9]. The structure is shown in Figure 1.1.

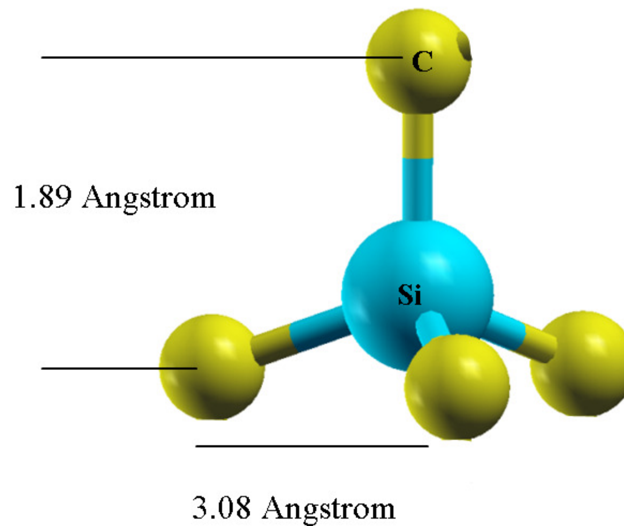

Figure 1.1: Atomic structure of SiC: tetrahedrally bonded Si-C_4 cluster.

Many different polytypes have been identified so far [10], but only 3C, and the hexagonal 4H, and 6H have the most technological importance. Although the chemical compound and the building block of all the polytypes are the same Si-C tetrahedron, their stacking sequences are varied. Each Si-C bilayer can be located at three possible positions in the crystal, named for simplicity A, B, and C [11], as is shown in figure 1.2. The bonding between Si-C atoms in the adjacent bilayer planes has either in the form of zinc blende (cubic) or wurtzite (hexagonal).

All the bilayers of the zinc blend structure have the same orientation, with ABC(ABC...) stacking order. The 3C-SiC lattice is shown in figure 1.2. In figure 1.2, two unit cells in [0001] are shown, and the view plane is $(11\bar{2}0)$; the red line shows the stacking sequence of the Si-C bilayers.

The hexagonal wurtzite structure has the bilayers rotated by 60 degree with respect to each other. There are other combinations in which the unit cell has consecutive stacks of identically oriented bilayers which in turn are rotated with respect to each other. the 4H-SiC polytype is shown in the centre of figure 1.2, with the sequence of ABCB(ABCB...). The 6H-SiChas six bilayers, with ABCACB (ABCACB...) stacking sequence, as is shown in the right hand side of figure 1.2.

Figure 1.2: Crystal of difference polytypes displayed to the $(11\bar{2}0)$ plane: from left to right: Zinc blend (cubic 3C-SiC), hexagonal 4H-SiC and hexagonal 6H-SiC [11].

SiC in cubic crystal structure is called β-SiC, while all other configurations are referred to as α-SiC. The cubic structure with 3 bilayers per unit cell is called 3C-SiC, while the two hexagonal structures with 4 and 6 bilayers per unit cell are named 4H-SiC and 6H-SiC [10]. Table I classifies the properties of the most common SiC polytypes: 3C, 4H, and 6H [11].

Table 2.1: The properties of the most important technological SiC polytypes [11, 12].

Polytype	Stacking Sequence	Number of Atoms/ Unit Cell	Lattice Parameter: a [A°]	Lattice Parameter: c [A°]	Bandgap [eV]
3C	ABC	6	4.3596	4.3596	2.39
4H	ABCB	8	3.0730	10.0530	3.26
6H	ABCABC	12	3.0806	15.1173	3.08

Despite the differences, all polytypes have wide band gaps; nevertheless, 4H-SiC has the widest band gap and the highest mobility, which usually makes it the best candidate for electronic devices. Figure 1.3 shows the energy gaps and relative band-offsets of Si, SiO_2, and common SiC polytypes [13].

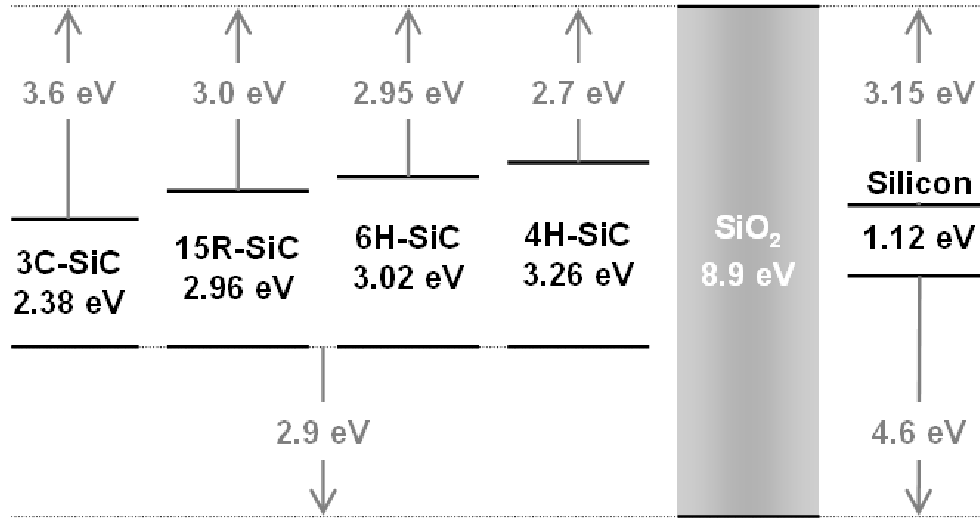

Figure1.3: Energy gaps and relative band-offsets of Si, SiO_2, and common SiC polytypes [13].

The hexagonal unit cell is shown in Figure 1.4. The most commonly used crystal faces for device processing are the (0001) Si-face, the $(000\bar{1})$ C-face and the $(11\bar{2}0)$ a-face. They each have a different density of silicon and carbon atoms; the Si-face has 100% Si atoms, the C-face has 100% C atoms and the a-face has 50% of each. This leads to distinct oxidation rates and interface properties.

SiO_2 can be grown thermally on SiC, which makes it a very attractive candidate wide band-gap material for electronics application as the Si technology and tools can be directly transferred to its processing, and it can give rise to SiC MOSFETs. However, the rate of oxide thicknesses obtained by dry oxidation at 1150 $^{\circ}$C on the different faces and of SiC is different. Such distinctive kinetics can be related to the complex oxidation process which requires the ejection of carbon.

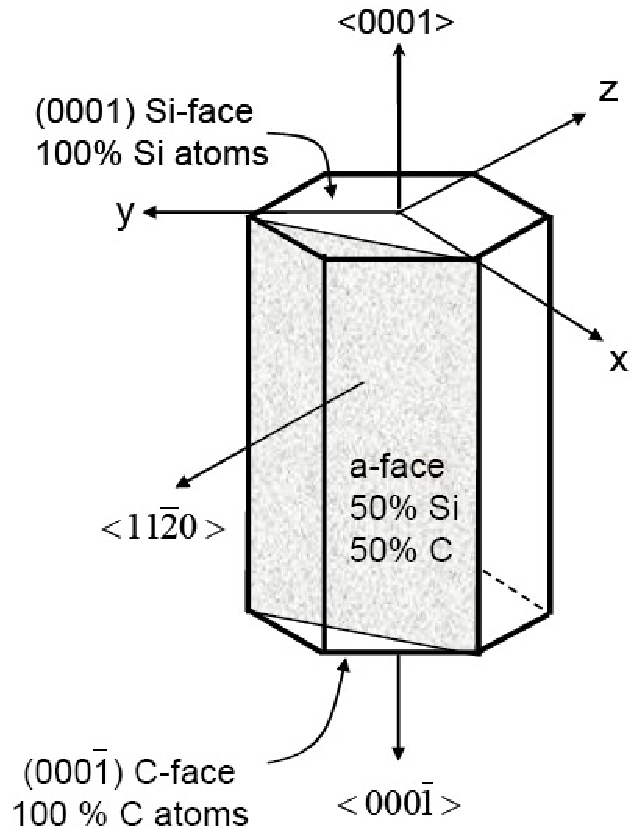

Figure 1.4: Hexagonal unit cell, and common orientations used to grow oxides on SiC [14].

1.3. SiC Properties, and Applications

The electronic properties of SiC differ for different polytypes. Almost all high temperature, high electric, and high frequency advantages of SiC devices are as the result of its wide bandgap. The most important electrical properties of 4H-, and 6H-SiC are given in Table 2 [15].

Table 1.2: Electric properties of 4H-, and 6H-SiC [15].

	4H-SiC	6H-SiC
Bandgap (eV)	3.2	3
Lattice a, and c (A°)	3.08	3.08
E_c (MV/cm)	10.08	15.12
v_{sat} (cm/s)	2×10^{7}	2×10^{7}
$\mu_n \perp_c$ (cm^2/Vs)	950	500
$\mu_n \|_c$ (cm^2/Vs)	1150	100
μ_p (cm^2/Vs)	120	80
ε_r	10	10

From temperature point of view, SiC-based devices can operate at extremely high temperatures without suffering from intrinsic conduction effects as the result of the wide energy bandgap.

Due to the wide bandgap, the impact ionization energy is high, and hence the electric field can become very high without facing the avalanche breakdown. The high electric field enables the device to withstand high breakdown voltage, as well. Therefore, the devices can be fabricated smaller for the same breakdown voltage, and the smaller the devices can be fabricated, the faster they can operate.

The high thermal conductivity allows high power density [15]. The high thermal conductivity makes SiC a better thermal conductor. Heat will flow more readily through SiC than Si materials. This property enables SiC devices to operate at

extremely high power levels and still dissipate the large amount of excess heat. Power losses are substantially reduced since SiC-based devices have high blocking voltage, low on resistance and high operating temperatures as compared with silicon-based devices.

Due to the technological developments in SiC device fabrication, the range of applications became wide. SiC high-temperature devices, high-power, and high-frequency devices have wide spectrum of applications from automotive engine sensors, jet engine ignition systems, transmitters for deep well drilling, to power supplies [16], high-frequency power supplies, small, lightweight RF and microwave transmitters [17].

1.3.1. Electronic Structure of SiC/SiO_2

One of the advantageous of SiC devices is the fact that SiC can be thermally oxidized to grow insulating SiO_2 layers, which are known to have superior dielectric properties for metal oxide semiconductor (MOS) applications. The quality of oxides thermally grown on SiC in terms of the breakdown electric field is comparable to that of SiO_2 layers grown on silicon [18]. The main problem of SiC MOSFET devices is the great density of imperfections at the SiC/SiO_2 interface, which not only degrades the device performance but also causes reliability problems related to the extreme operating conditions. The quality of the interface affects the channel mobility of MOSFETs, which is a vital parameter of devices [18].

1.4. SiC/SiO_2 Interface

The energy levels in the band gap are created as the result of the SiC/SiO_2 interface defects and surface-induced states. As it mentioned earlier, despite good bulk electron mobility, channel mobility in SiC MOSFETs is low. In contrast to Si, channel electron mobility of SiC is more than two orders of magnitude smaller than their bulk values. The origin of the trouble was traced to very high interface trap densities (D_{it}). D_{it} provides important information of the energy distribution of the SiC/SiO_2 interface states across the SiC band gap. Figure 1.5 shows the density of states versus energy for three polytypes of SiC [18].

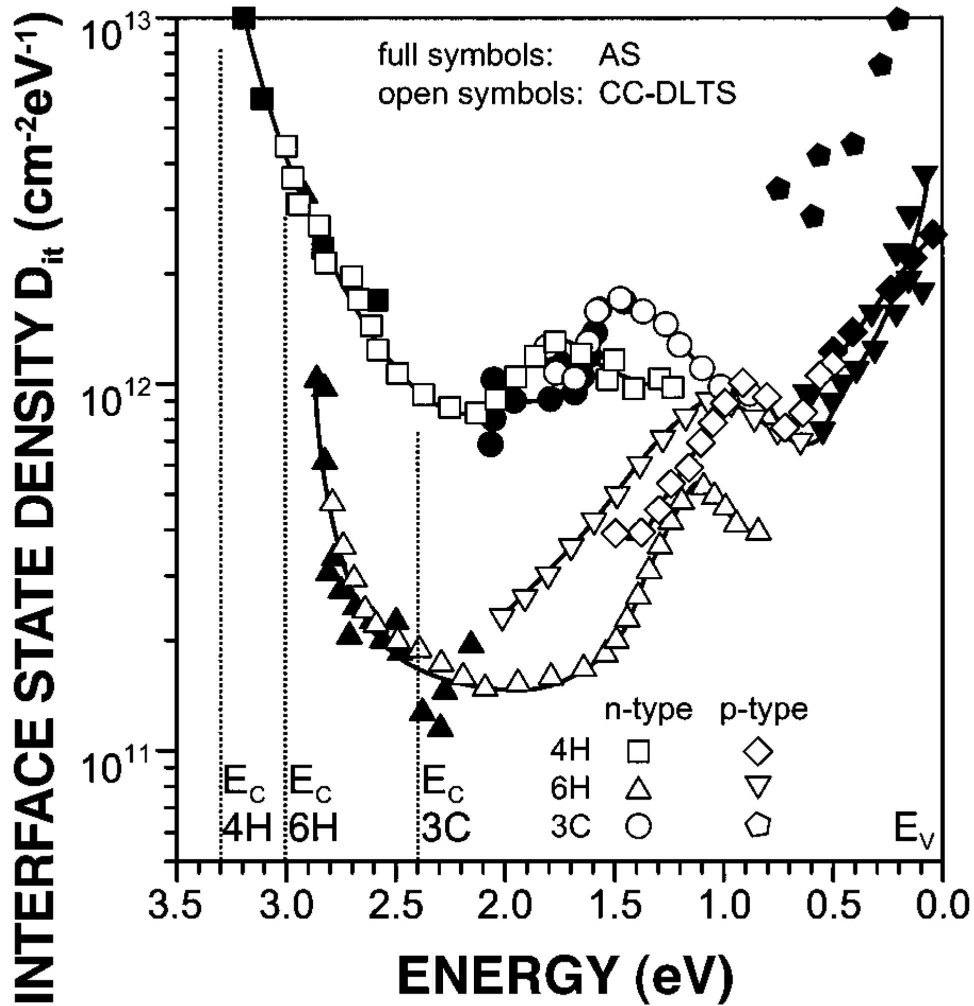

Figure1.5: Schematic of the interface trap density in SiC/SiO_2 for several SiC polytypes [18].

The D_{it} distribution in figure 1.5 is obtained by oxidation of Si faces of the three polytypes in dry O_2 [18]. D_{it} remains above 10^{11} eV^{-1} over the entire SiC band gap. Moreover, there are two regions with high D_{it}; in the lower half of the SiC band gap, D_{it} is in the range of $10^{12}cm^{-2}$ eV^{-1}; in the vicinity of conduction band edge, particularly in 4H-SiC, D_{it} approaches $10^{13}cm^{-2}eV^{-1}$ [19]. In addition, D_{it} is sensitive to the SiC polytype, and the crystallographic orientation of the SiC surface. In the regions close to the valence band, the D_{it} difference between 4H-SiC and 6H-SiC is small. However, D_{it} in the upper part of the SiC band gap is higher for 4H-SiC [19].

In the case of n-channel SiC-based MOSFET device, the Fermi level becomes close to the SiC minimum of the conduction band edge at the interface, and then inversion layer is formed. In this case, most states in the band gap are filled with electrons, and hence the density of free electrons and the electron mobility reduce. Those states in the bandgap which capture electrons become the coulomb scattering centers, and reduce the mobility in turn. Therefore, SiC MOSFET channel mobility is by far lower that its counterpart in bulk.

Therefore, the reduction of the interface defects density becomes a key issue in SiC MOS technology, and better understanding of the defect nature in the oxidized SiC would be essential for further development.

1.5. SiC Oxidation

Oxidation is the critical process of device fabrication, especially for high interface trap density interfaces such as SiC/SiO_2. The first procedure of oxidation is surface cleaning, in which SiC surface is degreased by organic solvents such as trichlorethane, acetone, and ethanol. In wet cleaning, HF based solutions are used to remove the native oxides; while hydrogen or ozone plasma is used in dry cleaning. Oxide is produced thermally by dry or wet oxidation. The oxidation procedure is accomplished by loading the wafers at 700-800 $^{\circ}C$ under oxygen flow, either in pure O_2 for the dry oxidation or water vapor from nitrogen or other carrier gases flowing through boiling deionized water for wet oxidation, and then ramp up the furnace to the oxidation temperature (1100 and 1200 $^{\circ}C$) [15].

The oxidation rate of SiC is lower that that of Si and the required temperature is above $1000^{\circ}C$. Although the detail of the process is not clear, the suggested reactions are:

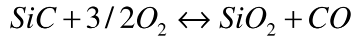

$SiC + 3/2O_2 \leftrightarrow SiO_2 + CO$

$SiC + O_2 \leftrightarrow SiO_2 + C$.

The excess carbon is the key differentiation between SiC and Si oxidation process. The fact that a part of the excess carbon forms CO gas and diffuse through SiO_2, has been proven for cubic SiC both theoretically [20], and experimentally [21]. Carbon cluster [21], carbon interstitial, and a stable pair of carbons [22] have been suggested to form as the result of CO breakage at the interface or bulk SiC.

The oxidation kinetics is described by Deal and Grove empirical model [23]:

$$t = \frac{X_0^2}{B} + \frac{X_0}{(B/A)} - \tau \qquad 1.1$$

where X_0 is the oxide thickness, and t is the oxidation time. The time constant τ is the initial oxide layer and can be neglected. The oxidation is limited by the reacting species through the oxidation. In the case of dry oxidation, the reaction is limited by transport of oxygen through the SiO_2. The diffusion-limited oxidation rate of SiC is 2/3 that of Si, which means that more oxygen is consumed in oxidizing SiC. The parameter B is proportional to the diffusion coefficient of the reacting species and is called the parabolic rate constant [23, 24].

Despite the discrepancies in reported temperatures, and activation energies, it is known that the oxidation differs for different faces of the SiC. The oxide grown on Si face has better electrical quality than that of carbon face [24].

Although there is a debate over the existence of carbon excess at the interface of SiC/SiO_2, several interface composition measurements, such as electron energy loss spectroscopy (EELS) [25], X-ray photo-electron spectroscopy (XPS) [26] and surface enhanced Raman spectroscopy (SERS) [27] have detected the presence of a near-interfacial region (almost several angstroms) with excess carbon atoms. The reported thickness of the interface region is different from experiment to experiment, but the mere existence of a layer rich in carbon is very critical for the electronic device.

1.6. Defect at SiC/SiO_2 Interface, and Defect Classifications

Apart from having a wide bandgap, the particular importance of SiC is the fact that it can be thermally oxidized to grow a SiO_2 layer, which is the superior dielectric for metal oxide semiconductor (MOS) devices. Although the quality of the thermally grown oxide on SiC is comparable to that of Si devices, the density of interface states in SiC/SiO_2 system is by far higher [18, 19]. Comparing SiC/SiO_2 and Si/SiO_2 systems provide information about the higher density of states of the former with respect to the latter one.

The first distinction between SiC/SiO_2 and Si/SiO_2 systems is the existence of carbon in the SiC compound semiconductor, which may add both chemical complexities to the oxidation process and cause undesirable defects. It is generally assumed that the oxidation process generates SiO_2 and emits CO. Although CO and CO_2 are believed to diffuse into SiO_2 and get removed from the interface, some of the excess carbons may remain in the interface [20-22]. Despite the fact that carbon removal from the interface is fast, the process is thought to be limited by the reaction time [15].

Secondly, the wide bandgap of SiC material may make it more susceptible to those oxide traps which normally lie above the Si narrow bandgap. Therefore, the oxide traps of Si/SiO_2 system may act as near interface traps for SiC/SiO_2 [18]. Some experiments show that the electron traps in the upper half of the band gap have fixed energy positions with respect to the valence band edge of different types. Moreover, the higher the band gap of the different SiC polytypes becomes, the higher the density of states shows up [22].

The other distinction between SiC/SiO_2 and Si/SiO_2 systems is the different surface density of atoms per unit areas results in different dangling bonds at the interface of two systems [18].

In one classification, the interface traps are classified to fast and slow. The fast traps are referred to those states located deep in the band gap; while the slow ones (called near interface traps, N_{IT}) are the acceptors near the conduction bands, located near the oxide phase. The near interface traps are called slow because of their slow response time. Although the nature of defects in the upper part of the band gap is not well-understood, it is thought that these defects could be the intrinsic of oxide [18, 28].

Another way of classifying the SiC/SiO_2 interfacial defects is by the potential species that my form at the interface. In this category, one can attribute SiC/SiO_2 defects to the carbon-related defects, oxide-related traps, and dangling bonds at the interface.

Carbon related defects vary from carbon interstitial to a pair of carbon atoms, and carbon cluster both in SiC, and oxide side of the interface [28-30, 66, 67]. From experimental point of view, carbon dangling bonds in oxidized porous SiC were

identified by electron spin resonance [31]. While some theoretical studies attribute the states in the midgap, and vicinity of the valence band to the carbon-related defects in the form of carbon interstitial, and a pair of carbon atoms [22, 28, 32], some others found that carbon interstitial could account for the interface defects below the conduction band. Recently carbon di-interstitial cluster $(Ci)_2$ in SiC was proposed to cause low channel mobility [33, 66, 67]. Small carbon clusters may form by either graphitic flakes or small bonded carbons at the interface of SiC/SiO_2; it is believed that large clusters are not likely to form at the interface [34, 35]. Experimentally, although there are several experiments which detect the carbon clusters at the interface of SiC-oxide interface by the means of X-ray photoelectron spectroscopy [36], atomic force microscopy [37] and transmission electron microscopy [38], there are other investigations which rule out the occurrence of these clusters [39-41].

Due to the similarities between silicon, and SiC systems, silicon dangling bonds which are the dominant defects in Si-based electronic devices, are one of the first potential candidates for high trap density in SiC interface. The presence of Si dangling bonds in Si/SiO_2 system has been revealed by Electron spin resonance (ESR) [42, 43]. Moreover, their saturation with the hydrogen atoms eliminates the related states from the bandgap, which is called hydrogen passivation [44]. There are two differences that distinguish Si-oxide, and SiC-oxide systems with respect to silicon dangling bonds; firstly, no electron spin resonance (ESR) spectroscopy measurements have yet revealed the existence of silicon dangling bonds at the SiC-oxide interface. Nevertheless, some authors suggest that the spread energy levels and orientations of silicon dangling bonds is the reason that they have not been detected

by experiments yet [19]. Secondly, hydrogen passivation with the same conditions as performed on Si-oxide system is not very effective in eliminating the silicon dangling bonds in the SiC-oxide system [45]. However, one can not completely rule out the existence of silicon dangling bonds, or threefold-coordinated silicon, with the variety of backbones and spread energy levels [19], especially after several published reports [46, 47] which prove the improvement of interface quality, and channel mobility by hydrogen annealing in elevated temperature.

On the other hand, intrinsic oxide defects in the oxide side such as oxygen deficiency, and silicon interstitial have been suggested to give rise to either the states in the gap, or near the conduction band. It is suggested that the energy of these traps are fixed with respect of the oxide conduction band edge for all SiC polytypes, and oxidation process [18, 28]. The same energy level with respect to the oxide conduction band edge is reported for the Si/SiO_2 system [13], which supports the idea that the near interface traps are caused by the oxide defects.

Experimentally, except the silicon vacancy in SiC side of the interface (the carbon dangling bonds around the Si vacancy in SiC) detected by spin-dependent recombination (SDR) [48, 49], and carbon dangling bonds in oxidized porous SiC [31], there is no non-controversial or clear experimental evidence of any other defects. Therefore, the origin of the high interface states in SiC-oxide system still remains unclear. In fact, there is no experimental evidence for the high density of states in the vicinity of 4H-SiC conduction. Therefore, more theoretical simulations of the interface defects, and interface compositions would be useful to help the experimentalists for further investigations. Theoretically, some potential defects have

been identified, and their energy levels have been located in the bandgap [19, 22, 28, 32, 40].

1.7. Transition Layer

During the oxidation process, a layer of SiO_2 is naturally growing on the surface of SiC. Form chemical point of view, unlike the Si/SiO_2 system, the interface between silicon carbide and its oxide is not abrupt due to the fact that the removal of carbon, by any process is not completed immediately. Moreover, due the topological reasons, the bond lengths of SiC are too small to accommodate an abrupt interface [24].

There are various experiments that support the formation of a several nanometer transition layer between SiC, and its oxide [30, 50-53]. Spatially resolved EELS analyses confirm chemical modifications of interfacial region, consistent with the presence of a ternary Si-O-C phase in the vicinity of the interface. The chemical shifts show the presence of oxygen and carbon atoms at the SiC near the interface.

The transition oxide layer is a ternary SiO_xC_y phase, called silicon oxycarbide. The presence of a transition oxide layer at the interface could alter the electronic properties of a multilayer SiC-based electronic device [53].

In the SiC structural unit cell, each Si atom is surrounded by four carbon atoms, forming a tetrahedron. However, during the oxidation process, either the carbon atom in SiC may be substituted by oxygen or the oxygen atoms in SiO_2 unit cell are replaced by carbon atoms and led to the formation of a SiO_xC_y phase. These replacements with different amounts result in different possible structural configurations of the transition layer. However, the nature of this transition layer, i.e.,

its actual atomistic structure, is not yet well understood. Characterizing the transition layer is useful for making a robust device based on SiC.

1.8. Passivation, and Annealing of Interface Defects

From the early stages of the semiconductor device fabrication, based on silicon, germanium, and GaAs substrates, it was known that the dangling bonds, or un-saturated valence electrons, reduce the carrier lifetime. Dangling bonds occur at the surface of semiconductors, or at the vacancies, dislocations, and certain interstitials. The reduction of the dangling bonds have been achieved either by optimization of the oxidation procedure, or passivation. Passivation is a technique to attach the atoms to the dangling bonds. The main effort of these techniques is to reduce the density of interface states.

In the case of 4H-SiC/SiO_2, the focus is on improving the interface by either modifying the oxidation process, or the post-oxidation annealing in ambient such as NO, N_2O, NH_3, and H_2.

Re-oxidation is a method that leads to slight reduction of deep interface states [54]. Although the mechanism is not clear, the reduction of the states is attributed to the removal of carbon atoms from the interface without additional oxide growth.

In the case of silicon-based electronic devices, hydrogen passivation is a technique to reduce the interface state density, especially the dangling bonds. This is done by the post-metallization annealing (PMA) at temperatures between 350-450 $^{\circ}C$. This process reduces the interface state density to $10^{10} cm^{-2} eV^{-1}$ in the midgap [55]. However, hydrogen annealing of the SiC-based devices with the same condition has limited effects on the deep interface states [45]. Hydrogen annealing in elevated

temperature is reported to improve the channel mobility, though [46, 47]. Moreover, the detection of C-H, and Si-H right at the interface has been attributed to carbon, and silicon related defects or dangling bonds [56-59].

Nitridation reduces the density of states both near the valence, and the conduction bands of SiC/SiO_2 system. Although is an efficient technique in reducing the density of states in general, its effect is much stronger on the reduction of the near interface states. It leads to channel mobility improvement up to 50 cm^2/Vs [18, 22, 35, 45, 60]. It should be noted that high density of nitrogen atoms, between $10^{14} - 10^{15} atoms/cm^2$, incorporates at the interface, after nitridation [61, 62].

Comparing the nitridation in NO, N_2O, and NH3 ambient, nitridation in NO has the best results. Nitridation in NH_3 introduces excess hydrogen atoms at the interface, and nitridation in N_2O produces NO, N_2, and O_2, which results in re-oxidation, and diminishes the effect of nitridation [63].

Although the mechanism of nitridation is not clear yet, it has been proposed that nitrogen either neutralizes the unpaired electrons, or dissolves the carbon clusters and helps the removal of carbon from the interface (probably in the form of C≡N molecules). Moreover, nitrogen may saturate dangling bonds by Si=N formation and replace oxygen in strained Si–O–Si bonds [18, 22, 35, 45, 60].

Recently, the better improvement of mobility has been reported by phosphorous postoxidation annealing in phosphoryl chloride ($POCl_3$) [64, 65].

1.9. SiC Mobility

Low mobility, caused by excessive scattering of carriers at the SiC/SiO_2 interface is the biggest challenge in the development of SiC devices. A large number of traps become filled during the inversion, causing the coulomb scattering of mobile charges, and decreasing the mobility.

The overall mobility values of 4H-SiC devices shows a tenfold reduction in interface. Theoretical and experimental simulations [68, 69] on 4H-SiC MOS devices indicate that the coulomb and surface roughness mobilities are dominant in the subthreshold and linear regions of operations [70]. According to the simulations, coulomb scattering dominates at low gate biases, and over a wide range of temperatures. At high gate biases and almost independent of temperature, it is the surface roughness that controls the scattering mechanism [71, 72].

The density of states for the traps near the edge of the conduction band is so large, that they become comparable to the conduction band density of states for electrons. This implies that a conduction band electron will have similar probabilities of occupying a conduction band trap or a conduction band state [72, 73].

Moreover, a DFT-DOS based method for calculating electron dispersion relations , and drift-diffusion modeling of 4H-SiC MOSFETs have suggested that the band-edge interface trap DOS in 4H-SiC MOSFETs are comparable to conduction band electron DOS. This leads to similar probabilities of an electron to occupy a conduction band electron state or a conduction band trap [74].

Therefore, accurate evaluation of the density, location and energy-distribution of these interface traps is very important for designing complex circuits using SiC devices.

1.10. Dissertation Goal, and Outline

In order to understand the electronic properties of the (0001)4H-SiC/SiO_2 structure, a DFT-based approach is taken to find the effect of the potential defects, and various transition layers on electronic properties of an interface-like structure. The same approach is used for defect passivation.

Using the information obtained from DFT-based calculations, such as the total density of states, DOS, as the input into a Monte Carlo simulator, we then calculated, and compared both the phonon-limited and Coulomb-limited mobilities of bulk, and different interface structures.

Lastly, a Monte Carlo technique is adapted to calculate the noise of 4H-SiC/SiO_2 structures by the use of the near interface trap densities obtained from DFT calculations.

In this dissertation, we first described the principle of density functional theory in general, and its application to semiconductor bulk, and interface calculations, in particular. Chapter two is what is needed from density functional theory as the theoretical background.

Then the real journey starts with calibrating the calculations with the basic electronic properties of two common polytypes of SiC: 4H-, and 6H-SiC. The reasonable band structures obtained for both 4H-, and 6H-SiC together with the accurate 4H-SiC effective masses ensured us that we were on the right track.

The next step was generating an abrupt interface model for (0001)4H-SiC/SiO_2 interface. The electronic characteristic of this structure which is called "abrupt" together with its band evolution is provided in chapter three.

We then investigated the effects of several potential defects, suggested in the literature, on the electronic properties of the interface in chapter four. Almost all the potential defects which were introduced in the structures have been passivated by several passivants such as hydrogen, nitrogen, and phosphorus to study the impact of passivations on the proposed defects.

Since there are several theoretical and experimental evidences support the idea that the interface between 4H-SiC, and its oxide is not abrupt, we constructed transition-like structures, and found the most probable atomic configurations that may happen during the oxidation. In doing so various distorted bridges in both SiC, and SiO_2 side of the interface have been created. We then tried to passivate the damaged bridges by nitidation. Chapter four starts from the silicon oxycarbide, and ends in silicon oxynitride.

All band structures, and defect level investigations in this dissertation are based on a two-step DFT calculation. First, the DFT solver "Quantum Espresso" [75] is used to perform relaxation, band-structure and DOS calculations of the bulk SiC, and SiC/SiO_2 structures, which augments the standard classical coulombic interactions with the Perdew-Burke-Ernzerhof (PBE) exchange-correlation functional [76] to approximate many body effects. The DFT calculations are performed within the plane-wave basis set to obtain a single electron wavefunction, position dependent density, and the minimum energy of the system; then the bandgap, and defect energy

levels have been re-calculated and modified in a hybrid functionals [77] paradigm to overcome the “bandgap problem” of DFT, and provide accurate defect level estimation.

To determine mobilities, and carrier velocities in bulk SiC, and various structures, we used a Monte Carlo transport simulator that uses the deformation potential approximation, Fermi’s golden rule, and the densities of states provided by DFT to calculate carrier scattering rates, velocities, and mobilities versus field. The details have been described in chapter five.

Lastly, a Monte Carlo scheme is developed to calculate the noise spectral densities of several structures by the use of the near interface trap densities obtained by DFT-based simulations. Chapter six gives more information about noise calculation.

Figure 1.6 shows a flow chart as a guideline for this dissertation simulations, and calculation.

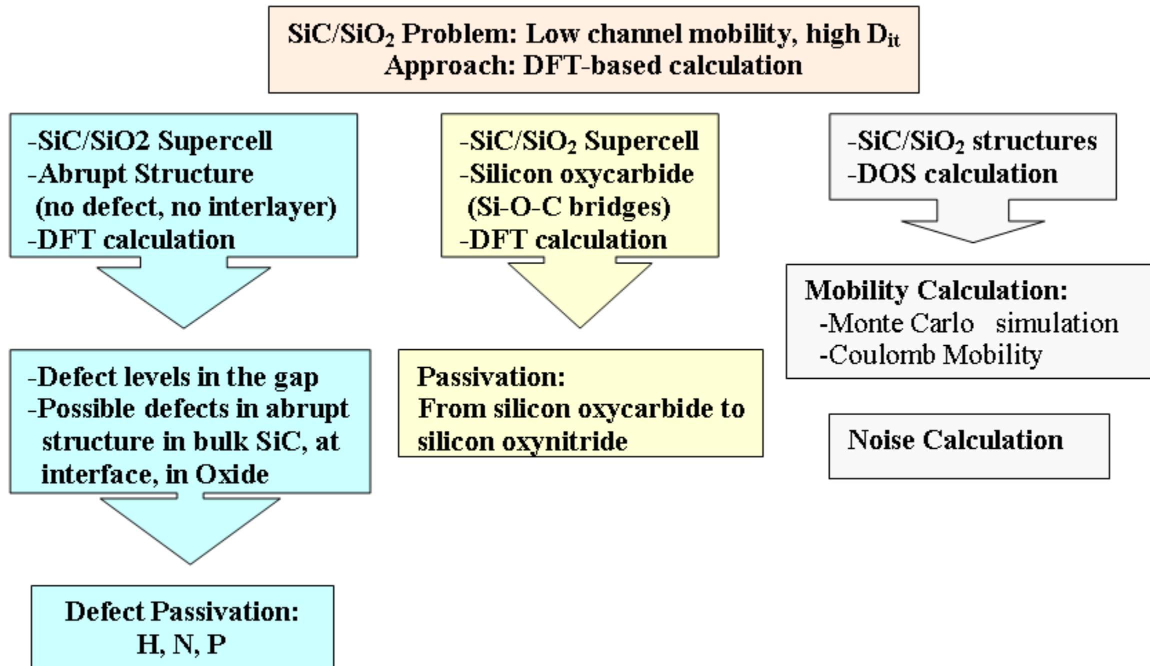

Figure 1.6: Flow chart as a guideline for the dissertation simulations, and calculations.

1.11. Contributions

In this work a hybrid functional density functional theory framework is employed to model the (0001)4H-SiC/SiO_2 abrupt interface. Then the accurate defect levels in the bandgap have been calculated through the total and projected density of states. Since there are experimental evidences for improvement of the quality of the interface by passivations, but the mechanisms are not clear yet, the impact of various passivations on the potential defects has also been studied.

Since in reality the interface of SiC/SiO_2 is not abrupt, several atomic configurations for (0001)4H-SiC/SiO_2 transition layers have also been modeled, and their effect on the bandgap, and the near interface trap density has been studied.

A DFT-based Monte Carlo carrier transport simulation technique is employed to compute the average velocities, phonon-limited and ionized-impurity-limited mobilities of the most probable transition layer structures.

Finally, since low frequency noise calculation is a powerful tool to diagnose quality, and reliability of semiconductor devices, a DFT-based method is proposed to calculate the current spectral noise density of the (0001)4H-SiC/SiO_2 transition layers.

The list of publications:

- S. Salemi, N. Goldsman, A. Akturk, A. Lelis; "Density Functional Theory Based Investigation of Defect Passivation of 4H-Silicon Carbide/SiO_2 Interfaces"; SISPAD 2012, Denver, USA.
- S. Salemi et al. "Silicon Carbide-Silicon Dioxide Transition Layer Mobility"; Materials Science Forum, Vols. 717-720 (2012), pp 449-452.

- S. Salemi et al. "Total near Interface Trap Density Calculation of 4H-SiC/SiO2 Structures before and after Nitrogen Passivation"; Materials Science Forum, Vols 717-720 (2012) pp457-460.
- S. Salemi et al.; “The Effect of Different Passivations on Near Interface Trap Density of 4H-SiC/SiO2 Structures”; ISDRS 2011 Conference Proceedings, Maryland, USA.
- S. Salemi et al.; “The Effect of Different Silicon Carbide Dioxide Interface Passivations on Transition Region Mobility and Transport”; ISDRS 2011 Conference Proceedings, Maryland, USA.
- A. Akturk, S. Salemi, N. Goldsman, S. Potbhare, A. Lelis; ”Simulation of Carrier Transport in Bulk Silicon Carbide and Near Silicon Carbide-Silicon Dioxide Interface”; International Conference on Simulation of Semiconductor Processes and Devices; September 8-10, 2011; Osaka, Japan.
- S. Salemi, A. Akturk, N, Goldsman and A. Lelis; “DFT Prediction, and DFT-Based Carrier Transport Simulation of 4H-SiC(0001)/SiO_2 Interface”; submitted to the Journal of Applied Physics;
- S. Salemi, A. Akturk, N, Goldsman and A. Lelis; “The Effect of Defects, and their Passivation on the Density of States of the 4H-SiC(0001)/SiO_2 Interface”; submitted to Journal of Applied Physics.

Chapter 2: Theoretical Background; From Schrodinger Equation to Density Functional Theory Calculation of Semiconductors

2.1. Introduction

In this thesis, we use Kohn-Sham formalism of Density Functional Theory (DFT) to probe and potentially optimize the SiC-SiO_2 interface. DFT allows investigators to make extremely complex many body quantum mechanical systems more tractable. DFT is based on solving the Kohn-Sham equation, for which a Nobel Prize was awarded to Kohn in 1998. Since the roots of the Kohn-Sham equation were formed on quantum mechanics, we start this chapter by the basic concepts of fundamental formulations, and their related concepts. The story begins with the complexities of solving Schrodinger equation, which is the backbone of the quantum formulation. Several approximations have been formulated to overcome the intractability of this equation which is built on the second differential of a cryptic entity, the wavefunctions, which stores information of not only all electrons and nuclei forming the atomic system, but also their correlations. Using the simple words, Born-Oppenheimer approximation separates the mere nuclear from the electronic parts, although the electrons are still dependent on the nuclear positions. Hartree manage the electron-electron correlation by reducing the many-electron wave function to single-electron ones; Hartree-Fock deals with the negligence of Hartree approximation by introducing the Slater determinant, which represents the Pauli's exclusion principle. Density functional theory is centered on the density of the electrons instead of the wavefunction. Finally, Kohn-Sham formalism which is formally based on the electron density separates the parts of electron-electron

connections which can be calculated from those which can not, and ignore the latter part in the first step. Kohn-Sham genius idea in making approximations for their "ignorance" part, which is called the exchange-correlation, gained for Kohn the Nobel Prize.

This chapter shows the journey from the Schrodinger equation to the Kohn-Sham's calculation of semiconductor materials. Since some of the Schrodinger's approximations are needed to overcome the shortcoming of Kohn-Sham's formulation in explaining the semiconductor systems, we kept, and explained them in the simplest possible form. The readers who do not like the theoretical aspects may starts from chapter three.

2.2. Many-Body Schrodinger Equation

"I do not like it, and I am sorry I ever had anything to do with it." Erwin Schrödinger

Quantum mechanics is a mathematical tool for predicting the behaviors of microscopic particles. The results of quantum formalism cover wide range of phenomena. In fact, one of the advantages of quantum mechanical calculations is its ability to predict the total energy of a system of electrons and nuclei. The rules of calculating the energies of the complicated systems are the extension of those for simple one-atom systems. Having found the total energy of system, all of those physical properties which are related to the total energies or the differences between the total energies can be calculated; the instances are the equilibrium lattice constant that minimizes the total energy, or the fact that the surfaces and defects of solids adjust themselves in a way that minimize the related total energies. If total energies

are calculated precisely, most of the physical properties can be estimated. Hence, electronic and geometric structure of solids can be predicted by total energy calculations and the relevant minimizations with respect to the electronic and nuclear coordinates.

However, the Schrodinger equation, which is the central equation of energy calculation, is too complicated to be solved analytically for all but the simplest (and hence most trivial) systems; it is exactly solvable just for harmonic oscillator, two-particle system (analytically), and a very-few-particle systems (numerically). The only way of using the power of quantum mechanics is to solve the equations numerically by modeling the processes of interest computationally.

The properties of a non-relativistic, many-body quantum system are formulated in many-body Schrodinger equation. The simplest form of time-independent Schrodinger equation in SI units is:

$$\hat{H}\Psi_i(\vec{x}_1,\vec{x}_2,...,\vec{x}_N,\vec{R}_1,\vec{R}_2,...,\vec{R}_M) = E\Psi(\vec{x}_1,\vec{x}_2,...,\vec{x}_N,\vec{R}_1,\vec{R}_2,...,\vec{R}_M) \qquad 2.1$$

The Hamiltonian of a system of electrons and nuclei is given by:

$$\hat{H} = -\frac{\hbar^2}{2m_e}\sum_i \nabla_i^2 + \sum_{i,I}\frac{-Z_I e^2}{\left|\vec{r}_i - \vec{R}_I\right|} + \frac{1}{2}\sum_{i\neq j}\frac{e^2}{\left|\vec{r}_i - \vec{r}_j\right|} - \sum_I \frac{\hbar^2}{2M_I}\nabla_I^2 + \frac{1}{2}\sum_{I\neq J}\frac{Z_I Z_J e^2}{\left|\vec{R}_I - \vec{R}_J\right|} \qquad 2.2$$

where $\hbar$ is the reduced Plank constant, e is the electron charge, Z is the nuclei charge and electron and nuclei properties are shown by lower case and upper case respectively. The first term is the electronic kinetic energy, the second term is electron-nuclei Coulomb attraction, the third term is the electron-electron repulsion, the fourth term is the nuclear kinetic energy and the last term is nuclei-nuclei repulsion. In the presence of external electric or magnetic fields, Hamiltonian may

contain even more terms. The above Hamiltonian can be written in the following form:

$$\hat{H} = \hat{T}_e + \hat{V}_{N-e} + \hat{V}_{e-e} + \hat{T}_N + \hat{V}_{N-N} \,. \qquad 2.3$$

Schrodinger equation is the second order differential equation with 3N (for electrons) plus 3P (for nuclei) degrees of freedom, which is too complicated to be solved in a full quantum mechanical framework. Apart from the different statistics of electrons and nuclei, and the fact that there are (3N+3P) coupled degrees of freedom in the system, the so called term “electron-electron interaction” is a term which brings the most part of complication; the complexity relates to the fact that the correlation term doesn’t allow the wave function separation.

Solving quantum mechanics quantitavely requires several approximations, of which the most widely used is independent-electron approximation. Within this approximation each electron moves independently of the others, except that the electrons obey the exclusion principle and each move in some average effective potential which may be determined by the other electrons. Then the state of the system is specifies by independent-particle eigenstates.

The range of simplifications starts with Born-Oppenheimer approximation that separates the electronic and nuclear coordinates of the many-body wave function and extends to the theories that approximate the electron-electron and electron-ion interactions. Once the approximations are applied to the equation, unit cell and supercells model the periodic and non-periodic systems and iterative minimization is used to find the electronic coordinates [78-80].

2.3. Born Oppenheimer/ Classical Nuclei Approximation

Born-Oppenheimer approximation, which is the first step in simplifying the Schrodinger equation, assumes that electrons remain in a given state as the nuclei move. It suggests that the electronic and the nuclear motions in molecules can be separated. Therefore, the electronic wave function depends upon the nuclear positions but not upon their velocities. The nuclear motion (such as rotation, vibration) feels the potential of fast-moving electrons [78].

The idea is to consider the wave functions of the couple system of nuclei and electrons as a combination of a complete set of states for electron at each nuclear position and the states of coupled electron-nuclear system; the latter ones are the functions of nuclear coordinates:

$$\Psi(\vec{x}_1, \vec{x}_2, ..., \vec{x}_N, \vec{R}_1, \vec{R}_2, ..., \vec{R}_M) = \sum_i \psi_i(\vec{x}_1, \vec{x}_2, ..., \vec{x}_N, \vec{R}_1, \vec{R}_2, ..., \vec{R}_M)\chi_i(\vec{R}_1, ...\vec{R}_M) \qquad 2.4$$

where $\chi_i(\vec{R})$ is a nuclear wave function and $\psi_i(\vec{r}, \vec{R})$ is an electronic wave function that depends parametrically on the nuclear positions. The total energy of the system is calculated by adding the nuclear part. If the nuclei are fixed, one should solve Schrodinger equation for electrons moving in the atoms and molecules:

$$H\Psi_K(\vec{r}|\vec{R}) = E_K(\vec{R})\Psi_K(\vec{r}|\vec{R}) \qquad 2.5$$

This Hamiltonian has a term related to the sum of kinetic energies of electrons, a term dealing with the sum of potentials that each electron feels in the presence of nuclei, and the pair-wise interactions among the electrons, V_{ee}:

$$V_{ee} = \sum_{j<k=1}^{N} \frac{e^2}{r_{j,k}} \qquad 2.6$$

V_{ee} is also a term which still makes solving the Schrodinger equation very complicated. Apart from the fact that one mole of a solid contains $N=10^{23}$ electrons and the many-electron wave function contains 3N degrees of freedom, which makes it simply intractable; the electron-electron correlation is very hard to be quantified. Consequently since the many-body wave function is a complicated mathematical object, more approximations should be introduced to make the Schrödinger equation tractable to numerical solution, while retaining the key elements of physics [78-81].

2.4. Mean-Field Theories/ Non-Interacting Electrons

Non-interacting electron approximation is another method to make the N-electron Schrodinger equation tractable.

In this approximation, each electron feels the mean potential created by all the other electrons in the system together with the ionic potential. The equation governing the motion of non-interacting electrons in this effective potential is given by:

$$(\sum_i -\frac{1}{2}\nabla_i^2 + \sum_i V_{eff}(r_i))\Psi = E\Psi . \qquad 2.7$$

In summary, each electron moves in an effective potential, representing the attraction of the nuclei and the average effect of the repulsive interactions of all other electrons. This average repulsion is the electrostatic repulsion of the average charge density of all other electrons.

2.5. Hartree Approximation

Although the Born-Oppenheimer approximation considerably reduces the complexity of the Schrödinger equation, the resulting electronic Schrödinger equation is still extremely complicated, due to the electron-electron interactions.

Hartree keeps the idea of the mean-field potential, which supposes that each electron moves in an effective potential, representing the attraction of the nuclei and the average effect of repulsive interactions of all the other electrons; the average electron-electron repulsion in Hartree approximation is the electrostatic repulsion of the average charge density of all other electrons.

Hartree's wave function is written as the functions that are written as the product of single orbitals:

$$\Psi(\vec{r}_1,\vec{r}_2,...,\vec{r}_N)=\phi_1(\vec{r}_1)\phi_2(\vec{r}_2)...\phi_N(\vec{r}_N) \qquad 2.8$$

where each $\phi(\vec{r})$ is a single particle orbital. Using the product of single orbitals is a harsh approximation that eliminates the complexity of interacting electrons and turns an N-body Schrodinger equation into N equations of single electron.

Hartree equation consists of three terms that operates on the single particle orbitals. The first term is the kinetic energy of electrons, $-\frac{1}{2}\sum_i^N \langle \phi_i | \nabla^2 | \phi_i \rangle$, the second term is the interaction of the single electron with the Coulomb distribution of nuclei (called the external potential), $-\sum_i^N \int \sum_A^M \frac{Z_A}{\vec{r}_{1A}} |\phi_i(\vec{r}_1)|^2 d\vec{r}_1$, and the third term that describes the interaction between the ith electron and the charge distribution of jth electron, $\frac{1}{2}\sum_i^N\sum_j^N \iint |\phi_i(\vec{r}_i)|^2 \frac{1}{\vec{r}_{ij}} |\phi_j(\vec{r}_j)|^2 d\vec{r}_i d\vec{r}_j$.

Considering the single-particle approximation and changing the three Hamiltonian terms to the simple forms, the Hartree equation could be written as:

$$[-\frac{1}{2}\nabla_i^2 + \sum_I V(\vec{R}_I - \vec{r}_i) + \sum_{j\neq i}\int \left|\phi_j(\vec{r}_j)\right|^2 \frac{1}{\vec{r}_{ji}} dr_j]\phi_i(\vec{r}_i) = \varepsilon\phi_i(\vec{r}_i) \quad 2.9$$

Then a many-body Schrodinger equation decomposes to N separate single-particle Schrodinger equations with the following Hamiltonian:

$$\hat{H}_H = -\frac{1}{2}\nabla_i^2 - \sum_I V(\vec{R}_I - \vec{r}_i) + V_H(i) \quad 2.10$$

The mean field theory in Hartree approximation becomes as follow:

$$\hat{V}_{eff}(\vec{r}) = \hat{V}_{ext} + \hat{V}_H \quad 2.11$$

Unlike the standard formulation, the Hamiltonian depends on the orbitals that are the solution of all other Hartree equations. Therefore, the Hamiltonian needs to be found in the process of finding the solution. This is why it is called a self-consistent operator.

The process of solving the Hartree equation is to simulate N equations for the N orbitals; then solution is obtained iteratively. In fact, one must guess the form of the orbitals, and then find the solution of the single-particle pseudo-Schrodinger equations. The next step is to re-construct the Hartree operators with the new sets of orbitals. The iteration continues until the convergence is reached.

The energies obtained from Hartree approximation are not very accurate. In fact, the product wave function is symmetric, i.e. stays precisely the same after the exchange of two fermions It doen't consider the Pauli Exclusion Principle. Hartree product wave function is symmetric, i.e. stays precisely the same after the exchange of two fermions [81].

2.6. Hartree-Fock Approximation

Hartree-Fock approximation is the basis of almost all calculations in quantum chemistry and has great conceptual importance. Hartree-Fock gives the simplest yet physically meaningful approximation to many-body problem. Electron wave function is approximated by an antisymmetric product of N one-electron wave functions, called a Slater determinant. This determinant is written as:

$$\Psi \approx \phi_{SD} = \frac{1}{\sqrt{N!}} \det\{\chi_1(\vec{x}_1),...,\chi_N(\vec{x}_N)\} \qquad 2.12$$

The one-electron functions $\chi_i(\vec{x}_i)$ are called spin orbitals, and are composed of a spatial orbital $\phi_i(\vec{r})$ and one of the two spin functions α(s) and β(s):

$$\chi(\vec{x}) = \phi(\vec{r})\sigma(s) \qquad 2.13$$

which σ=α,β.

The spin functions are orthonormal and the spin orbitals are also chosen to be orthonormal. The Slater determinant in Hartree-Fock method is the approximation to the true N-electron wave function.

In the case of the ground state wave function of two electrons can be written as:

$$\Psi(\vec{x}_1,\vec{x}_2) = \frac{1}{\sqrt{2}} \det\{\phi_0(\vec{r}_1)\alpha(s_1),\phi_0(\vec{r}_2)\beta(s_2)\} \qquad 2.14$$

It may have either the same spatial coordinate but antisymmetric in spin coordinate like:

$$\Psi(\vec{x}_1,\vec{x}_2) = \frac{1}{\sqrt{2}} \phi_0(\vec{r}_1)\phi_0(\vec{r}_2)(\alpha(s_1)\beta(s_2) - \alpha(s_2)\beta(s_1)) \qquad 2.15$$

or the same spin and different spatial states like [82]:

$$\Psi(\vec{x}_1,\vec{x}_2)=\frac{1}{\sqrt{2}}(\phi_A(\vec{r}_1)\phi_B(\vec{r}_2)-\phi_B(\vec{r}_1)\phi_A(\vec{r}_2))(\alpha(s_1)\alpha(s_2)) \qquad 2.16$$

Once the form of the wave function is chosen, the variational principle is applied to obtain the best Slater determinant, which gives the lowest energy in return.

Hatree-Fock Hamiltonian has the following form:

$$\hat{H}_{HF} = -\frac{1}{2}\nabla_i^2 - \sum_i V(\vec{r}_i) + V_{HF}(i) \qquad 2.17$$

The spin orbitals are chosen in order to minimize the expectation energy of the electron:

$$E_{HF} = \min_{\phi_{SD}\to N}\left\langle \phi_{SD}\right|\hat{T}+\hat{V}_{Ne}+\hat{V}_{ee}\left|\phi_{SD}\right\rangle \qquad 2.18$$

The energy expectation value is given by:

$$E_{HF} = \sum_i^N \int \chi_i^*(-\frac{1}{2}\nabla^2 - \sum_i V_{ext}(\vec{r}_i))\chi_i d\vec{r}_i + \frac{1}{2}(\sum_i^N\sum_j^N\{\int\int|\chi_i(\vec{r}_1)|^2 \frac{1}{\vec{r}_{12}}|\chi_j(\vec{r}_2)|^2 d\vec{r}_1 d\vec{r}_2 -$$
$$\int\int \chi_i(\vec{r}_1)\chi_j^*(\vec{r}_1)\frac{1}{\vec{r}_{12}}\chi_j(\vec{r}_2)\chi_i^*(\vec{r}_2)d\vec{r}_1 d\vec{r}_2)\} \qquad 2.19$$

The first term is the contribution of the kinetic energy and the electron-nuclei attraction, while the second term is Coulomb potential minus the exchange potential. The exchange lowers the total energy; this is because the antisymmetrical N-electron wave function keeps the particles of similar spin out of each others' way, so their Coulomb repulsion energy is lowered. Moreover, the effect of exchange energy is subtracting the unphysical self-energy from Hartree energy. This is why Hatree-Fock approximation is called self-interaction free. In fact, the advantage of Hartree-Fock approximation over Hartree (and even density functional theory) is the fact that it is self-interaction free.

The exchange term, which is the manifestation of the Pauli Exclusion Principle, acts so as to separate electrons of the same spin; the consequent depletion of the charge density in the immediate vicinity of a given electron due to this effect is called the exchange hole. However, it still doesn't deal with the electron correlation. The correlation energy is the difference between the true energy and the Hartree-Fock energy. As the result of neglecting the electron-electron correlation, the electrons get too close to each other.

The shortcoming of Hartree-Fock approximation arises from the fact that it doesn't screen the exchange interaction by the correlation hole. However, it gives almost accurate results for small molecules (because there are far fewer electrons than in a solid), which the correlation effects are minimal compared to exchange effects [83-84].

2.7. Introduction to Density Functional Theory

"The underlying laws necessary for the mathematical theory of a large part of physics and the whole of chemistry are thus completely known, and the difficulty is only that exact applications of these laws lead to equations which are too complicated to be soluble."

P.M.A. Dirac, Proc. Roy. Soc. A 123, 714 (1929)

Density-functional theory, DFT, is an alternative approach to many-electron problem. The original density functional theory was suggested by Thomas and Fermi (appendix A.3) in 1927. Then the formalism has been developed by Hohenberg, Kohn, and Sham. In general, density functional theory is a way of treating the system

of interacting particles by transferring it to a system of non-interacting particles, which is easier to solve [80, 81].

This theory states that any property of the system of many interacting particles can be considered as a functional of the ground state; hence, the electron density, rather than the many-electron wave function, contains all the information of a given system. Although the existence of such functionals was proved by Hohenberg and Kohn's two theorems, the form of the density functional was not provided. The theorems don't formulate a way for calculating the ground state, either. The Kohn-Sham's ansatz shed light to approximate the ground sate functional of given systems; moreover, it provides the physical insight for atomic/molecular system of study [84, 85].

2.7.1. Electron Density

Conceptually, electron density is a probability density which shows the probability of finding one electron of arbitrary spin in a volume of space while all other electrons may be anywhere. The probability of finding an electron in $d\vec{r}_1$ is given by taking the integral over the spin coordinates of all electrons and the spatial coordinates of all except one:

$$\rho(\vec{r}_1) = N\int ...\int \left|\Psi(\vec{x}_1,...,\vec{x}_N)\right|^2 ds_1 d\vec{x}_2 ... d\vec{x}_N \qquad 2.20$$

It is an observable, presented by a non-negative function, which can be measured experimentally (by methods like X-ray diffraction); it becomes zero at infinity and integrates to the total number of electrons, N, at $\vec{r}_1$:

$$\rho(\vec{r} \to \infty) = 0; \qquad 2.21$$

$$\int \rho(\vec{r}_1) d\vec{r}_1 = N. \qquad 2.22$$

It has a discontinuity at nuclei and decays exponentially from the nuclei.

The pair density is defined as the probability of finding two electrons with different spins at two spatial volumes. In fact, the pair-density $\rho_{pair}(\vec{x}_1,\vec{x}_2)$ gives the probability of simultaneously finding an electron at the point $\vec{x}_1$ within volume element $d\vec{x}_1$, and another electron, $\vec{x}_2$, in volume element $d\vec{x}_2$, among the other (N-2) electrons in the system and it is defined as follow:

$$\rho_{pair}(\vec{x}_1,\vec{x}_2) = N(N-1)\int ... \int \left|\Psi(\vec{x}_1,\vec{x}_2,...,\vec{x}_N)\right|^2 d\vec{x}_3 ... d\vec{x}_N \qquad 2.23$$

Then the electron density is given by:

$$\rho(\vec{x}_1) = \frac{1}{N-1}\int \rho_{pair}(\vec{x}_1,\vec{x}_2)d\vec{x}_2 \qquad 2.24$$

As the result of the density constraint, $\int \rho(\vec{r})d\vec{r} = N$, the pair density constraint is as follow:

$$\iint \rho_{pair}(\vec{x}_1,\vec{x}_2)d\vec{x}_2 d\vec{x}_1 = N(N-1)\,. \qquad 2.25$$

Electrons are Fermions (therefore, have anti-symmetric wave function) and obey Fermi statistics; Pauli Exclusion Principle and Coulomb repulsive energy keep them apart. The effect of the former, called the exchange interaction, and the latter, called correlation interaction, is to reduce the classical value of the electron density at $\vec{x}_1$ due to the second electron located at $\vec{x}_2$. Therefore each electron creates a depletion, or hole, of electron density around itself as a direct consequence of exchange-correlation effects, which distinguish the quantum, electronic system from the classical one and leads to the following expression for the pair-density:

$$\rho_{pair}(\vec{x}_1,\vec{x}_2) = \rho(\vec{x}_1)\rho(\vec{x}_2) + \rho(\vec{x}_1)\rho(\vec{x}_2).f_{exchange-correlation}(\vec{x}_1,\vec{x}_2)\,. \qquad 2.26$$

Function f is the exchange, correlation factor which has the un-physical self-interaction [80].

Due to electrostatic repulsion, the immediate region around the electron has fewer electrons than average. Pictorially, it seems that there is a hole around each electron with the negative density which imposes attractive energy to the electrons. Hence, it is possible to consider the actual electron-electron potential energy as a sum of the classical interaction between electron densities together with the interaction of electron density with exchange, correlation hole. The exchange, correlation hole could be split into Fermi/exchange hole and Coulomb/correlation hole; while the Fermi hole is because of Pauli Principle (the antisymetry of the wave function), the Coulomb hole (applies to electrons with either spin) is the result of electrostatic interaction. Hole-function has all information about non-classical contributions to the potential energy due to electron-electron interaction. More information about the functional is given in Appendix A.2.

2.7.2. Hohenberg-Kohn Theorems

In 1964, Hohenberg and Kohn formulated and proved a theorem that (became the solid mathematical grounds of the Thomas-Fermi approximation, given in Appendix A.3) established the density functional theory as a theory of many-body system. The theorem is proven for every system of non-interacting particles which has the Hamiltonian consisting of the electronic kinetic energy, external potential, and the electron-electron potential.

The theorem is divided into two parts:

Theorem I: The external potential is a unique functional of the electron density only. Thus the Hamiltonian, and hence all ground state properties, are determined solely by the electron density.

The proof is based on reductio ad absurdum (proof by contradiction); the original proof supposes that if the external potential doesn't determine the density uniquely, then there should be two external potentials which make the same density. These two potentials are the part of two different Hamiltonians which their only difference is in the external potential:

$$\hat{H} = \hat{T} + \hat{V}_{ee} + \hat{V}_{ext} \tag{2.27}$$

$$\hat{H}' = \hat{T} + \hat{V}_{ee} + \hat{V}'_{ext} \tag{2.28}$$

Subsequently, these Hamiltonians are related to two different wave functions and hence two different ground states E_0 and E'_0, which, with the use of variational principle results in absurdum (contradiction). The proof shows that there can not be two different external potentials producing the same ground state energy densities or the ground state density uniquely determines the external potential. On the other words, the ground state density would provide all information about the number of the electrons, the atomic number and the position of the nuclei, Hamiltonian and therefore the energy ground state.

Then the ground state energy could be written as the functional of the ground state electron density:

$$E_0[\rho_0] = T[\rho_0] + E_{ee}[\rho_0] + E_{Ne}[\rho_0] \tag{2.29}$$

which could be split to the system-dependent potential energy due to the nuclei-electron attraction (the last right-hand side term), $E_{Ne}[\rho_0] = \rho_0(\vec{r})V_{Ne}d\vec{r}$, and a

universal function which is independent of the number of electrons, the atomic number and the positions of the nuclei (the first two right-hand side terms), $F_{HK}[\rho] = T[\rho_0] + E_{ee}[\rho_0]$. The universal functional could be written as:

$$F_{HK}[\rho(\vec{r})] = \left\langle \Psi \middle| \hat{T} + \hat{V}_{ee} \middle| \Psi \right\rangle \tag{2.30}$$

The universal term is the functional of the kinetic energy and the electron-electron interaction, which neither has the simple form. The electron-electron interaction could also be divided into the classical repulsion and non-classical part. The non-classical term is what is called "exchange-correlation" [79-81].

Theorem II: The ground state energy may be obtained variationally: the density that minimizes the total energy is the exact ground-state density.

The second theorem is similar to the variational principle of the wave function. Therefore, one can start with a trial density function; it results in a new Schrödinger's-like equation, expressed in terms of the charge density only:

$$E[\rho] = \int \rho(\vec{r}) V_{ext}(\vec{r}) d\vec{r} + F_{HK}[\rho] \geq E_0 \tag{2.31}$$

which the used density is the trial one. In performing the minimization of E[ρ] the constraint is the number of electrons, N, knowing that the integration of density over all space gives rise to the total number of electrons. By considering the Euler-Lagrange equation and replacing the constraint minimization of E[ρ]:

$$\delta\{E[\rho] - \mu[\int \rho(\vec{r}) d\vec{r} - N]\} = 0 \tag{2.32}$$

$$\mu = \frac{\delta E[\rho]}{\delta \rho(\vec{r})} = V_{ext}(\vec{r}) + \frac{\delta F_{HK}[\rho]}{\delta \rho(\vec{r})} \tag{2.33}$$

The Lagrangian multiplier, μ, is the chemical potential and does not depend on $\vec{r}$. Therefore, the electronic density function, $\rho(\vec{r})$, is chosen in a way that makes the right-hand side independent of $\vec{r}$.

One of the complications of the Hohenberg-Kohn procedure is defining a universal functional which should be independent of the external potential. Although, the universal functional is unknown, the Hohenberg-Kohn formalism gives a simple approach to quantum mechanics [79-81]. The V- and N-representivity are explained in Appendix A.4.

2.7.2. Kohn-Sham Formalism

Kohn and Sham made the density functional theory as a practical tool to find the exact properties of many-body system. In 1965, Kohn and Sham proposed the idea of replacing the kinetic energy of the interacting electrons with that of an equivalent non-interacting system to facilitate the process of calculation. They assumed that the equivalent non-interacting system, called as "non-interacting reference system" and also "non-interacting-V-representability (Appendix A.4), has the same ground state density as the original interacting one. They proposed to use orbitals in such a way that the kinetic energy can be simply calculated with good accuracy, leaving a small term that is approximated separately.

In fact, Kohn-Sham formalism has two main parts; on one hand, it provides the ground for treating the complicated kinetic energy functional of interacting, real system, $T[\rho]$, by decomposing it into the kinetic energy of fictitious non-interacting system of particles, $T_s[\rho]$ (subscript s refer to "single-particle"), and the remainder, $T_c[\rho]$ (subscript c refer to the "correlation").

The next step is to construct the Hamiltonian of a non-interacting reference system; it has the usual kinetic operator and an effective potential acting upon electrons with a particular spin (although the external potential is taken as spin-independent for simplicity). The Hamiltonian of a non-interacting reference system is written as:

$$\hat{H}_S = -\frac{1}{2}\sum_i^N \nabla_i^2 + \sum_i^N V_{S-eff}(\vec{r}_i) \qquad 2.34$$

The "giant leap" of Kohn-Sham formalism is to relate the energy of non-interacting system with the true-N-electron one. As mentioned before, the idea is to calculate the great fraction of kinetic energy with high accuracy and deal with left-over later!

Kohn-Sham method calculates the kinetic energy of the non-interacting system with the same density as the interacting real one; since the resulting kinetic energy is different from the true kinetic energy of the interacting system, it decomposes the universal functional to three terms:

$$F_{KS}[\rho(\vec{r})] = T_S[\rho(\vec{r})] + J[\rho(\vec{r})] + E_{XC}[\rho(\vec{r})] \qquad 2.35$$

The first left-hand-side term, $T_S[\rho(\vec{r})]$, is the independent-particle kinetic energy, while $J[\rho(\vec{r})]$ is the classical electrostatic energy of charge density distribution (long-range Hartree energy), and the last left-hand-side term is the exchange-correlation term (the remainder part). The exchange-correlation term is the unknown part that relates the exact calculated terms of fictitious system with the interacting, true system. It contains the non-classical effects of exchange and correlation of the potential energy of the system together with the ignored part of kinetic energy:

$$E_{XC}[\rho] \equiv (T[\rho] - T_S[\rho]) + (E_{ee}[\rho] - J[\rho]) = T_C[\rho] + E_{non-classical}[\rho] \qquad 2.36$$

which shows the exchange-correlation term is the difference between the real kinetic energy and that of non-interacting one, $(T[\rho]-T_S[\rho])$, plus the difference between the real electron-electron potential energy and the classical Coulomb electron-electron repulsion, $(E_{ee}[\rho]-J[\rho])$.

Now that the form of Kohn-sham universal functional is known, it is possible to find the Kohn-Sham energy in terms of non-interacting, single-particle electron kinetic energy, Coulomb repulsive potential, exchange-correlation energy and the external potential energy:

$$E_{KS}[\rho(\vec{r})]=T_S[\rho]+J[\rho]+E_{Ne}[\rho]+E_{XC}[\rho] \qquad 2.37$$

The classical, Coulomb repulsive electron-electron term is the Hartree energy:

$$J[\rho]=E_{Hartree}=\frac{1}{2}\sum_i^N\sum_j^N\iint\frac{\rho(\vec{r}_1)\rho(\vec{r}_2)}{\vec{r}_{12}}d\vec{r}_1 d\vec{r}_2 \qquad 2.38$$

and $E_{Ne}[\rho]$ is:

$$E_{Ne}=-\sum_i^N\int\sum_A^M\frac{Z_A}{\vec{r}_{1A}}|\phi_i| \qquad 2.39$$

Assuming the differentiability of $E_{KS}[\rho]$, the Kohn-Sham energy is minimized either by using variational or Lagrange-Euler equations. Variational minimization is differentiating the energy equation with respect to wave function:

$$\frac{\delta E_{K-S}}{\delta\psi_i^*}=\frac{\delta T_s}{\delta\psi_i^*}+[\frac{\delta E_{ext}}{\delta\rho(\vec{r})}+\frac{\delta E_{Hartree}}{\delta\rho(\vec{r})}+\frac{\delta E_{x-c}}{\delta\rho(\vec{r})}]\frac{\delta\rho(\vec{r})}{\delta\psi_i^*}=0 \qquad 2.40$$

Leading to Kohn-Sham Schrodinger-like equation:

$$(\hat{H}_{K-S}-\varepsilon_i)\psi_i(\vec{r})=0\,. \qquad 2.41$$

Minimization by using Euler-Lagrange equation results in:

$$\delta\{E_{KS}[\rho] - \mu[\int \rho(\vec{r})d\vec{r} - N]\} = 0 \qquad 2.42$$

The constraint is the equation that relates the density functional and the number of electrons in the system:

$$\int \rho(\vec{r})d\vec{r} = N \qquad 2.43$$

which gives the Euler-Lagrange equation:

$$\mu = \frac{\delta E_{KS}}{\delta\rho(\vec{r})} = \frac{\delta F[\rho(\vec{r})]}{\delta\rho(\vec{r})} + V_{ext}(\vec{r}) \qquad 2.44$$

this leads to:

$$\mu = \frac{\delta T_s[\rho(\vec{r})]}{\delta\rho(\vec{r})} + V_{KS}(\vec{r}) \qquad 2.45$$

The chemical energy, μ, with the negative sign is the ionization energy.

The Kohn-Sham effective potential energy has the following form:

$$V_{KS} = V_{eff}(\vec{r}) = V_{ext}(\vec{r}) + \frac{\delta J[\rho]}{\delta\rho(\vec{r})} + \frac{\delta E_{XC}[\rho]}{\delta\rho(\vec{r})} \qquad 2.46$$

$$V_{KS}(\vec{r}) = V_{ext}(\vec{r}) + V_{XC}(\vec{r}) + \int \frac{\rho(\vec{r}')}{|\vec{r} - \vec{r}'|}d\vec{r}' \qquad 2.47$$

with the following exchange-correlation potential:

$$V_{XC}(\vec{r}) = \frac{\delta E_{XC}[\rho]}{\delta\rho(\vec{r})} \qquad 2.48$$

Then the process is to solve the N one-electron equations in an effective, Kohn-Sham potential:

$$(-\frac{1}{2}\nabla_i^2 + V_{eff}(\vec{r}))\phi_i = \varepsilon_i\phi_i \qquad 2.49$$

As it is shown, V_{eff} depends on the electron density through the Coulomb (Hartree) term and this means that Kohn-Sham equation (like Hartree-Fock) should be solved

iteratively. Unlike Hartree-Fock method that starts with the Slater determinant approximation, Kohn-Sham formalism is an “exact theory in principle”; the approximation comes to the picture by exchange-correlation or by the form of the functional. Moreover, the charge density in KS approach is (by the definition) the exact density of the real GS, while the HF orbitals give HF ground state wave function whose square doest not give the correct GS density $\rho_0^{HF}(\vec{r}) \neq \rho_0(\vec{r})$ [80-85].

The Kohn-Sham equations are a set of pseudo-Schrodinger independent-particle equations which should be solved in the special effective potential considering the suitable electronic density. The main difference of Kohn-Sham equation with the many-body Schrodinger equation is that the former one doesn’t have the summations that appear in the latter one as the result of Kohn-Sham independent-single particle treatment. The procedure of solving Kohn-Sham problem starts with an initial guess for the electronic density and continues with calculating the effective potential, substituting them in the Kohn-Sham formula and finds the electron density again until the self-consistency reaches which leads to obtain important system properties such as energies. Kohn-Sham Hamiltonian is self-consistent, which means that it depends on the charge density.

In summary, Kohn and Sham made the basis of a theory that is able to solve the complicated many-body electronic ground state problem by transferring the many-body Schrodinger equation into a set of N coupled single-particle equations. Then, the electronic density could be found by an external potential and therefore the energy and any other ground state properties. They assumed that the density of the non-interacting reference system is equal to that of the true interacting system. The

approximation came to the system with the exchange-correlation term which contains all the ignorance about the many-electron interaction, while the remaining terms in the energy are well known. The exchange, correlation energy is the energy responsible for screening Coulomb repulsion energy. Methods that don't take it into account underestimate the strength of the chemical bonds and overestimate their length.

If the exchange-correlation functional were known, then the exact ground state of energy and the electronic density of the real, interacting system would be found by solving the Kohn-Sham equation for the non-interacting system of electrons. Since it is not known, its reasonable approximation would help to find the electronic density and properties.

2. 8. Solving Kohn-Sham Equation/ DFT in Practice

Kohn-Sham equation, based on the Hohenberg-Kohn theorems, claims that ground state density could be found by minimizing the energy of the energy functional which is obtained by finding the self-consistent solution to a set of single-particle equations.

Kohn-Sham equation has four terms that should be defined and calculated accurately: the kinetic energy of non-interacting system, the external potential imposing by the nuclei, the Hartree potential arising from the classical Coulomb repulsion of that electron taking part in the Kohn-Sham equation and the total electron density defined by all electrons in the problem and the exchange-correlation potential. Since the electron involved in Kohn-Sham equation is a part of the total electron density, then a part of Hartree potential includes the Coulomb interaction between the electron and itself, the Hartree potential is a self-consistent term. The

self-interaction is a non-physical phenomenon that can be compensated in the exchange-correlation potential. Finally, the exchange-correlation potential compensates all the ignored quantum mechanical phenomena.

The external potential is treated either explicitly (all electron calculation) or approximated by the process called “pseudopotential approximation”; the Hartree potential could be calculated from charge density integration or by solving Poisson equation. The exchange-correlation potential is the functional derivative of the exchange-correlation energy; however, there is no universal form for exchange-correlation functionals and there are several methods suggesting the exchange-correlation functional approximation [86].

In fact, finding the best functional for the given problem is only one of the issues in solving Kohn-Sham equation. Choosing a basis to expand single-particle wave function together with finding an accurate description for external potential experienced by electrons is at the heart of solution.

Kohn-Sham equation is an eigenstate, Schrodinger-like equation in which the single electrons are in the presence of the effective potential; hence, the equation could be expanded according to the appropriate basis.

In general, the single-particle wave function could be expanded as a function of a linear combination of plane waves, atomic orbitals, Gaussian functions, or a mixed basis (combination of plane waves and atomic orbitals).

The external potential experienced by the (valence) electron is either all-electron picture (purely Coulomb ion-electron interaction without the spin-orbital interaction)

or pseudopotential, which is weaker than the former one. In fact, the choice of external potential is limited to all-electron or valence-electron approaches.

2.8.1. Exchange-Correlation Functionals

The main goal of the electronic structure calculation is to predict the system properties accurately. In fact, the quality of Kohn-Sham prediction is in the hand of exchange-correlation functionals. The design of a calculation begins with the choice of an exchange-correlation functional, commonly referred to simply as the 'functional'. Choosing the most precise exchange-correlation functional would increase the numerical accuracy.

One classification of exchange-correlation functional is given by John Perdew [9]; he resembles the classes of exchange-correlation functionals to the Jacob'a ladder, which becomes more physically informative as the steps move upward. The first step is the local density functional, LDA, which depends solely on electron density; generalized gradient approximation (GGA) [87], the second rung of Jacob's ladder adds the gradient of the density as an independent variable. The gradient introduces non-locality into the description of exchange and correlation. GGA functionals have evolved in two main directions. One is called 'parameter free', where the new parameters are determined from known expansion coefficients and other exact theoretical conditions. The other is empirical, with the parameters that are determined from fits to experimental data or accurately calculated atomic and molecular properties. The GGA functionals most commonly used in physics, Perdew, Burke and Ernzerhof (PBE) [76] and Perdew–Wang from 1991 (PW91) [87] are parameter free. Most GGAs used in chemistry applications, e.g. Becke, Lee, Parr and Yang (BLYP)

[88] are empirical. The LYP correlation uses the Laplacian (second derivative) of the density and thus formally belongs to the third rung of Jacob's ladder but is commonly classified as a GGA.

Meta-GGAs are functionals from the third rung which use Laplacians of the density and/or kinetic energy densities as additional degrees of freedom. Tau, Perdew [88] and co-workers constructed a parameter free meta-GGA. The fourth rung on Jacob's ladder adds 'exact exchange' (EXX). The exchange energy per particle is obtained from the Hartree-Fock exchange formula. If the Kohn-Sham single-particle wave functions are used in this expression instead of Hartree-Fock orbitals, it is commonly called 'exact exchange'. All existing functionals are approximations whose accuracy varies with the properties of the given system. No single one is best, or even 'good', for all situations.

The other classification is based on whether the functional is empirical or non-empirical. Non-empirical functionals are constructed to satisfy certain constraints. They belong to the higher rungs of the ladder and have more ingredients and constrain to satisfy. Empirical functionals are constructed to fit the empirical data and contain fitting parameters and also provide accurate predictions for certain problems. There is no guarantee that the higher rungs functionals are more accurate than the lower ones, especially if the upper ones are the empirical ones [88].

Hybrid functionals generated to overcome the semiconductor DFT-based bandgap problem. They are not pure DFT functionals; instead it is a mixture of a DFT and a Hartree-Fock calculation. Hybrid functionals [77, 80, 88, 94] uses the Hatree-Fock exchange term and a functional for the correlation part as:

$$E_{XC} = E_X^{exact.H-F} + E_C^{functional.approximation} \quad 2.50$$

The details of the exchange correlation functional are given in Appendix A.5.

2.8.2. The Choice of Basis

Generally, the choice of basis is one of the methods to classify the density functional theory calculations. In principle, Kohn-Sham orbitals are expanded in a set of basis functions. Making and choosing the suitable basis functions is one of the most important tasks in solving Kohn-Sham equation. Basically, the orbitals are used to construct the approximate wave function, despite the fact that the Kohn-Sham equation directly depends on the electron density.

There are three choices for expressing the single-particle wave function: a plane-wave basis, a mixed basis involving plane waves and localized atomic orbitals, and purely localized atomic orbitals. Plane wave basis is the common choice among the solid-state-physics community.

In one category, the methods using the basis functions are classified to those ones that apply fixed basis (independent of energy), and the methods that use the energy dependent ones. Plane-wave, linear combination of atomic orbitals (LCAO), and orthogonalized plane wave (OPW) methods use the independent energy while augmented plane wave (APW), Korringa-Kohn-Rostoker [80, 81] (KKR) use the dependent basis functions. Linear muffin tin orbitals (LMTO) and linear augmented plane waves (LAPW) linearly expand the energy dependent basis functions around fixed reference energy. On the other hand, chemical community prefers to use the specially localized basis functions; the reason is the wave function of the isolated molecules decays to zero in the areas far from the molecule. The common basis

functions are Slater type orbitals (STOs), which decay exponentially far from the origin, and Gaussian type orbitals (GTOs), which have a Gaussian behavior [80, 81].

2.8.2.1. Periodic Supercells/ Solid State Basis Functions

Despite all the approximations introduced so far, there are still infinite number of electrons moving in a static potential of the infinite number of ions in solids; not only each electron has a wave function, but also each wave function extends over the entire solid, which requires a set of infinite basis set. The solution is to perform calculations on periodic systems and applying Bloch's theorem to electronic wave function. The point is that the periodicity exploited by Bloch theorem reduces the size of the problem. Bloch's theorem replaces the problem of solving Schrodinger equation for the whole solid with solving it in a supercell. Then, what remains is to approximate the potential in the areas near the nuclei.

2.8.2.2. Bloch's Theorem

"When I started to think about it, I felt that the main problem was to explain how the electrons could sneak by all the ions in a metal…

By straight Fourier analysis, I found to my delight that the wave differed from the plane wave of free electrons only by a periodic modulation." Bloch

Bloch's theorem states that when the potential in the single-particle Hamiltonian has the translational periodicity of the Bravais lattice:

$$V(\vec{r}+\vec{R}) = V(\vec{r}) \qquad 2.51$$

then the single-particle wave functions have the same symmetry, up to the phase factor:

$$\psi_{\vec{k},}(\vec{r}+\vec{R}) = \exp(i\vec{k}.\vec{r})\psi_{\vec{k}}(\vec{r}) \; . \qquad 2.52$$

A different formulation of the Bloch's theorem states that in a periodic solid, each electronic wave function can be written as the product of a cell-periodic part and a wavelike part:

$$\psi_{\vec{k},n}(\vec{r}+\vec{a}) = \exp(i\vec{k}.\vec{a})u_{\vec{k},n}(\vec{r}) \qquad 2.53$$

where:

$$u_{\vec{k}}(\vec{r}+\vec{R}) = u_{\vec{k}}(\vec{r}) \qquad 2.54$$

The cell-periodic part, $u_{\vec{k}}(\vec{r})$, has the full translational periodicity of the Bravais lattice.

The two formulation of Bloch's theorem are equivalent.

The theorem relates the value of the wave function within any periodic cell of a periodic potential to an equivalent point in any other unit cell and hence focus on a single primitive unit in dealing with the Schrodinger equation.

Although the wave function is not periodic from a unit cell to a unit cell, it has the form of plane wave modulated by a function that shows the periodicity of the crystalline lattice and associated periodic potential.

More generally, the wave function has the following form:

$$\psi_{\vec{k},n}(\vec{r}) = \frac{1}{\sqrt{NV_{cell}}}\exp(i\vec{k}.\vec{r})u_{\vec{k},n}(\vec{r}) \qquad 2.55$$

The function $u_{\vec{k},n}(\vec{r})$, with the same periodicity of the crystal, can be written as:

$$u_{\vec{k},n}(\vec{r}) = \frac{1}{\sqrt{V_{cell}}}\sum_{m} c_{n,m}(\vec{k})\exp(i\vec{G}_m.\vec{r}) \; . \qquad 2.56$$

Since the wave functions should be orthonormal over the volume, then $u_{\vec{k},n}(\vec{r})$ are orthonormal in the primitive cell.

Since the Schrodinger equation is calculated at each k point, each state is labeled by k. The wave functions at each k are independent unless they differ by a reciprocal lattice vector. For the large volumes, the k points are too close and form a band. Moreover, each k has a discrete set of eigenvalues labeled as n. The numbers n and k are the band index and crystal momentum, respectively. The index number distinguishes all the wave functions which are labeled by $\vec{k}$ -vector in the first Brillouin zone. It is a discrete integer index that classifies the different eigenvectors; the eigenvectors can also have any wavelength. The wavelength of the Bloch wave functions is another quantum number that characterizes a given system. Moreover, Bloch theorem requires that a translation can not change the density. The solid bands show how the energy of the eigenvector changes with the wavelength [89, 90].

The wave term with a translation has the form of $\exp(i\vec{k}(\vec{r}+\vec{R}))$, which disappears in the charge density ($\rho(\vec{r}) \propto \left|\psi_{\vec{k},n}(\vec{r})\right|^2$). The interesting part is the fact that charge density is proportional to $\left|u_{\vec{k},n}(\vec{r})\right|^2$.

The detail of real and reciprocal lattice is given in A.6.

2.8.2.3. k-Point Sampling

Electronic states are allowed at a set of k-points determined by boundary conditions that applied to bulk solid. The density of allowed k points is proportional to the volume of the solid. Due to the presence of the infinite number of electrons in the solid, there are infinite numbers of k points which only a finite number of electronic

states are occupied at each k point. Given that each electron occupies a state of definite k, the infinite number of electrons within the solid gives rise to an infinite number of k-points. At each k-point, only a finite number of the available energy levels will be occupied. Thus one only needs to consider a finite number of electrons at an infinite number of k-points. This may seem to be replacing infinity (number of electrons) with another one (number of k-points) to little advantage. However, one does not need to consider all of these k-points; rather, since the electron wave functions will be almost identical for values of k that are sufficiently close, one can represent the wave functions over a region of reciprocal space by considering the wave function at a single k-point. It is therefore sufficient to consider the electronic states at a finite number of k-points in order to determine the ground state density of the solid. The net effect of Bloch's theorem therefore has been to change the problem of an infinite number of electrons with the finite number of electrons in the unit cell at a finite number of k-points sampled in the Brillouin Zone.

Moreover, evaluation of many quantities, such as energy and density, requires integration over the Brillouin zone with the following form [91]:

$$\overline{g} = \frac{V_{cell}}{(2\pi)^3} \int_{BrillouinZone} g(\vec{k}) d\vec{k} \qquad 2.57$$

The integral is defined in reciprocal space and integrates over the possible values of $\vec{k}$ in Brillouin zone. For insulators, the sum is over filled bands in the full Brillouin zone. Since the function $g(\vec{k})$ is a function of wave functions and eigenvalues, it is smoothly varying (except at crossing with the other bands) and periodic function of k; thus it can be expanded in Fourier transform.

Therefore accurate integration with a discrete set of points in the Brillouin zone is needed. In the case of insulators, the filled bands can be integrated by using only a few well-chosen points which is called “special points”. While for metals, careful integration is needed near the Fermi surface for those bands that cross the Fermi energy.

In general, since all independent information can be found from the states with k in the first Brillouin zone, symmetry can be used to reduce the calculations.

Besides, several methods have been suggested to obtain very accurate approximations for the total energy obtained from a filled band by calculating the electronic states at special sets of k points in the Brillouin zone [91].

The simplest special point is the Baldereschi point [91], where the integration reduces to a single point. The idea is to take a so-called “mean-value point” such that the values which any given periodic function of wave function assumes in this point is an excellent approximation to the average value of the same function throughout the Brillouin zone; the point is found by considering crystal symmetry.

The most widely used method for sampling k-points is a method proposed by Monkhorst and Pack [92]. To use this method, all is needed is to specify how many k points are to be used in each direction in the reciprocal space.

A uniform mesh of k-points, valid for any crystal, generated by Monkhorst-Pack procedure has the following form:

$$\vec{k}_{n1,n2,n3} = \sum_{1}^{3} \frac{2n_i - N_i - 1}{2N_i} \vec{G}_i \qquad 2.58$$

where N_i is the number of k-points in each direction and n_i=1,…, N_i and G_i is the primitive vectors of the reciprocal lattice.

For supercells with the same length along each lattice vector (and therefore along each reciprocal lattice vector), it is natural to use the same number of k points in each direction. If M k points are used in each direction, it is useful to label the calculations with using $M \times M \times M$ k points [92]. The number of k points used in any calculations is reported in each calculation because different k points result in different results. Increasing the volume of supercell reduces the number of k points needed to obtain convergence because volume increases in real space correspond to volume decreases in reciprocal space.

Integral over the Brillouin zone can be replaced by integrals only over the irreducible Brillouin zone. Irreducible Brillouin zone is the first Brillouin zone reduced by all of the symmetries in the point group of the lattice [91, 92].

2.8.2.4. Plane Wave Basis and Plane-Wave Representation of Kohn-Sham Equation

While methods based on calculations in real space are appropriate for finite systems, plane waves are especially appropriate for periodic crystals; they not only provide the intuitive understanding of problem, but also simplify the calculations.

As it has been mentioned, the eigen states of independent particle Schrodinger-like equation in which the electrons are moving in an effective potential (such as Kohn-Sham equation) satisfy the eigenvalue equation:

$$(-\nabla^2 + V_{eff})\psi_i(\vec{r}) = \varepsilon_i \psi_i(\vec{r}) \tag{2.59}$$

An arbitrary wave function could be expanded in $\vec{k}$ -space as:

$$|\psi\rangle = \sum_k C_k |\vec{k}\rangle = \frac{V}{(2\pi)^3} \int C_k |\vec{k}\rangle d\vec{k} \tag{2.60}$$

In the periodic systems, V is the volume of supercell. Then the coefficients are given by:

$$C_k = \frac{1}{V}\int_V \exp(-i\vec{k}.\vec{r})\langle\vec{r}|\psi\rangle d\vec{r} \qquad 2.61$$

Now considering the above equations and in order to distinct this $\vec{k}$ from the previous one, it is labeled as $\vec{q}$:

$$\langle\vec{r}|\psi_{k,n}\rangle = \sum C_q^{k,n}\langle\vec{r}|\vec{q}\rangle \, . \qquad 2.62$$

Considering the wave function of periodic system, the expansion coefficients are given by:

$$C_q^{k,n} = \sum\langle\vec{q}|\vec{r}\rangle\langle\vec{r}|\psi_{k,n}\rangle = \frac{1}{V}\int_V \exp(i(\vec{k}-\vec{q}).\vec{r})u_{k,n}(\vec{r})d\vec{r} \qquad 2.63$$

Applying the periodicity of $u_{k,n}$ by writing the integral over V as a sum of integrals over each cell of volume V_c with its origin at the lattice vector $\vec{R}$ and considering the sum over lattice vectors, $\vec{R}$:

$$C_q^{k,n} = \frac{1}{V}\sum_R \exp(i(\vec{k}-\vec{q}).\vec{R})\int_{V_c} \exp(i(\vec{k}-\vec{q}).\vec{r})u_{k,n}(\vec{r})d\vec{r} \qquad 2.64$$

If $\vec{k}-\vec{q}$ is a reciprocal lattice vector, then each term of the sum is unity (because $\exp(i\vec{G}.\vec{R}) = 1$). When $\vec{k}-\vec{q}$ is not a reciprocal lattice vector, the sum over $\vec{R}$ vanishes. The only $\vec{q}$ for which the sum over $\vec{R}$ does not vanish are those for which $\vec{q} = \vec{k}+\vec{G}$, where $\vec{G}$ is the reciprocal lattice vector and hence:

$$\langle\vec{r}|\psi_{k,n}\rangle = \frac{1}{\sqrt{V}}\sum_G C_{\vec{k}+\vec{G}}^{n} \exp(i(\vec{k}+\vec{G}).\vec{r}) \qquad 2.65$$

In general, the expansion of a wave function in a plane wave basis could be written as:

$$\psi_i(\vec{r}) = \frac{1}{\sqrt{V}} \sum_{\vec{q}} C_{\vec{q}}^{n} \exp(i\vec{q}.\vec{r}) = \sum_{\vec{q}} C_{\vec{q}}^{n} \left| \vec{q} \right\rangle \qquad 2.66$$

Considering the orthonormality of the plane waves in the plane wave basis, one can write:

$$\left\langle \vec{q}' \middle| \vec{q} \right\rangle = \frac{1}{V} \int_V \exp(-i\vec{q}'.\vec{r}) \exp(i\vec{q}.\vec{r}) = \delta_{\vec{q}'\vec{q}} \qquad 2.67$$

By substituting the wave function into the Schrodinger-like equation and multiplying it by $\left\langle \vec{q}' \right|$ from the left:

$$\sum_{\vec{q}} \left\langle \vec{q}' \middle| \hat{H}_{eff} \middle| \vec{q} \right\rangle C_{\vec{q}}^{n} = \varepsilon_i \sum_{\vec{q}} \left\langle \vec{q}' \middle| \vec{q} \right\rangle C_{\vec{q}}^{n} = \varepsilon_i C_{\vec{q}'}^{n} \qquad 2.68$$

Then the matrix element of the kinetic energy operator is:

$$\sum_{\vec{q}} \left\langle \vec{q}' \middle| -\frac{1}{2} \nabla^2 \middle| \vec{q} \right\rangle = \frac{1}{2} \left| q^2 \right| \delta_{\vec{q},\vec{q}'} \qquad 2.69$$

Since the effective potential is periodic, it can be expressed in Fourier components:

$$V_{eff}(\vec{r}) = \sum_m V_{eff}(\vec{G}_m) \exp(i\vec{G}_m.\vec{r}) \qquad 2.70$$

By re-writing the effective potential equation for reciprocal lattice vector and integrating over the volume of primitive cell:

$$V_{eff}(\vec{G}) = \frac{1}{V_{cell}} \int_{V_{cell}} V_{eff}(\vec{r}) \exp(-i\vec{G}.\vec{r}) d\vec{r} \qquad 2.71$$

Therefore, the matrix elements of the potential are:

$$\left\langle \vec{q}' \middle| V_{eff} \middle| \vec{q} \right\rangle = \sum_m V_{eff}(\vec{G}_m) \delta_{\vec{q}'-\vec{q},\vec{G}_m} \qquad 2.72$$

which implies that the matrix elements are not zero if $\vec{q}$ and $\vec{q}'$ differ by reciprocal lattice vector. By defining $\vec{q}$ and $\vec{q}'$ as:

$$\vec{q} = \vec{k} + \vec{G}_m , \tag{2.73}$$

$$\vec{q}' = \vec{k} + \vec{G}_{m'} \tag{2.74}$$

in which the difference between $\vec{G}_m$ and $\vec{G}_{m'}$ is another reciprocal vector such as $\vec{G}_{m''}$.

Then the Schrodinger equation for any $\vec{k}$ can be written as a matrix equation:

$$\sum_{m'} H_{m,m'}(\vec{k}) C_{i,m'}(\vec{k}) = \varepsilon_i(\vec{k}) C_{i,m'}(\vec{k}) \tag{2.75}$$

where:

$$H_{m,m'}(\vec{k}) = \left\langle \vec{k} + \vec{G}_m \middle| \hat{H}_{eff} \middle| \vec{k} + \vec{G}_{m'} \right\rangle = \frac{\hbar^2}{2m_e} \left| \vec{k} + \vec{G}_m \right|^2 \delta_{m,m'} + V_{eff}(\vec{G}_m - \vec{G}_{m'}) . \tag{2.76}$$

In this form, the kinetic energy is diagonal and the various potentials are described in term of their Fourier transforms. Solutions are obtained by digitalization of the Hamiltonian matrix. The size of the matrix is determined by the choice of cut-off energy [81, 89, 90].

2.8.2.5. Cut-off the Basis Set

Bloch theorem states that the electron wave function at each k point can be expanded in terms of plane waves. In principle, the basis should be infinite; however Bloch's theorem allows the electronic wave functions to get expanded in terms of discrete plane waves; therefore, truncating the plane wave would limit the number of plane waves. The coefficients of the plane waves with the small kinetic energies than

(smaller than $E=\frac{\hbar^2}{2m}\left|\vec{k}+\vec{G}\right|^2$) are more important. In other word, only those plane waves whose kinetic energies are less than the cut-off energy are considered.

In fact, the problem is choosing the radius of a sphere that includes plane waves with wavelengths compatible with the periodic lattice up to a certain resolution. By making this cutoff sphere larger and larger, the resolution becomes systematically fine.

Considering the wave function of the periodic system expanded in the plane waves, evaluating the solution at even single point in k-space involve a summation over an infinite number of possible values of $\vec{G}$. Since the wave functions are the solutions of the Schrodinger equation, with the following kinetic is:

$$E=\frac{\hbar^2}{2m}\left|\vec{k}+\vec{G}\right|^2 \tag{2.77}$$

it is reasonable to expect that the solutions with lower energies are more physically important than solutions with very high energies [79, 81, 91]. Then the infinite sum reduces to:

$$\left\langle \vec{r} \middle| \psi_{k,n} \right\rangle = \frac{1}{\sqrt{V}} \sum_{\left|\vec{G}+\vec{k}\right|<G_{cut}} C^n_{\vec{k}+\vec{G}} \exp(i(\vec{k}+\vec{G}).\vec{r}) \,. \tag{2.78}$$

2.8.3. The Supercell Approximation

The application of periodic boundary conditions imposes periodicity on the system. Many applications of electronic structure calculations are on systems which do not have full thee dimensional translational symmetry. Therefore, the Bloch's theorem can not used for a system that contains defect, impurities or even the interaction of molecules and surfaces. Supercell approximation allows performing the plane wave

basis on such systems. In supercell approximation, the non-periodic systems are approximated by enclosing the region of interest in either bulk material or vacuum.

Figure 2.1.a shows a supercell which contains a defect surrounded by the bulk material. By applying periodic boundary conditions to the supercell, it is repeated in the space; thus the calculated energy is the energy per unit cell of a crystal containing a chain of defects rather than the energy of the crystal with a single defect. The environment should have enough bulk material to avoid the defect-defect interaction.

Figure 2.1.b shows how to make a supercell for surface calculation. Since a surface lacks the periodicity in one direction, the supercell is chosen such that a vacuum region separates the slab. Therefore, the calculated energy is the energy of an array of crystal slabs. Figure 2.1.c shows how to make a supercell for a molecule. The supercell should be large enough to prevent the molecules interaction [79].

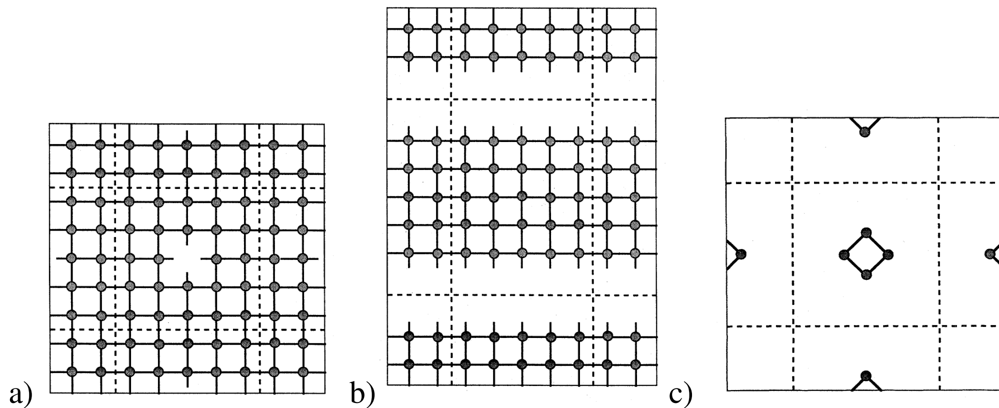

Figure 2.1: Supercell approximation for a single defect, a surface area and a molecule [79].

2.8.4. Pseudopotential

The pseudopotential plane wave is one of the most common methods used for calculating the external potential of Kohn-Sham equation. The applicability and

simplicity of the plane waves and the concept of core-valence electrons division leads to the idea of pseudopotential. The idea is to remove the core electrons from the calculation because of the negligibility of their contribution to the chemical bonding. Moreover, the pseudopotentials replacing the valence electron wave functions is considered in such a way that they match their true wave functions outside the core region but nodeless inside. The advantage of using pseudopotential is approximate the properties of core electrons in a way that could reduce the number of plane waves in a calculation. In fact, one of the advantageous of using pseudopotentials is reducing the computational complexities.

In 1940, Herring proposed the band calculation technique called the orthogonalized plane wave method (OPW) which allows the separation of the core and valence electrons. In this method, the valence wave functions are a linear combination of plane waves and core wave functions. By choosing appropriate coefficient of expansion, the valence wave functions would be orthogonal to the core states. Therefore, the problem is simplified by dividing the whole wave function into the core orbitals and the smooth part represented by plane waves. The orthogonalized plane wave consists of valence plane waves orthogonalized to the atomic core functions, such that the electron behaves like a core electron while inside the core and like a plane wave outside the core region. The orthogonalized plane wave basis can be written as:

$$\chi_{\vec{k}}(\vec{r}) = \frac{1}{\sqrt{NV_{primitive-cell}}} \exp(i\vec{k}.\vec{r}) - \sum_j \mu_{k,j}\phi_{k,j}(\vec{r}) \qquad 2.79$$

where $\phi_{k,j}$ are the core wave functions (Bloch wave function) for constant j. N is the number of atoms and the term $\mu_{k,j}$ is chosen to make:

$$\int \phi^*_{k,j}(\vec{r})\chi_k(\vec{r})d^3\vec{r} = 0 . \qquad 2.80$$

The subscript j indicates the orbitals of the core electrons, such as 1s, 2s, 2p, wave functions. As it was mentioned before the coefficient $\mu_{k,j}$ is determined such that the plane orthogonalized plane wave functions would be orthogonal to the ones of core electrons.

By re-writing the total wave function in the terms of smooth and core wave functions, the true wave function is the sum of a smooth wave function, ϕ, and a sum over occupied core states:

$$|\psi\rangle = |\phi\rangle + \sum_j^{core} b_j |\chi_j\rangle \qquad 2.81$$

The orthogonality dictates that:

$$\langle \chi_j | \psi \rangle = 0 \qquad 2.82$$

$$b_j = -\langle \phi_j | \phi \rangle \qquad 2.83$$

Then the total wave function is:

$$|\psi\rangle = |\phi\rangle - \sum_j \langle \chi_j | \phi \rangle \chi_j \qquad 2.84$$

By substituting the above wave function in the Schrodinger equation with the core potential (which has this Hamiltonian: $\hat{H} = p^2 / 2m + V_c$):

$$\hat{H}(|\phi\rangle - \sum_j \langle \chi_j | \phi \rangle | \chi_j \rangle) = E|\psi\rangle = E|\phi\rangle - E\sum_j^{core} |\chi_j\rangle\langle \chi_j | \phi\rangle \qquad 2.85$$

Therefore, by rewriting the equation:

$$\hat{H}|\phi\rangle - \sum_{j}(E - E_j)\langle\chi_j|\phi\rangle|\chi_j\rangle = E|\phi\rangle \quad 2.86$$

Then, by organizing the terms and write them as the Schrodinger equation, one can find the expression for the long-range, repulsive potential:

$$V_R = \sum_{j}^{core}(E - E_j)|\chi_j\rangle\langle\chi_j| \quad 2.87$$

The V_R is non-Hermitian repulsive potential; its effect is localized in the core and cancels parts of the strong Coulomb potential. The true potential is the sum of the core and long-range, repulsive potentials, which makes it very softer than the original one:

$$V = V_R + V_c \,. \quad 2.88$$

In the case of interaction, the energies of the eigen states would change, but if the core states are reasonably far from the valence sates, then $\delta E << E - E_j$ and hence it would be reasonable to use the valence Eigen states [79, 81, 93].

Figure 2.2 shows the all-electron potential and wave function versus the pseudopotential ones. As figure 2.2 shows the real and the pseudo wave function and potentials match with each other above a certain cutoff radius r_c.

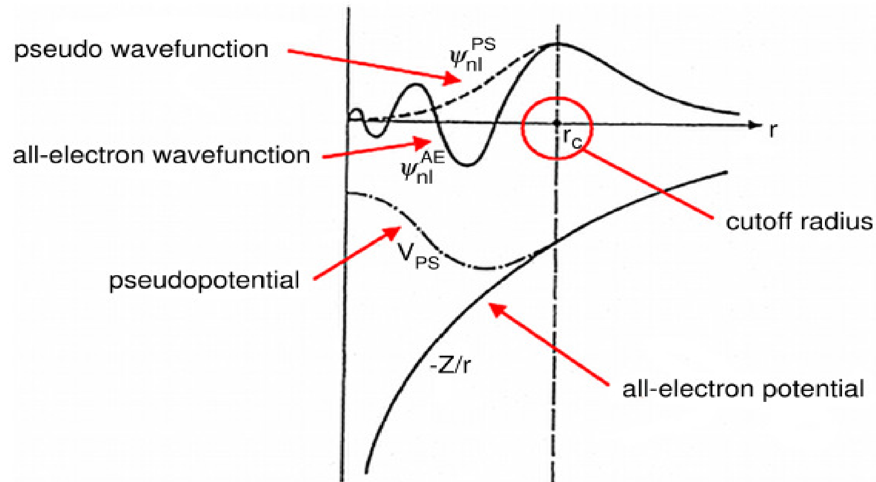

Figure 2.2: Comparison of a wave function in the potential of the nucleus to the one in the pseudopotential. The real and pseudo wave function and potentials match above a certain radius r_c [79].

Due to the strong ionic potential, the valence wave functions oscillate very fast inside the core region. The reason is the orthogonality of a state to all states with lower energies; besides, the higher the state in the atom, the more the electron wave function oscillates. According to the Pauli Exclusion Principle, and since there are already core electrons in the vicinity of the nucleus, the probability of finding a valence electron near the nucleus is small. Pseudopotential approximates the real potential with a new weaker one which is supposed to give the correct behavior of the electron wave function in the bonding region, and nearly zero probability for the valence electron to be close to the nucleus.

Removing core electrons from the calculation would reduce the Kohn-Sham orbitals, the memory required to store the orbitals, the time required to evaluate orbital-dependant quantities, and the time required to orthonormalize a set of orbitals. Moreover, since there are no core-electrons, there would be no valence electrons normalized to them. This, in return, lowers the cut-off energy, resulting in lower

memory requirements and greater speed. There are generally three significant motivations behind the pseudopotential philosophy; first of all, it reduces the basic set size in the calculation, secondly it decreases the number of electrons and lastly it allows the possibility of including the relativistic effects in the whole estimation [79, 93]. The details of pseudopotential approximation and classification are given in A7.

2.8.5. The Calculation of Coulomb Term in General

Hartree energy is another term of Kohn-Sham equation which needs to be calculated. There are various strategies to compute the classical electrostatic contribution to the electron-electron repulsion:

$$J[\rho] = E_{Hartree} = \frac{1}{2}\sum_{i}^{N}\sum_{j}^{N}\iint \frac{\rho(\vec{r}_1)\rho(\vec{r}_2)}{\vec{r}_{12}} d\vec{r}_1 d\vec{r} \qquad 2.89$$

Becke and Dickson suggested using the Poisson's equation to find the Hartree operator. For a given charge density, the equation has the following form:

$$\nabla^2 V_H(\vec{r}) = -4\pi\rho(\vec{r}) . \qquad 2.90$$

Then the problem is to solve the above equation in the self-consistent reference from the orbitals obtained of the diagonalized Hamiltonian.

Considering the plane wave basis, the Hartree potential has the periodicity of the lattice and can be written as a linear combination of plane waves:

$$V_H(\vec{r}) = \sum_{\vec{G}} V_H(\vec{G}) \exp(i\vec{G}.\vec{r}) . \qquad 2.91$$

Moreover, it is also possible to write the charge density as a linear combination of plane waves:

$$\rho(\vec{r}) = \sum_{\vec{G}} \rho(\vec{G}) \exp(i\vec{G}.\vec{r}) \qquad 2.92$$

Substituting these expressions in the differential equation results in:

$$\sum_{\vec{G}} G^2 V_H(\vec{G}) \exp(i\vec{G}.\vec{r}) = \sum_{\vec{G}} 4\pi\rho(\vec{G}) \exp(i\vec{G}.\vec{r}) \qquad 2.93$$

By multiplying both sides by $\exp(i\vec{G}.'\vec{r})$ and integrating over r and considering the orthonormality of the basis (which dictates that each coefficient corresponding to the same G vector on the left and right hand sides should be separately equal):

$$G^2 V_H(\vec{G}) = 4\pi\rho(\vec{G}) \qquad 2.94$$

Therefore, the Fourier transform of the charge density in real space would give the $\rho(\vec{G})$, which would result in the coefficient of $V_H(\vec{G})$.

As the size of a system in real space become large, the Brillouin zone (and therefore G^2) become smaller, that makes $V_H(\vec{G})$ instable [81, 82].

2.9. Application of Density Functional Theory to Semiconductors

Semiconductors are the key materials of electronic industry. The electronic and structure of the semiconductor devices have been subject of density functional theory applications. Bulk properties, such as band gap and lattice constants of most of the semiconductor materials are accurately known from the related experiments, which provide a basis for density functional theory approximations. In the case of defect and interface properties, density functional theory provides a predictive tool, whose results should be compared and confirmed by experiments.

2.9.1. Bulk Semiconductors

Density functional theory provides a framework for ground state total energy calculation of a system bound by electrons. In the case of crystals, the energy is

calculated as a function of volume, E(V). The minimum of that function gives the equilibrium volume and hence the lattice constant; subtracting the energy of separate atoms gives the bonding energy and the second derivative of energy at the minimum volume gives the bulk modulus.

In order to find the band structure, the dispersion relation between the wave vector and the energy eigenvalues is considered. In general, the energy eigenvalues make a complicated function of k.

2.9.1.1. Band Gap Calculation with Density Functional Theory

The eigenstates of Kohn-Sham equation are the eigenvalues of a fictitious single-particle equation. However, their eigenfunctions give the true electron density.

The band structure of semiconductors can be defined as the energies of one-particle excitations, which is related to the difference between total energies of states differing by one electron. In particular, the lowest conduction-band energy is given by:

$$E_c = E_{N+1} - E_N \qquad 2.95$$

where E_N is the negative of the first ionization energy of the N-particle system and E_{N+1} is the negative of the electron affinity of the same N-particle system.

Similarly, the highest valence-band energy is given by:

$$E_v = E_N - E_{N-1} \qquad 2.96$$

Therefore, the band gap is given by:

$$E_g = E_c - E_v \qquad 2.97$$

The zero-temperature-limit chemical potential at the mid-gap is given by:

$$\mu = \frac{E_c + E_v}{2}. \qquad 2.98$$

Chemical community uses the chemical expressions to define band gap which leads to the same results. According to this definition, the band gap of an N electron system is defined as the difference between the electron affinities:

$$A = E_N - E_{N+1} = -\varepsilon_{LUMO} \qquad 2.99$$

and the ionization potential:

$$I = E_{N-1} - E_N = -\varepsilon_{HOMO} \qquad 2.100$$

$$E_g = I - A = \varepsilon_{LUMO} - \varepsilon_{HOMO} \qquad 2.101$$

LUMO and HOMO stand for lowest unoccupied and highest occupied molecular orbitals.

The true band gap is defined as the ground state energy difference between the N and $N \pm 1$ systems:

$$E_g = E(N+1) + E(N-1) - 2E(N)\,. \qquad 2.102$$

In Kohn-Sham formalism the highest occupied eigenenergy for N-electron system $E_N(N)$ is the Fermi energy; the conduction and valence energies are given as:

$$\varepsilon_c = \varepsilon_{N+1}(N+1) \qquad 2.103$$

$$\varepsilon_v = \varepsilon_N(N)\,. \qquad 2.104$$

However, from the definition of the valence band edge:

$$\varepsilon_v = E[\rho_N(N)] - E[\rho_{N-1}(N-1)]\,. \qquad 2.105$$

The attempt is focused on finding terms on the right-hand side to neglect the difference between $E[\rho_{N-1}(N-1)]$ and $E[\rho_{N-1}(N)]$. Therefore, the valence-band energy becomes:

$$\varepsilon_v = E[\rho_N(N)] - E[\rho_{N-1}(N)]\,. \qquad 2.106$$

This means that while the true naïve Kohn-Sham band gap has the following form:

$$E_g^{K-S} = \varepsilon_{N+1}[\rho(N+1)] - \varepsilon_N[\rho(N)], \qquad 2.107$$

the band gap of only N-particle energy is:

$$\varepsilon_g^{K-S} = \varepsilon_{N+1}[\rho(N)] - \varepsilon_N[\rho(N)], \qquad 2.108$$

only with replacing $\varepsilon_{N+1}[\rho(N)]$ by $\varepsilon_{N+1}[\rho(N+1)]$. The deviation is written as:

$$E_g = \varepsilon_g + \Delta_{xc}. \qquad 2.109$$

The subscript xc implies that the difference is due to the exchange-correlation effects. The deviation is given by:

$$\Delta_{xc} = \varepsilon_{N+1}(N+1) - \varepsilon_{N+1}(N). \qquad 2.110$$

In summary, when an electron is added to a semiconductor, the exchange-correlation potential jumps by a constant. This discontinuity gives the difference between the true band gap and the one obtained from the ground state, one-particle equation. This partial contribution to the gap arises from the difference between the conduction-band valleys obtained from the ground state self-consistent equations for N and (N+1)-particle systems, which comes from the difference in the exchange and correlation effects [83, 93].

The band gap underestimation can be removed by adding quasi-particle correction proposed by Bechstedt and Del Sole [95]. Their model for correction is based on the difference in self-energies obtained from LDA and GW approximation and the correction is given by:

$$\Delta_{QP} = e^2 q_{TF} / \varepsilon_\infty / (1 + 7.62 q_{TF} r_0) \qquad 2.111$$

where ε_∞ is the high-frequency dielectric constant and q_{TF} is the Thomas-Fermi wave number. The radius r_0 is the average decay constant of the valence electron wave function of the anions and cations. The correction value is 1.13 eV and it is almost equal for all SiC polytypes.

Moreover, as long as self-interaction is concerned, hybrid functionals (which are based on the combination of density functional and Hartree-Fock theories) obtain more reasonable estimation for band gap [77, 94].

2.9.1.2. Density of States in Bulk Semiconductors

Density of states is one of the main concept in finding the carrier concentrations and energy distributions of carriers in semiconductors.

The density of states (DOS) of a system describes the number of states that could be occupied at each energy level. Integrating the density of states between two energies gives the number of allowed states available for electrons (in energy per the volume of crystal). A high DOS at a specific energy level means that there are many states available for occupation. The density of states can be calculated from band theory calculations. It is calculated either as a function of energy or the wave vector k.

If all atomic sites in a crystal are considered to be equivalent, the crystal is called perfect and the density of states is called “total”. Local density of states, on the other hand, could be applied to one atom and is valid even in an amorphous material. The local density of states varies with the local atomic environment.

To find the density of states, it is reasonable to start by considering an eigenstate $|\psi_k\rangle$ (with energy E_k) which is expressed in an orthonormal basis set of atomic states $|a\rangle$, with expansion coefficients $\langle a|\psi_k\rangle$:

$$|\psi_k\rangle = \sum_a \langle a|\psi_k\rangle |a\rangle. \qquad 2.112$$

All atoms for which the expansion coefficient $\langle a|\psi_k\rangle$ is not zero contribute to this eigenstate. For this eigenstate the probability of finding an electron at the particular basis state $|n\rangle$ is $|\langle n|\psi_k\rangle|^2$. The coefficient, $|\langle n|\psi_k\rangle|^2$, is the factor to weight the contribution of total density of states at site n.

The total density of states D(E) is a counter which shows the total number of eigenstates with energies less than E. The contribution of the eigenstate $|\psi_k\rangle$ to the total number of the states up to energy is E is zero, unless $E \geq E_k$. When $E \geq E_k$, the contribution of the eigenstate $|\psi_k\rangle$ is one. The contribution of the eigenstate at $E=E_k$ to the total density of states is $\delta(E-E_k)$ and therefore D(E) can be expressed as:

$$D(E) = \sum_{allE_k} \delta(E-E_k). \qquad 2.113$$

In the limit of an infinite system, where the number of Eigen states becomes infinite and the energy interval between successive delta function contributions to D(E) becomes very small, the D(E) becomes a smooth, continuous function.

The local density of states $d_n(E)$ associated with the basis state $|n\rangle$ at energy E is calculated by considering the weight factor for each energy contribution:

$$d_n(E) = \sum_{allE_k} |\langle n|\psi_k\rangle|^2 \delta(E-E_k). \qquad 2.114$$

If normal to the interface is considered in z direction, then the band gap evolution across the interface models can be studied through the planar-averaged local density of states:

$$d(z;E) = 2\sum_{n} \left|\langle z|\psi_n\rangle\right|^2 \delta(E - E_n) \qquad 2.115$$

where z indicates a coordinate along the interface normal, $\left|\langle z|\psi_k\rangle\right|^2$ corresponds to the electron density integrated in x-y planes, the factor of two accounts for the spin degeneracy, and ψ_n is the Kohn–Sham Eigen states of energy E_n. In the calculations, the Dirac delta functions can be replaced by Gaussian functions with known standard deviation.

In general, the total density of states is recovered by summing all local densities of states:

$$D(E) = \sum_{al\ln} d_n(E) = \sum_{allE_k} \delta(E - E_k)\,, \qquad 2.116$$

where the normalization condition of the eigenstate is [96]:

$$\sum_{allE_k} \left|\langle n|\psi_k\rangle\right|^2 = 1\,. \qquad 2.117$$

2.10. Geometric Optimization

To find the electronic structure, it is supposed that the ions are fixed, classical entities. In fact, not only the position of atoms but also the dimension of unit cell is fixed. Then the Kohn-Sham equation calculates the ground state of electrons in the fixed unit cell.

By changing the position of ions in the unit cell, new degrees of freedom are introduced to the system. Hellman-Feynman theory provides a framework for

calculating the forces on the ions. Moreover, the stress on ions can also be calculated by the stress theorem. Changing the position of ions, finding the force and stress on them and minimizing them are a way to relax a system of nuclei and electrons.

Accepting this framework, there are two paradigms governing the movements of the electrons and ions. While electrons obey the Schrodinger equation in a quantum world, the ions obey the Newton equation and therefore the classical world.

Relaxing the system means force and stress minimization on the ions. Therefore, there are two paradigms governing the electrons and ions; on one hand, the electrons are obeying the Schrodinger equation, and therefore move according to the quantum paradigm; on the other hand, ions are considered to obey the classical mechanics.

2.10.1. Hellmann-Feynman Theorem

Hellmann-Feynman theorem demonstrates a relation between perturbations in an operator on a complex inner product space and the corresponding perturbations in the operator's eigenvalue.

The theorem states that for any perturbation, one can write:

$$\frac{\partial\langle E\rangle}{\partial\lambda}=\left\langle\frac{\partial\Psi}{\partial\lambda}\right|H_\lambda\left|\Psi\right\rangle+\left\langle\Psi\right|\frac{\partial H_\lambda}{\partial\lambda}\left|\Psi\right\rangle+\left\langle\Psi\right|H_\lambda\left|\frac{\partial\Psi}{\partial\lambda}\right\rangle \tag{2.118}$$

Considering that the wavefunctions are the eigenfunctions of the Hamiltonian, it can be written as:

$$\frac{\partial\langle E\rangle}{\partial\lambda}=E\left\langle\frac{\partial\Psi}{\partial\lambda}\right|\left.\Psi\right\rangle+E\left\langle\Psi\right|\left.\frac{\partial\Psi}{\partial\lambda}\right\rangle+\left\langle\Psi\right|\frac{\partial H_\lambda}{\partial\lambda}\left|\Psi\right\rangle \tag{2.119}$$

By assuming the orthonormality of solutions $\langle\Psi(\lambda)|\Psi(\lambda)\rangle=1$, the first two terms become zero, $\frac{\partial}{\partial\lambda}\langle\Psi|\Psi\rangle=0$, and hence:

$$\frac{\partial\langle E\rangle}{\partial\lambda}=\langle\Psi|\frac{\partial H_{\lambda}}{\partial\lambda}|\Psi\rangle \,. \qquad 2.120$$

Since the electronic ground state energy calculated by Kohn-Sham equation is a function of ionic coordinates, R_I, implicitly, one can find the force on ions by the following equation:

$$\vec{F}_I=-\frac{\partial E}{\partial\vec{R}_I}\,. \qquad 2.121$$

By varying the position of ions, the Kohn-Sham wavefunction would change, which make the force on the ions. The ions feel the force caused by special electronic configuration. Therefore, the forces on ions can be calculated according to Hellmann-Feynman theorem [81].

2.11. Algorithm for Solving Kohn-Sham Equation, and Geometric Relaxation

In summary, the algorithm for solving Kohn-Sham equation and geometric relaxation, used in most DFT software, is given in figure 2.3. In order to calculate the semiconductor bandgap more accurately, the same Kohn-Sham equation should be solved with hybrid functional.

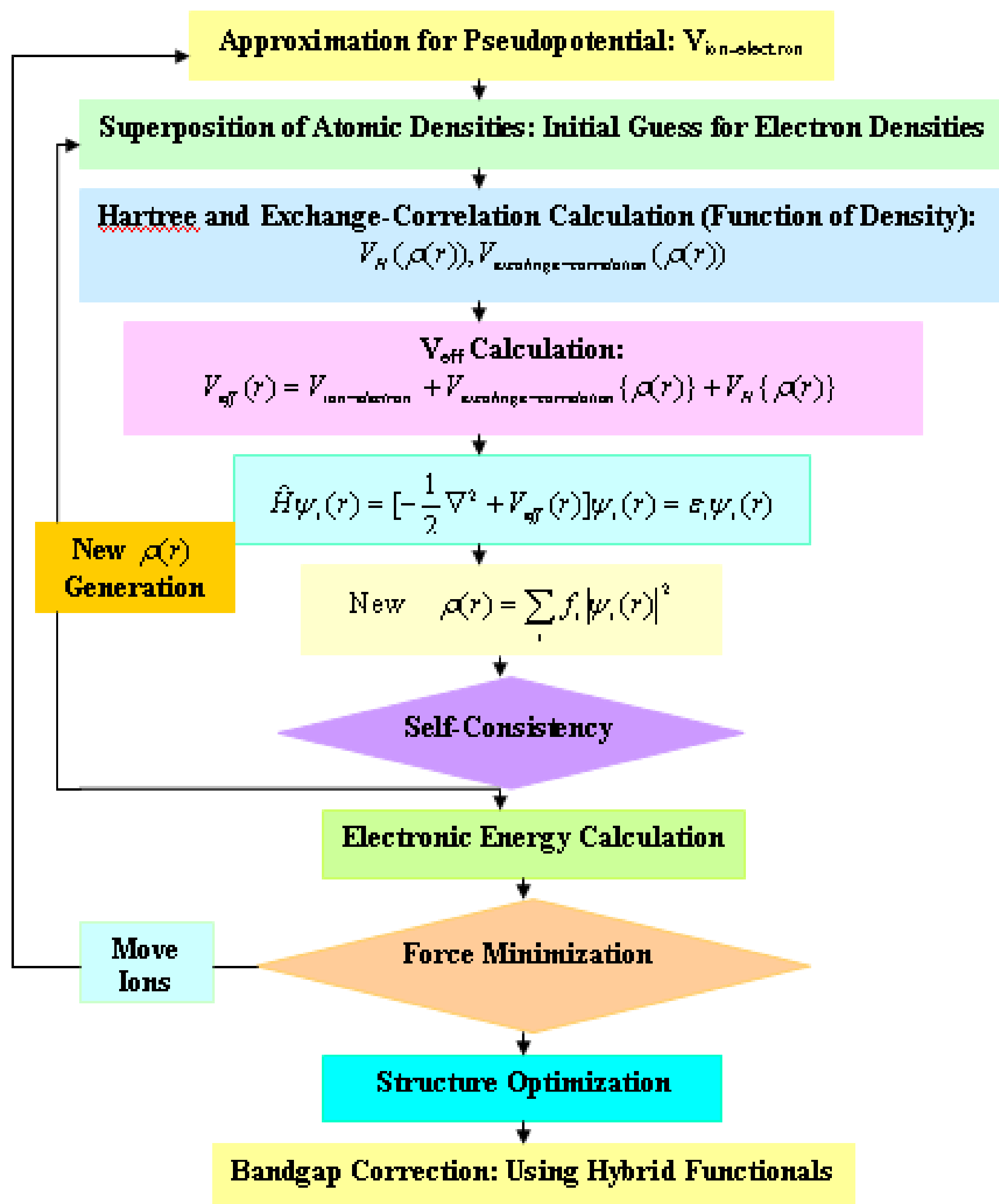

Figure 2.3: Algorithm for Solving Kohn-Sham equation, geometric relaxation, and bandgap correction.

2.12. Summary

This chapter gave the essential key definitions, and theoretical framework of DFT-based calculation, and simulation. The algorithm of solving the Kohn-Sham equation, as employed by most of the DFT simulation code is given as well.

Chapter 3: From Bulk to (0001)4H-SiC/SiO_2 Interfacial Mode

3.1. Introduction

The first step of our DFT theoretical studies of the semiconductor/oxide system is the interfacial model creation. The most critical key element in model generation is the bond adjustment between semiconductor, and the oxide.

In the case of SiC, although several studies have been focused on the defect generation in the bulk crystal [22, 32, 41], there are only a few attempts in modeling the direct interface [22, 97, 98]. The problem is the complexity of SiC/SiO_2 interface model generation.

On one hand, the interface model should provide a backbone for further defect/ passivation studies; therefore it should be free of any chemical defects itself. Hence the connection of SiC substrate to the oxide layer should be free of any unsatisfied bonds, coming from either side of the interface. Although this kind of SiC/ SiO_2 connection may not be realistic but it provides a solid theoretical framework to study the states of the potential defects on both sides of the interface. On the other hand, the oxide lying on the top of the SiC substrate should have the physical properties of a reasonable form of SiO_2. This oxide layer should not distort the SiC crystalline properties either.

Although each SiC/SiO_2 interfacial supercell may have its own unique properties such as band evolution, oxide density and interfacial orientation, the realistic bond arrangement and connection provide a free of defect background which leads to a general knowledge of the interface defect issues.

In this chapter, we start from calibrating our simulation with the known parameters of crystalline SiC polytypes, and SiO_2. Obtaining the optimum key parameters, such as bandgap or effective mass for crystalline SiC polytypes would be a good staring point for modeling the final supercell. Moreover, a comparison between bulk semiconductor and its oxide would shed light to the interfacial bandgap evolution together with a reasonable bond arrangement.

An abrupt interfacial supercell of (0001)4H-SiC/SiO_2 is then modeled as the original framework for further defect, transition layer, and passivation studies. All other calculations would be compared with the properties of this original abrupt structure.

Regarding the crystalline and supercell bandgap, a hybrid functional framework [77] is taken to complete and modify the information provided by PBE [76] simulation. The knowledge coming from both simulations would complete each other and provide a better understanding of the system of study. The hybrid functional provides the essential information to deal with the DFT problem of bandgap underestimation.

Lastly, the evolution of the bandgap from SiC to SiO_2 has been studied with the help of the projected density of states together with the band edge alignment.

3.2. SiC Bulk Simulation

Silicon carbide (SiC) is a promising semiconductor material with desirable properties for many applications. SiC-based electronic devices and circuits are being developed for use in high-temperature, high-power, and high-radiation conditions under which conventional semiconductors cannot function. Due to its high maximum electron velocity, the SiC-based devices can operate at high frequencies; its high

thermal conductivity allows the devices to easily dissipate excess heat. Its high breakdown electric field makes the devices operable at high voltage levels.

The harsh environment in which SiC-based electronic devices are meant to operate, make knowledge of system energy important.

The fundamental physical and electronic properties of any semiconductor materials can be obtained via the band structure. The band structure study is essential in understanding the behavior of semiconductor materials especially near the conduction band minimum, and valence band maximum. Such information is crucial to the understanding of physical properties of the material.

SiC is the only semiconductor material that exhibits a wide range of polytypes. Among all SiC polytypes, 6H and 4H polytypes are attracting more attention because of their favorable electronic properties.

In this section, we perform DFT ab-initio simulations to find the electronic structure of both 6H and 4H-SiC together with the effective mass of 4H-SiC. This ab-initio approach is based on density functional theory, in the general gradient approximation (GGA(PBE)) [76], and hybrid functionals [77].

So far, several theoretical calculations on the band structures of SiC polytypes have been performed [99-104]. The aim of this chapter is to calibrate the system of study with the theoretical and experimental [105] publications for further 4H-SiC/SiO_2 interface modeling. Moreover, the band structure of the α-quartz has also been calculated in both GGA, and hybrid functional DFT frameworks.

Silicon carbide has several polytypes, which differ in stacking arrangement. The arrangements for two most common polytypes 4H–SiC and 6H–SiC are shown in figure 3.1 [99, 101].

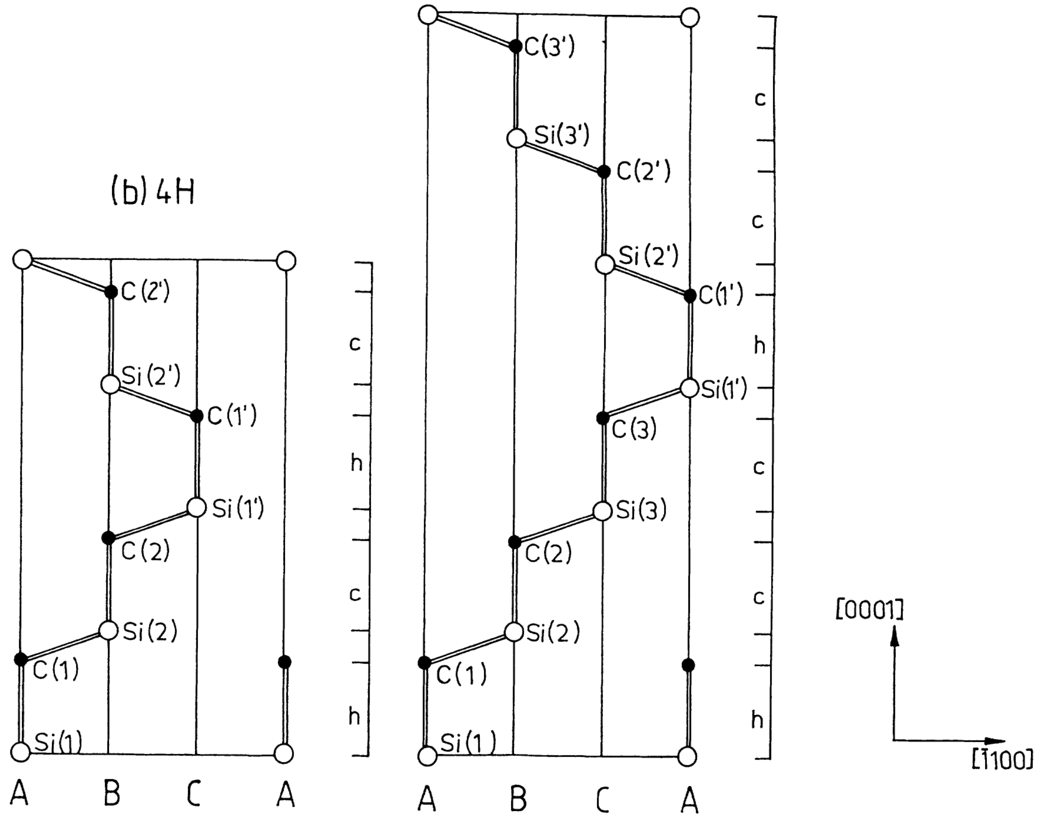

Figure 3.1: Two-dimensional views of primitive hexagonal cells for 4H-SiC and 6H-SiC [99, 101].

To define the 4H-SiC, and 6H-SiC crystal structures, the atomic positions of the silicon, and carbon atoms are specified in the hexagonal structure, with the initial known lattice parameters, a, and c. The lattice constants were obtained by minimizing the total energy with respect to changes in the size of the unit cell, using PBE [76] exchange-correlation potential. For the hexagonal structure, the minimization was carried out by varying the parameters a, and c with the same volume. The best cell

dimension is obtained by the total energy minimization with respect to cell dimension. Figure 3.2 shows that the best cell dimension a is 5.8 Bohr, which is in good agreement with the theoretical publications [99].

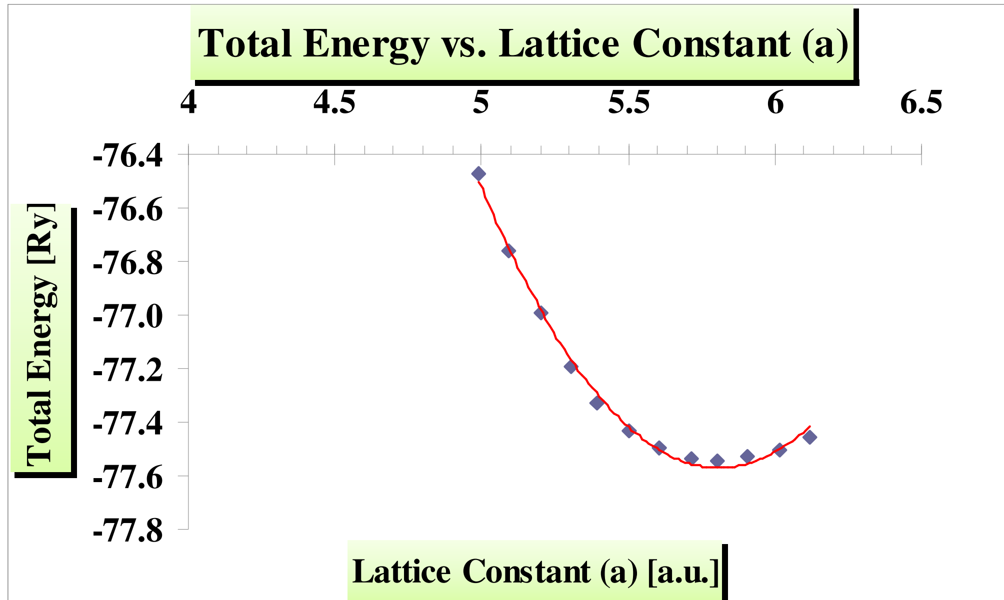

Figure 3.2: Theoretical determination of the 4H-SiC equilibrium lattice constant in PBE calculations through the minimization of total energy vs. lattice constant a.

By using the appropriate cell dimension, a=5.80 Bohr (3.032 Angstrom) and c=18.997 Bohr (10.053 Angstrom), the 4H-SiC unit cell is constructed. The cell dimensions used for 6H-SiC is considered as a= 5.73 Bohr and c=26.8 Bohr. Figure 3.3 shows the configuration of 4H-, and 6H-SiC unit cells (using software called XCrysDen [106]).

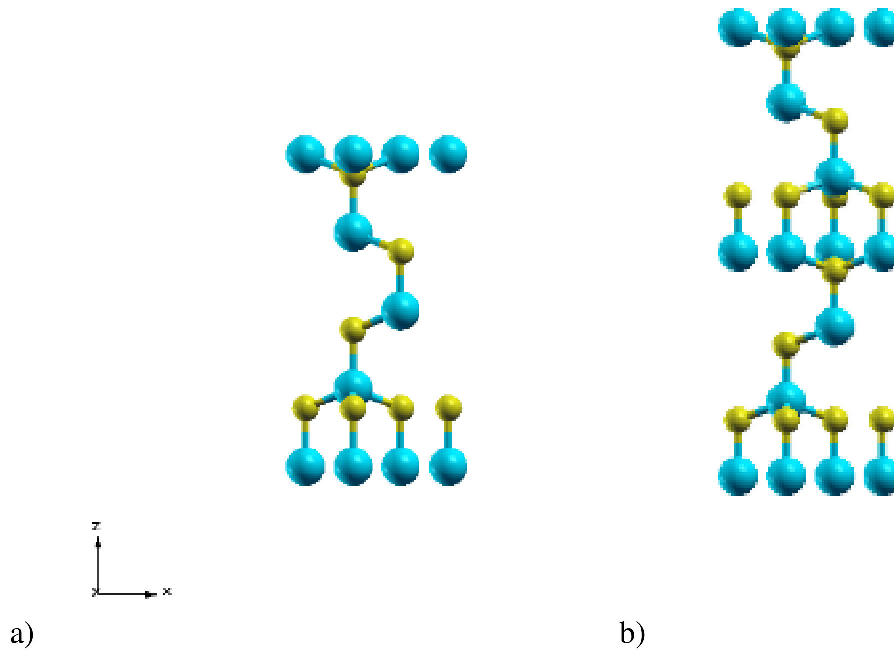

Figure 3.3: The unit cell of: a) 4H-SiC, b) 6H-SiC (xcrysden); the blue large, and the yellow small spheres are silicon, and oxygen atoms, respectively.

The best cutoff energy for DFT bulk calculations is found by plotting the total energy with respect to cutoff energy. The flat part of the diagram shows system convergence with respect to cutoff energy. The cutoff energy chosen here is 130 Ry for bulk calculations. Figure 3.4 shows the convergence with respect to cutoff energy for 4H-SiC.

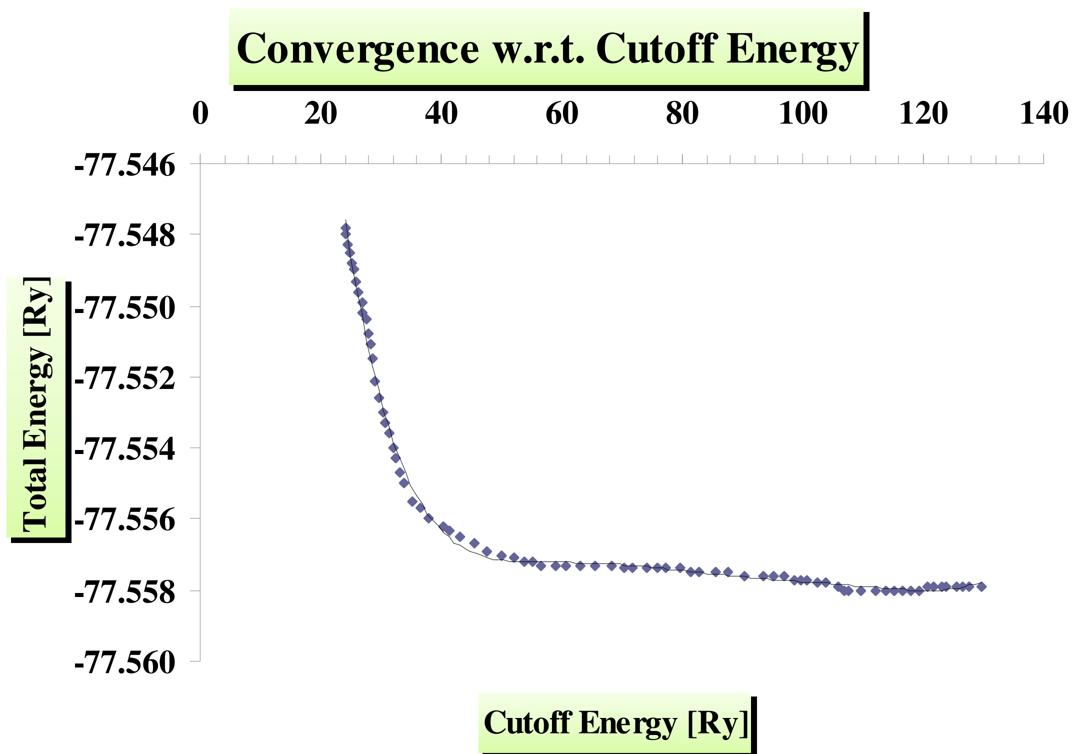

Figure 3.4: Convergence with respect to total cutoff energy for 4H-SiC.

Having established the geometric structure for the 4H-, and 6H-SiC polytypes, the electronic band structures were calculated along the high symmetry points. To obtain the bandstructure, and density of states (DOS), the Perdew-Burke-Ernzerhof (GGA (PBE)based) exchange-correlation energy, and the norm-conserving pseudo potential are used for both silicon (atomic configuration [Ne] $3s^2$, $3p^2$), and carbon (Atomic atomic configuration: [He] $2s^2$ $2p^2$). The 1*s* wave function of the carbon atom and 1s, 2s, and 2p of the silicon atom were considered to be core states and all higher lying states were treated as valence states.The DFT solver Quantum Espresso [75] is used to perform relaxation, band-structure and DOS calculations. Plane waves with a cutoff-energy of 130 Ry are used to expand the basis functions. The resulting DFT-GGA bandstructure for 4H-SiC, and 6H-SiC are calculated versus high-symmetry

lines A-L-M-Γ-A-H-H-K-Γ. for 156 number of k points (along A-L-M-Γ-A-H-H-K-Γ).

The bandgaps are retrieved in two steps; first the band structure is calculated by DFT-GGA (PBE) [76]. The band gap is almost 2.2 eV. In the next step, the hybrid functional [77] is used for all those high symmetry points. The bandstructure and the resulting density of states (DOS) are corrected, accordingly. The modified bandgaps obtained for 4H-, and 6H-SiC are 3.2 eV, 3 eV, respectively, which are in good agreement with the experimental results. Experimentally, the bandgap obtained is 3.26 eV, and 3eV for 4H-SiC [107], and 6H-SiC, respectively [108]. Figure 3.5 shows the results for both 4H- and 6H-SiC structures.

There are similarities in the band structures between the hexagonal polytypes, both in the valence, and the conduction bands. As figure 3.5-3.7 show, the top of the valence band for both 4H-SiC, and 6H-SiC, is located at Γ point of the first Brillion Zone. The Γ point is taken as zero of energy. There is a second minimum of the conduction band at the M point, which is located almost 0.1 eV above the first one. The minimum of the conduction band in 4H-SiC is at M point, and for 6H-SiC is along the ML line. There is a second minimum of the conduction band at the M point, which is located almost 0.1 eV above the first one. The numbers of the bands in the band structure is determined by the number of valence electrons in the unit cell of the polytype. In the case of 4H-SiC with 8 atoms in the unit cell, there are 16 valence bands. For 6H-SiC, with 12 atoms in the unit cell, the valence bands are 24. Electrons move along c-axis when they move from M to L, and perpendicular to this axis, when they move from M to K.

One of the primary quantities used to describe the electronic state of a semiconductor material is the electronic density of states (DOS). Once a DFT calculation has been performed, the electronic total DOS can be determined by integrating the resulting electron density in k space. Using a large number of k points to calculate the DOS is necessary because the details of the total DOS come from integral in k space. Figures 3.5 and 3.7 show the total density of states of 4H-, and 6H-SiC.

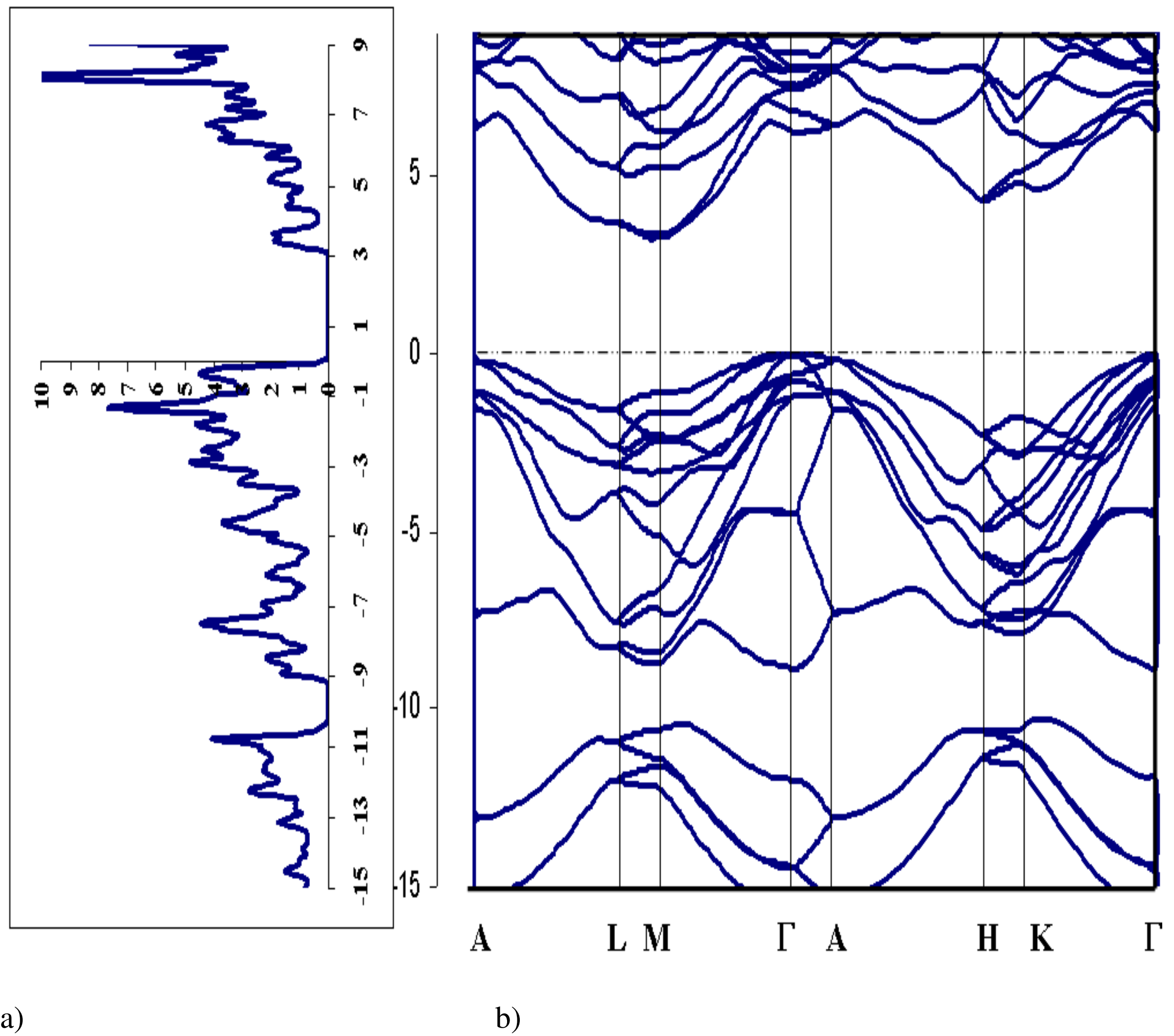

Figure 3.5: a) DOS, and b) Band diagram of 4H-SiC along A L M Γ A H K Γ.

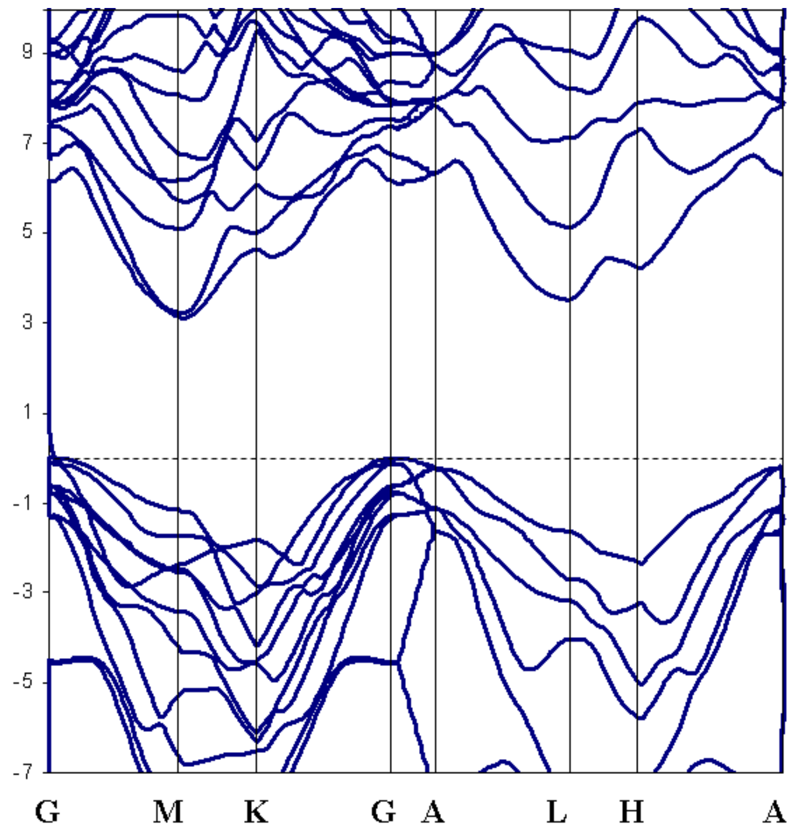

Figure 3.6: Band diagram of 4H-SiC along Γ M K Γ A L H A.

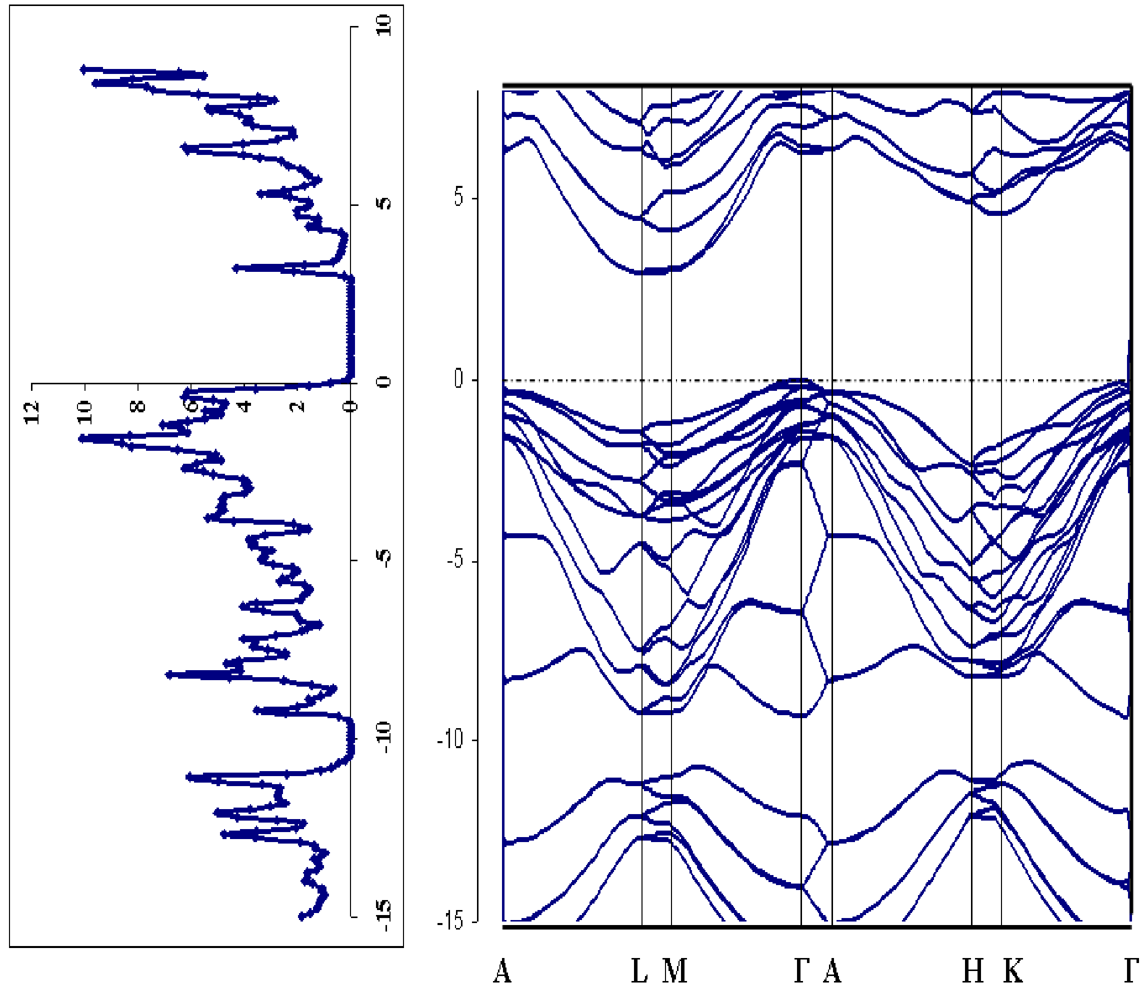

a) b)

Figure 3.7: a) DOS, and b) Bandstructure of 6H-SiC along A L M Γ A H K Γ.

3.2.1. Effective Masses for 4H-SiC

The effective electron masses for 4H-SiC have been measured by several groups [103-105]. The effective electron mass tensor $m(\vec{k})$ is defined as:

$$\frac{1}{m(\vec{k})} = \frac{\partial^2 E(\vec{k})}{\hbar^2 \partial k_i \partial k_j}. \quad 3.1$$

The effective masses are the measure of the curvature of the calculated bands. The agreement between previously calculated and measured effective masses with the one obtained by DFT simulation indicates an accurate determination of the shape of the bands.

In 4H-SiC, as mentioned earlier, the conduction band minimum is found at the M point of Figures 3.5, 3.6. The shape of lowest conduction band in 4H-SiC along the MΓ, and MK direction is shown in Figure 3.8a), and 3.8b) resoectively. The calculated electron effective mass in this direction is $0.57m_0$.

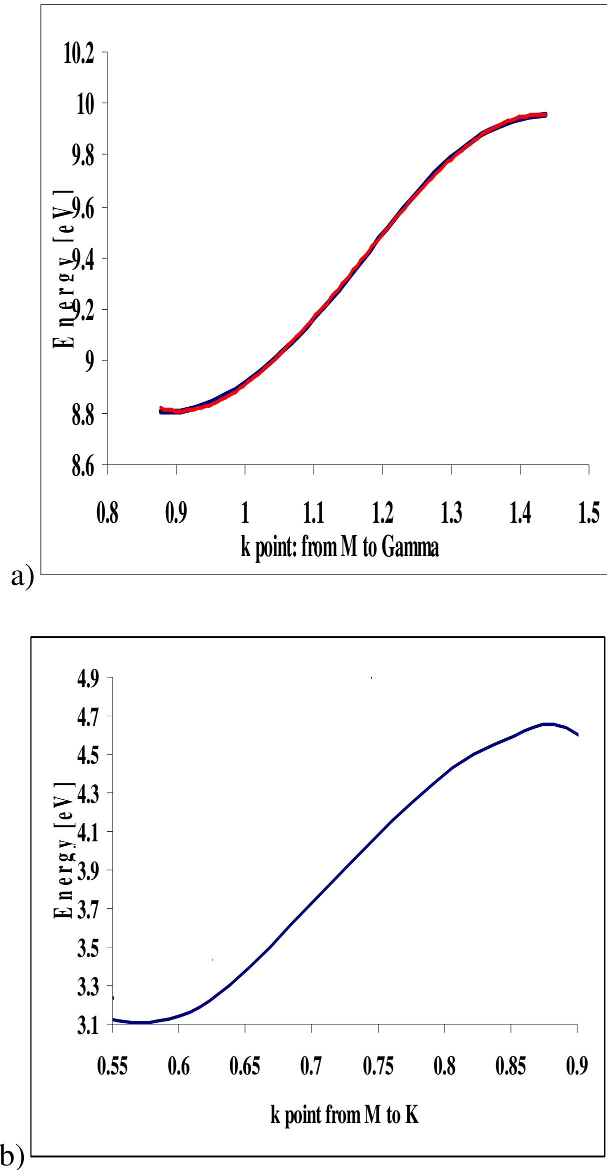

Figure 3.8: The shape of the lowest conduction band branch in 4H-SiC along a) MΓ, b) MK.

The ML direction corresponds to electron motion along the hexagonal c-axis, while the directions MΓ and MK correspond to electron motion in a plane perpendicular to the c-axis in the first Brilloin zone. The calculated effective masses for 4H-SiC along MK, and ML are 0.29, and 0.31, which are in good agreement with the published results [109, 110].

3.3. The SiO_2 Bulk Model

To become familiar with the properties of the oxide layer growing on SiC, a model for the α-quartz structure is chosen because of its stability at room temperature [111]. The electronic energy bands of α-quartz structure in a hexagonal lattice are simulated by DFT simulator. Again, the calculation is carried out in a GGA approximation, with the PBE exchange-correlation functional, at first. Then the energy calculation is repeated with the help of hybrid functional to obtain the most accurate results for the bandgap.

The alpha-quarts has the hexagonal unit cell; the lattice constants after the optimization with respect to the total energy are a=9.285, and c=10.21 Bohr. The primitive cell contains nine atoms, three atoms of silicon and six atoms of oxygen; each oxygen atom has two silicon neighbors with $\angle Si - O - Si = 144^\circ$. Figure 3.9 shows the atomic configurations of the Si and O atoms in the hexagonal unit cell.

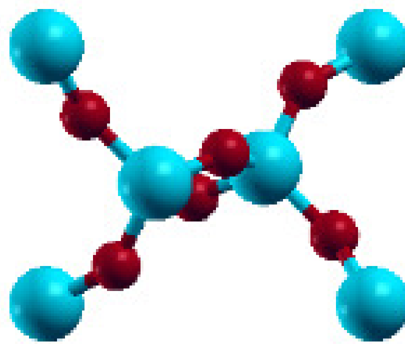

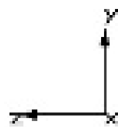

Figure 3.9: α-quartz unit cell; the large blue spheres are silicon, and the small red spheres are oxygen atoms by xcrysden.

The energy calculation is performed for high symmetry points in the first Brillouin zone. The minimum of the conduction band is located at Γ. The calculated bandgap is 6.2 eV, and 9 eV after using PBE, and hybrid functional, respectively; the latter one is in good agreement with the experiment [112]. The band structure and total density of states of α-quartz are calculated, as illustrated in Figure 3.10.

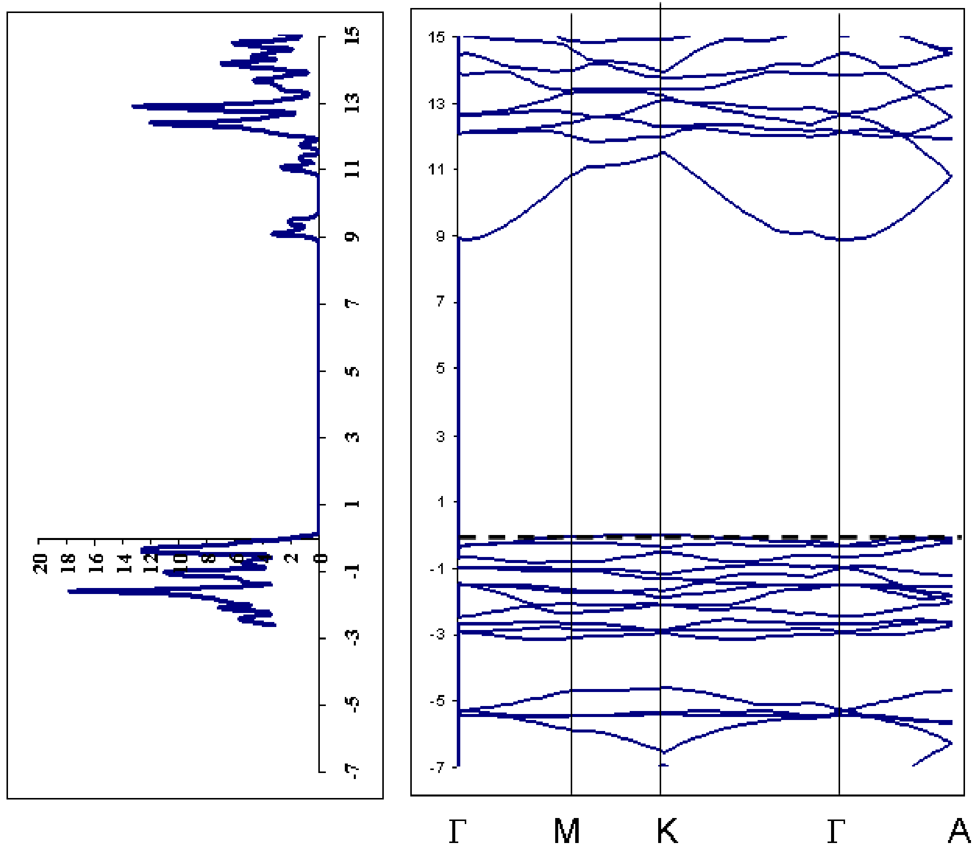

Figure 3.10: a) DOS, and b) Band structure of α-quartz.

3.4. Toward Modeling the (0001)4H-SiC/SiO_2 Interface

To construct the supercell for further defect calculation, and interface comparison, first a 72-atom (0001)4H-SiC is prepared, and its total energy is compared with that of 4H-SiC by considering the convergence of total energy with respect to k points. The DFT total energy calculated for 72-atom 4H-SiC is exactly 9 times of that of 8-atom SiC. The (0001)4H-SiC is chosen because it is the common substrate used in SiC-based MOSFET devices. The model contains eight layers of Si, and C planes, and nine atoms on the surface of each plane. The bulk structure has nine C atoms on the first plane, and after eight alternating planes, ends in nine Si atoms on the surface. The lattice constants have been optimized with respect to the total energies after several relaxation simulations. The lattice constant ration c/a has been found to be 1.6371 for this 72-atom 4H-SiC bulk structure. The calculated bandgap with PBE simulation is 2.1eV, which is very smaller than the published experimental value.

To overcome the bandgap underestimation, a hybrid functional simulation is carried out for every k points of a mesh, one at the time. Since the hybrid functional calculation is very expensive computationally, the simulations should be performed in a reduced k-point sampling. The calculated bandgap is 3.2eV with the use of hybrid functional.

For the oxide layer, we took the tetrahedral backbone of the α-quartz structure that we modeled before, and is shown in the upper part of figure 3.9. By connecting their corners, we made a regular network of tetrahedral structures which is used as the first oxide layer of the interface.

To model a layer of oxide on the top of our $3\times3(0001)$4H-SiC supercell, we connect every one of the Si atoms of the substrate to one oxygen atoms of the SiO_2 tetrahedral backbone. The average bond length of Si-O atoms at the interface is almost 1.6 angstrom. Our interfacial structure involves three Si atoms of the SiC substrate to three oxygen atoms of the SiO_2 tetraedral. Then some other SiO_2 tetrahedrals are added to the top of this layer, and eventually a layer of oxide is grown on the surface of SiC substrate. It should be noted that after connecting the Si atoms of SiC substrate to the first layer of oxide, the number of interfacial bond density reduces. Figure 13 shows our method for interfacial connection between (0001)4H-SiC, and SiO_2 of the abrupt model. As it is seen in figure 3.11, three Si atoms of 4H-SiC are saturated with three oxygen atoms of SiO_2.

The structure is called "abrupt" because each of the nine Si atoms located at the interface of the (0001)-4H-SiC is saturated by an oxygen foot of a tetrahedral oxide.

To improve the properties of the oxide layers lying on the top of the SiC substrate, and minimize the force, and stress of each atoms of the interface, we relaxed the atomic positions within the DFT scheme. During the relaxation, the interfacial atoms are evolves in the vicinity of their original position.

Then final abrupt (0001)4H-SiC/SiO_2 supercell is constructed by putting 36-atom of oxide on the top of the 72-atom of 4H(0001)-SiC.

The mass density of the oxide at the top of the 4H-SiC is 2.347 gr/cm^3, close to both the density of vitreous SiO_2 obtained from the melt (2.2 gr/cm^3), and the oxide densities near the interface found in models of the Si(100)/SiO_2 interface (2.3–2.4 gr/cm^3) [113].

The average bond length between silicon, and oxygen atoms in oxide side of the structure is almost $1.67\,A^{\circ}$, and the average angle between Si, O, and Si in the oxide side is almost $\angle Si - O - Si = 140^{\circ}$. The average angle among C, and Si, and O atoms at the interface of (0001)4H-SiC/SiO2 is almost $\angle C - Si - O = 109^{\circ}$.

The dangling bonds at the top and bottom of the structures are terminated with hydrogen. Layers of vacuum have been placed on the top and bottom of the structures to isolate them in the z direction.

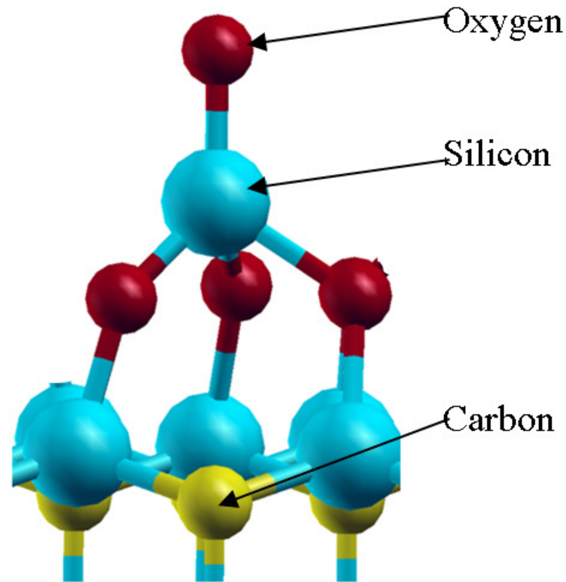

Figure 3.11: The interface of the (0001) 4H-SiC/SiO_2, used in the abrupt model; in this model three Si atoms of 4H-SiC are saturated with three oxygen atoms of SiO_2.

Again a DFT solver called Quantum Espresso [75] is used to perform the band-structure and DOS calculations of the SiC/SiO_2 structures, with the Perdew-Burke-Ernzerhof (PBE) exchange-correlation functional. The norm-conserving pseudopotential is used for both silicon and carbon atoms. The DFT simulation is

performed within the plane-wave basis set until the maximum force becomes smaller than 0.1 eV / A°. The cut off energy of the plane wave is set to be 70 Rydberg.

Determining the exact energy levels and retrieving the bandgap take place in two steps; first, the geometry optimization, and energy calculations were carried out within the normal PBE framework.

To achieve a realistic value for bandgap, the hybrid density functional [77], which incorporates a portion of exact exchange from Hartree-Fock theory, is employed. The idea is to use the exact exchange energy which dominates the exchange, correlation term from the Hartree-Fock calculation, and use any kind of approximations for the correlation part. In doing so, the so called "DFT bandgap problem" is solved.

In the next step, the hybrid functional is used for calculating the energy of the high symmetry points, again. Then, the bandstructures are compared to those obtained with PBE, and the bandgap, and (projected) densities of states ((pDOS)) are corrected, and modified, accordingly. The DOS is calculated in a $4 \times 4 \times 4$ Monkhorst-Pack mesh [92].

The calculated band gap of 72-atom 4H-(0001)SiC/SiO_2 terminated in Si with PBE approximation is 2.3eV, which is 1 eV smaller than the real band gap of SiC. The bandgap is corrected by the use of hybrid functional to modify the gap underestimation; as the result, the bandgap obtained for the original abrupt structure of (0001)4H-SiC/SiO_2 is almost 3.28 eV, which is in good agreement with experiment. Figure 3.12 shows this supercell which is kept as the reference for the further calculations.

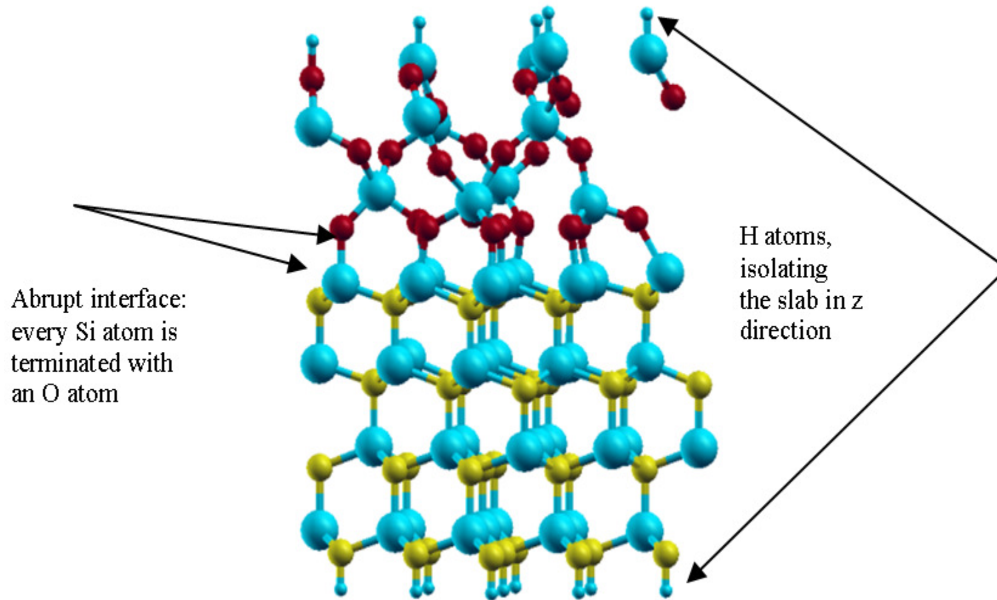

Figure 3.12: The atomic structure of abrupt structure.

3.4.1. The Evolution of Bandgap

The electronic properties of the abrupt structure are determined by the use of the total, and projected density of states (p(DOS)). In fact, total, and projected density of states provide the means to establish the evolution of bandgap in the bulk, and at the interface.

The projected density of states provides the contributions of each atomic orbital in the structure. It shows the contributions of each carbon, silicon, and oxygen atoms in almost 4.5 angstrom in bulk SiC, at the interface, and in the oxide. As Figure 3.13b)-d) shows, in both SiC, and interface the silicon atoms shape the minimum edge of the conduction band, while carbon atoms form the edge of the valence band. In the oxide, however, the valence band is mostly dominated by the oxygen atoms, whereas the minimum edge of the conduction band is as the result of the silicon atoms.

As it mentioned the comparison between the atomic contributions in different layers of the abrupt structure provides a map to study the bandgap evolution. The arrows in figure 14 show the maximum, and minimum of the valence, and conduction bands, respectively, and give an idea about the evolution of bandgap on parallel surfaces in z direction. As it can be seen in figure 3.13, the bandgap of the abrupt structure increases from the SiC base of the structure to the oxide for each 4.5 angstrom.

e)
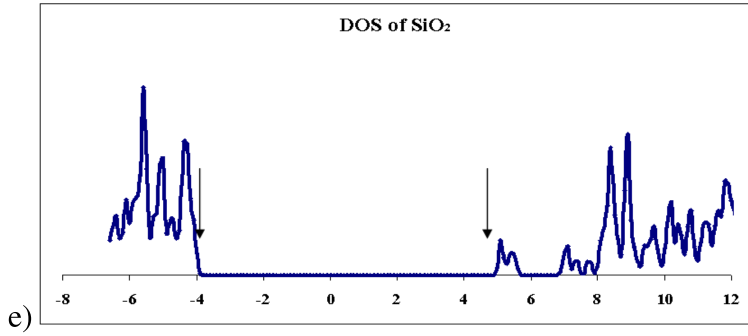

d)
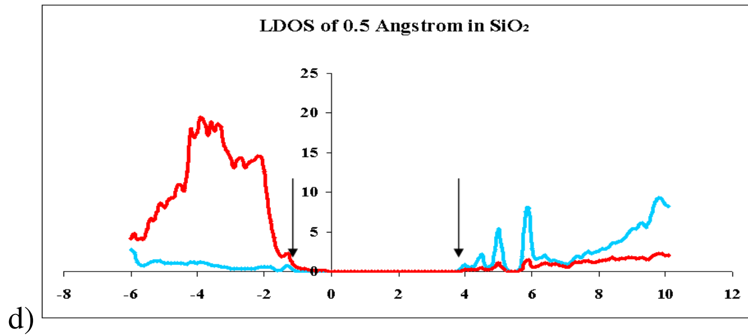

c)
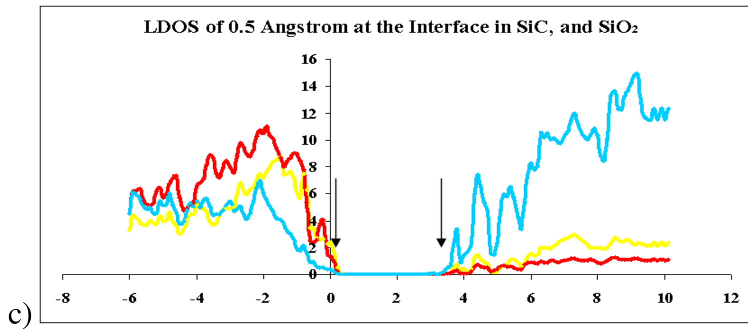

b)
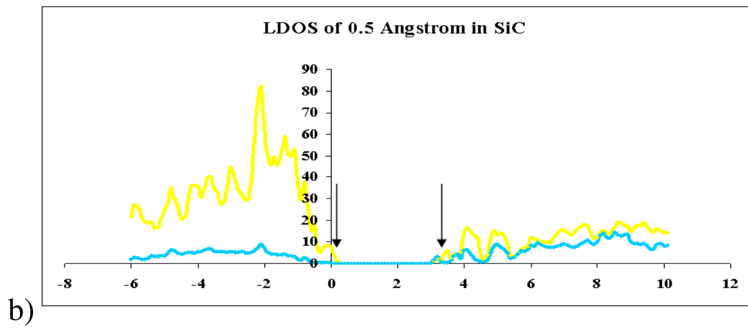

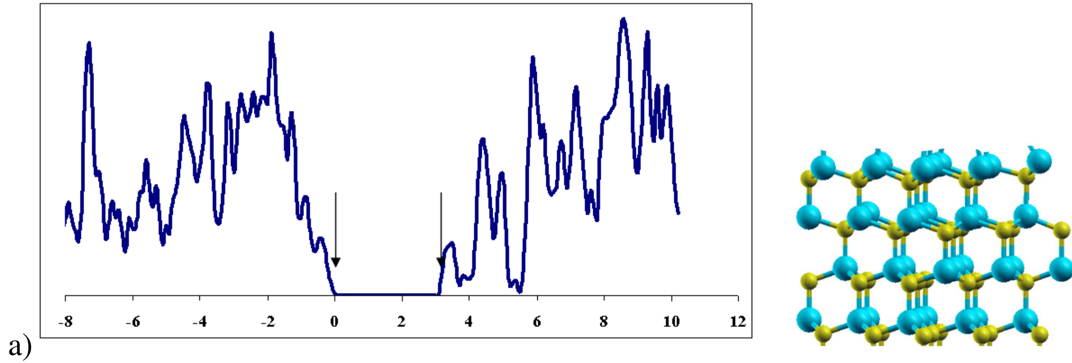

Figure 3.13: The evolution of bandgap of the interface obtained by the total and projected DOS, corrected by hybrid functionals. The DOS contributions of Si, C, and O atoms are light blue, yellow, and red, respectively. The total DOS of SiC (figure a)), and SiO_2 (figure e)) in general are shown in navy. The pDOS figures between SiC, and SiO_2 are the pDOS of almost 4.5 angstrom (from figure b) to figure e)), each.

Figure 3.14 shows the total DOS of the abrupt structure in a $4\times4\times4$ Monkhorst-Pack mesh [92]. As it seen, the bandgap of the whole structure is almost 3.28 eV.

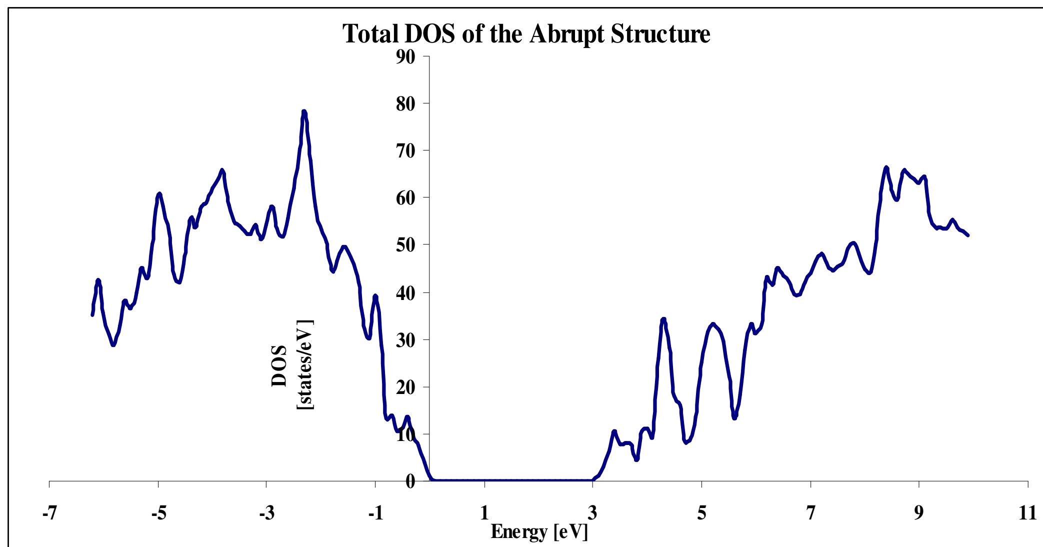

Figure 3.14: The total DOS of the abrupt structure.

By considering the band extremes of each segment of the interface illustrated in figure 3.13, it is possible to find the bandgap evolution of (0001)4H-SiC/SiO_2 abrupt

model at the interface. As it is seen, although the model is called abrupt, the bandgap evolves through a transition region. The top line shown in figure 3.13 represents the evolution of the minimum of the conduction band edge, while the bottom line demonstrates the evolution of the maximum of the valence band edge. As mentioned before, each segment shown by pDOS in figure 3.15 is the representative of 4.5 Angstrom of the interface. The zero point in x-axis of figure 3.15 shows the band edge extremes in 4H-SiC, which is shown by figure 3.13a). Then as the band edge extremes goes from the structures shown in 3.13b) to the ones in figure 3.13-d), the bandgap becomes wider, until it reaches that of the oxide, which is shown in figure 3.13e).

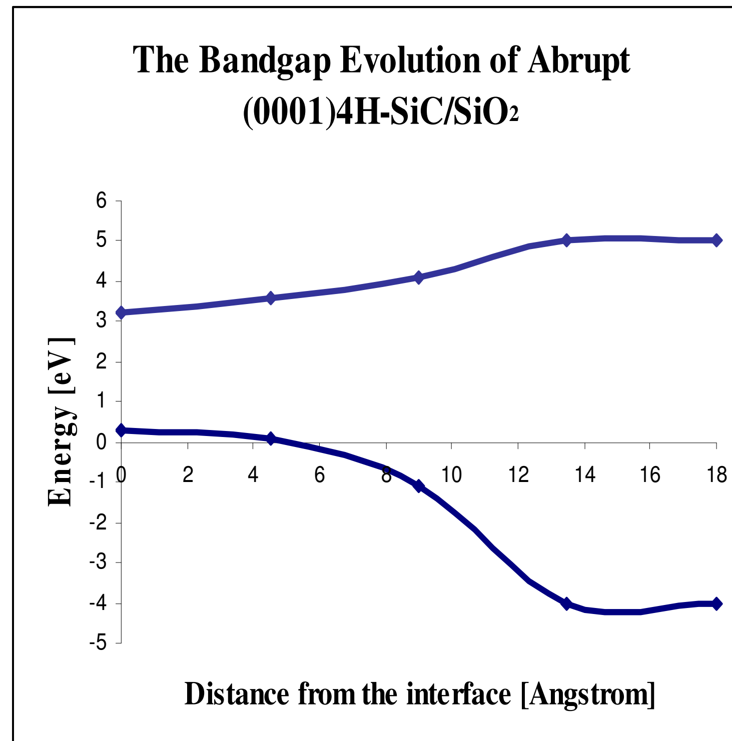

Figure 3.15: The bandgap evolution of (0001)4H-SiC/SiO_2 abrupt model at the interface; the top line shows the evolution of the minimum of the conduction band edge,

while the bottom line represents the the evolution of the maximum of the valence band edge.

3.5. Summary

In this chapter, we constructed the unit cell of 4H-, and 6H-SiC and calculated their bandstructure, and total density of states (DOS) with both PBE, and hybrid functional framework of DFT. The hybrid functional overcome the DFT bandgap underestimation, and provides more accurate approximation. The bandgaps calculated for 4H-, and 6H-SiC with this method is in good agreement with the experimental results.

After calibrating the DFT simulations, an original structure of (0001)4H-SiC/SiO_2 is generated for further defect, passivation, and transition layer studies. To realize such a structure, the tetrahedral backbones of oxide structure are located at the top of the Si atoms of (0001)4H-SiC substrate; the oxide layer is formed by connecting the corners of these tetrahedral together. The structure is abrupt in the sense that every Si atoms at the interface of SiC is satisfied by an oxygen atom, and no dangling bonds are left in between. After the geometric relaxation, the resulted bond lengths and bond angles are within a reasonable range. The energy calculations and electronic properties are obtained both with PBE, and hybrid functionals.

The evolution of bandgap is studied with the use of projected density of states over all the atoms within 4.5 angstrom of the structure in z direction.

In conclusion, we found that the generated model structure of the 4H(0001)-SiC/SiO_2 interface have reasonable properties both from the structural and electronic standpoints. The bandgap retrieved by the hybrid functional provides a reliable

framework. This model is kept as the reference for further defect, passivation, and transition layer investigations.

Chapter 4: The Effect of Defects, and their Passivation on the Density of States of 4H-SiC(0001)/SiO_2 Interface

4.1. Introduction

The most likely defects on both sides of the 4H-SiC(0001)/SiO_2 interface have been identified from the literature, and their energy levels in the band gap have been determined. The defects studied are carbon interstitial, and a pair of carbons in both SiC, and oxide sides of interface, (charged) silicon vacancy in SiC side, oxygen deficiencies in different levels of oxide side, and silicon dangling bonds at the interface. In addition, the effects of hydrogen, nitrogen, and phosphorus passivation on the defect levels have been investigated. Density functional theory has been employed to calculate the total and partial density of states ((p)DOS), and the energy levels of the defects. The results of our calculations show that carbon interstitial, and a pair of carbons in SiC side, the oxygen deficiency at the interface, and silicon dangling bonds at the interface give rise to the traps near the conduction band. Besides, hydrogen, nitrogen, and phosphorus passivation can eliminate both the states near the conduction, and valence bands, although in some cases they may introduce some levels in the midgap.

4.2. Introduction to SiC/SiO_2 Defects

Although SiC is one of the most suitable semiconductor material for high power, high temperature power electronic, and its native oxide is SiO_2, the fabricated devices suffers from very low channel mobility. This drawback is the result of high density of interface states between SiC, and SiO_2.

In the lower half of the SiC band gap, the density of interface states, D_{it}, is in the range of $10^{12}cm^{-2}\,eV^{-1}$, while in the vicinity of conduction band edge, particularly in 4H-SiC, D_{it} approaches $10^{13}cm^{-2}eV^{-1}$ [18,115]. Not only that the density of state increases at the vicinity of both valence, and conduction band edges, but also several distinct peaks have been already observed by experiments. Capacitance–voltage technique (CV) [115], Internal photoemission (IPE) [13], photon simulated tunneling (PST) [116], and X-ray photoemission experiments [117] provide the evidences for donor-like peaks near the valence band edge, and in the midgap of the SiC/SiO_2 MOS devices. On the other hand, thermal dielectric relaxation current (TDRC) measurements on 4H-SiC/SiO_2 [29, 118] revealed two acceptor-like peaks, one sharp peak at E_c-0.1 eV, and a broad peak between 0.1 and 0.7 eV below the conduction band edge of 4H-SiC.

The problem of low channel mobility in 4H-SiC based MOSFET, caused by the high interface state density between SiC, and SiO_2, may originate from the SiC oxidation. Although, eventually the oxide grown on SiC devices is identical to that grown on silicon, the high temperature oxidation process[15], together with the presence (removal process) of carbon lead to not only the high state density, and also high near interface states, but also to new types of defects at the interface. Furthermore, due to the wide band gap of SiC, the oxide traps of Si/SiO_2 system may behave as the interface states in SiC/SiO_2. In fact, the photon simulated tunneling (PST) measurements reveal the peaks with the same energy position with respect to the conduction band edge of SiO_2 both in Si-, and SiC-based MOS devices [116].

In one classification, the interface traps are classified according to their location in the bansgap. The states that are located deep in the band gap, and those near the conduction band (called near interface traps, N_{IT}). The latter ones are the acceptors near the conduction bands, located near the oxide phase. The near interface traps are fixed with the respect of the conduction band of the oxide and they are independent of the polytypes [119].

Although, the physical origins of the high interface trap density (D_{it}), and the nature of individual parts of it remain unclear, several defects have been frequently proposed in literature.

By studying the most probable energetic routes of SiC oxidation process theoretically, Deak, and Knaup et al. [22, 32] attributed the deep levels of interface trap density of states near the valence band, and the mid-gap to carbon, and carbon correlated defects.

Based on density functional theory calculation, Devynck et al. concluded that carbon interstitial (extra carbon atoms) in various states can account for the high density of interface defects measured just below the conduction band [66, 67].

Recently, Shen proposed that the carbon di-interstitial cluster $(Ci)_2$ in SiC, generated by pairing of carbon interstitials during oxidation, is a major cause of the low channel mobility in thermally grown SiC MOSFETs [33].

Although some experiments provide supports of the existence of carbon clusters at the interface of SiC/SiO_2 [120], several other subsequent studies have questioned the occurrence of such clusters [25, 39-40].

On the other side, oxide defects in the oxide side have been suggested to give rise to the near interface trap density (N_{it}). Knaup et al. considered the possible defects in the SiO_2 side of the structure, and proposed that Si interstitial, and a pair of doubly-bounded carbon dimmers as the potential candidates for near interface trap density (N_{it}) [28]. Afanas'ev at al. proposed that the origin of all traps near the conduction band is the oxide defects such as oxygen deficiency [18].

4.3. Introduction to Passivation

Semiconductor interface states have been the focus of investigation from the early stages of this industry. The interface states reduce the mobility and minority carriers, in some cases produce undesirable charges, and also make device instability. Trap states, in general, and interface states, in particular, degrade electrical characteristics of semiconductor devices even in the case that their densities are low. To eliminate or reduce undesirable effects of the interface on device properties, the process of passivation is actively in progress.

To overcome the problem of high defect density at the 4HSiC-SiO_2 interface, which is located near the conduction band of 4H-SiC, and results in degradation of inversion channel mobility MOSFETs, many attempts have been made. These attempts have been focused on either oxidation or post oxidation annealing process in different ambient environment. Post-oxidation is variety of techniques ranging from re-oxidation to hydrogen, nitrogen, argon, and phosphorous annealing [121]. Post-oxidation annealing is performed mainly to reduce the density of interface states.

Re-oxidation annealing or post oxidation treatment is the process of oxidation performed at a lower temperature (than the real oxidation), after the bulk of oxide has

been grown in order to oxidize the impurities such as residual carbon or dangling bonds, without additional oxidation of SiC [121, 122].

In next section, we review the history of SiC/SiO_2 interface passivation both from theoretical and experimental point of view.

4.3.1. Hydrogen Passivation

Hydrogen is well-known for the passivation of dangling bonds (P_b center) at the SiO_2/Si interface. P_b center is tri-coordinated silicon which has non-bonding orbital electron in the oxide near the interface. These centers in silicon devices are responsible for more than 50%-100% of the interface trap density (N_{it}) [123]. Annealing of Si/SiO_2 interfaces in hydrogen containing ambient gas at 400-$500^{\circ}C$ reduces P_b defect density (from 10^{12} cm^{-2} eV^{-1} to less than 10^{11} $cm^{-2}eV^{-1}$ at midgap). Moreover, the rate at which the interfacial density of P_b centrs decreases is proportional to the volume concentration of H_2 molecule at the interface [45].

The effect of hydrogen passivation on $4H-SiC/SiO_2$ density of interface states in general and crystal orientations in particular is controversial and the matter of debate. One of the most important reasons is that the sources of the interface traps are a variety of defects, from carbon clusters, sub-oxides and Si/C dangling bonds to intrinsic oxide defects, while those of Si/SiO_2 interface traps have less diversity.

From the historic point of view, the debate goes back to Afanas'ev et al. [45], who argued against the existence of P_b centers, and silicon dangling bonds at the interface of SiC/SiO_2 structures, saying firstly that the interface traps at SiC/SiO_2 are different from Pb centers of Si/SiO_2, and secondly that the hydrogen passivation with the same

Si/SiO_2 conditions is ineffective for SiC/SiO_2 interface. They concluded that the traps at SiC/SiO_2 interface are due to carbon clusters.

However, Fukuda, et al. [46] reported the reduction of interface trap densities at energies of 0.2–0.6 eV below the conduction band for n-type 4H-SiC MOS structures on the (0001) Si face above $800^{\circ}C$, and hence the improvement of channel mobility of 4H-SiC MOSFETs on the (0001) Si face. They clarified that the reduction did not happen in $400^{\circ}C$, as it happens for Si/SiO_2 interface traps. They then concluded that the observed interface defects originated from the dangling-bonds of carbon atoms as well as silicon atoms.

Moreover, Senzaki et al. [47] reported the reduction of interface traps at E_c-E=0.6 eV to $1x10^{11}$ $eV^{-1}cm^{-2}$ by using hydrogen annealing above 800 °C. Based on secondary ion mass spectroscopy and D_{it} analysis, they claimed that D_{it} decreases with the increase of hydrogen concentration accumulated at the SiO_2/4H–SiC interface. They deduced that interface states at SiO_2/4H–SiC are supposed to be originated from the dangling bonds of C atoms as well as Si atoms, because *D*it decreases as the hydrogen annealing temperature increases and saturates around 800°C. In support of their argument, they also referred to the paper published by Tsuchida et al. [56-59] which observed the clear absorption bands of Si-H and C-H stretching vibrations on the 6H–SiC surface after hydrogen annealing around 1000 °C, using Fourier-transformed infrared-attenuated total reflection technique.

P. Jamet et al. supposed that hydrogen-based passivation does not result in net reduction of the interface-trap density; however, it makes a shift of the interface traps energy levels from the mid gap. They believed that the reason is the wider energy gap

of SiC, particularly the 4H polytypes, which encompasses the energy levels of Si–H bonds [59, 124].

These contradictory results show an ongoing debate on not only the origin of the interface traps, but also the role of hydrogen passivation.

This is the reason that further study and investigation is needed to shed light on the matter.

4.3.2. Nitrogen Passivation

The process of post oxidation annealing in NO, NO_2, NH_3 ambient or direct growth in oxide nitridation is called nitrogen passivation.

Nitridation improves the oxidation quality, and reduces the trap density of both silicon, and SiC interface. Relatively high values of channel mobility, up to about 50 cm^2/Vs can be obtained via nitridation [59, 124-127]. Nitridation in NO at elevated temperatures (more than $1150^\circ C$) reduces the near interface trap density by at least a factor of magnitude [124]; post oxidation annealing in N_2O is either less effective than NO ambient or the results are controversial [124-128].

Moreover, X-ray photoelectron spectroscopy (XPS), and secondary ion mass spectroscopy (SIMS) depth profiles of nitrogen at the SiC/SiO_2 interface [59, 124] show the removal of suboxides and carbon, and the creation of Si-N bonds. Jamet et al. [59, 124] proposed that the mechanism leading to creation of $Si \equiv N$ bonds in SiC/SiO_2 is similar to that of Si/SiO_2; according to their theory, silicon dangling bonds passivated by nitrogen, and silicon strained bonds are replaced by strong $Si \equiv N$ bonds.

Removal of carbon atoms, especially carbon interstitials [59, 124] from the interface probably in the form of $C \equiv N$ molecules [127, 128] is one of the distinct roles attributed to nitrogen passivation in SiC/SiO_2 system.

Afanas'ev et al., suggest that nitrogen passivates both the oxide, and sub oxide defects at the interface, which results in reduction of near interface trap density. The idea is that nitridation might affect the density of vacancies either through reducing the interface strained Si– O–Si bonds by nitrogen incorporation into the oxide network. They also assumed that nitrogen may saturate dangling bonds by Si=N formation and replace oxygen in strained Si– O–Si bonds [127, 128].

By modeling the relation between the nitrogen content and the interface trap density, McDonald et al. [62] suggest that nitrogen passivates atoms of carbon clusters at the interface via shifting their energy to the conduction band completely, and hence make them electrically inactive.

In summary, nitridation not only reduces the carbon-related compounds at the interface, but results in the formation of Si-N, and C-N bonds [129]. Hence, nitridation is beneficial in either binding to the defects and removal of the silicon, and carbon three-fold coordinated defects. Since, threefold-coordinated nitrogen has a lone pair in its outer shell, the nitrogen atom substituting either carbon, or silicon atoms brings an extra valence atom to the system. If this extra valence atom does not bond to neighboring atoms, it introduces a donor state near the valence band, which is less detriment for n-channel devices.

4.3.3. Phosphorus Passivation

Even after nitrogen passivation, trap density is still high, and channel mobility is still very low with respect to the bulk mobility.

To achieve higher inversion layer mobility, phosphorous post oxidation anneal has been performed on SiC/SiO_2 interface. The techniques is the incorporation of phosphorus atoms in SiO_2 side of the (not the 4H-SiC side) of 4H-SiC MOSFETs by thermal annealing, using phosphoryl chloride ($POCl_3$) [64]. Okamoto et al reported the peak field mobility as high as 89 cm^2/Vs, and the trap density as low as 9×10^{10} $cm^{-2}eV^{-}1$ around 0.2 eV from conduction band [64]. Due to small diffusion of phosphorus atoms in SiC bulk material, they uniformly distributed in the oxide side with a concentration as high as $2x10^{21}$ cm^{-3} [65].

The effect of the phosphorous passivation on the threefold coordinated carbon atoms in an interfacial transition layer, and Si–Si bonds at the interface is studied by Y. K. Sharman et al. [130]. According to their study, phosphorus atom can replace a threefold carbon at the interface and remove the states associated with the carbon atom. They also attributed an electronic level at about 0.6 eV above the valence band of 4H-SiC, to the lone-pair state of the threefold P atom (similar to nitrogen replacement).

4.4. Methodology

Total, and projected density of state ((p)DOS) curves are obtained via density functional theory (DFT) calculation. The projected density of states is a way of

partitioning the total density of states into its contributions, such as atomic orbitals; the projected density of states is describes in 2.8.1.2

The original super cell is an abrupt structure of SiC/SiO_2, formed by putting 36-atom of oxide on 72-atom of 4H(0001)-SiC, as is describes in chapter 3. Various defect configurations, which have already been proposed in the literature and their possible passivated forms are then incorporated into the structure.

The procedure is introducing a defect to the abrupt interface model, performing the geometric relaxation at gamma point, and then calculate the energy, and (p)DOS in the GGA-PBE framework of DFT. In the next step, the energy of the relaxed structures is calculated with the use of hybrid functionals. Since hybrid functional calculation is very expensive computationally, the simulation is performed for two k points, each time. Then the energies of the k points are gathered, and compared with their counterpart obtained from the first step. As the result, the bandgap, and location of states in the gap obtained and restored in the first step are then modified, and adjusted by the new data. Figure 4.1 shows the schematic algorithm of this simulation.

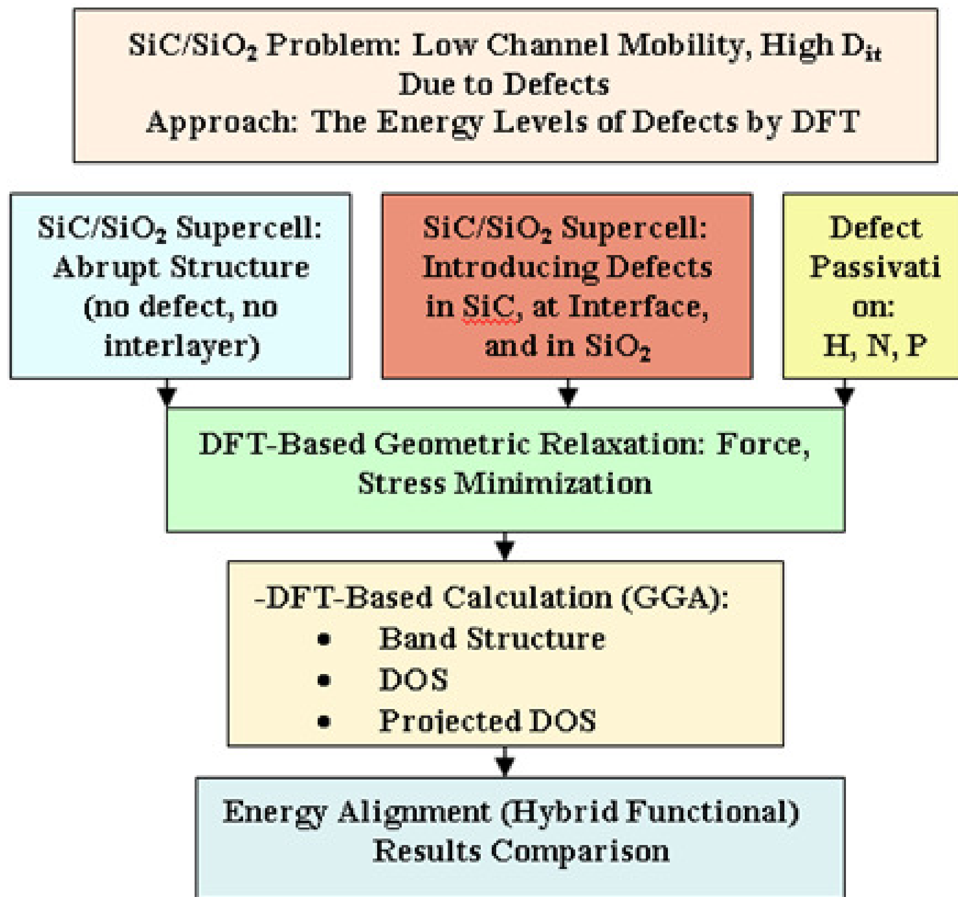

Figure 4.3: Algorithm for energy calculation of defects, and their passivations.

One of the most crucial factors in finding the defect levels in the DFT simulation is the alignment of the defect states. In this dissertation, we made the defects in both the bulk, and interface to make a parallel investigation. For each defect, full geometric relaxation is performed by GGA(PBE), and at gamma point. We then studied the defect levels through hybrid density functionals. The levels are labels with respect to the band extrema of both SiC, and SiO_2. Moreover, the defect states are also aligned with respect to an s orbital of one of the atoms far from the interface.

4.5. Defect Level at SiC Side of the (0001)4H-SiC/SiO_2 Interface, and their Passivation

4.5.1. Neutral Silicon vacancy

The defects such as vacancies and interstitials are the native point defects in semiconductors which alter the optical and electrical properties of the material. Vacancies are created by electron or proton bombardment at low temperature [131]. In fact, both silicon and carbon vacancies can occur in SiC. From experimental point of view, Cochrane et al. and Meyer et al. [48, 49] linked the spin-dependent recombination (SDR) spectrum to silicon vacancy. Theoretically, Zywiets et al. [132] used the first principle calculations for the neutral and charged silicon, and carbon vacancies in both cubic and hexagonal SiC.

To realize the vacancy structure, one of the silicon atoms in SiC side of the interface is removed, and the geometry relaxation is performed. As the result, one electron of every first neighbor carbon atoms around the Si vacancy loses the Si shared electron, and becomes unpaired.

Figure 4.2a) shows the structure with dangling bonds after the geometric relaxation. As it is seen in left hand side of figure 4.2a) the carbon atoms relax outward to keep the symmetry, which is in agreement with previous reports [132]. Moreover, due to localization of the four carbon atoms, their dangling bonds do not create any long bonds [132].

Then the total density of states is calculated for the relaxed structure. In addition, the projected density of states, or the contribution of the four carbon atoms around silicon vacancy, is calculated as well. The results are compared with those of the original

structure. Our DFT calculation shows that the energy levels caused by dangling bonds of the four carbon atoms around the silicon vacancy are located above the valence band, at E_v+0.1, E_v+0.5, and E_v+0.7eV. A comparison between the projected DOS of carbon atoms around the silicon vacancy, and the total DOS of the whole structure shows that all levels near the valence band are caused by the carbon dangling bonds. Figure 4.2a) shows the structure made for the silicon vacancy calculation. Figure 4.2b) shows the DOS contribution of four carbon atoms around the silicon vacancy to the density of states as a function of energy.

In Figure 4.2c) the total DOS of the structure (dotted line) is compared with the DOS contribution of four carbon atoms around the silicon vacancy (solid line); it clearly shows that the states in the bandgap are the result of those four carbon atoms with dangling bonds.

It should be noted that the small supercell dimension creates the artificial interaction among the vacancies in the adjacent supercell. This is the reason that the same type of Si vacancy is introduced to a bigger supercell. The calculation shows almost the same results for the bigger supercell.

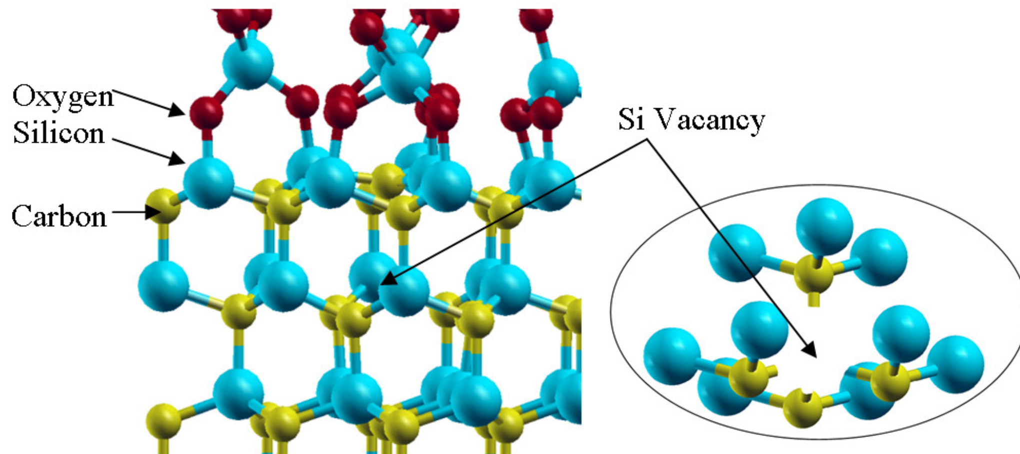

a)

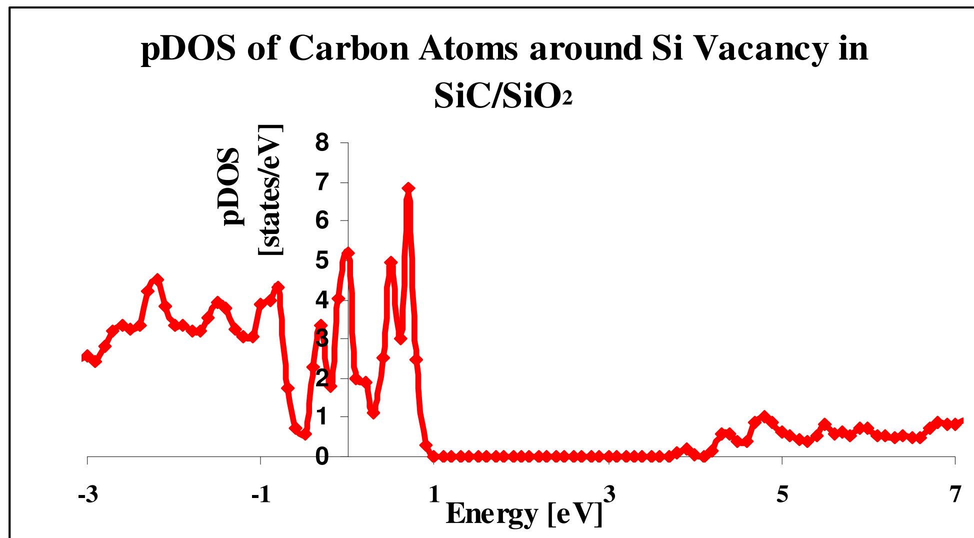

b)

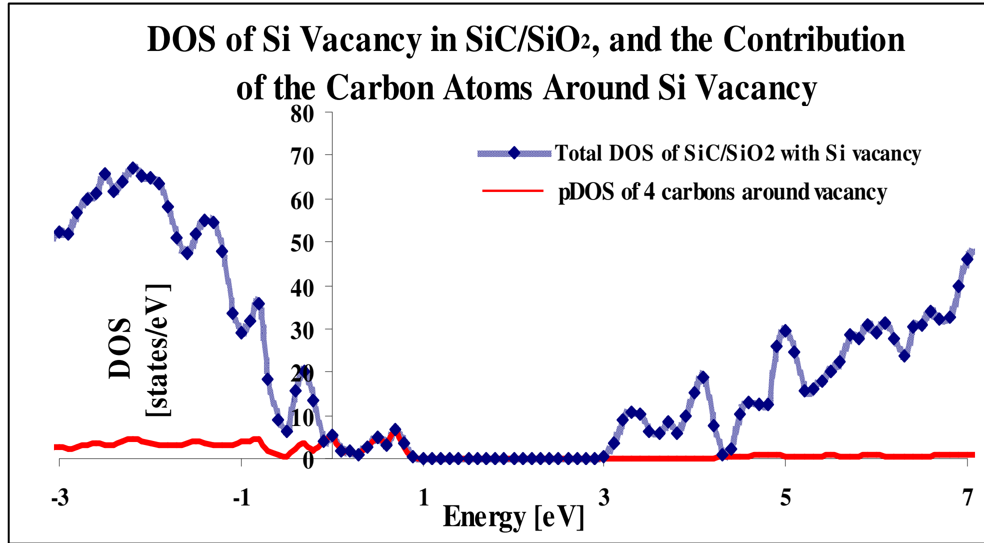

Figure 4.2: a) The atomic structure with silicon vacancy, and schematic of silicon vacancy and four carbons with four dangling bonds around it; b) pDOS of four carbon atoms around Si vacancy; c) total DOS of the abrupt structure (dotted line), and pDOS of carbon atoms around silicon vacancy (solid line).

4.5.1.1. Passivation of Silicon Vacancy

There is little existing theory that shows a mechanism for which the silicon vacancy is passivated by passivant atoms, such as hydrogen or nitrogen. Bosckstedte et al. [133] considered the recombination of the vacancies with the interstitials as one of the annealing mechanisms. The metastability of the silicon vacancy in SiC could be another mechanism of the vacancy annealing [134]. Nevertheless, since it is reported that hydrogen post oxidation annealing improves the channel mobility of 4H-SiC MOSFETs on the (0001)-Si face [39], we use hydrogen passivation to neutralize the dangling bonds in our DFT studies. In this investigation, each carbon dangling bond is passivated by a hydrogen atom. Figure 4.3a) shows how each carbon is connected to one hydrogen atom for further energy calculation. The comparison between the pDOS of those four carbon atoms before hydrogen passivation (solid line), and their

DOS contribution together with all the hydrogen atoms after the passivation (dotted circle line) is shown in Figure 4.3b). This figure shows that, if four hydrogen atoms could passivate the four dangling bonds, then the density of states in the vicinity of the valence band will be significantly reduced. In this case, due to the geometric configuration of four hydrogen atoms passivating the dangling bonds, passivation with hydrogen molecules faces large energy barrier [97], and therefore atomic hydrogen passivation would be more effective.

a)

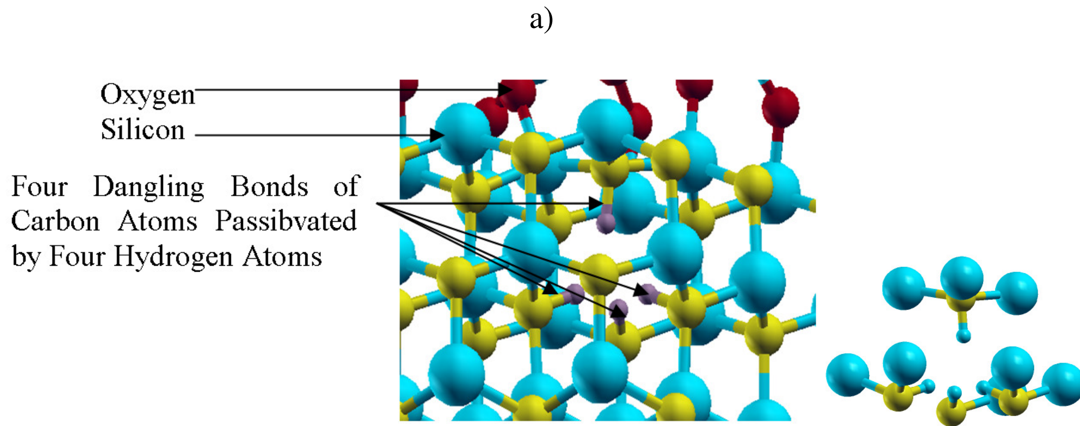

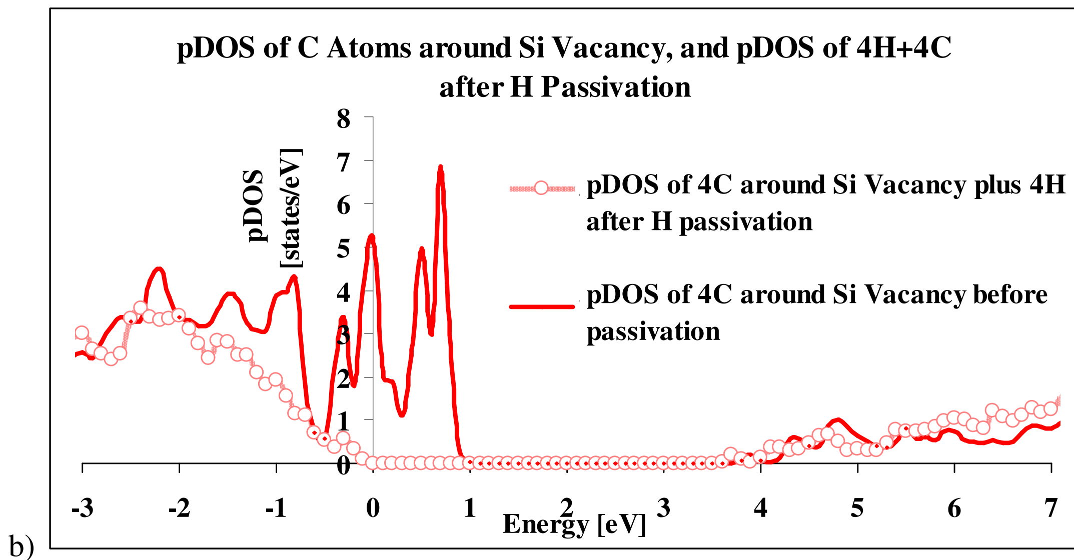

b)

Figure 4.3: a) Atomic structure of the carbon atoms around silicon vacancy passivated by four hydrogen atoms. b) pDOS of C atoms around silicon vacancy before passivation (solid line), pDOS of all carbon atoms together with hydrogen atoms after 4H (dotted circle line).

Since post oxidation annealing in both NO and N_2O ambient may improve the 4H-SiC MOSFET channel mobility, and experiments demonstrated that nitridation provides critically important improvements in the quality of the SiC/SiO_2 interface and effective channel mobilities [124-126, 129], we position a nitrogen atom in the vicinity of the silicon vacancy to study the nitrogen passivation. Figure 4.4a) shows the way that a nitrogen atom passivates the Si vacancy. Figure 4.4b) shows the pDOS of the nitrogen atom together with all four carbon atoms around the vacancy (dotted triangle line) with respect to the DOS contribution of carbon atoms with bare dangling bonds (solid line). Here, the nitrogen atom binds with the dangling bonds of the carbon atoms, which results in defect level elimination near the valence band as shown in Figure 4.4b). As figure 4.4b) shows, passivating the silicon vacancy with just one nitrogen atom gives rise to an energy level at E_v+1 eV. The DOS contributions of nitrogen and all carbon atoms around the silicon vacancy show that this level comes from one of the carbon atoms which is not passivated by nitrogen completely.

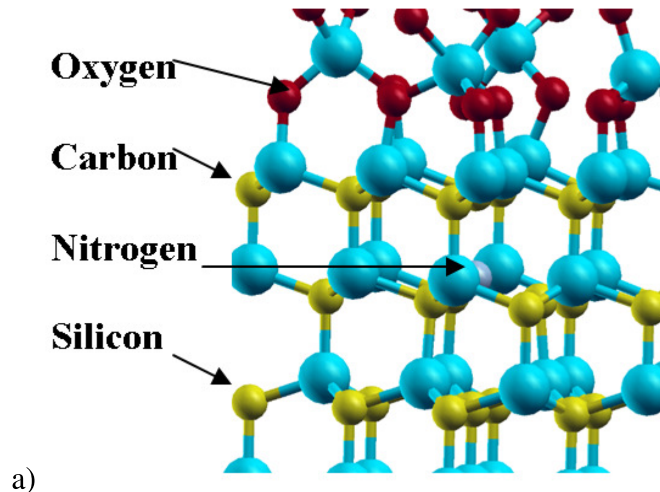

a)

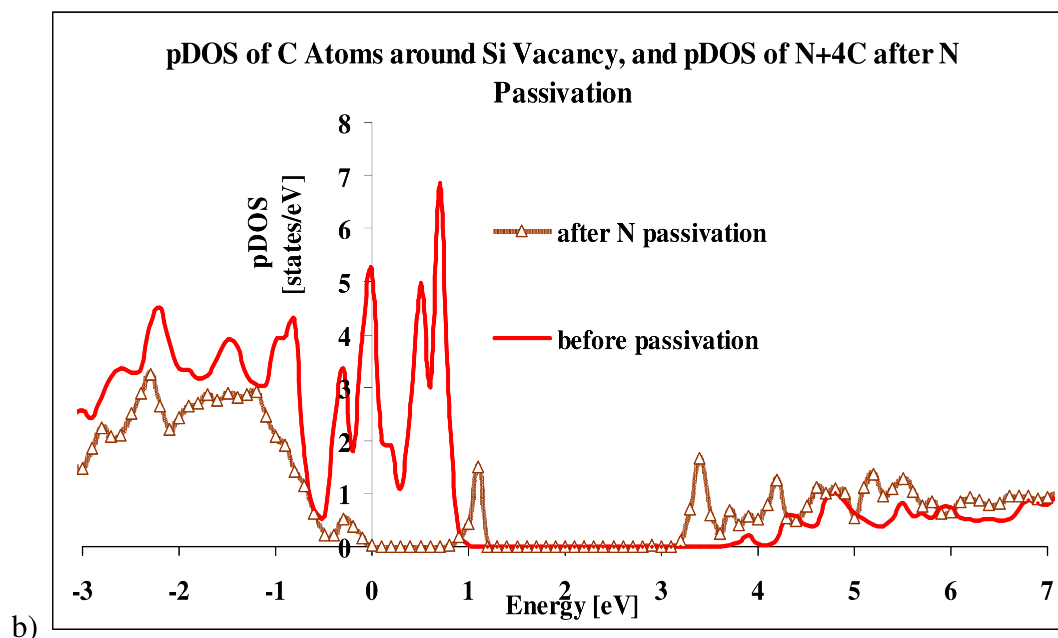

b)

Figure 4.4: a) Atomic structure of the structure with Si vacancy; b) pDOS of four atoms around the Si vacancy (solid line), and pDOS of all C atoms together with N after N passivation (dotted triangle line).

4.5.1.2. Negatively Charged Silicon Vacancy

Wimbauer et al. [135] used electron paramagnetic resonance and electron nuclear double resonance, and identified negatively charged silicon vacancy, experimentally. To investigate the affect of negatively charged Si vacancy, an electron is added to the

supercell. Adding an electron to the supercell to a reservoir level corresponds to a single-particle excitation [132]. It is like making a charged background for the entire cell to neutralize the structure. Then the silicon vacancy with one ionization level (0/-) is formed. The defect levels of charge transition levels are defined by the difference in total energy.

The total and pDOS of all C atoms around the Si vacancy in a neutral (the solid line) and negatively charged supercall (dotted circle line) are compared, and shown in figure 4.5. As it seen in figure 4.5, each negative charge transfers shifts the energy levels between 0.2 to 0.3 eV toward the mid gap. All are in reasonable agreement with positions determined experimentally [135].

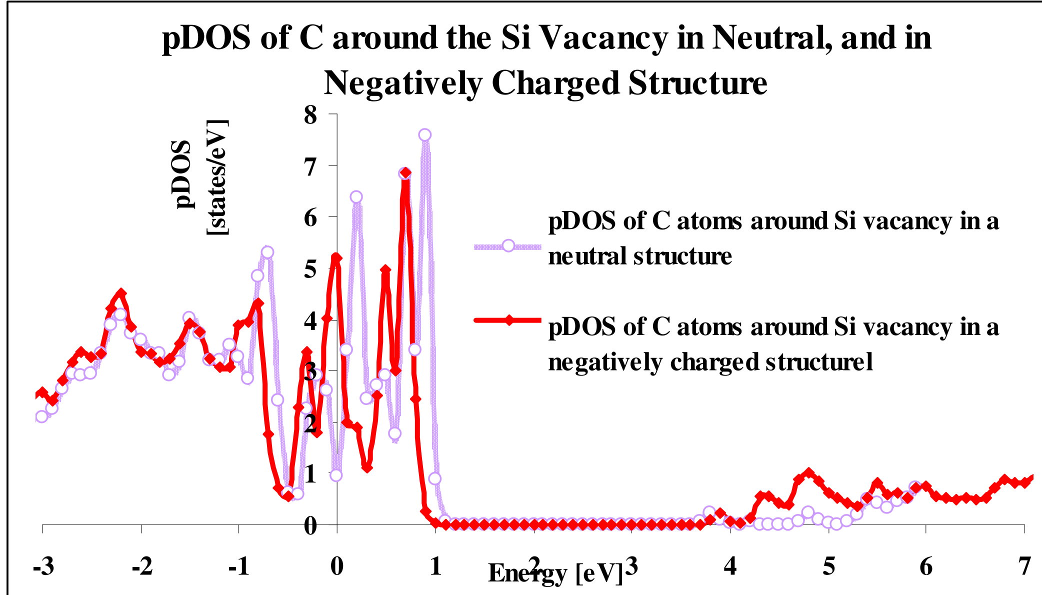

Figure 4.5: pDOS of the carbon atoms around Si vacancy for neutral (red), and one negatively charged structure (purple).

Figure 4.6 shows the comparison between the pDOS of all four carbon atoms around the Si vacancy (dotted circle line), and the total DOS of the whole structure (solid line) with one negatively charged Si vacancy. As it is seen, almost all the states in the bandgap are the result of the carbon atoms around the Si vacany.

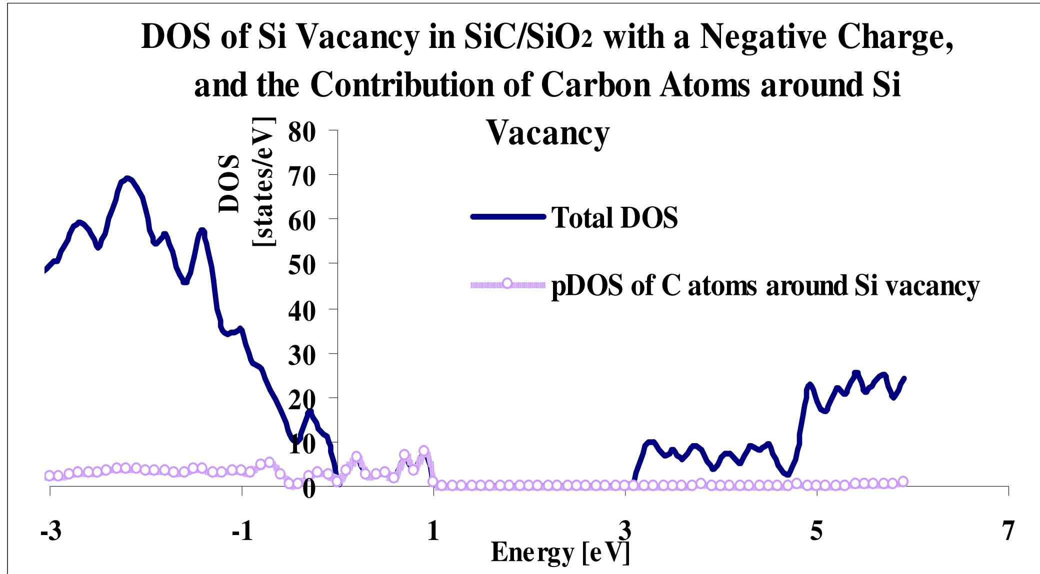

Figure 4.6: Comparison between the pDOS of all four C atoms around Si vacancy, and the total DOS of the whole structure with a Si vacancy.

4.5.2. Carbon Contaminations in SiC Side of SiC/SiO_2

In the oxidation process, some of the emitted carbon atoms are oxidized, form CO molecules, and leave the material. If the removal process is not done completely, some of the carbon atoms remain at the interface region.

In previous DFT calculations, the deep levels near the valence band and near the mid-gap were attributed to carbon, and carbon correlated defects [22, 32].

Although, the existence of large carbon clusters, and graphite particles have been largely ruled out [30], the role of a single carbon atom, in the form of carbon interstitial, and a pair of carbon atoms at the interface should not be excluded.

4.5.2.1. Carbon Interstitials in SiC Side of SiC/SiO_2

To investigate the energy levels of carbon interstitial, which has been proposed to have non-negligible concentrations in SiC side [67], we placed a single carbon interstitial in a couple of locations of SiC substrate. While in one case the peaks of carbon interstitial are at E_v+1eV, E_v+1.2eV, in the other situation, carbon interstitial makes three levels in the band gap: one near the valence band at E_v+0.7eV, and two of which are near the conduction band, at E_v+2.7eV and E_v+3eV, respectively. Figure 4.7a) shows the latter atomic configuration. Figure 4.7b) shows the DOS contribution of a C interstitial.

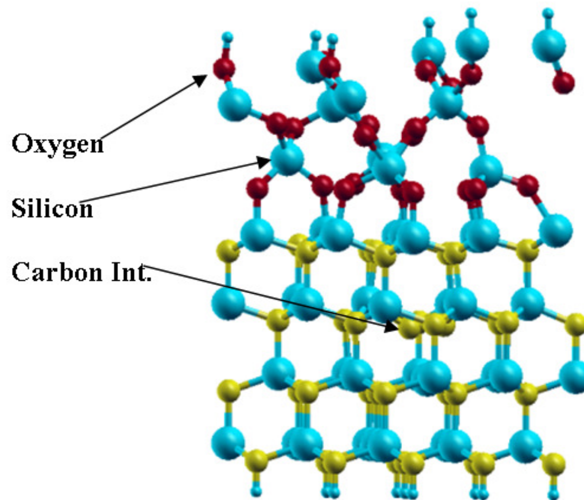

a)

b)

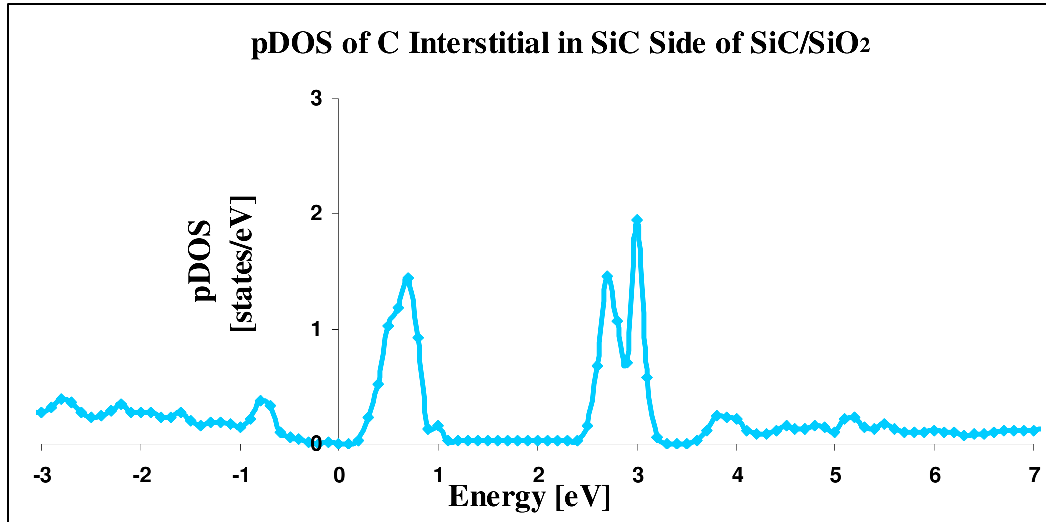

Figure 4.7: a) atomic structure with a carbon interstitial in SiC side, b) pDOS of carbon interstitial.

4.5.2.1.1. Passivation of Carbon Interstitials in SiC Side of SiC/SiO_2

To study the mechanism behind carbon interstitial passivation, we performed several calculations with different passivants. In the first case, a hydrogen atom is located in the vicinity of the carbon interstitial; after geometric relaxation, the DOS contribution of carbon interstitial together with the hydrogen atom after the passivation (dotted circle line in figure 8b)) is compared with that of carbon interstitial before the hydrogen passivation (the solid line in figure 8b)). As figure 9b) shows, while hydrogen passivates the states near the valence and conduction bands, it introduces new states in the midgap.

Since the mechanism of nitrogen passivation is not clear, this kind of passivation is studied in two ways; first we placed a nitrogen atom in the vicinity of the carbon interstitial. Figure 4.8a) shows the atomic configuration of the carbon interstitial

connected to a nitrogen atom. After relaxation, and energy calculation, the pDOS of nitrogen and the carbon atoms is found (dotted triangle line in figure 4.8b)), and compared with the DOS contribution of carbon interstitial before the passivation (the solid line in figure 4.8b)). As figure 8b shows, this type of nitrogen passivation eliminates all states made in the bandgap as the result of carbon interstitial. The role of nitrogen passivation in this case is pairing with the unsatisfied carbon bonds.

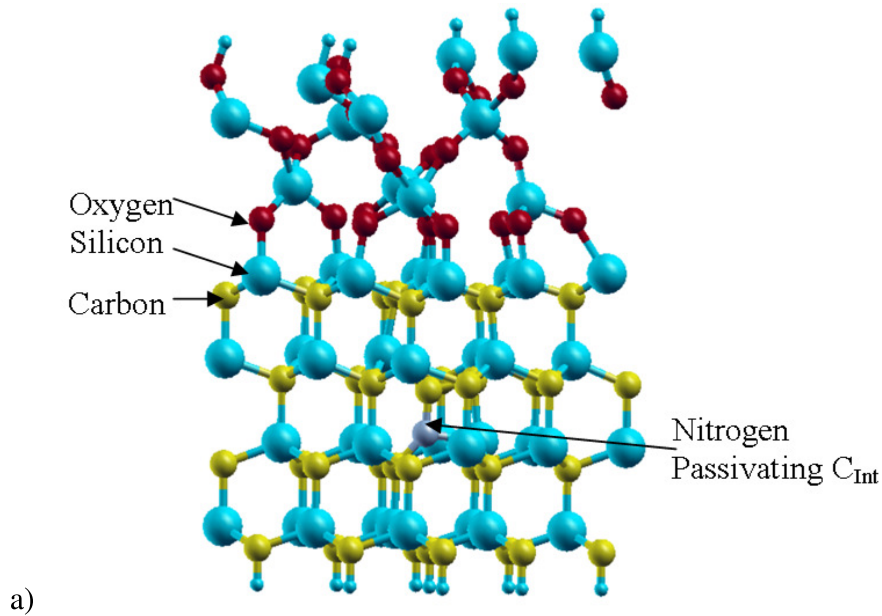

a)

b)

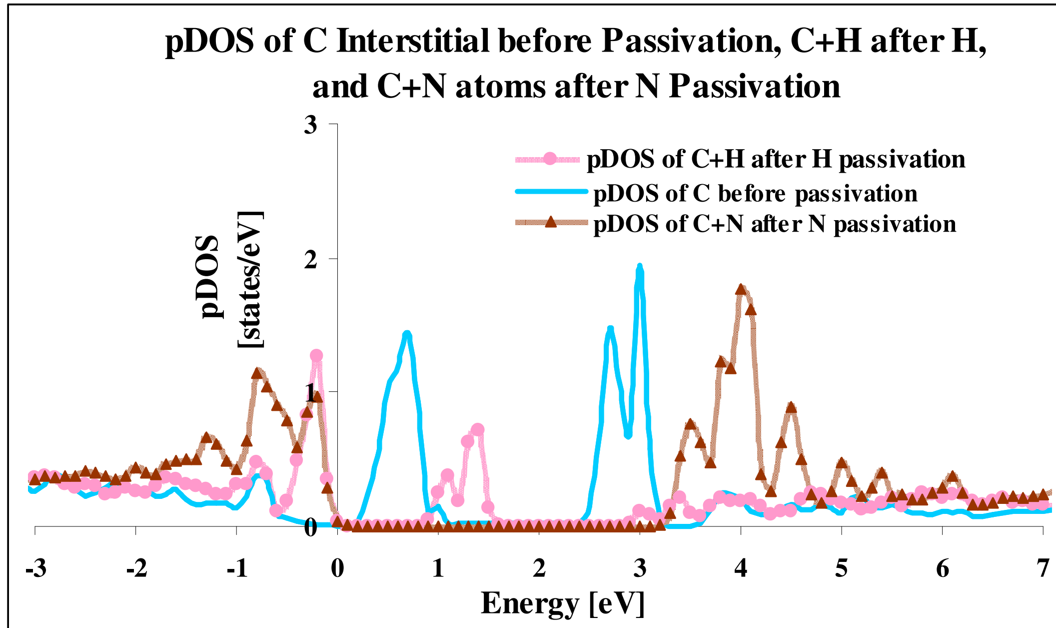

Figure 4.8: a) Atomic configuration of the abrupt structure with a carbon interstitial in SiC side; b) pDOS of carbon interstitial (solid line), carbon and hydrogen atoms after H (dotted circle line), and carbon atom plus nitrogen atom after N (dotted triangle line) passivation.

To study the effect of nitrogen passivation via carbon removal from the interface, the carbon interstitial is replaced with a nitrogen atom; again after the geometric relaxation, the (p)DOS is calculated. Figure 4.9 shows the pDOS of nitrogen atom after the replacement (dotted triangle line), compared to that of carbon interstitial (solid line). As it is seen, the carbon removal by nitrogen eliminates the levels near the conduction band, while makes a peak at E_v+0.8eV. The same type of C interstitial removal is investigated via phosphorus passivation. The dotted square line in figure 4.9 shows the pDOS of phosphorus after C interstitial removal by P passivation. As is seen in figure 4.9, the carbon removal by phosphorus reduces the levels near the conduction band, while makes a peak at E_v+0.8eV. These energy levels may be

attributed to the lone pair of electron that nitrogen and phosphorus bring to the system.

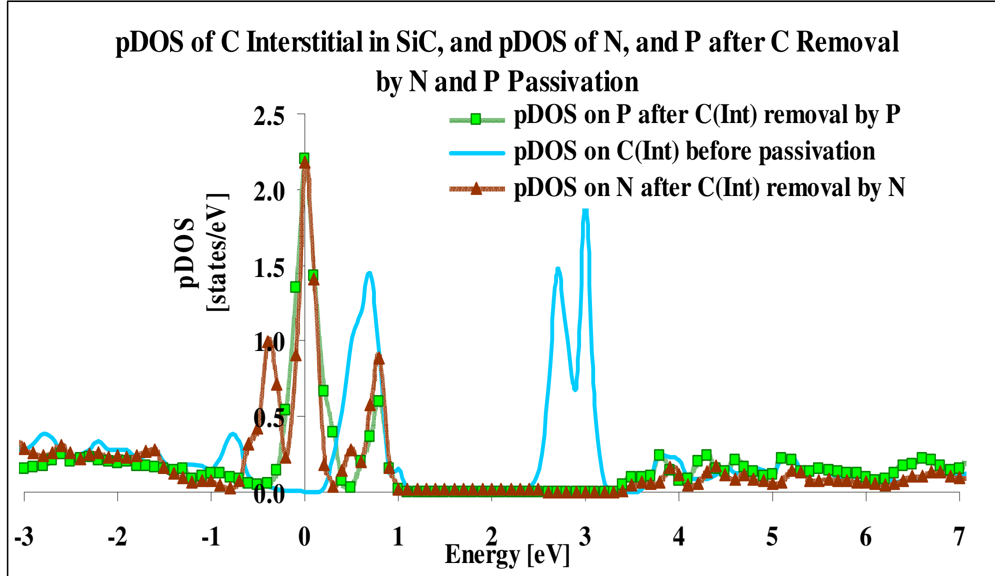

Figure 4.9: a) pDOS of carbon interstitial before passivation (solid line), pDOS of nitrogen replacing carbon interstitial (dotted triangle line), and pDOS of phosphorus replacing the carbon interstitial (dotted square line).

4.5.2.2. A Pair of Carbon Interstitials in SiC Side of SiC/SiO_2

A pair of carbon interstitials is another carbon related defect that may form during the oxidation. To investigate the possible states, they were situated in two locations in SiC near the interface. In both structures, each carbon of the pair bonds to one Si and one C in different neighborhoods, and result in a SiC-C-C-SiC form. The pair of carbon atoms makes sp^2 hybridizations with the average bond length of 1.39 A°. The difference between the structures comes from the relative position, and the local environment of the carbon pairs. While in one configuration, a pair of carbons makes two levels in the band gap, one close to the valence band, at E_v+0.4, and one close to the conduction band at E_v+3.1eV, in the other configuration, it makes three levels in

the band gap, one close to the conduction band, at E_v+0.4, one in the mid gap at E_v+1.6, and one near the conduction band at E_v+3.1eV. Figure 4.10a), and b) show the atomic configuration of a pair of carbon interstitials in the SiC side of the interface, and pDOS of this defect, respectively.

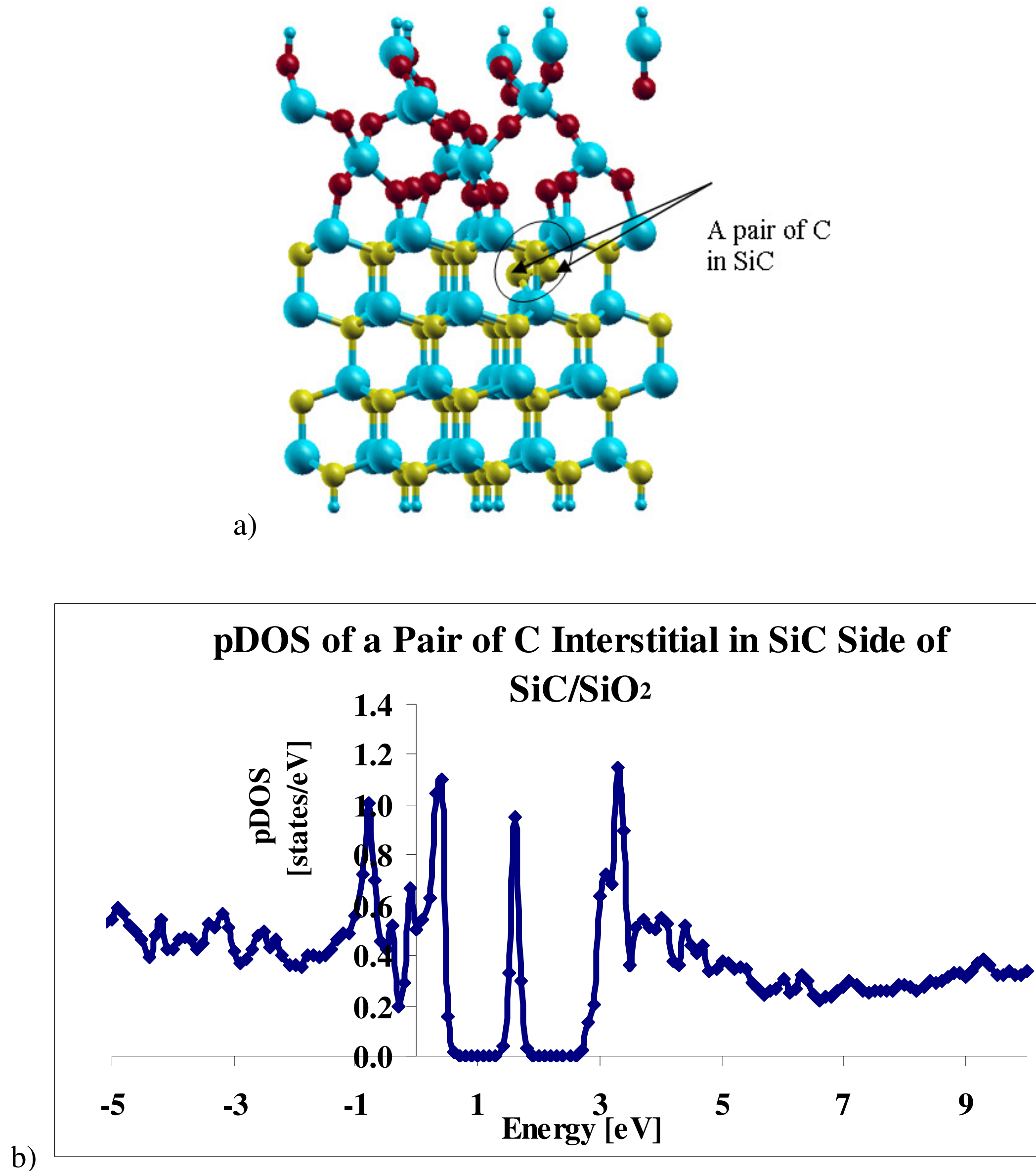

Figure 4.10: a) atomic configuration of a pair of carbon interstitials in SiC side of interface, b) pDOS of a pair of C atoms in SiC side of SiC/SiO_2.

4.5.2.2.1. Passivation of a Pair of Carbon Interstitials in SiC Side of SiC/SiO_2

To passivate the structure with a pair of carbons, two different methods are studied. At first, two hydrogen atoms are placed next to each carbon atoms, and the energy calculation is performed after full relaxation. The length of the C-H bonds after the relaxation is $1.05\,A^{\circ}$. Figure 4.11 a) shows the structure with a pair of carbon interstitials located at the SiC side after hydrogen passivation. As is seen in figure 4.11 b), hydrogen atoms could eliminate the states near the conduction band, but introduce a peak at E_v+1.5eV in the bandgap. To explain the process of hydrogen passivation for a pair of carbon atoms, Wnag et al. [97] mentioned that two C-H bonds, formed in this process should have opposite directions, which requires a large energy barrier for H_2 molecule to do the passivation. Instead, they suggested that this type of hydrogen passivation is a step-by-step process, which may happen by hydrogen atoms, instead of hydrogen molecule.

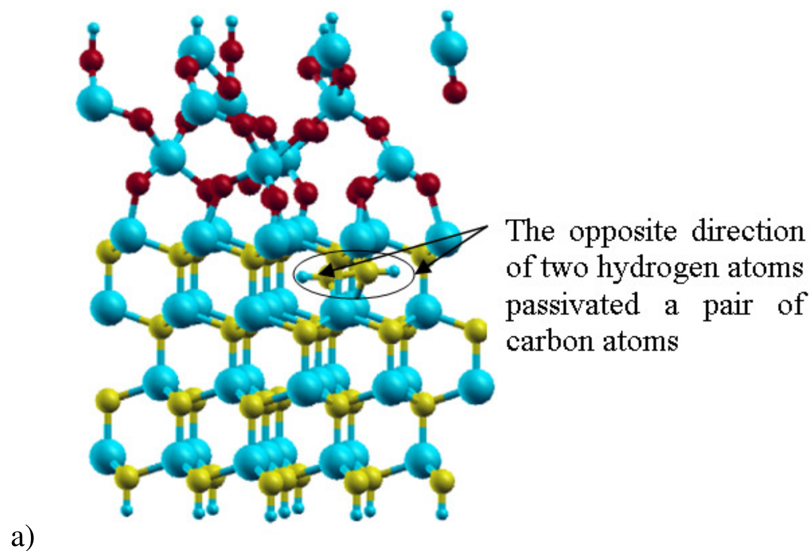

a)

b)

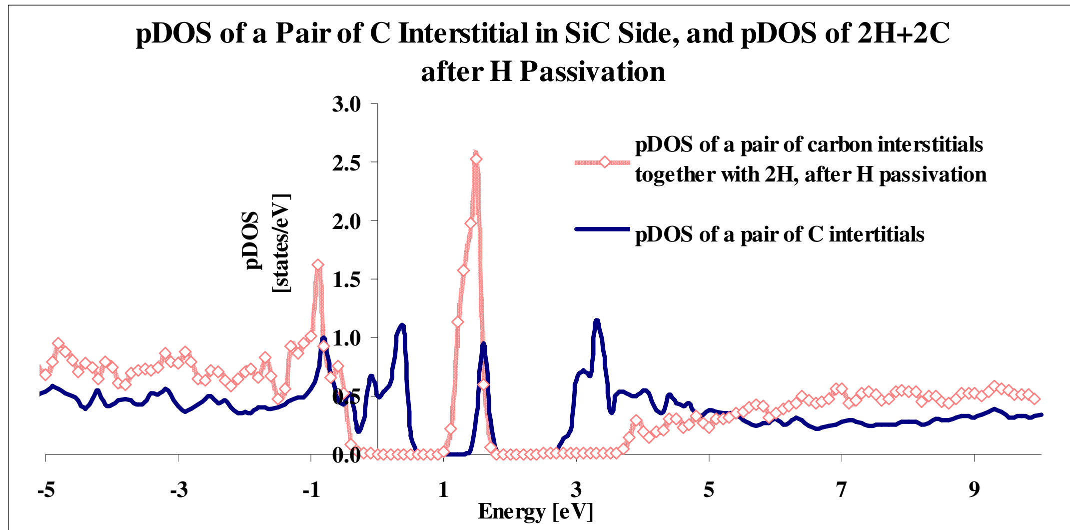

Figure 4.11: a) atomic structure of a pair of carbon atoms passivated by two hydrogen atoms; b) pDOS of a pair of carbons before (solid line), and after hydrogen passivation (dotted circle line).

In another attempt, the pair of carbon atoms is replaced by a pair of nitrogen atoms. As it is seen in figure 4.12 (dotted triangle line), this replacement eliminates those levels near the conduction, and valence bands, but has a sharp peak at 1.1eV.

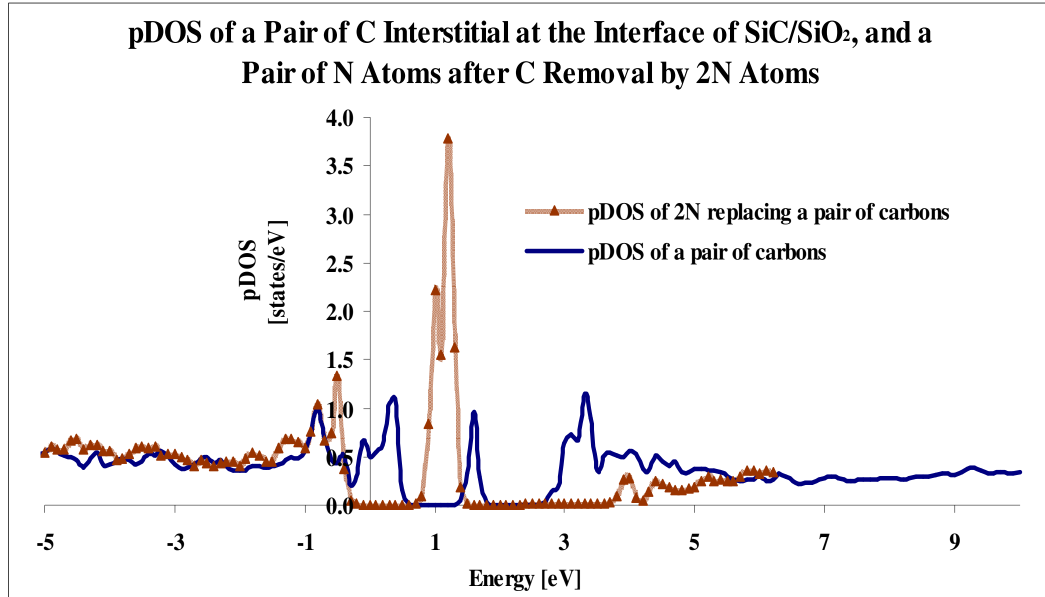

Figure 4.12: pDOS of a Pair of Carbon atoms (solid line) before, and after C removal by a pair of Nitrogen atoms (dotted triangle line).

4.6. Defect Level at SiC Side of the (0001)4H-SiC/SiO_2 Interface, and their Passivation

4.6.1. Carbon Excess in Oxide Side

In the case that some of the excess carbons remain in the oxide side of the interface, they may be either in the form of carbon interstitial or a pair of carbon atoms; therefore the effect of these two forms of carbon excess in oxide side of the interface have been studied via the pDOS.

Carbon interstitial in the oxide side makes no energy level in the band gap of the structure. Figure 4.13 shows the C interstitial levels located out of the SiC bandgap.

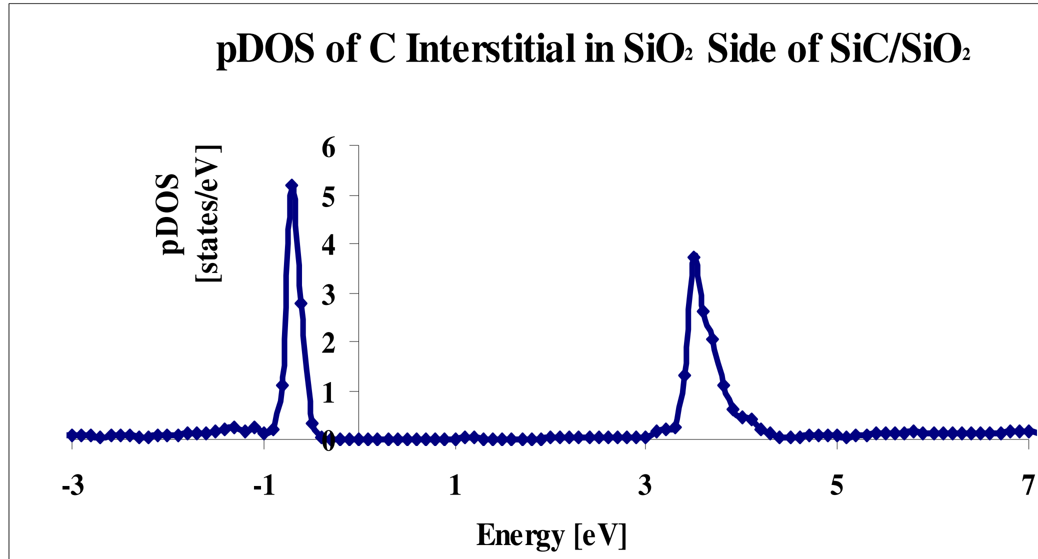

Figure 4.13: pDOS of carbon interstitial in oxide side of the structure.

A pair of carbon interstitials in the oxide makes a peak at E_v+0.4 eV.

4.6.2. Oxygen Deficiency at the Interface

Oxygen deficiency is one of the intrinsic defects in oxide that leads to the formation of Si-Si bonds. Si-Si bond is one of the notorious damaged bonds, which may result in transition layer formation [19].

To study the effect of this defect, we removed one of the oxygen atoms at the interface of (0001)4H-SiC/SiO_2 structure. After relaxation, a hybrid functional is used for further calculations. This type of defect leaves a Si atom with an unpaired electron perpendicular to the interface. Figure 4.14a) shows the atomic configuration of an O deficiency at the interface, and the resulting Si-Si bond. The solid line in Figure 4.14b) shows the contribution of all the Si atoms at the interface together with the one that is not connected to the O. As Figure 4.14b) shows, this defect makes an energy level near the conduction band, at E_v+2.8 eV. Based on this DFT calculation, O deficiency located deeper of the oxide does not introduce any levels in the band gap.

The N atom that is located at the vicinity of the damaged Si, binds with it after the relaxation process. As the result, the state caused by the O deficiency is eliminated from the bandgap. The dotted triangle line in Figure 4.14b) shows the DOS contributions of all the Si atoms at the surface after N passivation. N Passivation eliminated the O deficiency states.

a)

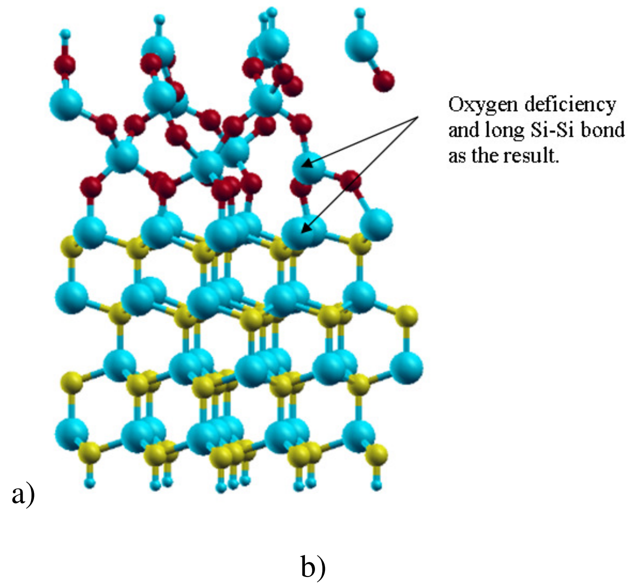

b)

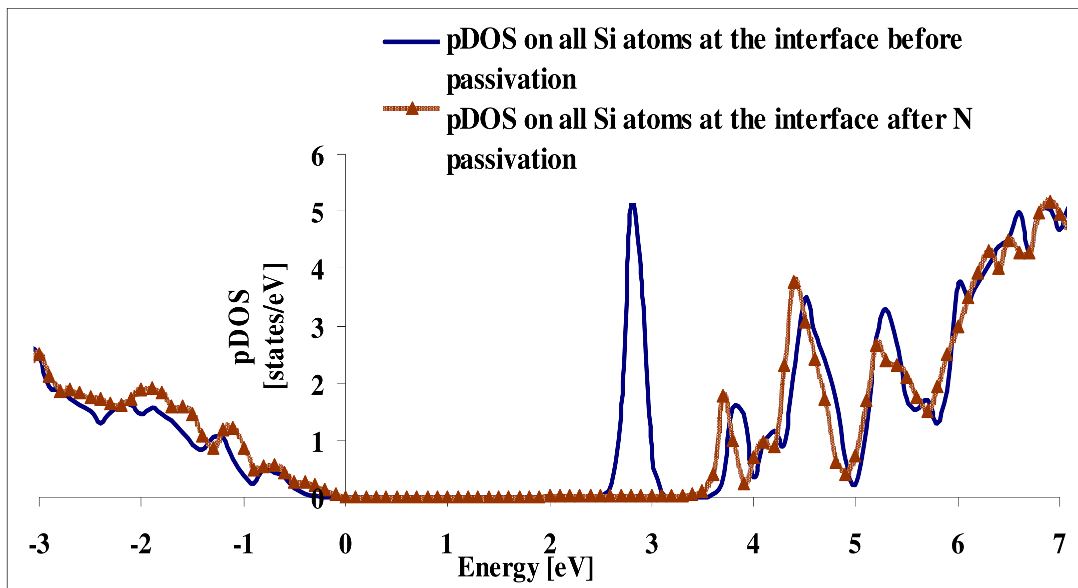

Figure 4.14: a) Atomic configuration of an O deficiency at the interface, and the resulting Si-Si bond; b) pDOS on all Si atoms with an oxygen deficiency at the interface (solid line), pDOS on all Si atoms after N passivation (dotted triangle line).

4.7. Silicon Dangling Bonds, and their Passivations

To investigate the effect of three-fold-coordinated Si at the interface, a new kind of SiC/SiO_2 structure with three Si dangling bonds perpendicular to the interface is formed. Some literature gave the evidence of detecting Si-H after H passivation, which may show the creation of Si dangling bonds in the process of oxidation, and annealing [28-121].

To find the energy levels of the silicon dangling bonds, we calculated the DOS contribution of all silicon at the surface of the structure. Figure 4.15 shows the pDOS versus energy for all silicon atoms on the surface of SiC with three dangling bonds. As is seen in this figure, three silicon dangling bonds make two sharp peaks at 2.4, and 2.9 eV.

Our calculations show that a large number of Si dangling bonds at and perpendicular to the interface make broad states close to the conduction band. The process of passivation is studied by locating the passivant atoms near those three-fold coordinated Si atoms: one passivant atom for each damaged bond. The studied passivants are H, N, and P. The average bond length of the Si-H after the relaxation is 1.4 A°, Si-N is 1.7 A°, and Si-P is 2.1 A°. In the case of nitrogen passivation, strong $Si \equiv N$ bonds as well as Si-N-O bridges are created, which passivate the interface traps reducing Nit.

In the case of H passivation, the Si-H bonds are not strong enough to push the states away from the gap into the conduction band (dotted circle line in Fig. 16), while N, and P passivate almost all those states. Figure 4.16 shows the total DOS of the structure with dangling bonds perpendicular to the surface (solid line), and the same structure after nitrogen (dotted triangle line), and phosphorus (dotted circle line) passivation.

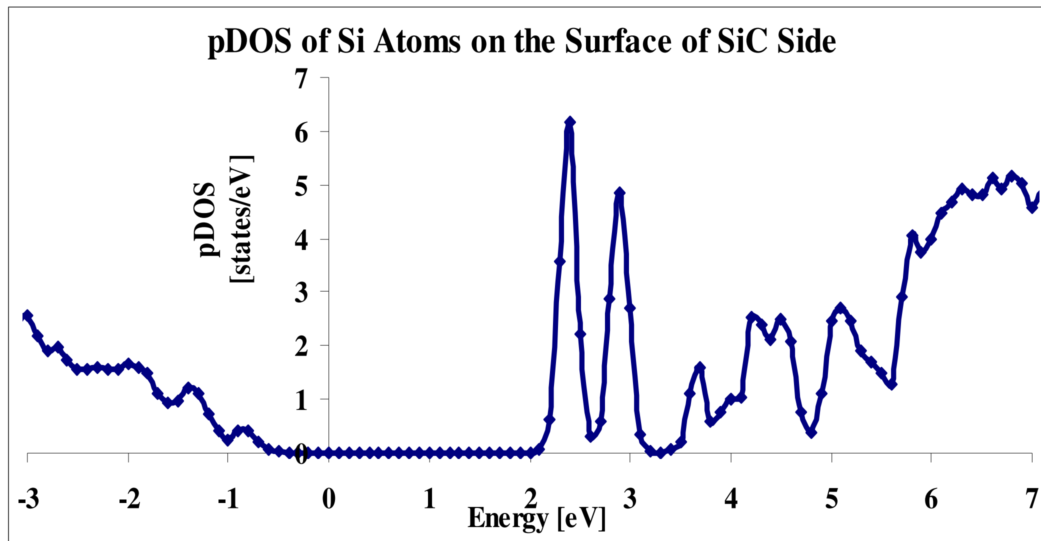

Figure 4.15: The contribution of all silicon atoms with three dangling bonds on the surface of SiC side of SiC/SiO_2.

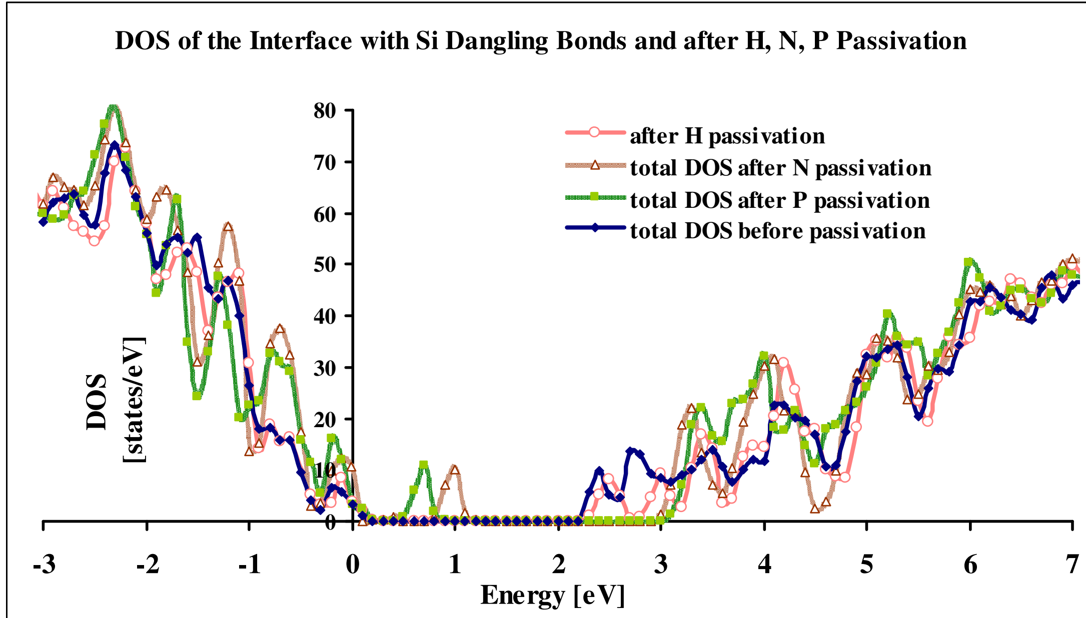

Figure 4.16: Total DOS of the structure with unpassivated three Si dangling bonds perpendicular to the interface (solid line), and after N Passivation (dotted triangle line), after P passivation (dotted circle line), and H passivation (open circle line).

Since arsenic has high conductivity, and it is used successfully for eliminating the surface roughness in some semiconductors materials [136, 137], it is used as a passivant for neutralizing the dangling bonds. Again the arsenic atoms are placed at the vicinity if the silicon with oxygen deficiency, and after full relaxation, they make bonds with them; the average bond length of Si-As is almost 2.3 A°. The total DOS after this type of passivation shows that arsenic could passivate the silicon dangling bonds, as well. Figure 4.17 shows the total DOS of the structure after arsenic passivation (the light color line). As is seen in figure 4.17, arsenic, like nitrogen and phosphorus eliminates the silicon dangling bond states near the conduction band.

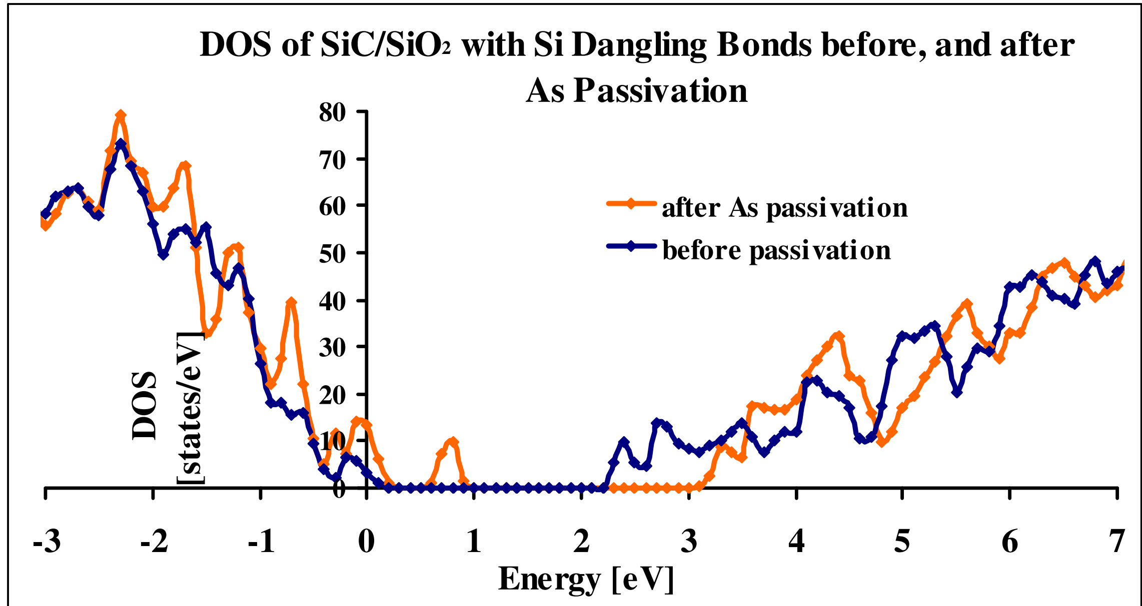

Figure 4.17: Total DOS of the structure with silicon dangling bonds (blue), and after arsenic passivation (orange).

To show the trend of density of interface states, Dit, reduction, the density of interface traps near the conduction band is calculated for the structures before and after hydrogen, nitrogen and phosphorus passivation, relative to one another. As can be seen in Figigure 4.18, the density of interface traps is reduced after nitrogen and even more after phosphorus passivation.

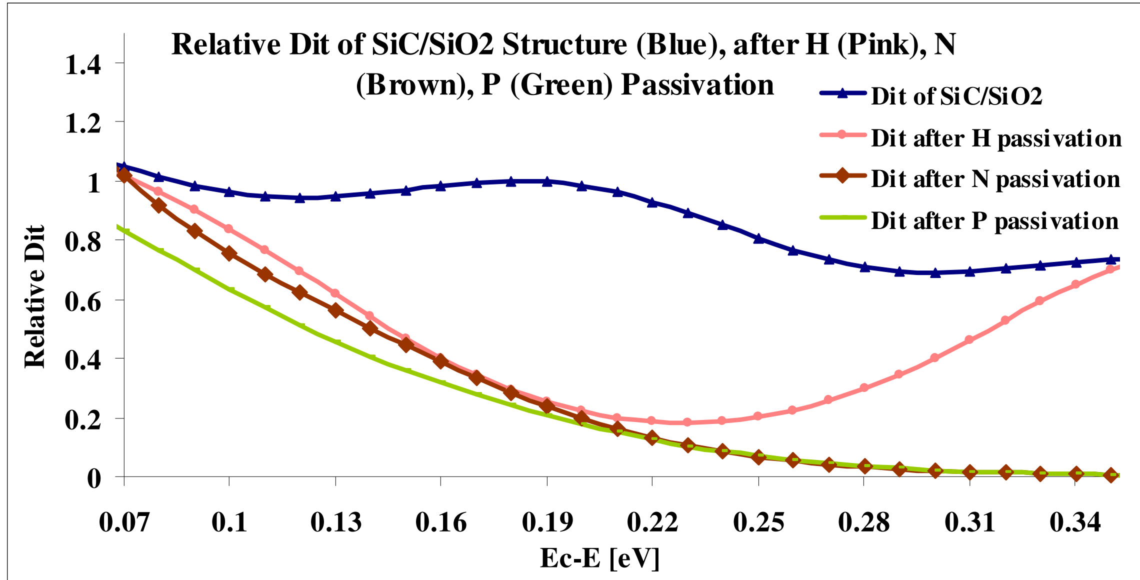

Figure 4.18: The relative Dit of the structures with three silicon dangling bonds (blue), and after nitrogen (brown), and phosphorous (green) passivation.

4.8. Conclusion and Discussion

The energy levels of various defects in both sides of the interface have been investigated by density functional theory. It is showed that projected density of states can be used to illustrate the energy of the defects, and the effect of the defect passivation.

According to the calculations, silicon vacancy in SiC side of the structure makes states near the valence band; besides each negative charge in this structure shifts the trap levels 0.2 to 0.3 eV toward the mid and conduction band. Since silicon vacancy introduces carbon dangling bonds, and almost all of the dangling bonds make states in the bandgap, the mechanism of passivation (either with 4H, or a N) is clear; the subsequent attachment of the passivant bond forms bonding and antibonding states, located in the valence, and conduction bands, respectively. None of them is electrically active, anymore.

Th calculations show that carbon interstitial, and a pair of carbons in SiC may introduce states in the bandgap, and near the conduction band, depending on their locations. A way of explaining the location of the states in the bandgap is by studying the orbital hybridization; The hybridization of the carbon atoms in a pair is sp^2, which results in one sigma, with the energy level in the valence band, and two pi orbitals, introducing states near the valence band, and in the midgap; their antibonding gives rise to the states just below the conduction band. One of the roles of passivations in this case may be the simple pairing, or passivating of unsatisfied bonds.

In some situations, the deep levels buried in the valence band may give rise to the energy in the bandgap; however, these are lattice levels which pushed into the gap. In these cases, the mechanism of the passivation is not clear. The passivant may either interacts with the lattice levels, or chemically reconstruct the bonds.

Moreover, the DFT calculation shows that, even upon full geometric relaxation, both carbon defects increase the stress of the structure, which may introduce states in the gap. DFT simulation shows that the removal of the carbon atoms releases the stress, which may explain the mechanism of nitrogen passivation.

On the other side, oxygen deficiency at the interface, and the silicon dangling bonds perpendicular to the interface make traps near the conduction band. The mechanism of dangling bond passivation is the same as that explained in the case of silicon vacancy.

In the case of both silicon vacancy, and oxygen deficiency, the structure compresses a little bit after nitrogen passivation, which may show the formation of bonding among the dangling bonds, and passivants.

In summary, if the energy barrier allows the passivation, both hydrogen and nitrogen may passivate almost all the defects by neutralization, pairing, reconstruction and passivation of the unsatisfied bonds, on one hand, and the removing of the stress (carbon removal by nitrogen), on the other hand.

In some cases, the passivation introduces some levels near the valence band or in the mid gap.

It should be mentioned that DFT calculation is very sensitive to the location of the defect. Moreover, the energy alignment is very critical to find the defect energy levels.

Chapter 5: DFT Prediction, and DFT-Based Carrier Transport Simulation of 4H-SiC(0001)/SiO_2 Interface

5.1. Introduction

The presence of a transition layer at SiC/SiO_2 interface may affect the electronic characteristics of SiC devices. Several experiments show the presence of C-O-Si bridges [52, 138, 139] at the interface. In this chapter, we investigated, and compared the effect of possible interface structures on the total, and projected density of states of SiC/SiO_2 system with the use of density functional theory (DFT). We also utilized Monte Carlo carrier transport technique [72] to obtain the average velocities, and mobilities of each structure. The ionized impurity limited mobility of the most likely structures has been calculated, too. In doing so, we made various structures with the forms of SiO_xC_y, and $Si_{1-x}C_xO_2$ in both SiC, and SiO_2 sides of the interface. According to our calculations, the possible candidate for making the traps near the conduction band is the SiO_xC_y structures formed by replacing carbon atoms in SiC with oxygen. The overall mobility, and the ionized impurity limited mobility decrease as the number of O(C) in SiC side of the SiO_xC_y structures increase. Moreover, the calculated ionized impurity limited mobility is less than 30 cm^2/V.s in low external field. Lastly, the nitridation of the damaged bridges of the most probable transition layer structure is investigated. According to our calculations, if nitrogen replaces the distorted bridges in SiO_xC_y structures formed by replacing carbon atoms in SiC with oxygen, a nitrogen-rich layer would form in the vicinity of the interface which improve the quality of the (0001)4H-SiC/SiO_2 Interface. We also show that nitrogen epi-layer form in the SiC

side of the structure can open the bandgap, which is in good agreement with the previous publications [140, 141].

Silicon carbide is a material of choice for high power high temperature applications due to its favorable intrinsic electrical properties such as high breakdown field, high thermal conductivity, low noise and wide bandgap. SiC also has the advantage of having a native oxide which is silicon dioxide. However, SiC-based electronic devices lack the latest mature fabrication methods developed for silicon devices, and thus exhibit current-voltage characteristics that are not within its full potentiality (high mobility and low channel resistance) [70, 73]. The main culprit that prevents SiC MOSFETs from reaching their full potential is the bandgap traps arising due to the silicon carbide-silicon dioxide interface, which results in low field effect mobilities (giving rise to low channel on-resistances) [68, 69].

Therefore, it is of utmost importance to understand the SiC/SiO_2 interface at the atomic level for finding passivation methods from one side, and investigating the effects of different structures on electron-phonon and Coulomb scattering limited mobilities in SiC power MOSFETs.

In this chapter, we focus on the transition layer which may form between SiC, and its native oxide SiO_2. We first provide the experimental evidences for the existences of such a region. Then we explain the Monte Carlo method that has been already developed to simulate the bulk mobilities [74].

We then find the most probable atomic structures, together with their probable ways of passivation with DFT-based simulation. Lastly, we obtain the electron-phonon limited bulk mobilities of the probable structures by Monte Carlo DFT-based

simulations. The effect of Coulomb scattering is investigated by studying the impact of high concentrations of ionized impurities on the calculated mobilities in low field.

5. 2. SiC/SiO_2 Transition Layer

During the oxidation process, a layer of SiO_2 is naturally grows on the surface of SiC. Although both Si/SiO_2 and SiC/SiO_2 systems share the same native oxide, their interfaces seems different. The advantage of Si-based electronic devices is primarily due to the properties of the Si/SiO_2 interface [142, 143]. While the interface of Si/SiO_2 is very abrupt and smooth with least inter-layers and a low density of point defects, there are both theoretical arguments and experimental evidences which show that the interface of SiC/SiO_2 is not abrupt [50- 53, 138, 144].

From the chemical point of view, the incomplete removal of carbon during the oxidation process may lead to formation of transition layer at the interface. The morphology and composition changes in the vicinity of SiC/SiO_2 interface also indicate the presence of a transition layer [144].

The initial stages that have been observed in SiC oxidation vary from study to study. Nevertheless, it is called silicon oxycarbide, in which the silicon atoms are bonded to oxygen and carbon atoms simultaneously.

The presence of a transition oxide layer at the interface could alter the electronic properties of a multilayer SiC-based electronic device. Electronic characterization of this layer is useful for making a robust device based on SiC.

5. 3. Experimental Evidences for, and Atomic Structure of the SiC/SiO_2 Transition Layer

Transition layer has been observed by different experiments [50- 53, 138, 144]. Several X-ray photoelectron spectroscopy (XPS) experiments provide the evidence of a transition layer at the interface of SiC, and the oxide [52, 138].

High resolution transmission electron microscopy (HRTEM) and electron energy loss spectroscopy (EELS) show a layer of several nm of partially amorphous material in SiC and SiO_2 [50].

HRTEM also shows a partial amorphization at the top surface of SiC, which expands both in SiC, and SiO_2 sides of the interface.

Moreover, spatially resolved electron energy loss spectroscopy (EELS) confirms the presence of a ternary Si-O-C phase in the vicinity of the interface [51].

Angle resolved x-ray photoelectron spectroscopy (ARXPS) measurement also reveals the formation of the SiO_xC_y species on the SiC surface, which leads to an oxide layer eventually [52].

X-ray photoelectron spectroscopy (ARXPS) showed the formation of the silicon oxycarbide layer by oxygen incorporation in the SiC substrate. According to these experiments, Si is bonded to a variable number of C and O atoms at the initial stages of oxidation.

Theoretically, there are several suggestions for generating the C-O-Si bridges, which are the backbone of the transition layer structure. Considering the SiC oxidation mechanism, C-O-Si bridges are either formed by substituting carbon in SiC with

oxygen, or/and oxygen in SiO_2 with carbon atoms [145]. In both cases a layer of SiO_xC_y is formed. Besides, a layer of $Si_{1-x}C_xO_2$ may be formed by replacing silicon atoms by carbon in the oxide side [146, 147].

If oxygen occupies a carbon site substitutionally in the SiC lattice, a complex $O(V_C)$ is formed, which has already been already detected by experiments such as extended energy-loss fine structure (EXELFS) and energy-loss near-edge structure (ELNES) [147].

We used the suggested structures, and made three types of silicon oxycarbide structures for further energy, and mobility calculations.

5.4. Introduction to Mobility Calculation

One of the interesting cases for investigating the mobility is the interface of SiC, and its native oxide. SiC MOSFET devices shows very poor channel mobility, very less than the low-field SiC bulk mobility, especially for 4H-SiC polytype. In fact, n-channel mobility in 4H-SiC MOSFET indicates a significant reduction of the free electron density at the interface. Large number of interface states near the conduction band is one of the reasons for low channel mobility [68-70]. The excessive number of trapped electrons near the conduction band edge of the SiC causes Coulomb scattering which reduces the mobility of the remaining electrons. This mechanism results in the drastic degradation of field-effect mobility.

The quality of the interface between semiconductor, and oxide determines the channel mobility of the MOSFET devices, which is one the most crucial parameters of the device. Therefore mobility calculation both experimentally and theoretically is essential.

The formula that shows the behavior of electron mobility in the low external field is defined by:

$$\vec{v}_d = \mu\vec{E} \qquad 5.1$$

where is the electron drift velocity, caused by the external field, $\vec{E}$. At low electric fields, the electron velocity increases linearly with the external field. Moreover, mobility is a function of both material impurities and temperature. Normally, at high fields, the mobility increases and reaches to a peak value, called the saturation velocity. On the other hand, the mobility is defined as:

$$\mu = \frac{q\tau}{m^*} \qquad 5.2$$

where m^* is the effective mass, q is the electron charge, and τ is the scattering time. In this sense, the mobility, μ, is determined by the various scattering processes that occur during carrier transport. Several scattering mechanisms affect the electron mobility.

The scattering mechanisms change not only the magnitude of drift velocity but also its direction. Several scattering mechanisms affect the electron mobility. The mechanisms are classified as defect, lattice, and carrier-carrier; while the defect scattering covers crystal defects, neutral and ionized impurities, and alloy, the lattice scattering is categorized as acoustic, and optical (polar, and non-polar).

Matthiessen's rule gives a good approximation for mobility calculation in the case that more than one scattering mechanism affects the electron motion. According to this rule, the electron mobility subjected to several scattering mechanisms can be found from:

$$\frac{1}{\mu} = \sum_i \frac{1}{\mu_i} \qquad 5.3$$

where m is the overall mobility, and μ_i is the mobility resulting from one special scattering mechanism.

It is the result of Matthiessen's rule that the overall mobility is dominated by the most severe scattering, which produces the smallest mobility. The bulk mobility of lightly doped semiconductors is thus limited by phonon scattering at room temperature.

The mobility of a MOSFET inversion channel is a combination of the bulk mobility, and the resulting mobilities from scattering processes happening mostly because of the defects at the oxide semiconductor interface and also from interface roughness.

Large number of defects at the semiconductor oxide interface can both scatter (and hence cause the degradation), and trap the electrons. The electrically active defects with the states near the conduction band may trap the electrons, as well. Therefore, the defects reduce both the mobility, and the number of electrons.

In the absence of any scattering mechanism, the mere electron wavefunction may enter the oxide layer, and cause further degradation.

5.4.1. Monte Carlo Bulk Transport Calculation in 4H-SiC

The electron transport in semiconductors is governed by the scattering events from any lattice imperfections such as impurities, and lattice vibrations. In a semiclassical approach the electrons are treated as the localized wavepackets, drifting in an external filed according to the Newton's equation:

$$\hbar\frac{d\vec{k}}{dt} = \vec{F} = eE(\vec{r}) = \frac{d\vec{p}}{dt} \qquad 5.4$$

$$\vec{v} = \frac{1}{\hbar}\nabla_k \varepsilon(\vec{k}) \qquad 5.5$$

where $\vec{p}$ is the electron momentum, t is the time, $\vec{k}$ is the electron wave vector, $\vec{F}$ is the force on electron, e is the electron charge, $\vec{E}$ is the electric field, $\vec{r}$ is the position in real space, $\vec{v}$ is the electron velocity, and ε is the electron energy. In the absence of potential energy, the electron is free, and if m is considered to be the electron mass, then:

$$\nabla_k \varepsilon(\vec{k}) = \frac{\vec{k}\hbar^2}{m} = \frac{\vec{p}\hbar}{m} \qquad 5.6$$

In the semiconductor lattice, the energy as a function of wave vector, or the band structure, determines the $\nabla_k \varepsilon(\vec{k})$ term of the above equation.

On the other hand, the three-dimensional DOS expression can be given by:

$$k^2 \frac{d\vec{k}}{dE} = DOS(E) \qquad 5.7$$

Then, an expression for energy versus average momentum is derived by multiplying both sides of the above equation by dE, and integrating the left, and right hand sides over the momentum, and energy, respectively. This results an average momentum for a given energy, which its momentum is proportional to the integral of the DOS curve from the conduction band minimum to that energy [4]:

$$\langle k \rangle = (\left| 3\times \int_{E_{\min}}^{E} DOS(E)dE \right|)^{1/3} \qquad 5.8$$

Any imperfections in the lattice such as phonons, and impurities, on the other hand, are seen as the small perturbations of the semiconductor periodic lattice. The

electrons are scattered by the imperfections, instantaneously, and according to the quantum mechanical rules. The scattering changes the momentum and energy of electrons in a random way. The random nature of the scattering phenomena needs to be solved stochastically. The stochastic motion of the electrons subjected to the scattering, and collisions are simulated via Monte Carlo, using the random numbers.

Basically, the Monte Carlo algorithm produces random free flight times for each particle, choosing the type of scattering occurring at the end of the free flight, changing the final energy and momentum of the particle after scattering, and then repeating the procedure for the next free flight. By sampling the particle motion at various times throughout the simulation, the simulator calculates the physical quantities such as the average drift velocity in the presence of an applied electric field [148].

5.4.2. Scattering Mechanisms

In the confrontation between an electron, defects, impurities, and lattice vibrations in the semiconductor, the electron wave scatters, and the center of its wave packet shifts from k to k'. The scattering probability rate $P(k,k')$ is obtained from Fermi's Golden rule. Fermi's Golden rule for and elastic interaction is given by:

$$P(k,k') = \frac{2\pi}{\hbar} \left| H_{k'k} \right|^2 \delta(E(\vec{k}') - E(\vec{k})) \tag{5.9}$$

where $\left| H_{k'k} \right|^2$ is the square of scattering matrix element of the scattering potential between the initial, and final wave vectors; the Dirac function ensures that the energy is conserved in the interaction. The scattering matrix element can be calculated from the scattering potential U_s :

$$H_{k'k} = \frac{1}{\Omega}\int d^3\vec{r}\exp(-i\vec{q}.\vec{r})U_S(\vec{r}) \quad 5.10$$

where $\vec{q} = \vec{k}' - \vec{k}$, and Ω is the unit volume. By finding the perturbation potential of each scattering mechanism, the matrix element can be found.

The scattering rate, the rate at which electrons with a specific momentum p_0 scatters to any other states, calculated by summing the scattering probability rate over all possible final states:

$$\Gamma(\vec{k}) = \sum_{k'} P(k,k'). \quad 5.11$$

For an electron with energy ε, the scattering rates Γ are given by:

$$\Gamma(\varepsilon) = \Lambda(\varepsilon)DOS(\varepsilon \pm E_q) \quad 5.12$$

where DOS is the density of states, Λ is the proportionality factor between the rate and the density of states and depends on the type of scattering involved. The energy transfer E_q depends on the scattering mechanism.

Since the semiconductor band structure is determined by the crystal potential, it is influenced by the changes in lattice spacing. For the small changes in lattice constant, the deformation potential approximation is used to calculate electron-phonon scattering. The deformation potential can be deduced from the experiments, and are tabulated for various semiconductors. The scattering rates of acoustic phonon emissions and absorptions, optical phonon absorptions, optical phonon emissions, polar optical phonon absorptions, polar optical and phonon emissions, which are considered in the Monte Carlo mobility calculation, are given as:

$$\Gamma_{acoustic}(E) = \frac{D_{acoustic}^2 k_B T}{\rho\hbar v_s^2 \pi} DOS(E) \quad 5.13$$

$$\Gamma_{optical}^{absorption}(E)=\frac{D_{optical}^{2}\hbar}{2\rho E_{optical}\pi}N(E_{optical})DOS(E+E_{optical}) \quad 5.14$$

$$\Gamma_{optical}^{emission}(E)=\sqrt{\frac{qD_{optical}^{2}}{\rho\pi}[N(E_{optical})+1]DOS(E-E_{optical})} \quad 5.15$$

$$\Gamma_{polar-phonon}^{absorption}(E)=\frac{D_{polar-phonon}q^{2}}{2\hbar k^{2}\pi}(\frac{\varepsilon_{lf}-\varepsilon_{hf}}{\varepsilon_{lf}\varepsilon_{hf}})\log(\beta_{a}+\sqrt{1+\beta_{a}{}^{2}})N(E_{polar-phonon})\cdot DOS(E+E_{polar-phonon}) \quad 5.16$$

$$\Gamma_{polar-phonon}^{emmision}(E)=\frac{E_{polar-phonon}q^{2}}{2\hbar k^{2}\pi}(\frac{\varepsilon_{lf}-\varepsilon_{hf}}{\varepsilon_{lf}\varepsilon_{hf}})\log(\beta_{e}+\sqrt{1+\beta_{e}{}^{2}})N(E_{polar-phonon}+1).\ DOS(E-E_{polar-phonon}) \quad 5.17$$

here, $N(E)$ is the Bose-Einstein phonon occupying number, and is given by:

$$N(E)=1/[\exp(E/k_{B}T)-1], \quad 5.18$$

and $\beta_{a}=\sqrt{\frac{E}{E_{polar-phonon}}}$, 5.19

$$\beta_{e}=\sqrt{\frac{E}{E_{polar-phonon}}-1}, \quad 5.20$$

$$\gamma=4L_{D}^{2}k^{2}, \quad 5.21$$

where L_{D} is the Debye length and is given as:

$$L_{D}=\sqrt{\frac{\varepsilon_{lf}k_{B}T}{q^{2}N_{D}}}, \quad 5.22$$

The Brooks-Herring model is used to simulate the ionized impurity scattering; this model uses the Coulomb potential to model the impurity, and includes the impact of screening from the charges around it [149]:

$$\Gamma_{impurity}(E) = \frac{N_{impurity} q^3}{16\hbar k^4 \varepsilon_{lf}^2 \pi} (\frac{\gamma^2}{1+\gamma^2}) DOS(E) \qquad 5.23$$

The starting point of the program is the definition of the physical system including the parameters of the material and the values of physical quantities. The 4H-SiC parameters are given in table I [74].

5.4.3. Monte Carlo Calculation Methodology for Bulk 4H-SiC

By using the deformation potential approximation, Fermi's golden rule in the semiclassical rules governing to field, and electron interaction, the average velocity, and hence the mobility versus field for each structure are obtained.

DFT is used to obtain the electron dispersion relations, and the DOS curves calculated for the conduction bands. These DOS curves are extracted from DFT-based calculations up to 10 eV above the conduction band.

In this calculation, we employ the code, and algorithm that developed by Akturk et al.[74] for 4H-SiC mobility calculation.

Figure 5.1 shows the conduction band DOS as a function of energy, away from the conduction band minimum for 4H-SiC.

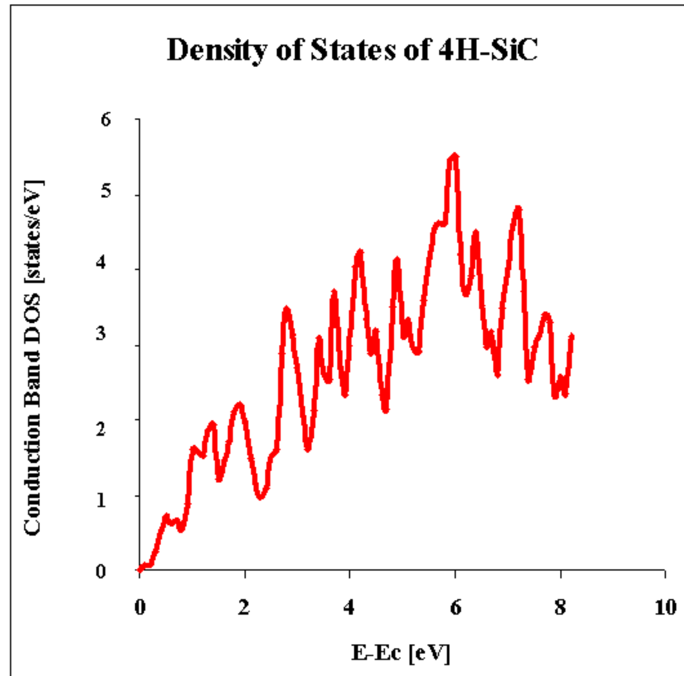

Figure 5.1: Conduction band DOS as a function of energy away from the conduction band minimum.

First, the simulator is used for finding the average velocity versus applied field curve for 4H-SiC, which is shown in figure 5.2. The average velocity is 7×10^6 cm/s at 10 kV/cm; it increases with the applied field, and reaches a peak value of approximately 2×10^7 cm/s at 2×10^5 V/cm, and it then decreases. The results agree reasonably with the other published Monte Carlo results [74, 150, 151], and the experimental data [152].

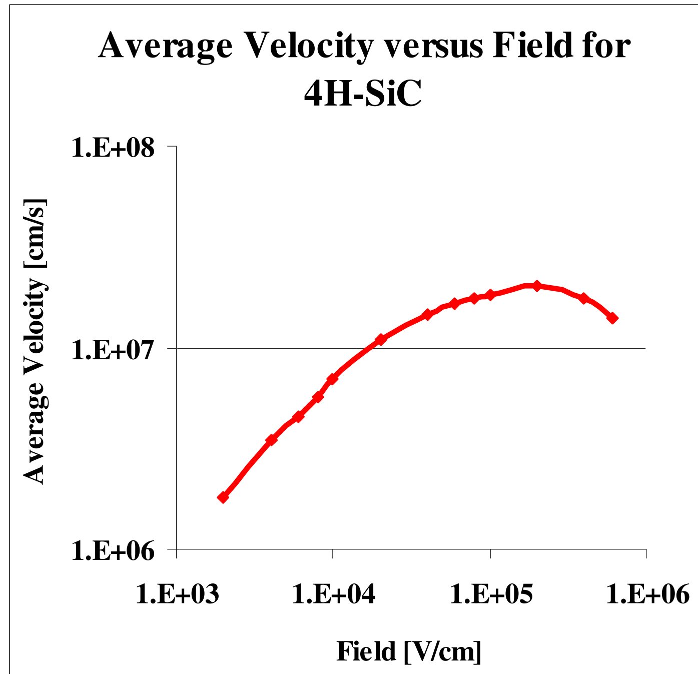

Figure 5.4: Average velocity versus field for 4H-SiC.

Figure 5.3 shows the mobility versus field for 4H-SiC. As it is seen, the mobility reaches 700 cm^2/V.s at 10 kV/cm, and drops with the decreasing field.

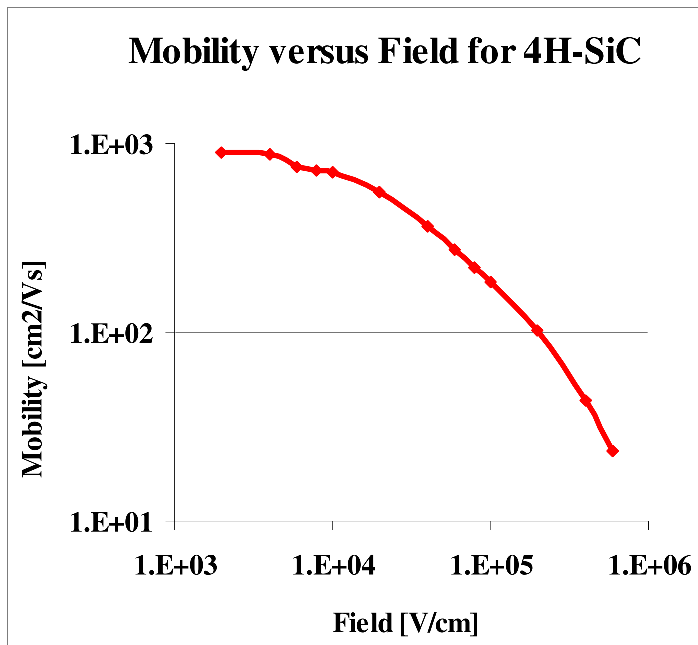

Figure 5.3: Mobility versus field for 4H-SiC.

Table 5.1: 4H-SiC electron-phonon coupling parameters [74].

4H-SiC	Electron
Density, $\rho(g/m^3)$	3.2
$D_{acoustic}$, acoustic deformation potential (eV)	19
$v[m/s]$, sound velocity	1.37×10^4
$E_{optical}[meV]$ optical phonon energy	85
$D_{optical}[eV/m]$ optical deformation potential	1×10^{11}
$E_{polar-optic}[meV]$ polar optic phonon energy	120
$D_{polar-optic}[eV/m]$ polar optical deformation potential	1×10^{11}
$\varepsilon_{lf}[\times\varepsilon_0]$ low frequency dielectric constant	9.7
$\varepsilon_{hf}[\times\varepsilon_0]$ high frequency dielectric constant	6.5
$\alpha[1/s]$ ionization constant	2×10^{14}
β ionization exponent	4
E_{th} first ionization threshold [eV]	3.23

5. 5. Density Functional Theory Methodology

Figure 4 shows the step-by step algorithm of the transition layer energy calculation, and passivation simulation by density functional theory. As is seen in this flowchart, in order to investigate the result of the silicon oxycarbide (C-O-Si) on the density of states, several changes have been made in the original abrupt supercell, explained in chapter 2. The bridges are made to form both SiO_xC_y, and $Si1_{-x}C_xO_2$ phases in both

sides of the interface. After geometric relaxation, the energy of each system is calculated, and their band structures, total, and projected density of states are obtained. Hybrid functional is used to overcome the bandgap problem, and provides the accurate effect of damaged bridges in the bandgap. The band structures and total and projected densities of states are then modified accordingly.

The comparison of the results with those of the abrupt structure shows the effect of each structure on the electronic structure. For the purpose of passivation, each problematic atom in the bridge is getting replaced by a nitrogen atom. Again, after the geometric relaxation, the band structure, and density of states are again calculated, and modified by both PBE, and hybrid functional.

To investigate nitrogen passivation, the damaged bridges that introduce levels near the conduction band are passivated by nitrogen atoms in each transition structure. The resulted structures based on Si-N-O bridges are the backbone of silicon oxynitride. Figure 5.4 shows the algorithm of transition layer generation, and passivation.

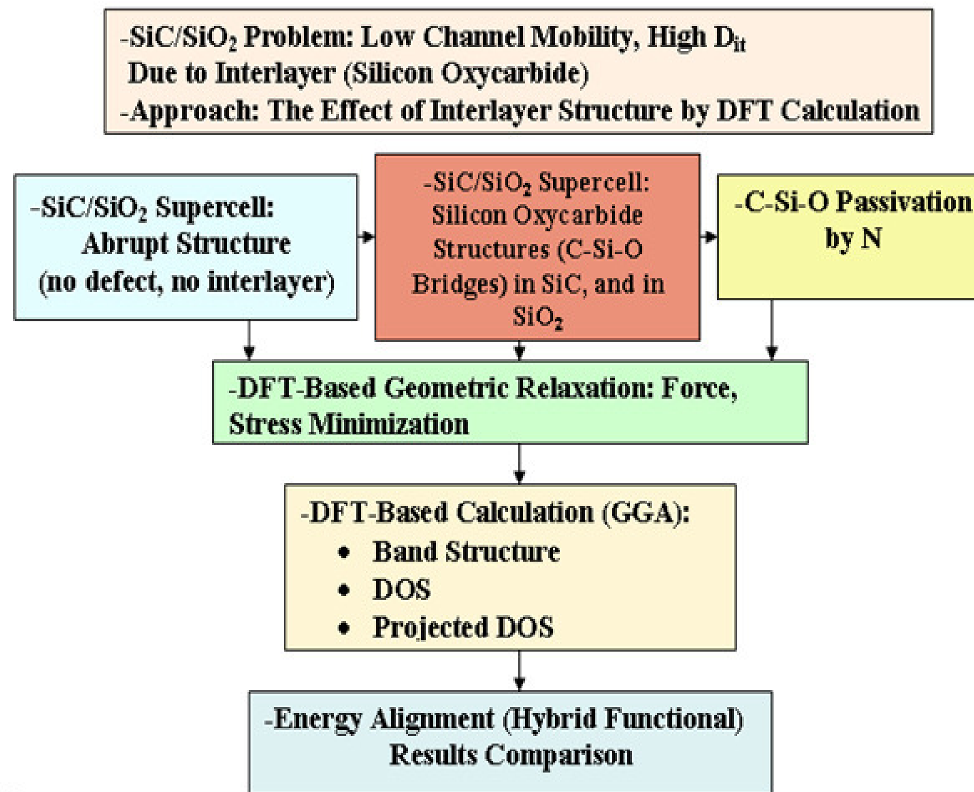

Figure 5.4: Algorithm of electronic calculation of transition layers, and the related passivations.

5. 6. DFT and DFT-Based Monte Carlo Calculations for Transition Layer

5. 6.1. $Si_{1-x}C_xO_2$ Structures in SiO_2

To construct the C-O-Si bridges, and hence the most likely interfaces, we first replaced silicon atoms in the oxide side by carbon atoms with different concentrations (x=1/3, and x=1/2) to form $Si_{1-x}C_xO_2$ layer. The band structure and total DOS are calculated by DFT simulator, and then compared with the abrupt structure. According to our calculations, these substitutions do not introduce levels in the bandgap. The same substitution in pure a-quartz gives the same outcome. Therefore we rule out the

$Si_{1-x}C_xO_2$ structure as the potential transition layer which may increase the near interface states.

5. 6.2. SiO_xC_y Structures in SiO_2

In the next step, the oxygen atoms in SiO_2 are substituted by carbon atoms with several concentrations to make the SiO_xC_y structures in the oxide side. To investigate the impact of these substitutions, we compared the total and projected density of states (pDOS) of C-Si-C bridges in the abrupt structure with the substituted C-Si-C(O) (C1-Si2-C3 bridge in figure 5.5a) ones in SiO_xC_y structures formed in the oxide side. Figure 5.5a) shows the atomic configuration of this structure with carbon substituting oxygen.

Figure 5b) shows this comparison for the distorted bridge in SiO_xC_y structure, with one oxygen atom substituted by one carbon atom. As it is seen, the distorted bridge (C1-Si2-C3 bridge in figure 5.5a) (dotted circle line) introduces states near the valence band, at E_v+0.6eV. The levels may be attributed to the extra electrons that carbon atoms bring to the system, as the result of more valence electrons in its shell. It should be noted that the pDOS of the chain represents by Si2-C3-Si4 in figure 5.5a) shows the same trend.

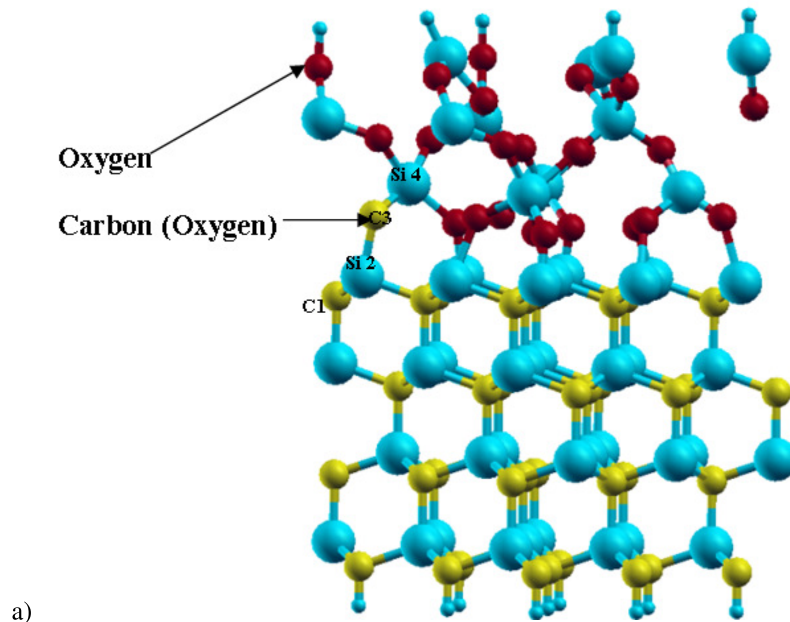

a)

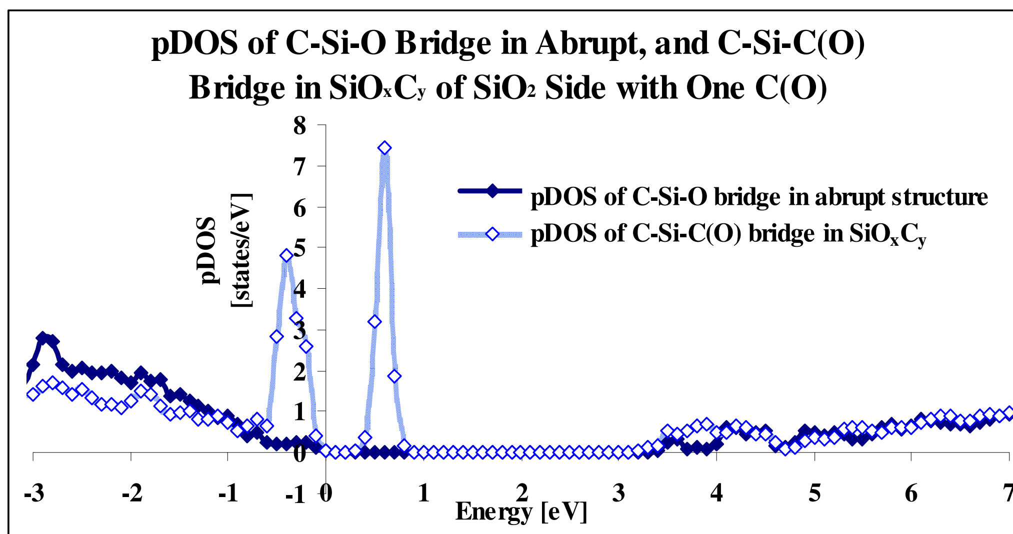

b)

Figure 5.5: b) Comparison between the pDOS of C-Si-O_C SiO_xC_y formed in SiO_2 with one C atom replacing oxygen in the oxide side of the interface with and C-Si-C of the abrupt structure. We represent carbon substituted for or replacing oxygen as C(O).

In figure 5.6b, we show the resulting pDOS obtained after substituting three oxygen atoms with 3 carbon atoms. In Figure 5.6a, we show the atomic structure used for the triple substitution. Although, these replacements make levels in midgap, they increase the number of states at energy levels that are within then conduction bands as

well. (Comment on notation: In the figure, we represent carbon substituted for or replacing oxygen as C(O)).

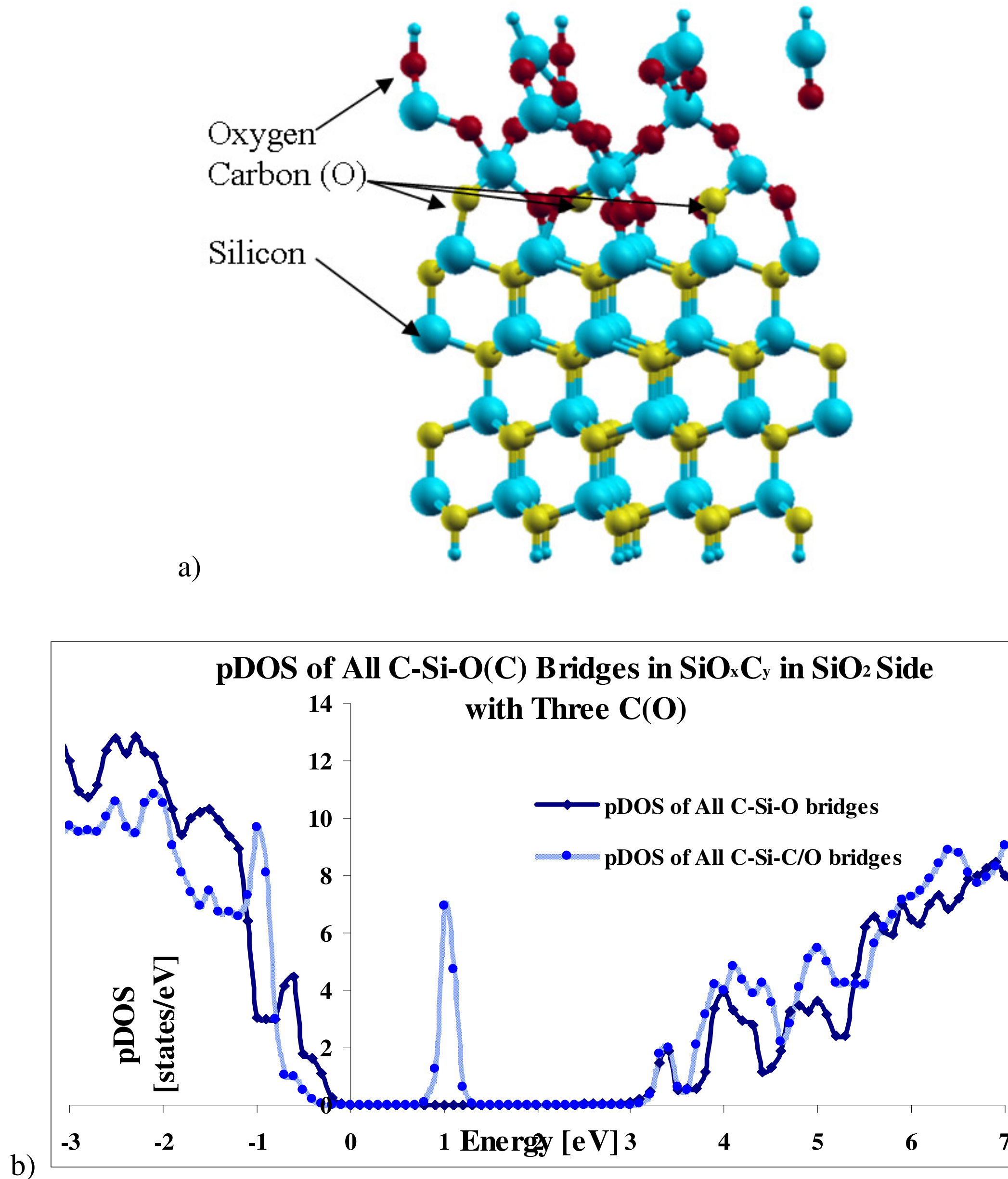

Figure 5.6: a) Super cell used in DFT calculations for SiO_xC_y structures with three C (O) in oxide side; b) Comparison between all the C-Si-C(O) bridges in SiO_xC_y formed in the oxide side with three C(O) and all C-Si-C bridges in the abrupt structure.

5. 6.2.1. Monte Carlo Mobility Calculations for SiO_xC_y Structures in SiO_2

We then simulated the average velocity and mobility of each of those SiO_xC_y structures, made in the oxide side, as a function of external electric field using Monte Carlo simulation. There are two inputs to the MC simulator. The first is the volume of the unit/super cell to calculate DOS per volume, and the second is the DFT-DOS curve or values starting from the conduction band edge of a given structure. The calculated electron mobilities are compared with those of bulk SiC. Figure 5.7 shows the mobility versus field for SiO_xC_y structures with one, three, and six C atoms substituted O atoms. The mobility at at the electric value of 10000 V/cm f has values of 700 cm^2/s for bulk SiC, 214 cm^2/Vs for one C(O), and to 200 cm^2/Vs, and 150 cm^2/Vs for three, and five C(O), respectively. The decrease in mobility may be the result of excessive states in conduction band.

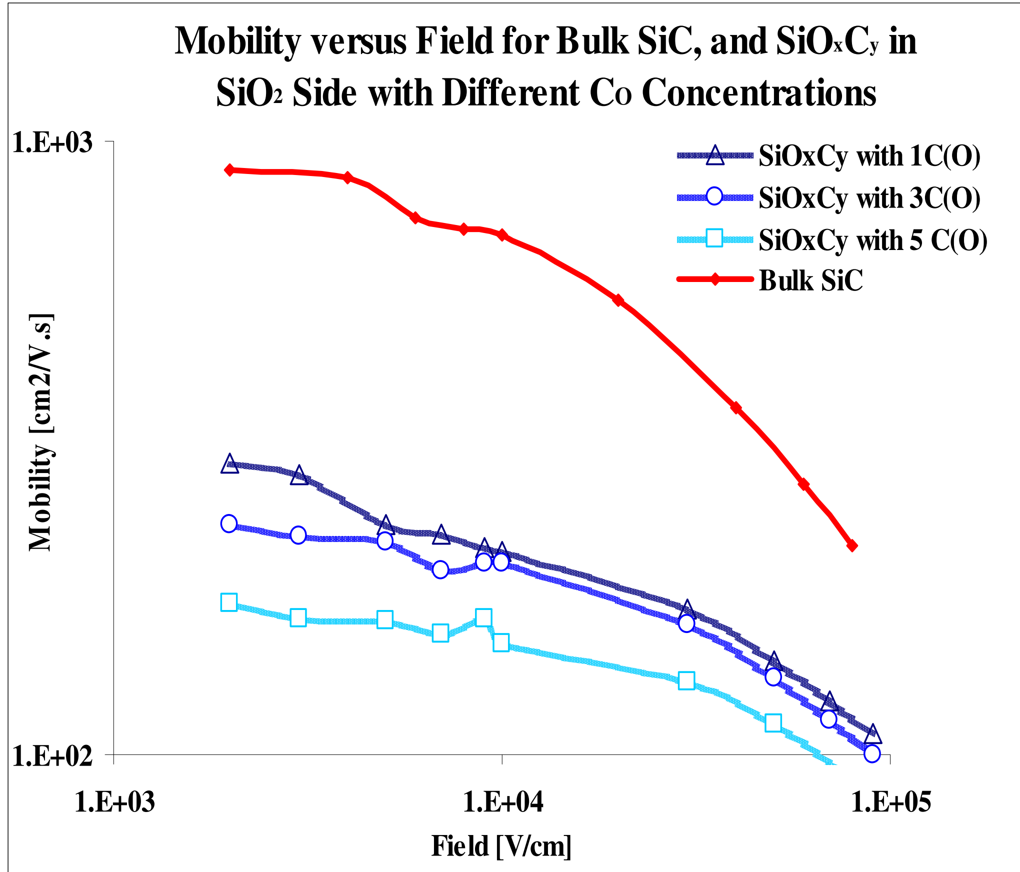

Figure 5.7: Electron-phonon limited bulk mobility for bulk SiC, and SiO_xC_y structures with various concentrations of C_O in the oxide side.

5. 6.3. SiO_xC_y Structures in SiC

Then, structures are formed by substituting the carbon atoms with oxygen atoms to make the SiO_xC_y in SiC side of the interface with different concentrations. This substitution is one of the potential mechanisms behind SiC oxidation [153]. According to our DFT calculation, an O atom replacing a C atom makes an O-V_C (carbon-vacancy) complex, which pushes the neighboring Si atoms away from O. This kind of substitution in SiC leads to formation of a thin oxygen contaminated Si-rich interface layer which needs a very small structural reconstruction to form SiO_2. Since the formation energy of the C vacancy is less than Si vacancy [158], and the Si-C bonds

are smaller than the Si-Si bonds in Si crystals, the C vacancy is the likely to be the preferred host for an O atom. Furthermore, several experiments indicated the evidence of oxide formation over this type of SiO_xC_y structure [52, 53, 147].

The comparison between C-Si-C bridges in abrupt and C-Si-O(C) bridges in SiO_xC_y structures shows that substitution of carbon with oxygen in SiC makes levels near the conduction band. We believe that the conduction band tail of this layer appears in the upper part of the SiC gap as a near-interface state density. Figures 5.8-5.9 show the contribution of C-Si-C, and O-Si-C bridges in abrupt, and SiO_xC_y structures with one, and three O(C) atoms.

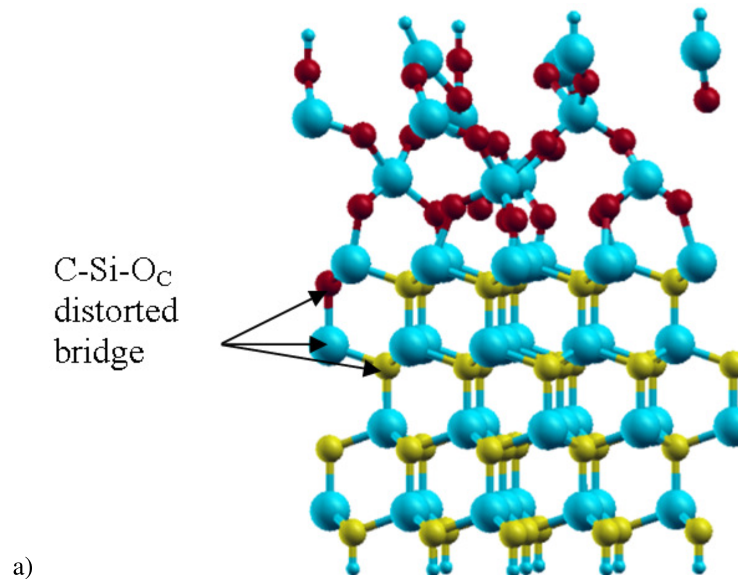

a)

b)

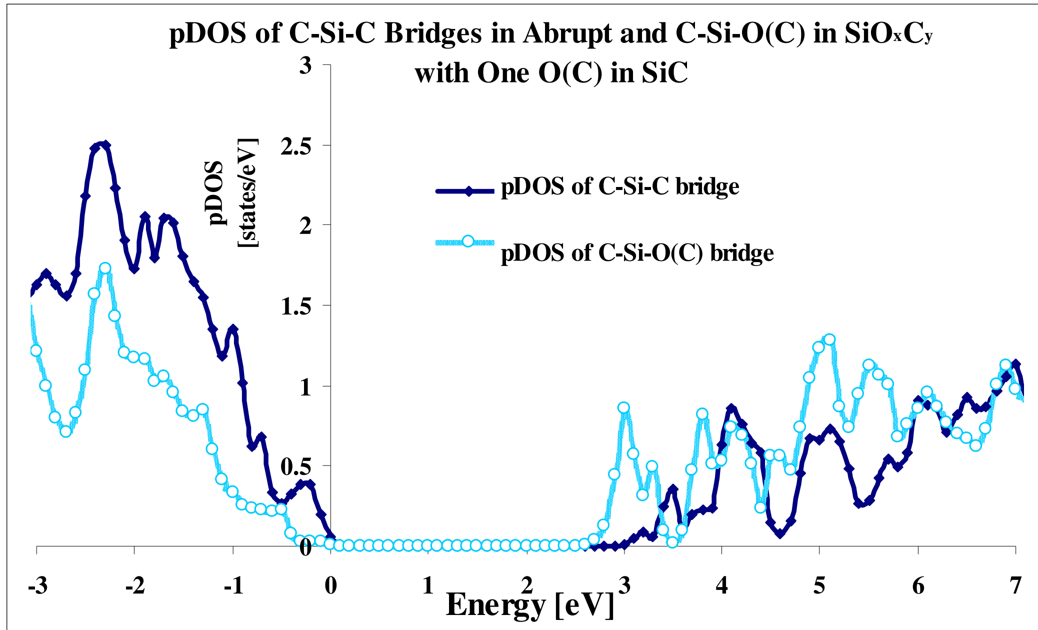

Figure 5.8: a) Super cell used in DFT calculations for SiO_xC_y structure with one O_C substitution; b) Comparison between pDOS of C-Si-C, and O-Si-C bridges in abrupt, and SiO_xC_y structure with one O_C in SiC side.

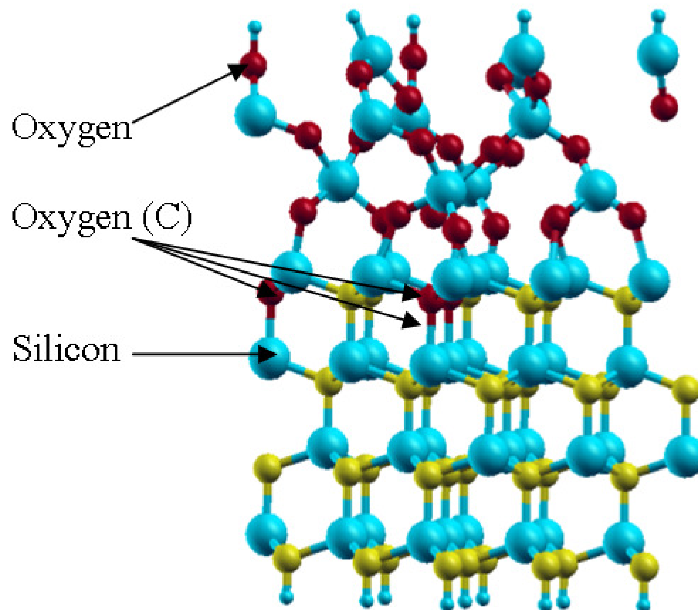

a)

b) 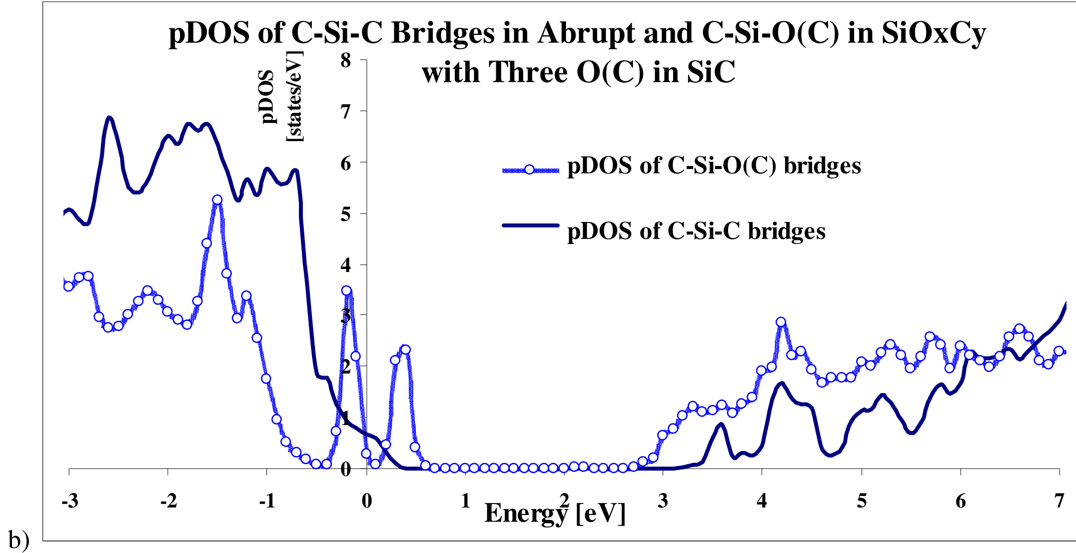

Figure 5.9: a) Super cell used in DFT calculations for SiO_xC_y structure with three O(C) substitutions; Comparison between pDOS of all C-Si-C bridges in abrupt and O-Si-C bridges in a SiO_xC_y structure with three O(C) in SiC side.

5. 6.3.1. Monte Carlo Mobility Calculation for SiO_xC_y Structures in SiC

To investigate nitrogen passivation on SiO_xC_y transition layer, formed in SiC, the damaged bridges are passivated by nitrogen atoms. In doing so, the C-Si-O(C) bridges are formed by replacing the damaged atoms in Si-O-C (silicon oxycarbide) chains by nitrogen. The resulted structures based on Si-N-O bridges are the backbone of silicon oxynitride. Then the electronic properties of two configurations are compared to find the most probable passivation of the transition layers.

We used the Monte Carlo simulator to investigate the effect of SiO_xC_y structures in the SiC side on the mobility. As it is seen in figure 5.10, the mobility at 10,000 V/cm field drops from 700 cm^2/V.s for bulk SiC to 338 cm^2/Vs for two O(C), and to 280 cm^2/Vs, and 186, and 143 cm^2/V.s for three, six, and nine O(C), respectively. Again, the mobility drop may be attributed to the more states in that can contribute to scattering conduction band electrons.

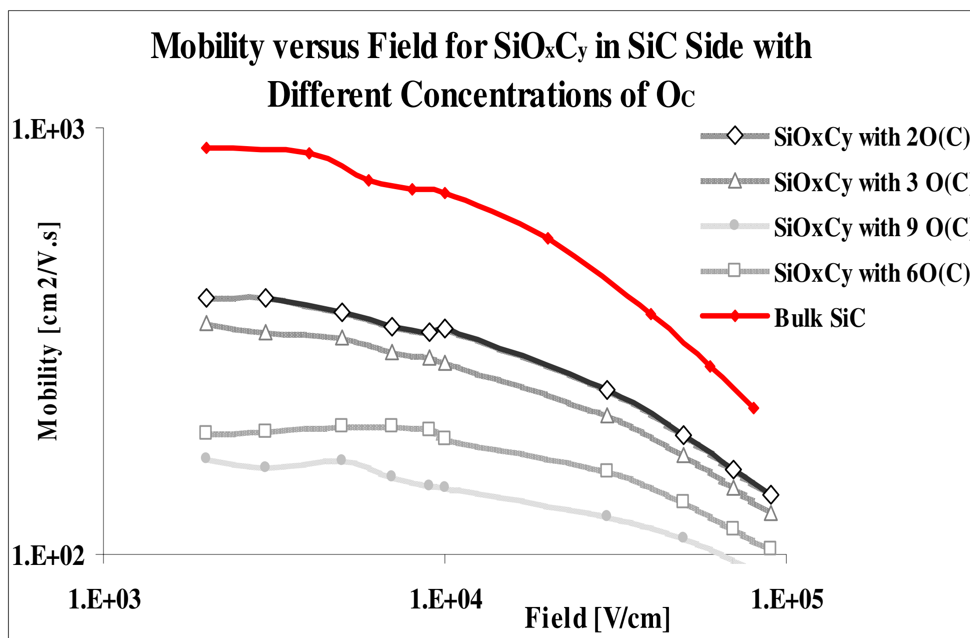

Figure 5.10: Electron-phonon limited bulk mobility for bulk SiC, and SiO_xC_y structures with several concentrations of O(C) in SiC.

In modern SiC MOSFETs, the peak field effect mobilities (generally measured in the linear region, using drain current versus drain voltage curves when gate-to-source voltage is roughly equal to V_{th}) are usually less than 50 cm^2/Vs. This is thought to be due to Coulomb scattering from trapped interface charges [51, 53]. To examine the effects of different amounts of interface traps on the transport calculations, we calculated the low field mobility as a function of different levels of ionized impurity concentration. The results plotted in Figure 5.11 shows mobilities are in lower double digits as ionized impurity concentration approaches 10^{20} cm^{-3}. Assuming a transition region thickness of 1nm, the above-mentioned ionized impurity concentration can be translated into an aerial concentration of 10^{13} cm^{-2}, which is consistent with total acceptor type trap levels measured for SiC/SiO_2 interfaces [156, 157]. The mobility

drops from 28 cm^2/Vs for the SiO_xC_y structure with two O(C) to 25 cm^2/Vs, and 10 cm^2/Vs for three O(C), and six O(C), respectively.

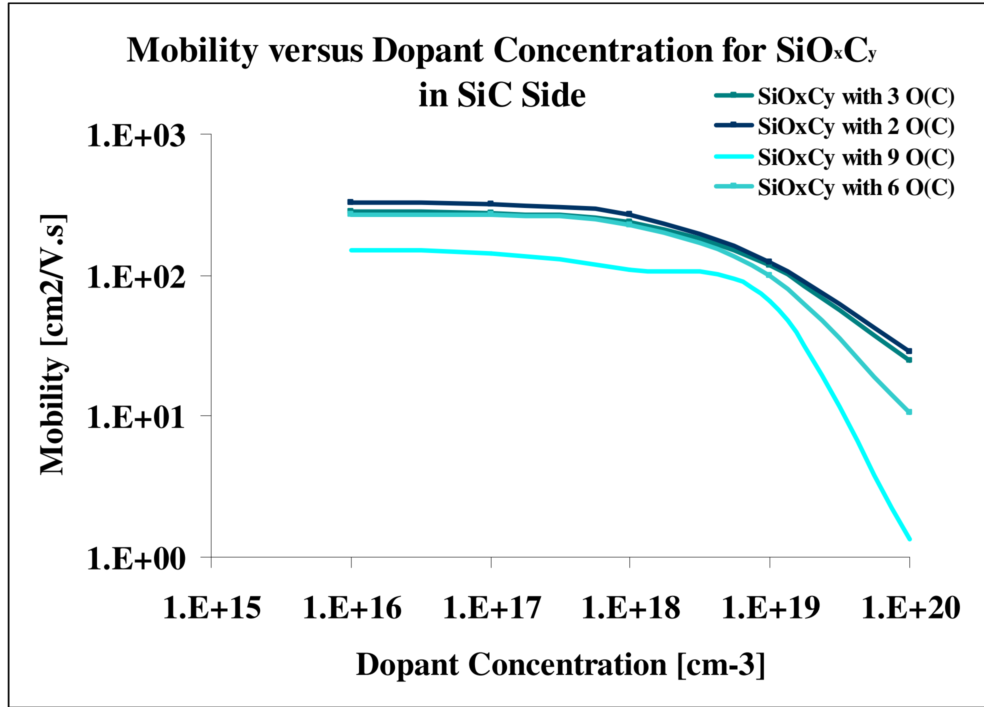

Figure 5.11: Electron-phonon and ionized impurity limited mobility as a function of ionized impurity for SiO_xC_y structures with various concentrations of O(C) in SiC side.

5. 6.3.2. Passivation of SiO_xC_y Structures in SiC

To investigate the impact of nitrogen passivation on SiO_xC_y transition layer, formed in SiC, the damaged bridges are passivated by nitrogen atoms.

As mentioned earlier, this type of oxygen substitution gives rise to states near the conduction band edge. To do the appropriate passivation, the back bone of the damaged bridge(s), which is the oxygen atom, is substituted by a nitrogen atom. Therefore, the C-Si-O(C) damaged bridge is replaced by C-Si-N(O). After this replacement, the geometric relaxation is done for each structure, and then the energy calculation is carried on, and (p)DOS is calculated. Figure 12 shows the contribution

of DOS of one distorted bridge before, and after passivation, in this figure, the dotted circle line is the pDOS of C-Si-N(O), and the solid line shows that of C-Si-O(C). As figure 5.12 shows, passivation eliminated the states near the conduction band, which are caused by C-Si-O(C) bridge.

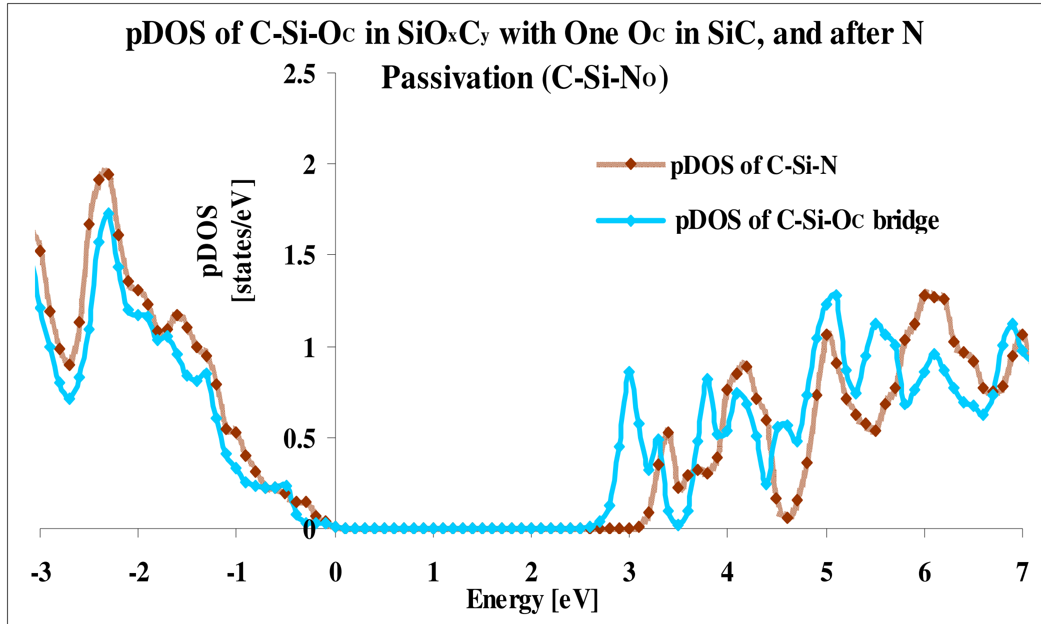

Figure 5.12: Projected density of states of C-Si-O_C bridge in SiC formed in SiC side with one O(C) (solid line), and the C-Si-N_O after N passivation (dotted circle).

The high concentration of oxygen atoms in the SiC increases the states not only near the conduction band but also in the vicinity of the valence band. The solid curve in figure 5.13 shows the total density of states of the SiO_xC_y in SiC side with six oxygen atoms substituted the carbon atoms. To study the effect of passivation, all the oxygen atoms in SiC are replaced by nitrogen atoms, and the total density of states is calculated after the geometric relaxation. The dotted line in figure 5.13 shows the total density of states of the structure after passivation. As this figure shows, passivation reduces the states near the conduction band.

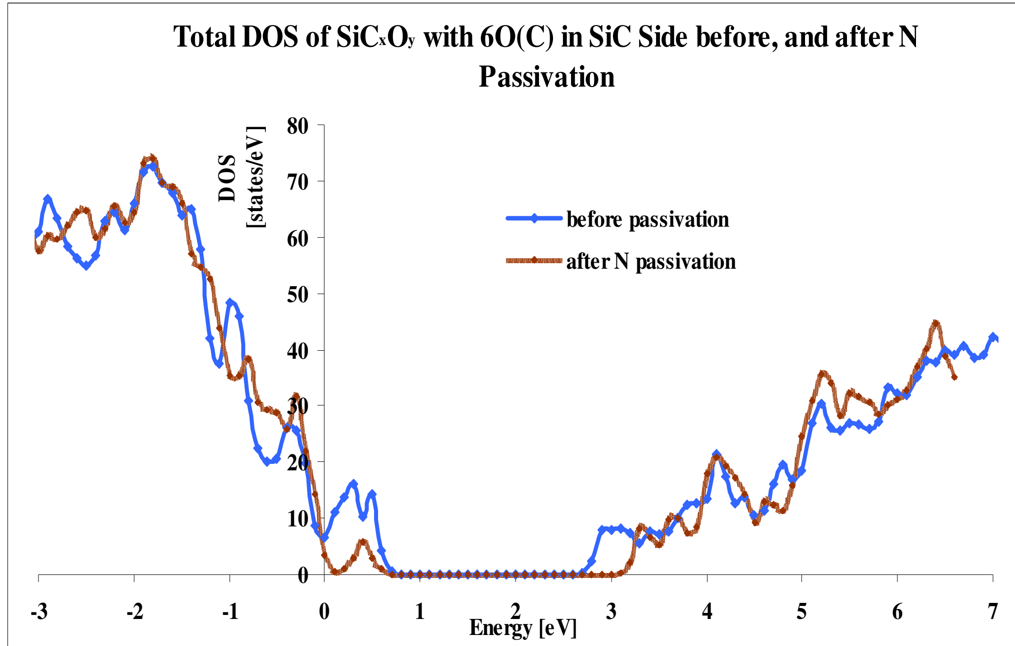

Figure 5.13: Total density of states of SiO_xC_y with 6O(C) in SiC side before (solid line), and after N passivation (dollted line).

5.7. Formation of Nitrogen Epi-Layer at the Interface

Shirasawa et al [141], and Bernhardt et al [140] proposed a technique other than post oxidation annealing to improve the quality of the interface of 6H-SiC/SiO_2. They used hydrogen gas etching and a subsequent annealing in nitrogen atmosphere. They experimentally showed that a SiON epitaxial layer is formed in SiC side of the interface, which improves the quality of the interface. Their technique is based on the formation of an epitaxial silicon oxynitride layer on the SiC side as an ideal seed for the epitaxial growth of the oxide layer.

Therefore, we study the effect of this structure by replacing all carbon atoms in the SiC side of the abrupt structure with a layer of nitrogen atoms. After the passivation, the average bond length of Si-N is almost 1.75 angstrom.

Then we perform the DFT simulation on the geometric relaxed structure, and compared the total DOS of nitrogen epi-layer structure with that of the abrupt one.

Figure 14a) shows the atomic configuration of this structure. As it seen in figure 5.14b), the total DOS of the epi-layer structure widens the bandgap. The maximum of valence band decreases and the minimum of conduction band increase almost 0.1 eV, repectively, which is in good agreement with the Shirasawa [141], and Bernhardt [140] about the improvement of the interface quality. However, this epi-layer introduces levels in the midgap, closer to the valence band, which matches the results of nitridation. It also agrees with our nitridation of SiO_xC_y in SiC side of the interface. In both cases, the corporation of nitrogen in SiC eliminates the levels near the conduction band, and opens the bandgap.

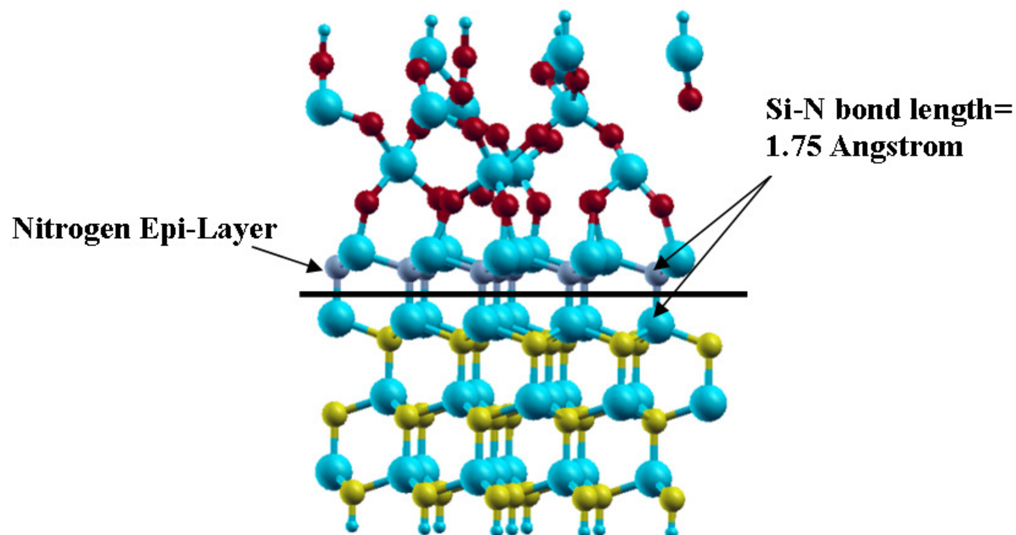

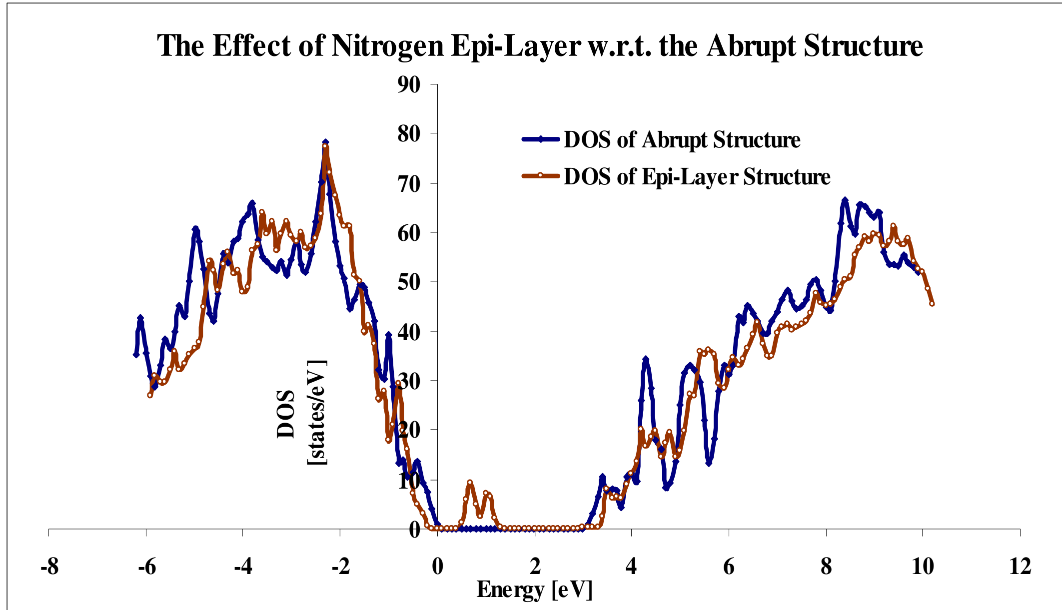

Figure 5.14:a) Atomic configuration of the structure with nitrogen epi-layer in SiC side; b) The total DOS of abrupt structure (solid line), and the epi-layer structure.

5.8. Conclusion

In summary, we constructed likely SiC/SiO_2 interface layers, and performed the energy calculation with DFT after geometric relaxation. We found the band diagram, dispersion relation, and density of states with the use of generalized gradient approximation (GGA); then we utilized the hybrid functional to retrieve the proper bandgap of each structure. The retrieved bandgap for 4H-SiC agrees with experimental data.

By comparing the total and projected density of states of C-Si-O bridges in various structures, we realized that SiO_xC_y structures made by substituting C atoms with O in SiC side may cause the traps near the conduction band.

Then, we calculated the Coulomb mobility stochastically (Monte Carlo simulation); the results indicate that the Coulomb mobility is less than 30 cm^2/Vs in all cases.

Furthermore, the more O(C) substitutions that were formed in SiO_xC_y structures in SiC, the less the mobility would be, as predicited by Monte Carlo calculations.

Passivation of SiO_xC_y structures made by substituting C atoms with O in SiC by nitrogen leads to the formation of silicon oxynitride which improves the quality of the band structure near the conduction band. Our calculations also indicate that the formation of a nitrogen epi-layer in SiC slightly widens the bandgap.

Chapter 6: Flicker Noise in MOSFET

6.1. Introduction

In this chapter, we present a DFT-based noise simulation method to calculate the current spectral noise density of (0001)4H-SiC/SiO_2 MOS devices. We use the DFT-based near interface trap density, and impurity-limited mobility as the input of the flicker noise unified [158], and statistical models [159]. The results of our calculations on SiC_xO_y in SiC side with both flicker models are in good agreement with the published data [160-162].

In electronics, noise is associated to the fluctuations that affect the voltages, and currents of the device. MOSFETS are particularly affected by low-frequency noise with the spectral density proportional to the inverse of the frequency.

Low-frequency noise is one of the critical factors for RF devices used as oscillators or mixers in microwave circuits. Low frequency noise measurements are also a powerful tool to study impurities and defects in semiconductor structures, to investigate the density of interface states, and to diagnose quality and reliability of semiconductor devices. Low frequency noise in Si MOSFETs has been studied extensively in several of papers, [162, 163]. However, the flicker noise studies of SiC field effect transistors have generally been limited [164, 165].

6.2. Introduction: Noise Definition and Classification

Noise is a fundamental aspect of all electronic circuits. Generally, adding any component to circuit increases the noise. It represents the random motion of the carriers in the electronic devices. Thermal, shot, and flicker are the most common

types of noise produced by an electrical component. Figure 1 shows the effect of the electrical noise in a range of frequencies.

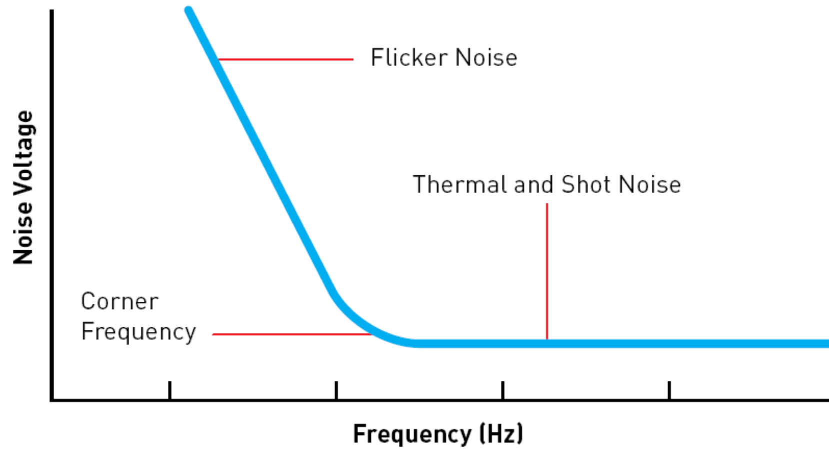

Figure 6.1: Noise versus frequency in an electrical component [167].

As is seen in figure 6.13, while thermal and shot noises are dominant in the high frequencies, flicker noise is a low frequency noise.

Thermal noise originates from the thermal motion of the charge carriers. In equilibrium situations this motion has an average of $\frac{1}{2}kT$ for each degree of freedom. The thermal noise in a homogenous-resistive channel of a MOSFET is typically given by:

$$S_v = 4kTR, \quad 6.1$$

$$S_I = 4kTG, \quad 6.2$$

where S_I, and S_V are the spectral densities related to current, and voltage fluctuations respectively, k is Boltzman constant, T is absolute temperature, R is the resistance, G is the conductance at zero drain-source voltage [167, 168].

Shot noise happens as a result of moving discrete charges. It does not vary much with temperature, and its current spectral density is white, and proportional to the amount of current flowing to the conductor, and charge of the carriers. It is given by [169]:

$$S_I = 2qI. \quad 6.3$$

Basically, it is caused by the fact that current flowing across a junction isn't smooth; the current is consists of individual electrons arriving at random times and passing randomly over a junction barrier in semiconductors. [171].

Flicker noise, was experimentally discovered by Johnson [171], and then modeled theoretically by Schottky [172]. It dominates the noise spectrum at low frequency. Flicker noise is also commonly called 1/f noise, because the noise spectrum varies as $1/f^{\alpha}$ where the exponent α is very close to unity. The spectra of these conductance fluctuations are inversely proportional to frequency, in a very wide range.

Fluctuations with a 1/f power law have been observed in practically all electronic materials and devices, including homogenous semiconductors, junction devices, and metal films. For a semiconductor, this noise with a 1/f spectrum has the variety of origins, such as impurities and traps in a conductive channel.

Since current density is proportional to the number of charge carries, and carrier mobility, therefore the fluctuations in the charge transport are caused by changes in either of these parameters [173]. Hence, the flicker noise has been modeled either by the carrier number or carrier mobility fluctuations or the combination of both; the last one is called the “unified/correlated model” [174]. Recently, a statistical model is proposed by Dunga [159] for noise calculation.

In this chapter, we use two models to estimate the current spectral noise density as a function of frequency in 4H-SiC MOSFET; first we use the "unified/combined model" and then we use a statistical noise model, proposed by Dunga [159], DFT and Monte Carlo simulation to perform the same calculation.

6.3. The Estimation of Spectral Noise Density as a Function of Frequency by Unified Model

Flicker noise originates from the traps in the gate dielectric. When the inversion channel electrons are trapped and de-trapped in the channel, the drain current fluctuates with time. The flicker noise in a MOSFET can be denoted as the spectrum S_{Id} (f) (in constant drain voltage V_d), or as the spectrum S_{VD}(f) (in constant drain current):

$$\frac{S_{Id}(f)}{I_d^2} = \frac{S_{Vd}(f)}{V_d^2}. \qquad 6.4$$

The rate of trapping as a function of the distance from the interface can be given by:

$$\tau = \tau_0 \exp(z\gamma) \qquad 6.5$$

τ_0 is defined as the trapping time constant at the interface, γ is decay coefficient [174] , and z is the depth of the trap in the dielectric measured from the silicon-dielectric interface. γ depends on temperature, frequency, and material properties [173]. The values of τ_0 and γ are given in the literature [173]. Figure 6.2 shows the cross section of a MOSFET device with random traps distributed in different locations of the oxide from the interface.

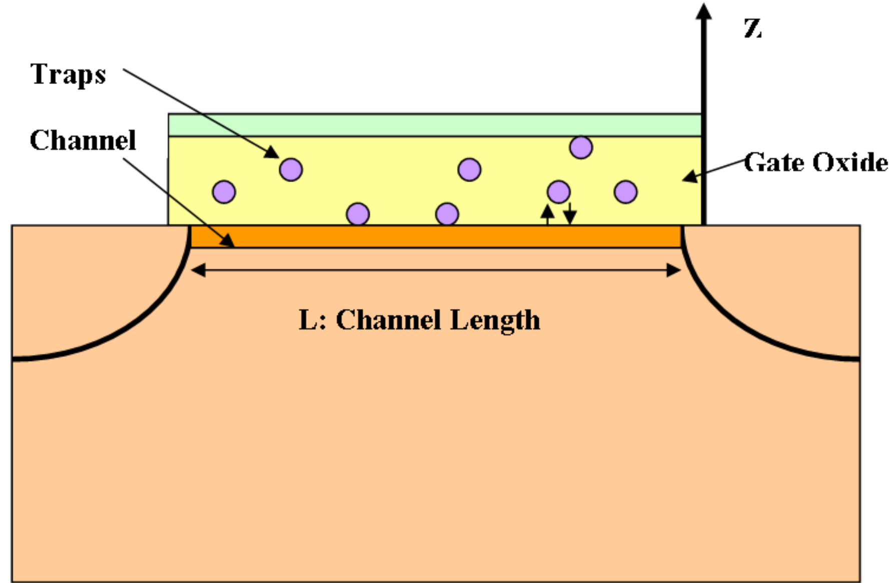

Figure 6.2: The cross-section of a MOSFET device with random traps distributed in different locations of the oxide from the interface.

The Flicker noise unified model [158] considers a section of a transistor channel with a given width W, and a given length Δx, and defines its drain current as:

$$I_d = W\mu qNE_x \tag{6.6}$$

where q is carrier mobility, N is the number of channel carriers per unit area, E_x horizontal channel field. Then fluctuations of occupancy of the oxide traps introduce correlated fluctuations in carrier number, and surface mobility:

$$\frac{\delta I_d}{I_d} = -[\frac{1}{\Delta N}\frac{\delta \Delta N}{\delta \Delta N_t} \pm \frac{1}{\mu}\frac{\delta \mu}{\delta \Delta N_t}]\delta \Delta N_t \tag{6.7}$$

where N_t is the number of occupied traps per unit area, and $\Delta N = NW\Delta x, \quad \Delta N_t = N_t W\Delta x$, and the sign of the mobility term is chosen according

whether the trap is filled. In strong inversion, the $\frac{\delta\Delta N}{\delta\Delta N_t} \equiv 1$, and $\frac{\delta\mu}{\delta\Delta N_t} = -\frac{\alpha\mu^2}{W\Delta x}$,

then:

$$\frac{\delta I_d}{I_d} = -[\frac{1}{N} \pm \alpha\mu]\frac{\delta\Delta N_t}{W\Delta x} \qquad 6.8$$

The power spectrum density of the local current fluctuations is defined as:

$$S_{\Delta Id}(x,f) = [\frac{I_d}{\Delta N}(1 \pm \alpha\mu N]^2 S_{\Delta Nt}(x,f) \qquad 6.9$$

where α is the scattering coefficient, $S_{\Delta Nt}$ is the power spectral density of the fluctuation in the number of occupied traps, and is give by:

$$S_{\Delta Id}(x,f) = \int_{Ev}^{Ec}\int_{o}^{W}\int_{o}^{tox} 4N_t(E,x,y,z)\Delta x f_t(1-f_t)\frac{\tau(E,x,y,z)}{1+\omega^2\tau(E,x,y,z)^2}dzdydE\,. \qquad 6.10$$

After integration, and at low drain voltage, the carrier density is uniform along the channel, and is found from [158]:

$$S_{\Delta Id}(f) = \frac{I_d^2}{WL}(\frac{1}{N} + \alpha\mu)^2\frac{kT}{q\gamma f}N_t(E). \qquad 6.11$$

where k is the Boltzmann constant, T is the temperature, γ is tunneling coefficient; this equation shows that the contribution of number fluctuation in generating the flicker noise is proportional to 1/N.

Equation 6.8 is the noise formula of unified modelwhich relates the current spectral noise density to both mobility, and the number of occupied traps.

6.3.1. Estimation of Spectral Noise Density as a Function of Frequency by Unified Model for SiC_xO_y in SiC side of Interface

To calculate the noise spectrum density as a function of frequency for the interface structures that we described in chapter 5.6.3. (SiC_xO_y in SiC side), we need to find the proper values for 4H-SiC parameters.

N_t (number of occupied traps per unit area) is approximated by the interface trap density, which has obtained from the DFT-based simulation of DOS.

We also assume that the number of traps exponentially distributed along the depth of the insulator as:

$$Nit = Nit_0.\exp(az), \quad 6.12$$

where a is trap distribution (when trap distribution is uniform, a=0), and z varies randomly through the oxide.

In order to consider small variations in the near interface trap density, we assume that it has a lognormal distribution; the lognormal distribution is chosen to show that the near interface density is positively skewed.

The mobilities are based on ionized impurity limited that we obtained from DFT-based Monte Carlo simulations in high concentrations trap density, and in low field (given in 5.6.3.1).

The parameter α is the scatterin coefficient, and for 4H-SiC/SiO_2 caould be calculated as:

$$\alpha = \frac{\pi m_e^* q^3}{16 \varepsilon_{av}^2 hkT} = 3.1\times10^{-14} Vs \quad for \quad 4H-SiC/SiO_2 \quad 6.13$$

The device parameters for SiC are given as: [160, 161]:

$N_{inv} = 1.2\times10^{13}$,

$I_d = 1.06\times10^{-6} A$

$W = 2.5\times10^{-4}$,

$L = 75\times10^{-4}$

$\gamma = 1.0\times10^{8}$.

Figure 6.3 shows the algorithm of DFT-based current spectral noise driven from unified/combined model.

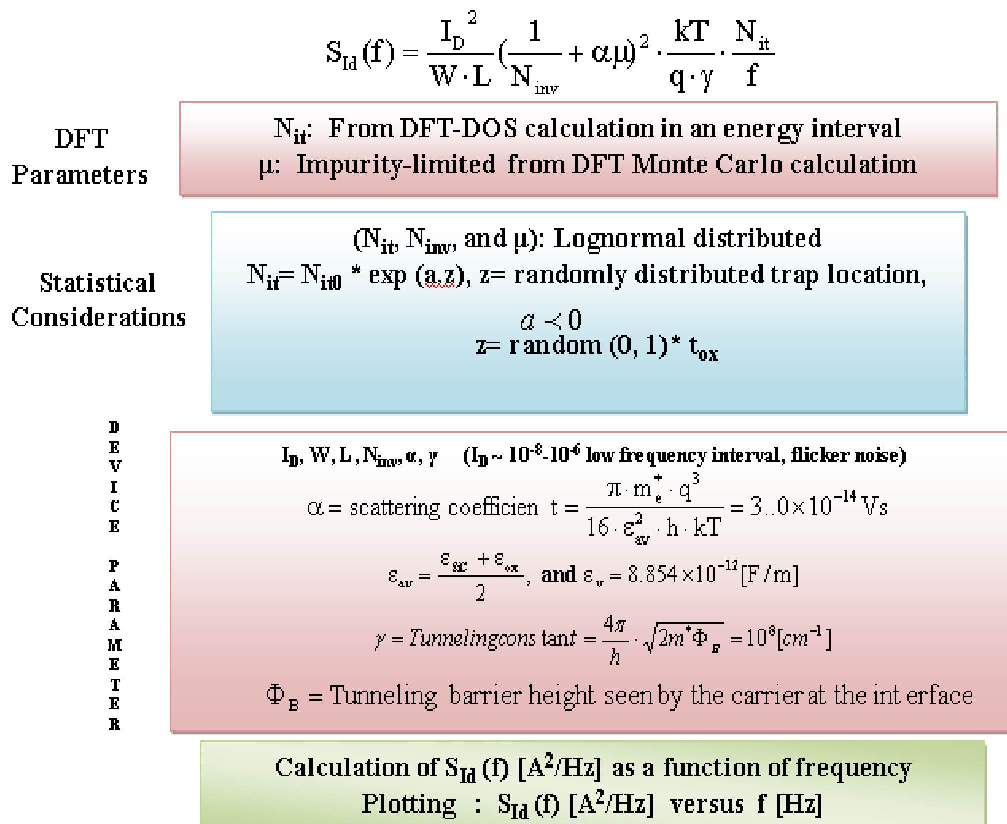

Figure 6.3: The algorithm for estimation the Current spectral noise density as a function of frequency calculated by MATLAB program according to the Unified or Correlated flicker noise model.

Then the current spectral noise density from 1Hz to 100 Hz is calculated by a MATLAB program. The results for SiC_xO_y in SiC with 1O(C), 3O(C), 6O(C) are shown in figure 6.3.

As it seen in figure 6.4 the noise spectrum for the SiC_xO_y with1O(C) is smaller than 3(O), and 6(O). The higher the Oxygen concentrations substituted for carbon in SiC becomes, the higher the flicker noise is. Our results are in good agreement with published noise data for 4H-SiC [159, 160]. The spectral noise density of figure 6.4 shows the 1/f behavior throughout the chosen frequency range.

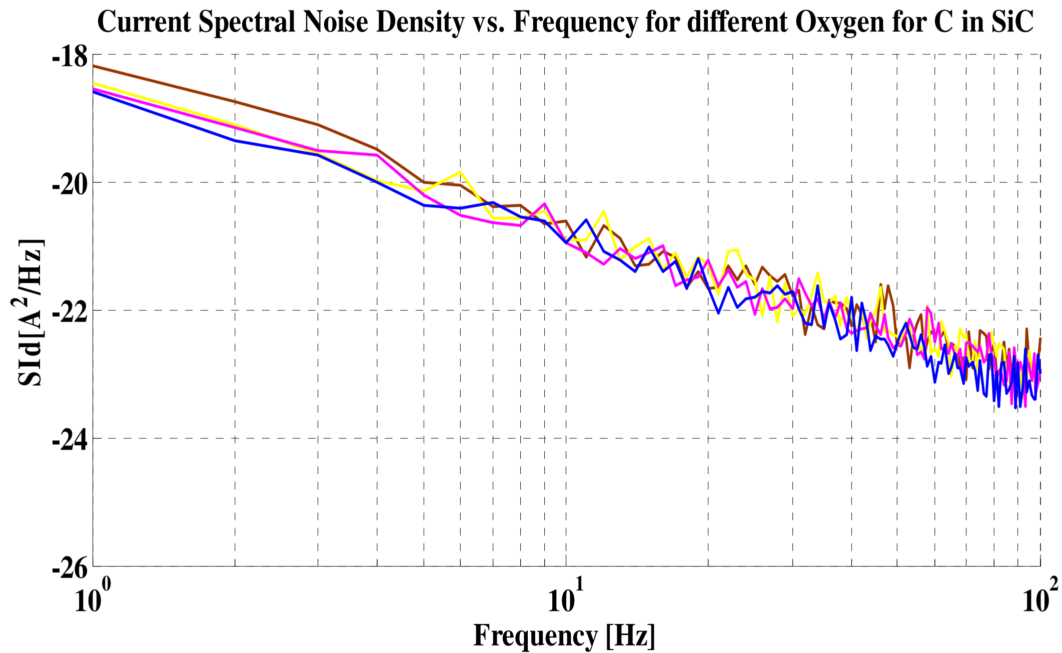

Figure 6.4: Current spectral noise density versus the frequency (between 1Hz to 100Hz), for Si SiC_xO_y in SiC with 1O(C) (blue), 2O(C) (Pink), 3O(C) (yellow), 6O (Brown).

6.4. Estimation of Spectral Noise Density as a Function of Frequency by Statistical Method

Dunga [159] uses the concepts of Random Telegraph Noise (RTN) in the framework of unified model with a statistical approach.

If each random telegraphic noise is produced as the result of the trapping-detrapping of the electrons by a trap randomly distributed in the oxide, then it is given by [173]:

$$RTN \propto \frac{\tau}{1+\omega^2\tau^2} \tag{6.14}$$

in which $\omega = 2\pi f$ is the angular frequency. The shape of RTN for each trap is Lorenzian. When the number of traps is large, and hence the number of the related noises, the sum of many Lorenzian spectra with the corner frequencies distributed exponentially yields the experimentally observed 1/f shape for flicker noise in large area devices [158]. Then the flicker noise is the superposition of all RTNs resulting from the interface traps over the oxide thickness [158]:

$$S_{Id}(f) \propto \int_0^{T_{ox}} RTN(z, f)dz. \tag{6.15}$$

Since RTN is a function of oxide thickness, and frequency, the integral of S_{Id} is proportional to the inverse of frequency:

$$S_{Id}(f) = \int_0^{T_{ox}} \frac{\tau}{1+\omega^2\tau^2} dz \tag{6.16}$$

by considering that $\tau = \tau_0 \exp(z\gamma)$, then:

$$\frac{d\tau}{dz} = \gamma\tau$$

and:

$$S_{Id}(f) = \frac{1}{\gamma}\int_0^{T_{ox}} \frac{1}{1+\omega^2\tau^2} d\tau = \frac{1}{\gamma\omega}[\tan^{-1}(\omega\tau)]_0^{T_{ox}} \approx \frac{1}{\omega\gamma}[\frac{\pi}{2} - 0] \approx \frac{1}{4\gamma f}. \tag{6.17}$$

which shows that $S_{Id}(f)$ is proportional to the inverse of frequency. The summation of large number of RTNs leads to 1/f frequency dependence of flicker noise.

For small area devices, the summation over RTN could be written as a discrete relation:

$$S_{I_D}(f) = \sum_{0}^{N_{tr}} RTN(z,f)dz \tag{6.18}$$

where N_{tr} is the number of traps in a small area device.

To calculate the current spectral noise density, we should find the number of traps, and the RTN for each trap.

The following formula is proposed by Dunga [159] to estimate the flicker noise as a function of trap numbers in a frequency interval:

$$S_{I_D}(f) = \frac{{I_D}^2}{W^2 \cdot L^2}\left(\frac{1}{N} \pm \alpha_{Sc}\mu\right)^2 \cdot \sum_{i=0}^{Ntr} F(1-F) * \frac{\tau_i}{1+(2\pi f_j \tau_i)^2} \tag{6.19}$$

where I_D is the drain current, W, and L are the width, and length of channel, N is the tran density, m is effective mobility, τ is the the rate of tunneling, F is Fermi distribution, α is the scattering rate.

The noise spectral of one trap can be written as:

$$S_{tr}(f) = \Delta I_d^2 \cdot \frac{\beta}{(1+\beta)^2} \cdot \frac{4\tau}{(1+2\pi f\tau)^2} \tag{6.20}$$

where ΔI_d is the fluctuation of drain current. β is defined as the ratio of trap capture time to the trap emission time, as is given by:

$$\beta = g * \exp(\frac{E_t - E_F}{kT}), \text{ and } \frac{\beta}{(1+\beta)^2} = F(1-F),$$

$$F = \frac{1}{1+\exp(\frac{E_t - E_F}{kT})} \quad 6.21$$

where F is the Fermi distribution and is considered to be 1, when the trap is full, and 0 when the trap is empty.

In this model, the noise is calculated by the number of traps, location of the traps inside the gate oxide, and the trap energy.

6.4.1. Estimation of the Number of Traps

To find the number traps, Dunga [159] define an average number of traps as:

$$N_{ave} = N_t . W . L . t_{ox} \Delta E \quad 6.22$$

where Nt is the trap density, W is the width, L is length, and t_{ox} is the oxide thickness. We use our DFT-based near interface trap density as Nt.

Then the number of traps in the gate oxide obeys the Poisson's distribution:

$$P(N_{tr}) = \frac{N_{Avg}{}^{N_{tr}} \cdot \exp(-N_{Avg})}{N_{tr}!} \quad 6.23$$

This statistical simulation uses the CDF (N_{tr}) to estimate the number of traps by the cumulative density function of the Poisson distribution:

$$CDF(N_{tr}) = \sum_{i=0}^{Ntr} P(N_{tr}) \quad 6.24$$

In this statistical simulation, an arbitrary random variable between 0, and 1, is chosen so that this random number lies between two cumulative density functions of CDF (Ntr) and CDF (Ntr-1):

$CDF(N_{tr}-1) < random(0,1) < CDF(N_{tr})$. We take the following form for this random number:

Random (Ntr) ~ {1-max [(CDF (Ntr)-CDF (Ntr-1)]} 6.25

Number of traps, N_{tr}, corresponding to this random number can be estimated by inversion of Poisson distribution (corresponding to the estimated N_{avg}).

The function RND (0, 1) which generates a random number between 0 and 1, the Cumulative Poisson's Distribution, CDF (Ntr), and CDF (Ntr-1) together with their difference for a case of an arbitrary $N_{avg} = 5$, is graphically illustrated in Figure 6.5.

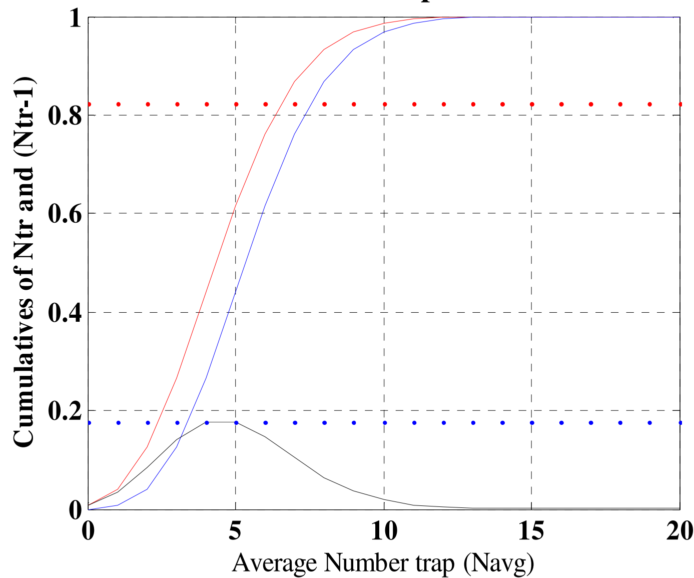

Figure 6.5: Cumulative of N_{tr} and (Ntr-1) vs. Average Number trap (Navg) with their difference as a poisson distribution.

6.4.2. Estimation of the Trap Location

Tunneling time constant depends on the place of randomly distributed trap, z, in channel or gate oxide and is given by:

$$\tau_i = Tunneling \text{ time constant} = \tau_0 * \exp(\gamma * z), \quad 6.26$$

$\tau_0 \approx 10^{-10}$, **and** $\gamma = \mathbf{10^8}$ = tunneling **parameter**

The location of trap is randomly chosen by:

$$y = random(0,1) * t_{ox} \quad 6.27$$

6.4.3. Estimation of the Trap Occupency

A random number between 0 (empty trap), and 1 (filled trap) is chosen to present the product of F(1-F) to show the probability of trap occupancy:

$$F(1 - F) = \text{random }(0,1) * (1 - \text{random }(0,1)).$$

Figure 6.6 shows the algorithm to calculate the current spectral noise density with the statistical method.

Algorithm for Statistical Method

$$S_{I_D}(f) = \frac{I_D^{\,2}}{W^2 \cdot L^2}\left(\frac{1}{N} \pm \alpha_{Sc}\mu\right)^2 \cdot \sum_{i=0}^{Ntr} F(1-F) * \frac{\tau_i}{1+(2\pi f \tau_i)^2}$$

N_{tr}: From DFT-DOS calculation in an energy interval

$N_{avg} = N_{it}$ .W. L. t_{ox}. ΔE

$$P(N_{tr}) = \frac{N_{Avg}^{\,N_{tr}} \cdot \exp(-N_{Avg})}{N_{tr}!}$$

-Statistical simulation for CDF (N_{tr}): $CDF(N_{tr}) = \sum_{i=0}^{Ntr} P(N_{tr})$

.A random variable between 0, and 1, is chosen so:

$$CDF(N_{tr}-1) < random(0,1) < CDF(N_{tr})$$

Random (N_{tr}) ~{1-max[(CDF(N_{tr})-CDF(N_{tr}-1)]}

.Number of traps is found with estimated by the inversion of Poisson distribution (corresponding to the estimated N_{avg})

$\beta = g * \exp(\frac{E_t - E_F}{kT})$, and $\frac{\beta}{(1+\beta)^2} = F(1-F)$, and $F = \text{Fermi Dis} = \frac{1}{1+\exp(\frac{E_t - E_F}{kT})}$

z= random (0, 1)* t_{ox} $\quad \tau_i = \textit{Tunneling}$ time constant $= \tau_0 * \exp(\gamma * z)$,

$F(1-F) = random\ (0,1) * (1 - random\ (0,1))$

+

Device Parameter: I_D, W, L, N_{inv}, α, γ ($I_d \sim 10^{-6}$)

μ: DFT-based Impurity-limited (Monte Carlo Simulation)

Figure 6.6: The algorithm for calculating current spectral noise density with statistical model.

6.4.4. Spectral Noise Density Simulation for SiC_xO_y Transition Layer in a Statistical Model

After providing the profile for trap, we calculated the term which associates the current spectral noise density to the mobility:

$$S_{I_D}(f) \propto \frac{I_D^{\,2}}{W^2 \cdot L^2}\left(\frac{1}{N} \pm \alpha_{Sc}\mu\right)^2 \tag{6.28}$$

We used the ionized impurity limited mobilities that we obtained from DFT-based Monte Carlo simulations in high concentrations trap density, and in low field (given in 5.6.3.1). All other parameters for a 4H SiC/SiO_2 are taken from the device parameters and are given by [158, 160, 161]:

$$\alpha = \frac{\pi m_e^* q^3}{16 \varepsilon_{av}^2 hkT} = 3.1 \times 10^{-14} Vs \quad for \quad 4H - SiC / SiO_2$$

$N_{inv} = 1.2 \times 10^{13}$,
$I_d = 1.06 \times 10^{-6} A$
$W = 2.5 \times 10^{-4}$,
$L = 75 \times 10^{-4}$
$\gamma = 1.0 \times 10^{8}$.

The current spectral noise density from 1Hz to 100 Hz, is calculated by a MATLAB program. The current noise spectral density simulated from the statistical model for SiC_xO_y in SiC with 1O(C), 3O(C), 6O(C) are shown in figure 6.7. As it seen the, again the current spectral noise density from 1Hz to 100 Hz increases with the number of O(C) in the SiC transition layer.

It is interesting to note that the current spectral noise density estimated by statistical model is nearly the same as the unified modes for the large number of traps.

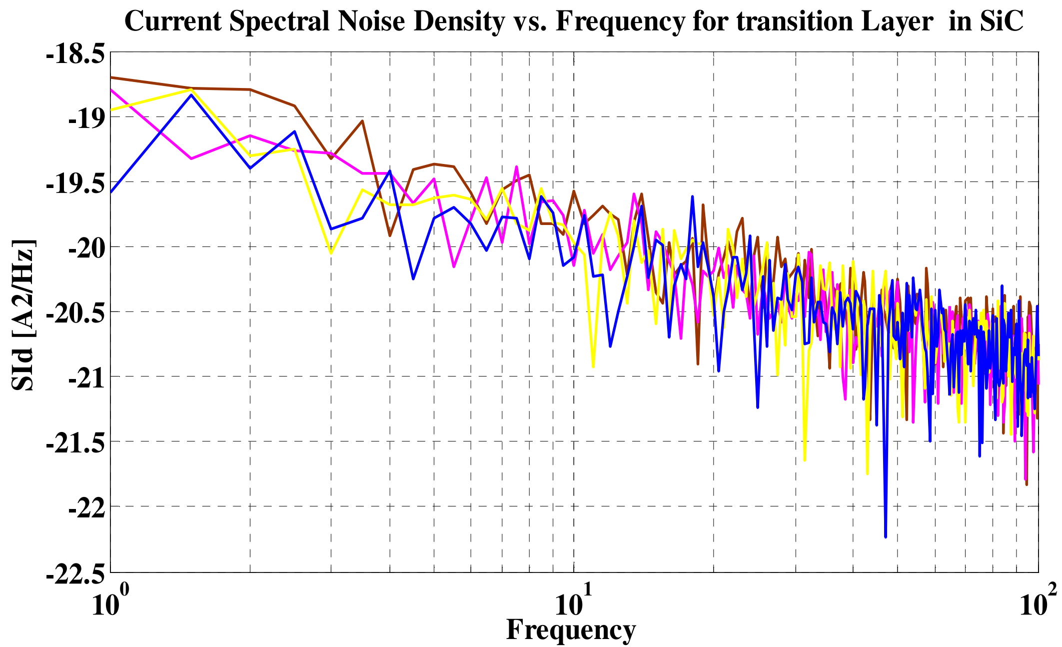

Figure 6.7: Current spectral noise density versus the frequency (between 1Hz to 100Hz), for Si SiC_xO_y in SiC with 1O(C) (blue), 2O(C) (Pink), 3O(C) (yellow), 6O (Brown).

6.5. Summary

We used the DFT-based near interface trap density and the ionized impurity limited mobilities that we obtained from the DFT-based simulation to calculate the current spectral noise density by both the unified and statistical approaches. The results show that noise increases with the increase the number of oxygen atoms substituting carbon in SiC side of interface. The results are in good agreement with published data. The interesting point is that the current spectral noise density estimated by statistical model is nearly the same as the unified modes for the large number of traps.

Conclusion and Future Work

In this thesis we employed the hybrid functional DFT approach to study the electronic properties of the (0001)4H-SiC/SiO_2 structure: from generating a model for atomic configuration of the abrupt interface, to an interface model with several defects, to a model for the most likely transition layer, and finally to the mobility and noise calculations. Furthermore, the effects of several forms of the passivation, either by employing the various passivants, or by using different passivation mechanisms, have been studied. The aim of this investigation is not only to find the structures responsible for the states in the bandgap, especially near the band edges of the (0001)4H-SiC interface, but also (and more importantly) to provide a link between the atomic structure and the macroscopic properties like mobility and noise.

After calibrating the DFT simulations with 4H-, and 6H-SiC bulk bandstructure, and effective mass calculations, an abrupt structure of (0001)4H-SiC/SiO_2 is generated for further defect, passivation, and transition layer studies. The structure is abrupt in the sense that every Si atoms at the interface of SiC is satisfied by an oxygen atom, and no dangling bonds are left in between. After the geometric relaxation, the resulted bond lengths and bond angles are within a reasonable range. Moreover, the 4H(0001)-SiC/SiO_2 interface has reasonable properties both from the structural and electronic standpoints. The bandgap retrieved by the hybrid functional provides a reliable framework. The details of the bandgap is studied with the use of projected density of states over all the atoms within 4.5 angstroms of the structure in z the direction

Then energy levels of various defects in both sides of the interface have been investigated by density functional theory. According to the calculations, silicon

vacancy in SiC side of the structure gives rise to states near the valence band; each negative charge in this structure shifts the trap levels 0.2 to 0.3 eV toward the mid and conduction band. Carbon interstitial and a pair of carbons in SiC introduce states in the bandgap, and in some occasions near the conduction band. On the other or SiO_2 side, oxygen deficiency at the interface, and the silicon dangling bonds perpendicular to the interface give rise to states near the conduction band. Therefore, the excess carbon either in the form of interstitial or a pair of interstitial in SiC substrate, and the oxygen deficiency, which leads to either Si-Si long bonds or Si dangling bonds, are the potential defects for creating the states near the conduction band.

In the case of defects, the passivation is carried out either by attaching the distorted atom directly to the passivant atom or through carbon removal. In the former case, the passivant atom binds with the dangling bonds, and forms bonding and antibonding states in the valence, and conduction bands, respectively; as a result, the states from the dandling bonds are removed from the bandgap. In the latter case, nitrogen and phosphorus eliminate the carbon states in the vicinity of the conduction band (or the valence band), but they introduce levels in the midgap, due to an extra electron that they bring to the system.

Next we modeled the likely SiC/SiO_2 interface layers, and performed the energy calculation with hybrid functional DFT, after geometric relaxation. By comparing the total and projected density of states of C-Si-O bridges in various structures, we realized that SiO_xC_y structures made by substituting C atoms with O in SiC side may cause the traps near the conduction band. This type of substitution is one of the potential mechanisms behind SiC oxidation. According to our simulations, an O atom

replacing a C atom makes an O-V_C (carbon-vacancy) complex, which pushes the neighboring Si atoms away from O. Eventually, it leads to the formation of a thin oxygen contaminated Si-rich interface layer which needs a very small structural reconstruction to form SiO_2. Since the formation energy of the C vacancy is less than Si vacancy, and the Si-C bonds are smaller than the Si-Si bonds in Si crystals, oxygen prefers to replace the C vacancy. The successful nitridation of the damaged bridges in the proposed structure for the transition layer (SiO_xC_y formed by substitution of C atoms in SiC side by O atoms) could be taken as a confirmation for the validity of our calculation.

We also used a DFT-based Monte Carlo simulation to calculate both the phonon-, and Coulomb-limited mobility of the SiO_xC_y structures that emulated the transition layer. Monte Carlo simulations show that the more damaged bridges in the abrupt structure, the less the phonon-, and Coulomb-limited mobility would be.

Finally, since low-frequency noise is a powerful tool to study impurities and defects in semiconductor structures, to investigate the density of interface states, and to diagnose quality and reliability of semiconductor devices, we used the near interface trap density and the ionized impurity limited mobilities simulated by DFT, to calculate the current spectral noise density by both the unified and statistical approaches. The results show that noise increases with the increase in the number of oxygen atoms substituting carbon in SiC side of the interface. The results are in good agreement with published data. The interesting point is that the current spectral noise density estimated by statistical model is nearly the same as the unified model when there are a large number of traps.

The future work needs to be conducted on the generating the larger structures, possibly with the amorphous silicon dioxide, to both provide the more realistic model for the 4H-SiC MOSFET channel area. In addition, a methodology for normalizing the number of defect states over the entire structure needs to be developed.

Appendices

A.1. Exchange-Correlation Hole

The exchange, correlation hole helps to visualize the impact of exchange and correlation on the electron density distribution.

The idea of exchange, correlation hole originated from the fact that due to electrostatic repulsion, the immediate region around the electron has fewer electrons than average. Pictorially, it seems that there is a hole around each electron with the negative density which imposes attractive energy to the electrons. Hence, it is possible to consider the actual electron-electron potential energy as a sum of the classical interaction between electron densities together with the interaction of electron density with exchange, correlation hole. The exchange, correlation hole could be split into Fermi/exchange hole and Coulomb/correlation hole; while the Fermi hole is because of Pauli Principle (the antisymetry of the wave function), the Coulomb hole (applies to electrons with either spin) is the result of electrostatic interaction. Hole-function has all information about non-classical contributions to the potential energy due to electron-electron interaction.

Considering the exchange-correlation factor in pair density, one can define the conditional probability $P(\vec{x}_2|\vec{x}_1)$ as the probability of finding any electron in $\vec{x}_2$, if there is already one in $\vec{x}_1$:

$$P(\vec{x}_2|\vec{x}_1) = \frac{\rho_{pair}(\vec{x}_1, \vec{x}_2)}{\rho(\vec{x}_1)}. \qquad \text{A.1}$$

The conditional probability contains all the electrons except the one in $\vec{x}_1$ and integrates to (N-1). Recalling the exchange-correlation factor in pair density, the difference between the conditional probability and the uncorrelated probability of finding an electron in $\vec{x}_2$ is the so-called the exchange-correlation hole:

$$H_{XC}(\vec{x}_1,\vec{x}_2) = P(\vec{x}_2|\vec{x}_1) - \rho(\vec{x}_2) = \rho(\vec{x}_2).f_{exchange-correlation}(\vec{x}_1,\vec{x}_2). \quad \text{A.2}$$

The exchange-correlation hole has negative sign. By considering the electron density and the conditional probability constraint, it integrates to minus one:

$$\int H_{XC}(\vec{x}_1,\vec{x}_2)d\vec{x}_2 = \int (P(\vec{x}_2|\vec{x}_1) - \rho(\vec{x}_2))d\vec{x}_2 = (N-1) - N = -1. \quad \text{A.3}$$

The exchange-correlation hole can be separated into a summation of exchange and correlation contributions, the Fermi and Coulomb holes; the exchange hole integrates to minus one, while the correlation hole integrates to zero and this is what is called the sum rule.

It should be noted that the exchange effect is the dominant one. Figure A.1 shows the exchange and correlation hole for Silicon calculated by Monte Carlo method [175].

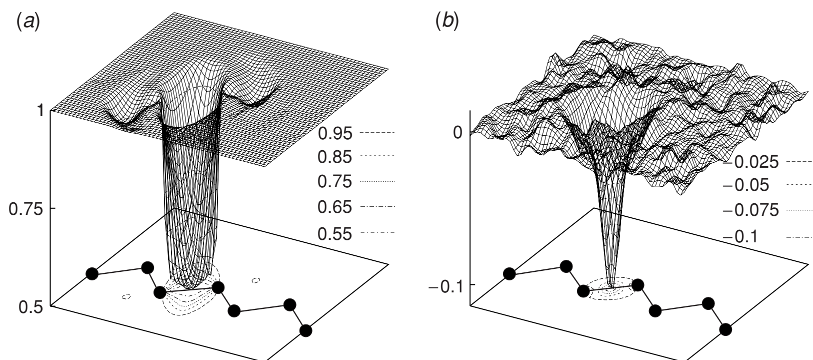

Figure A.5: Exchange a) and correlation hole b) for an electron at the bond center in Si, calculated by Monte Carlo method [175].

A.2. Functional

While a function maps one number to another, a functional is a rule for going from a function to a number; functional depends on the function itself, not on its variable.

Since density functional theory claims that the ground-state energy of a quantum mechanical system is a functional of the density, it would be essential to deal with energy minimization to find the true ground-state density, or to differentiate functionals.

The derivative formed in terms of the ordinary differential, df/dx, measures the first-order change of y = f(x) upon changes of x, which is the slope of the function f(x) at x:

$$f(x+dx) = f(x) + \frac{df}{dx}dx + O(dx^2) \qquad \text{A.4}$$

The functional derivative measures, similarly, the first-order change in a functional upon a functional variation of its argument:

$$F[f(x)+\delta f(x)] = F[f(x)] + \int s(x)\delta f(x)dx + O(\delta f^2) \qquad \text{A.5}$$

where the integral arises because the variation in the functional F is determined by variations in the function at all points in space. The first-order coefficient (or 'functional slope') s(x) is defined to be the functional derivative $\delta F[f]/\delta f(x)$. The functional brings the possibility of studying the functional variation upon changes in the form of the function it depends on. A general expression for obtaining functional

derivatives with respect to ρ(x) of a functional $F[\rho] = \int f(\rho, \rho', \rho'',..., x)dx$, where primes indicate ordinary derivatives of ρ(x) with respect to x, is:

$$\frac{\delta F[\rho]}{\delta \rho(x)} = \frac{\delta f}{\delta \rho} - \frac{d}{dx}\frac{\delta f}{\delta \rho'} + \frac{d^2}{dx^2}\frac{\delta f}{\delta \rho''} - \frac{d^3}{dx^3}\frac{\delta f}{\delta \rho'''} + ... \quad \text{A.6}$$

This expression is frequently used in DFT to obtain exchange potentials from exchange energies.

Euler-Lagrange equations provide procedure to solve the optimization of functionals subject to constraints. There is a well-known method for doing such problems, called the method of Lagrange multiplier. The problem is to optimize a functional like F[ρ] subject to constraint g[ρ]=k. The solution starts with building an equation with the following form:

$$M[\rho] = F[\rho] - \mu g[\rho] \quad \text{A.7}$$

the next step is to optimize M[ρ] by setting its functional derivative to zero [80, 81].

$$\frac{\delta M[\rho]}{\delta \rho} = \frac{\delta F[\rho]}{\delta \rho} - \mu \delta \frac{g[\rho]}{\delta \rho} = 0. \quad \text{A.8}$$

A.3. Thomas-Fermi Approximation

Thomas-Fermi approximation is the original form of density functional theory. Thomas and Fermi used the statistical considerations to approximate the distribution of electron density. Since finding the kinetic energy of a system is a tricky task, they suggested that the kinetic energy of electrons is a functional of the electron density. They approximated it by the kinetic energy of non-interacting electrons in homogeneous gas with density equal to the local density at any given point; the effect of exchange and correlation are neglected.

They divided the space into small cubes, with length l and volume l^3, each has a fixed number of non-interacting electrons, ΔN (which may have different values for different cells), at zero degree of Kelvin. Then the energy levels of a particle in a three dimensional infinite well is:

$$\varepsilon(n_x, n_y, n_z) = \frac{h^2}{8ml^2}(n_x{}^2 + n_y{}^2 + n_z{}^2) = \frac{h^2}{8ml^2}R^2 \quad \text{A.9}$$

For high quantum numbers (for large R), the number of distinct energy levels smaller than ε, can be approximated by the volume of one octant of a sphere with radius R, in the space (n_x, n_y, n_z); then the number of energy levels with energy smaller than ε is:

$$\Phi(\varepsilon) = \frac{1}{8}\left(\frac{4\pi R^3}{3}\right) = \frac{\pi}{6}\left(\frac{8ml^2\varepsilon}{h^2}\right)^{3/2} \quad \text{A.10}$$

The number of energy levels between ε and ε+δε is given by g(ε) which is the density of states at energy ε:

$$g(\varepsilon)\Delta\varepsilon = \Phi(\varepsilon + \delta\varepsilon) - \Phi(\varepsilon) = \frac{\pi}{4}\left(\frac{8ml^2}{h^2}\right)^{3/2}\varepsilon^{1/2}\delta\varepsilon + O((\delta\varepsilon)^2)\,. \quad \text{A.11}$$

Considering the Fermi-Dirac distribution:

$$f(\varepsilon) = \frac{1}{1 + e^{\beta(\varepsilon - \mu)}} \quad \text{A.12}$$

which at zero degree of Kelvin, it becomes a step function; as β goes to infinity f(ε) is 1 when the energy is less than the Fermi energy and is zero when the energy is more than that. The Fermi energy is the zero temperature limit of the chemical potential μ. Then the total energy of electrons in the cell is given by:

$$\Delta E = 2\int \varepsilon f(\varepsilon)g(\varepsilon)d\varepsilon = 4\pi(\frac{2m}{h^2})^{3/2} l^3 \int_0^{\varepsilon_F} \varepsilon^{3/2} d\varepsilon = \frac{8\pi}{5}(\frac{2m}{h^2}) l^3 \varepsilon_F^{5/2} \quad \text{A.13}$$

Considering the relation between the number of electrons and the Fermi energy which is given by:

$$\Delta N = 2\int f(\varepsilon)g(\varepsilon)d\varepsilon = \frac{8\pi}{3}(\frac{2m}{h^2})^{3/2} l^3 \varepsilon_F^{3/2} \quad \text{A.14}$$

By eliminating ε_F, the cell kinetic energy becomes:

$$\Delta E = \frac{3}{5}\Delta N \varepsilon_F = \frac{3h^2}{10m}(\frac{3}{8\pi})^{2/3} l^3 (\frac{\Delta N}{l^3})^{5/3} \quad \text{A.15}$$

By taking the electron density of each cell as:

$$\rho = \frac{\Delta N}{l^3} \quad \text{A.16}$$

Then the total kinetic energy in terms of electron density is:

$$T_{TF}[\rho] = C_F \int \rho^{5/3}(\vec{r})d\vec{r} \quad \text{A.17}$$

and C_F is given by:

$$C_F = \frac{3}{10}(3\pi^2)^{2/3} \quad \text{A.18}$$

Then they used the above results together with the nuclear-electron and electron-electron potentials to find the energy of an atom:

$$E_{TF}[\rho(\vec{r})] = \frac{3}{10}(3\pi^2)^{2/3}\int \rho^{5/3}(\vec{r})d\vec{r} + \int \rho(\vec{r})V_{ext}d\vec{r} + \frac{1}{2}\iint \frac{\rho(\vec{r}_1)\rho(\vec{r}_2)}{\vec{r}_{12}} d\vec{r}_1 d\vec{r}_2 \quad \text{A.19}$$

Although the Thomas-Fermi equation is based on a very coarse approximation which neglects the effect of exchange and correlation, it gives the energy functional in terms of electron density (not the wave function) without the necessity of more information. Then they use the variational principle to get the best electronic density.

They assumed that the ground state of the system is the one that its electronic density minimizes the variational principle under the following constraint:

$$\int \rho(\vec{r})d\vec{r} = N \tag{A.20}$$

Thomas and Fermi didn't prove that whether physically it is possible to write the energy as a function of the electronic density.

Fermi-Dirac approximation is the backbone of what is recently called "local density functional approximation, LDA"; in this approach, electronic properties are determined as functionals of the electron density for a homogeneous electronic system [80, 81, 83].

A.4. N- and V- Representability

Repsentability, which is divided as V- and N-, is a conceptual problem in Hohenberg-Kohn formalism. Hohenberg-Kohn theorems raise many questions about the one-to-one mapping between densities and external potentials. The V_{ext} representability is asking how it is possible to recognize those electron densities that related to an antisymmetric wave function and a Hamiltonian operator with some kind of external potential. Moreover, the HK theorem only guarantees that there cannot be more than one potential for each density. The other question is how one can recognize those electronic density functions that satisfy the following relation:

$$\rho(\vec{r}) = N\int d^3\vec{r}_2 \int d^3\vec{r}_3 ... \int d^3\vec{r}_N \Psi^*\Psi \tag{A.21}$$

It should be noted that those functions that minimize the energy but are not N-representative do not have any physical meaning [84].

A.5. Local Density Approximation (LDA)

Traditionally, the first approximation suggested by Kohn-Sham as the exchange-correlation functional is the local density approximation, LDA, which had already proposed by Thomas and Fermi. The LDA has been for a long time the common used approximation to the exchange-correlation energy.

The concept of uniform electron gas is at the center of LDA. The uniform electron gas refers to electrons moving in a positive charge distribution in a way that the system is electrically neutral. Although LDA is based on a not realistic assumption of uniform electron gas, its exchange-correlation functional is exactly calculated and this is the reason of its importance.

The exchange-correlation of Kohn-Sham equation is defined as the exchange potential for the spatially uniform electron gas with the same density as the local electron density:

$$V_{XC}^{LDA}[\vec{r}] = V_{XC}^{electrongas}[\rho(\vec{r})]. \qquad \text{A.22}$$

The effects of exchange and correlation are local and the exchange-correlation energy is the integral over all space with the exchange-correlation energy density at each point assumed to be the same as in the homogeneous electron gas with that density. The exchange-correlation energy which can be defined precisely by Monte Carlo calculation is written as:

$$E_{XC}^{LDA}[\rho] = \int \rho(\vec{r})\varepsilon_{XC}(\rho(\vec{r}))d\vec{r}) = \int \rho(\vec{r})(\varepsilon_{X}^{\hom}(\rho(\vec{r}) + \varepsilon_{C}^{\hom}(\rho(\vec{r}))d\vec{r}) \qquad \text{A.23}$$

$\varepsilon_{XC}(\rho(\vec{r}))$ is the exchange-correlation energy per particle of a uniform electron gas of density $\rho(\vec{r})$.

In general, the exchange-correlation energy density is not a local functional of ρ. It is the manifestation of the probability of finding an electron in $\vec{r}$ which depends on the presence of the other electrons in the neighborhood through the exchange-correlation hole and hence it is non-local.

The detail of the LDA is given by considering a system of large number of electrons, N, moving in a one-dimensional box, which its potential is $V(x) = \infty$, everywhere, except for $0 \le x \le l$, where V = 0. One can use the periodic boundary conditions such as $\phi(x+l) = \phi(x)$. Then the orbitals would have the following form:

$$\phi(k_x, k_y, k_z) = \frac{1}{l^{3/2}} e^{i(k_x x + k_y y + k_z z)} = \frac{1}{V^{1/2}} e^{i\vec{k}.\vec{r}} \qquad \text{A.24}$$

where $k_x = \frac{2\pi}{l} n_x$ and so forth with $n_x, n_y, n_z = 0, \pm 1, \pm 2, ...$ and the energies are given by:

$$E(n_x, n_y, n_z) = \frac{h^2}{8ml^2}[(2n_x)^2 + (2n_y)^2 + (2n_z)^2] \qquad \text{A.25}$$

Then the spinless, first-order density matrix of the form:

$$\rho_1(\vec{r}_1, \vec{r}_1') = 2\sum_i^{N/2} \phi_i(\vec{r}_1)\phi_i^*(\vec{r}_1') \qquad \text{A.26}$$

which ϕ_i are the doubly occupied spatial orbitals get the following form:

$$\rho_1(\vec{r}_1, \vec{r}_2) = \frac{2}{V} \sum_{alloccupied\vec{k}} e^{i\vec{k}.(\vec{r}_1 - \vec{r}_2)} = \frac{1}{4\pi^3} \int e^{i\vec{k}.(\vec{r}_1 - \vec{r}_2)} d\vec{k} \qquad \text{A.27}$$

It is possible to take $\rho_1(\vec{r}, \vec{r}) = \rho(\vec{r})$ and introduce the Fermi wave vector:

$$\rho(\vec{r}) = \frac{{k_F}^3}{3\pi^2} \qquad \text{A.28}$$

or

$$k_F(\vec{r}) = [3\pi^2 \rho(\vec{r})]^{1/3} \qquad \text{A.29}$$

Thomas-Fermi kinetic energy has the form of:

$$T_{TF}[\rho] = C_F \int \rho^{5/3}(\vec{r}) d\vec{r} \qquad \text{A.30}$$

and the coefficient is $C_F = \frac{3}{10}(3\pi^2)^{2/3}$. A.31

Hartree-Fock exchange energy which is the difference between the real electron-electron interaction and the classical, Coulomb, repulsive electron-electron potential energy for the doubly occupied spatial orbitals is given by:

$$E_{exchange}^{Hartree} = \frac{1}{4} \int \frac{1}{r_{12}} \left| \rho_1(\vec{r}_1, \vec{r}_2) \right|^2 d\vec{r}_1 d\vec{r}_2 \qquad \text{A.32}$$

and this leads to the following exchange energy:

$$E_{exchange}^{Hartree} = C_x \int \rho^{4/3}(\vec{r}) d\vec{r} \qquad \text{A.33}$$

and the coefficient is $C_x = \frac{3}{4}(\frac{3}{\pi})^{1/3}$. A.34

The above energy provides the exchange part of the exchange-correlation energy in the Kohn-Sham equation and the exchange-correlation could be written as the sum of the exchange and correlation energies.

The situation is complicated for the correlation energy. In a real system, electrons are under the spatially varying electric fields of nuclei and the interacting electron-electron. The LDA is still working for the slowly-varying densities but not for inhomogeneous systems. A partial explanation for its applicability even for slightly nonhomogeneous systems is systematic error cancellation; typically, LDA underestimates E_c but overestimates E_x, resulting in unexpectedly good values of E_{xc}.

In magnetic systems or, in general, in systems where open electronic shells are involved, better approximations to the exchange-correlation functional can be obtained by introducing the two spin densities, $\rho_\alpha(\vec{r}), \rho_\beta(\vec{r})$. In this case, the two spin densities sum up to the electron density:

$$\rho_\alpha(\vec{r}) + \rho_\beta(\vec{r}) = \rho(\vec{r}) \,. \qquad \text{A.35}$$

The spin oriented case is called "local spin density approximation, LSDA" and also its exchange-correlation energy is an integral over all space with the exchange-correlation energy density at each point is considered to be the same as in a homogeneous electron gas with that density:

$$E_{XC}^{LSDA}[\rho_\alpha, \rho_\beta] = \int \rho(\vec{r}) \varepsilon_{XC}(\rho_\alpha(\vec{r}) \rho_\beta(\vec{r})) d\vec{r} \qquad \text{A.36}$$

The related kinetic energy is given by:

$$T_{TF}[\rho_\alpha, \rho_\beta] = 2^{2/3} C_F \int [(\rho_\alpha)^{5/3} + (\rho_\beta)^{5/3}] d\vec{r} \qquad \text{A.37}$$

Similarly, the exchange-correlation energy is the sum of exchange and correlation energy:

$$E_{XC}[\rho_\alpha, \rho_\beta] = E_X[\rho_\alpha, \rho_\beta] + E_C[\rho_\alpha, \rho_\beta] \qquad \text{A.38}$$

which its exchange energy is given by:

$$E_X = 2^{1/3} C_X \int [(\rho_\alpha)^{4/3} + (\rho_\beta)^{4/3}] d\vec{r} \qquad \text{A.39}$$

For the spin polarized case $\rho_\alpha(\vec{r}) \neq \rho_\beta(\vec{r})$, a parameter is defined as the degree of polarization parameter:

$$\xi = \frac{\rho_\alpha(\vec{r}) - \rho_\beta(\vec{r})}{\rho(\vec{r})} \qquad \text{A.40}$$

The value of the spin polarization parameter is between zero and one (zero for un-polarized systems and one for fully polarized ones) and the exchange energy is found accordingly.

Local density approximation gives the satisfactory results for covalent, ionic and metallic bonds and its error is within a few percent. However, it is not successful in predicting atomic systems with large density variations, weak molecular bonds (because of binding inhomogenity), Van der Waals (closed-shell) systems (due to non-local, charge-charge correlation of two separate parts), metallic surfaces (because the exchange-correlation potential decays exponentially, while it should follow a power law), and negatively charged ions (because it fails to cancel exactly the electronic self-interaction). Moreover, it underestimates the energy band gap in semiconductors, because when one electron is removed from the ground state, the exchange hole becomes screened, which is neglected in LDA [80, 81, 93]

A.5.1. Generalized Gradient Approximation (GGA)

The local density approximation can be considered to be the zero order approximation to the semi-classical expansion of the density matrix in terms of the density and its derivatives. In fact, local density approximation uses the knowledge of the density at point r. The first step modification to local density approximation is to take into account not only the information in charge density but also the information about the gradient of charge density to deal with the non-homogeneity.

The idea behind the gradient expansion approximation (GEA) is to expand the exchange energy as a Taylor series with respect to the charge density; then the local density energy would be the first term of the expansion and to get the better

approximation is supposed to be given by using the other terms. However, the first added gradient term even worsen the LDA results. The added term violates the physical concept of exchange-correlation hole of local density approximation because the expanded term distorts the exchange, correlation hole properties.

The analysis of GEA failure made others to build another type of fucntionals. Generalized gradient approximation (GGA) is based on the lessons learned from GEA failures. Generalized gradient approximation considers the exchange, correlation hole requirements and eliminates the GEA parts that violate them. The expansion part, which is the problematic area, is considered very cautiously not to violate the normalization criteria of exchange-correlation hole, the negativity of the exchange density or the self-interaction cancellation (the diagonal of the exchange density matrix has to be minus a half of the density). Those proposed functionals which respect the hole requirements give reasonable results for exchange and correlation energies.

The general form of the GGA is as follow:

$$E_{XC}^{GGA}[\rho_\alpha, \rho_\beta] = \int d^3\vec{r} F(\rho_\alpha, \nabla\rho_\alpha, \rho_\beta, \nabla\rho_\beta) \qquad \text{A.41}$$

Although the general form of all GGA(s) is the same, there are several suggestions for considering the “F” term; however, it is known that the F function should satisfy the hole requirements such as sum rules and long-range decay. Moreover, GGA deals with the exchange and correlation terms separately.

The exchange and correlation energies in Langreth-Mehl exchange, correlation functional have the following form:

$$E_X = E_X^{LDA} - a\frac{|\nabla\rho|^2}{\rho^{4/3}}(\frac{7}{9} + 18f^2) \quad \text{A.42}$$

$$E_C = E_C^{RPA}(\rho) + a\frac{|\nabla\rho|^2}{\rho^{4/3}}(2e^{-F} + 18f^2) \quad \text{A.43}$$

where $F = b|\nabla\rho|/\rho^{7/6}$ and b= $((9\pi)^{1/6}f)$ and a= $\pi/(16(3\pi^2)^{4/3})$ and f=0.15.

The exchange and correlation energies in Perdew-Wang-86 functional are (PW86):

$$E_X = E_X^{LDA}(\rho) + (1 + 0.0864\frac{s^2}{m} + bs^4 + cs^6)^m \quad \text{A.44}$$

$$E_C = E_C^{LDA}(\rho) + e^{-\Phi}C_C(\rho)\frac{|\nabla\rho|^2}{\rho^{4/3}} \quad \text{A.45}$$

where:

$$\Phi = 1.745\tilde{f}\frac{C_C(\infty)}{C_C(\rho)}\frac{|\nabla\rho|}{\rho^{7/6}} \quad \text{A.46}$$

$$C_C(\rho) = C_1 + \frac{C_2 + C_3 r_s + C_4 r_s^2}{1 + C_5 r_s + C_6 r_s^2 + C_7 r_s^3} \quad \text{A.47}$$

$$\tilde{f} = 0.11, C_1 = 0.001667, C_2 = 0.002568, C_3 = 0.023266, C_4 = 7.389\times10^{-6}, C_5 = 8.723$$

$$C_6 = 0.472, C_7 = 7.389\times10^{-2}, r_s = (\frac{3}{4\pi\rho})^{1/3}, s = \frac{|\nabla\rho|}{2k_F\rho}, k_F = (3\pi^2\rho)^{1/3}. \quad \text{A.48}$$

The exchange and correlation of Perdew-Wang-91 functional are (PW91):

$$E_X = E_X^{LDA}(\rho)[\frac{1 + a_1 s\sinh^{-1}(a_2 s) + (a_3 + a_4 e^{-100s^2})s^2}{1 + a_1 s\sinh^{-1}(a_2 s) + a_5 s^4}] \quad \text{A.49}$$

where a_1=0.19645, a_2=7.7956, a_3=0.2743, a_4=-0.1508, and a_5=0.004.

$$E_C = [E_C^{LDA}(\rho) + \rho H(\rho, s, t)] \quad \text{A.50}$$

$$H = \frac{\beta^2}{2\alpha}\log[1+\frac{2\alpha}{\beta}\frac{t^2+At^4}{1+At^2+A^2t^4}] + C_{C0}[C_C(\rho)-C_{C1}]t^2 e^{-100s^2} \quad \text{A.51}$$

$$A = \frac{2\alpha}{\beta}[e^{-2\alpha\varepsilon_C(\rho)/\beta^2}-1]^{-1} \quad \text{A.52}$$

α=0.09, β=0.0667263212, C_{C0}=15.7559, C_{C1}=0.003521; $\varepsilon_C(\rho)$ is defined so that

$$E_C^{LDA}(\rho) = \rho\varepsilon_C(\rho) \text{ ,and } t = \frac{|\nabla\rho|}{2k_s\rho}, k_s = (\frac{4}{\pi}k_F)^{1/2}. \quad \text{A.52}$$

The exchange energy for Becke 88 functionals is:

$$E_X = E_X^{LDA}(\rho)[1-\frac{\beta}{2^{1/3}A_X}\frac{x^2}{1+6\beta x\sinh^{-1}(x)}] \quad \text{A.53}$$

where $x = 2(6\pi^2)^{1/3}\cdot s = 2^{1/3}|\nabla\rho|/\rho^{4/3}, A_X = (3/4)(3/\pi)^{1/3}, \beta = 0.0042.$

The correlation energy of Wilson-Levy functional is:

$$E_C = \frac{a\rho + b|\nabla\rho|/\rho^{1/3}}{c+d|\nabla\rho|/(\rho/2)^{4/3}+r_s} \quad \text{A.54}$$

where a=-0.74860, b=0.06001, c=3.60073, and d=0.900.

Closed shell Lee-Yang-Parr correlation energy functional is (LYP):

$$E_C = -a\frac{1}{1+d\rho^{-1/3}}\{\rho + b\rho^{-2/3}[C_F\rho^{5/3}-2t_W+\frac{1}{9}(t_W+\frac{1}{2}\nabla^2\rho)]e^{-C\rho^{-1/3}}\} \quad \text{A.55}$$

where $t_W = \frac{1}{8}(\frac{|\nabla\rho|^2}{\rho}-\nabla^2\rho)$, $C_F=3/10(3p^2)^{2/3}$, a=0.04918, b=0.132, C=0.2533, and d=0.249.

The exchange, correlation functional of Perdew-Burke-Ernzerhof (PBE) is:

$$E_{XC}[\rho] = \int \rho(\vec{r})\varepsilon_X^{LDA}[\rho(\vec{r})F_{XC}(\rho,\varsigma,s)]d\vec{r} \quad \text{A.56}$$

where $F_X(s) = 1 + \kappa - \frac{\kappa}{1 + \mu s^2 / \kappa}$, m=b(p/3)=0, b=0.066725, and ς is the spin polarization and $s = \left|\nabla \rho(\vec{r})\right| / (2k_F \rho)$ .The correlation energy is written in a form similar to PW91.

Although GGA improve binding energies and, bond lengths and angles, it is not successful for semiconductors.

Since there is no unique procedure for making the functionals and none of the existing functional is universal, there are still some attempts for making more accurate ones [79, 80, 81, 83].

A.5.2. Meta-GGA

Another recent beyond-GGA development is the so-called Meta-GGAs; it is the extension of GGA in such a way that the in addition to electron density and its gradient, the non-interacting kinetic energy is considered. Therefore, the functional depends not only on the density and its derivatives but also on the Kohn-Sham kinetic-energy density τ (r) and the exchange, correlation energy is written as $E_{XC}[\rho(\vec{r}), \nabla \rho(\vec{r}), \tau(\vec{r})]$. This functional is supposed to retain the good properties of the GGA, while adding other terms for more accurate approximation. The derivative of the kinetic energy is written as:

$$\tau(\vec{r}) = \sum_{i=1}^{occupied} \frac{\hbar^2}{2m} \left| \vec{\nabla} \phi_i(\vec{r}) \right|^2 \qquad \text{A.57}$$

More specifically, the kinetic energy derivative could conclude the spin (up or down) of the electron:

$$\tau(\vec{r})_{spin} = \sum_{i=1}^{occupied} \frac{\hbar^2}{2m} \left|\vec{\nabla}\phi_{i,spin}(\vec{r})\right|^2 \qquad \text{A.58}$$

In fact, F_X in PBE-GGA functional could be written as:

$$F_X^{meta-GGA} = 1 + \kappa - \frac{\kappa}{1 + x/\kappa} \qquad \text{A.59}$$

where it is related to electron density and the kinetic energy derivation through the following formula, D is a:

$$\mathrm{x} = \frac{10}{81}\frac{|\nabla\rho|^2}{[4(3\pi^2)^{2/3}\rho^{8/3}]} + \frac{146}{2025}\left(\frac{3\tau[\rho]}{[2(3\pi^2)^{2/3}\rho^{5/3}]} - \frac{9}{20} - \frac{1}{12}\frac{|\nabla\rho|^2}{[4(3\pi^2)^{2/3}\rho^{8/3}]}\right)^2 -$$
$$\frac{73}{405}\left(\frac{3\tau[\rho]}{[2(3\pi^2)^{2/3}\rho^{5/3}]} - \frac{9}{20} - \frac{1}{12}\frac{|\nabla\rho|^2}{[4(3\pi^2)^{2/3}\rho^{8/3}]}\right)\frac{|\nabla\rho|^2}{[4(3\pi^2)^{2/3}\rho^{8/3}]} +$$
$$[\mathrm{D} + \frac{1}{\kappa}(\frac{10}{81})^2]\left(\frac{|\nabla\rho|^2}{[4(3\pi^2)^{2/3}\rho^{8/3}]}\right)^2$$

A.60

The very kinetic energy derivative is connected to the electron density through:

$$\tau(\vec{r}) = \frac{3}{10}(3\pi^2)^{2/3}\rho^{5/3} + \frac{1}{72}\frac{|\nabla\rho|^2}{\rho} + \frac{1}{6}\nabla^2\rho \qquad \text{A.61}$$

The correlation energy is written as follow:

$$E_C^{meta-GGA}[\rho] = \int \begin{array}{l} \{\rho\varepsilon_C^{GGA}(\rho,\nabla\rho)[1 + C(\frac{\sum_{spin}\tau_{spin}^{Weiszac\ker-kinetic-energy-density}}{\sum_{spin}\tau_{spin}})^2] - \\ (1+C)\sum_{spin}\frac{\tau_{spin}^{Weissac\ker-kinetic-energy-density}}{\tau_{spin}}\rho_{spin}\varepsilon_C^{GGA}(\rho_{spin},\nabla\rho_{spin})\}d\vec{r} \end{array}$$

A.62

where $\tau_{spin}^{Weiszac\ker-kinetic-energy-density} = |\nabla\rho_{spin}|^2 / 8\rho_{density}$. Since C and D are parameters fitted to chemical data, meta-GGA is semi-empirical [79, 80, 81, 83].

A.5.3. Hybrid Functionals

Hybrid functionals are not pure DFT functionals; instead it is a mixture of a DFT and a Hartree-Fock calculation. Although, Hartree-Fock and Kohn-Sham equations seem similar, they are based on different theories. The difference arises from the fact that Hartree-Fock minimizes the energy with respect to the single particle wave functions building up the Slater determinant while the Kohn-Sham does the energy minimization with respect to density.

Moreover, this is the exchange energy which dominates the exchange, correlation term. Besides, even the most complicated exchange, correlation functionals may just estimate the exchange, correlation energy. Hence, instead of using the complicated functional, it seems reasonable to calculate the exchange term from Hortree-Fock and use the functional for the correlation part:

$$E_{XC} = E_X^{exact.H-F} + E_C^{functional.approximation} \qquad \text{A.63}$$

In fact, one could find a dependency factor between zero and one, such as λ, which gives the two extremes of the system which are the classical energy of non-interacting free system (λ=0) and that of fully-interacted (λ=1) system of particles. In this case, the simplest form is to assume exchange, correlation energy as a linear function of this dependency factor, λ:

$$E_{XC} = \frac{1}{2}E_{XC}^{\lambda=0} + \frac{1}{2}E_{XC}^{\lambda=1}. \qquad \text{A.64}$$

The above form of exchange, correlation energy is called half-and-half combination.

The next step was taken by Becke in 1993; his exchange, correlation energy is a semiepirical one with the weighted terms:

$$E_{xc}^{B3} = E_{xc}^{LSD} + a\left(E_{XC}^{\lambda=0} - E_{X}^{LSD}\right) + bE_{X}^{B} + cE_{C}^{PW91} \qquad \text{A.65}$$

where a, b, and c are the three empirical parameters determined by fitting the predicted values to a set of atomization energies, ionization potentials, proton affinities, and total atomic energies.

One of the most common hybrids functional is called B3LYP:

$$E_{xc}^{B3LYP} = (1-a)E_{xc}^{LSD} + aE_{XC}^{\lambda=0} + bE_{X}^{B} + cE_{C}^{LYP} + (1-c)E_{C}^{LSD} \qquad \text{A.66}$$

where a, b, and c are the empirical parameters.

Another functional is given by Becke in 1996 and it has the following form:

$$E_{XC}^{Becke-96} = E_{XC}^{GGA} + a\left(E_{X}^{HF} - E_{X}^{GGA}\right) \qquad \text{A.67}$$

where the amount of the exact exchange is empirically determined as a=0.28.

In 1997, Becke suggested another form of hybrids functional with separated exchange, correlation parts in the form of exchange, like-spin correlation, unlike-spin correlation and an exact, Hartree-Fock exchange term:

$$E_{XC}^{B97} = E_{X}^{like-up-spin} + E_{X}^{like-down-spin} + E_{C}^{like-up-spin} + E_{C}^{like-down-spin} + E_{C}^{unlike-spin} + c_{X}^{HF}E_{X}^{HF} \qquad \text{A.68}$$

All the above terms, except the Hartree-Fock exchange one could be consider as a power series of density and its gradient.

Bruke, Ernzerhof, and Perdew [28] made a purely theoretical functional in 1997. Its amount of exact exchanges is derived from perturbation theory and it has the following from:

$$E_{XC}^{hybrids} = E_{XC}^{GGA} + 0.25(E_{X}^{HF} - E_{X}^{GGA}) \,. \qquad \text{A.69}$$

Hybrids give significant improvement over GGAs for many molecular properties, consequently they are a very popular choice of functional in quantum chemistry.

Their successful applications demonstrate how non-local functionals are essential to obtain accuracy [79, 80, 81].

A.6. Crystal Structure; Real and Reciprocal Lattice

In quantum mechanics, the motion of non-interacting particles in a static potential is described by the time independent Schrodinger equation. In the bulk crystalline materials which are defined by an infinite, periodic system, the problem is to make the system finite by considering a fictitious periodicity. The advantage of imposing this reduction is to simplify the study and calculations. Therefore, it is possible to consider a supercell that reproduces the periodicity over the whole space. It should be noted that the supercells are not supposed to interact with each other.

The other useful concept is the idea of unit cell; the concept of unit cell is in the center of any crystal structure. A unit cell is a small portion of any given crystal that can be used to reproduce the crystal. The relationship between a given unit cell and the lattice that it characterizes can be more precisely in terms of basic vectors. There are a couple of misunderstandings about the unit cells; first of all, unit cells are not necessarily unique; second, the unit cell need not to be primitive (the smallest possible one).

There are two periodic structures related to every periodic lattice: the real space and the reciprocal lattice; the latter is the one that determines the interaction of the periodic structure with waves.

The real vectors are expressed in terms of the lattice basis vectors, $\vec{a}_1, \vec{a}_2, \vec{a}_3$:

$$\vec{R} = n_1\vec{a}_1 + n_2\vec{a}_2 + n_3\vec{a}_3 \qquad \text{A.70}$$

the coefficients, c_j, are integers.

Any periodic function of crystal can be transformed in Fourier form, in which the wave vectors are defined in reciprocal space.

The reciprocal lattice basis vectors $\vec{b}_i$, are defined as:

$$\vec{b}_i = \frac{2\pi.\vec{a}_j \times \vec{a}_k}{\left|\vec{a}_i.\vec{a}_j \times \vec{a}_k\right|} \quad \text{A.71}$$

The orthogonality relation between the real lattice basis vectors and the reciprocal ones is given by:

$$\vec{b}_i.\vec{a}_j = 2\pi\delta_{ij} \quad \text{A.72}$$

where δ_{ij} is Kronecker delta. Moreover, a reciprocal vector is a linear combination of the reciprocal basis vectors with the integer coefficient:

$$\vec{G}(\vec{b}_1,\vec{b}_2,\vec{b}_2) = g_1\vec{b}_1 + g_2\vec{b}_2 + g_3\vec{b}_3 \quad \text{A.73}$$

The scalar product of $\vec{G}$ and $\vec{R}$ is one of the important properties of the reciprocal lattice:

$$\vec{G}.\vec{R} = 2\pi(g_1 n_1 + g_2 n_2 + g_3 n_3) \quad \text{A.74}$$

Taking exponential of both sides leads to:

$$\exp(i\vec{G}.\vec{R}) = 1. \quad \text{A.75}$$

The first Brillouin zone is the primitive cell of the reciprocal lattice, which is analogous of the Wigner-Seitz cell in real space. It is unique because its boundaries are the bisecting planes of $\vec{G}$ vectors where Bragg scattering occurs; since there are no such boundaries inside the Brillouin zone, the bands are continuous and analytic.

The volumes of the real cell and Brillouin zone are given by:

$$V_{cell} = \vec{a}_1.(\vec{a}_2 \times \vec{a}_3) \quad \text{A.76}$$

$$V_{Brillouin-Zone} = \vec{b}_1 . (\vec{b}_2 \times \vec{b}_3) = \frac{(2\pi)^3}{V_{cell}} . \qquad \text{A.77}$$

Considering the fact that a solid is a regular periodic array of external pseudopotentials, the effective potential could be written in a periodic way:

$$V_{eff}(\vec{r} + \vec{R}) = V_{eff}(\vec{r}) \qquad \text{A.78}$$

Lattice periodicity is a property of electron density, as well.

An infinite perfect crystal with a repeating unit cell occurs when the V_{eff} is given by the periodic function. The bulk crystal is usually considered infinite in extend and the properties are calculated per unit cell. The unit cell is not necessarily the primitive, smallest one; on the contrary, in order to simulate the defects or crystal displacement in a crystal, the unit cell should contain many independent atoms and hence is bigger than a primitive cell. A unit cell which is built by multiplying lattice vectors by integers is called a supercell.

A.7. Basic Ideas of Pseudopotential/ Frozen-Core Approximation

In 1940, Herring proposed the band calculation technique called the orthogonalized plane wave method (OPW) which allows the separation of the core and valence electrons. In this method, the valence wave functions are a linear combination of plane waves and core wave functions. By choosing appropriate coefficient of expansion, the valence wave functions would be orthogonal to the core states. Therefore, the problem is simplified by dividing the whole wave function into the core orbitals and the smooth part represented by plane waves. Hence, part represented by the plane waves would be smooth and the smaller number of plane waves are required to represent the valence electrons.

According to Herring, the orthogonalized plane wave consists of valence plane waves orthogonalized to the atomic core functions, such that the electron behaves like a core electron while inside the core and like a plane wave outside the core region. The orthogonalized plane wave basis can be written as:

$$\chi_{\vec{k}}(\vec{r}) = \frac{1}{\sqrt{NV_{primitive-cell}}}\exp(i\vec{k}.\vec{r}) - \sum_j \mu_{k,j}\phi_{k,j}(\vec{r}) \qquad \text{A.79}$$

where $\phi_{k,j}$ are the core wave functions (Bloch wave function) for constant j. N is the number of atoms and the term $\mu_{k,j}$ is chosen to make:

$$\int \phi^*_{k,j}(\vec{r})\chi_k(\vec{r})d^3\vec{r} = 0\,. \qquad \text{A.80}$$

The subscript j indicates the orbitals of the core electrons, such as 1s, 2s, 2p, wave functions. As it was mentioned before the coefficient $\mu_{k,j}$ is determined such that the plane orthogonalized plane wave functions would be orthogonal to the ones of core electrons.

By re-writing the total wave function in the terms of smooth and core wave functions, the true wave function is the sum of a smooth wave function, ϕ, and a sum over occupied core states:

$$|\psi\rangle = |\phi\rangle + \sum_j^{core} b_j |\chi_j\rangle \qquad \text{A.81}$$

The orthogonality dictates that:

$$\langle\chi_j|\psi\rangle = 0\,, b_j = -\langle\phi_j|\phi\rangle \qquad \text{A.82}$$

Then the total wave function is:

$$|\psi\rangle = |\phi\rangle - \sum_j \langle\chi_j|\phi\rangle\chi_j \qquad \text{A.83}$$

By substituting the above wave function in the Schrodinger equation with the core potential (which has this Hamiltonian: $\hat{H} = p^2/2m + V_c$:

$$\hat{H}(|\phi\rangle - \sum_j \langle \chi_j|\phi\rangle |\chi_j\rangle) = E|\psi\rangle = E|\phi\rangle - E\sum_j^{core} |\chi_j\rangle\langle\chi_j|\phi\rangle \qquad \text{A.84}$$

Therefore, by rewriting the equation:

$$\hat{H}|\phi\rangle - \sum_j (E - E_j)\langle \chi_j|\phi\rangle |\chi_j\rangle = E|\phi\rangle \qquad \text{A.85}$$

Then, by organizing the terms and write them as the Schrodinger equation, one can find the expression for the long-range, repulsive potential:

$$V_R = \sum_j^{core} (E - E_j)|\chi_j\rangle\langle\chi_j| \qquad \text{A.86}$$

The V_R is non-Hermitian repulsive potential; its effect is localized in the core and cancels parts of the strong Coulomb potential. The true potential is the sum of the core and long-range, repulsive potentials, which makes it very softer than the original one:

$$V = V_R + V_c\,. \qquad \text{A.87}$$

In the case of interaction, the energies of the eigen states would change, but if the core states are reasonably far from the valence sates, then $\delta E << E - E_j$ and hence it would be reasonable to use the valence Eigen states.

In general since the electrons in the outermost shell are the ones that actively participate in determining the chemical and physical properties of molecules and solids, it is assumed that the valence electron wave functions do not overlap with the ion core wave functions. Core electrons are those lower energy orbitals localized around an atomic nucleus that their properties do not change significantly with the

atom's chemical environment. The valence-electron orbitals oscillate very rapidly in the vicinity of atomic nuclei, but this rapid oscillation is orthogonal to the core electrons.

The philosophy behind the pseudopotential is to replace the strong Coulomb potential of nucleus with a softer one. Figure A.2 shows how the strong Coulomb potential could be replaced a soft one.

Figure A.2: Replacing the strong Coulomb potential with a soft one [176].

This replacement also changes the potential that the valence electrons feel. With this assumption, the potential of bare nuclei and the core electrons is replaced by a fictitious potential in such a way that the valence-electron potential would remain the same outside of what is called “cut-off radius” from the nucleus.

Due to the strong ionic potential, the valence wave functions oscillate very fast inside the core region. The reason is the orthogonality of a state to all states with lower energies; besides, the higher the state in the atom, the more the electron wave function oscillates. According to the Pauli Exclusion Principle, and since there are already core electrons in the vicinity of the nucleus, the probability of finding a valence electron near the nucleus is small. Pseudopotential approximates the real potential with a new weaker one which is supposed to give the correct behavior of the

electron wave function in the bonding region, and nearly zero probability for the valence electron to be close to the nucleus.

Removing core electrons from the calculation would reduce the Kohn-Sham orbitals, the memory required to store the orbitals, the time required to evaluate orbital-dependant quantities, and the time required to orthonormalize a set of orbitals. Moreover, since there are no core-electrons, there would be no valence electrons normalized to them. This, in return, lowers the cut-off energy, resulting in lower memory requirements and greater speed. There are generally three significant motivations behind the pseudopotential philosophy; first of all, it reduces the basic set size in the calculation, secondly it decreases the number of electrons and lastly it allows the possibility of including the relativistic effects in the whole estimation [80, 81].

A.7.1. Pseudopotential Construction and Classifications

The pseudopotential is constructed in a way that resulted pseudopotentials would be the same as the all-electron wave functions outside the core region; moreover, the pseudo wave functions should not have any nodes inside the core region. Besides, the pseudopotential should have the same scattering and phase shift effects as the real potential on the valence wave functions outside the core region. However, since the phase shift produced by the real potential has angular momentum dependency, the pseudopotential also should have the same dependency. In general, pseudopotential is written as:

$$V_{NL} = \sum_{lm} |lm\rangle V_l \langle lm| \quad \text{A.88}$$

where $|lm\rangle$ is the spherical harmonics and V_l is the pseudopotential. As the result, the special harmonics of wave functions are multiplied by the amount of the pseudopotential.

A local pseudopotential with the same potential for all the angular momentum of the wave function is called a local pseudopotential. A local potential is a function of distance from the nucleus.

According to the degree of electron-core screening and cancellation, there are different prescriptions to obtain the pseudopotentials, which leads to the pseudopotential non-uniqueness conclusion. This is the reason of developing categories of pseudopotentials such as empirical, semi-empirical and first principles [93].

A.7.2. Norm-Conservative Pseudopotential

Since the terms of Kohn-Sham equation are functions of density, the pseudo wave functions outside the core should generate the same charge density as the real wave function. Therefore, the real and pseudo wave functions should be identical in spatial dependencies, absolute magnitude and the charge density production.

Norm-conserving pseudopotentials and shape-consistent ones are the basis of most ab-initio pseudopotentials. In order to build a non-conserving pseudopotential, one should make it from all-electron pseudopotential and change it in a way that not only becomes equal to the all-electron potential outside the sphere but also has the eigen value equal all-electron valence eigenvalue and has the eigen function whose norm inside the sphere is conserved. The second step is that the normalized function should be equal to the all-electron function outside the sphere, while the charge inside is the

same. Besides, the first logarithmic derivative of the phase shift as a function of energy should be the same as the one for the all-electron case, which ensures maximum transferability to situations where the eigenvalue is changed. If pseudopotential is written in the form of the spherical harmonics, the constructed potential is *l*-dependent:

$$V(\vec{r},\vec{r}') = \sum_{l,m} V_l(\vec{r})\delta(r-r')Y_{l,m}(\theta,\phi)Y_{l,m}(\theta',\phi'). \qquad \text{A.89}$$

By writing the wavefunctions as the product of a radial function and a spherical harmonic, the norm-conserving conditions can be classified as:

1. Real and pseudo valence eigenvalues agree for a chosen prototype atomic configuration.

2. Real and pseudo atomic wave functions agree beyond a chosen core radius r_l.

$$R_l^{pseudopotential}(\vec{r}) = R_{nl}^{all-electron}(\vec{r}), \text{if } r > r_l \qquad \text{A.90}$$

3. The integrals from 0 to r of the real and pseudo charge densities agree for $r \geq r_l$ for each valence state (norm conservation).

4. The logarithmic derivatives of the real and pseudo wave function and their first energy derivatives agree for $r > r_l$.

$$\int_0^{r_l} d\vec{r} \left| R_l^{pseudopotential}(\vec{r}) \right|^2 r^2 = \int_0^{r_l} d\vec{r} \left| R_l^{all-electron}(\vec{r}) \right|^2 r^2, \text{if } r < r_l \qquad \text{A.91}$$

Where $R_l(\vec{r})$ is the radial part of the wavefunction with angular momentum l, and the index n denotes the valence level. The distance beyond which the true and the two wavefunctions become equal also depends on l.

Pseudopotentials are usually written as the sum of a local (l-independent) and non-local (l-dependent) potentials.

Therefore, in general, the procedure for constructing a pseudopotential is to solve the atomic all-electron, choose the appropriate exchange and correlation functional, choose the spherical Hartree potential, consider the continuity and norm-conserving conditions, and find the pseudo wave functions. Starting with Kohn-Sham radial equations and considering all the electrons in a given reference:

$$[-\frac{1}{2}\frac{d^2}{dr^2}+\frac{l(l+1)}{2r^2}+V_{K-S}^{all-electron}[n^{all-electron}](\vec{r})]rR_{nl}^{all-electron}(\vec{r})=\varepsilon_{nl}^{all-electron}rR_{nl}^{all-electron}(\vec{r}) \quad \text{A.92}$$

Kohn-Sham potential is given by:

$$V_{K-S}^{all-electron}[n^{all-electron}](\vec{r})=-\frac{Z}{r}+V_{Hartree}[n^{all-electron}](\vec{r})+V_{XC}[n^{all-electron}](\vec{r})\,. \quad \text{A.93}$$

The second step of constructing procedure is using norm-conservation to find the wave functions. The diversity of this kind of pseudopotentials comes to the picture as the result of the shape of wave functions in the region smaller than r_l; the shape of them should be pre-defined.

Using the derived wave functions in the Kohn-Sham equation would give the pseudopotential:

$$V_{l,screen}(\vec{r})=\varepsilon_l^{pseudopotential}-\frac{l(l+1)}{2r^2}+\frac{1}{2rR_l^{pseudopotential}(\vec{r})}\frac{d^2}{dr^2}[rR_l^{pseudopotential}(\vec{r})] \quad \text{A.94}$$

Since the above pseudopotential has the screening effects, the final pseudopotential has the following form:

$$V_l(\vec{r})=V_{l,screen}(\vec{r})-V_{Hartree}[n^{pseudopotential}](\vec{r})-V_{XC}[n^{pseudopotential}](\vec{r}) \quad \text{A.95}$$

The small cut-off radii would result to the realistic but strong pseudopotentials; the large values would make them smooth but not very accurate. The best cutoff radius is the result of making balance between basis size and pseudopotential accuracy. The cutoff radii are a measure of the quality of the pseudopotential accuracy.

A class of pseudopotentials such as Hamann and Troullier-Marins is constructed upon the norm-conserving scheme [93].

A.7.3. Troullier-Martins Pseudopotential

Troullier-Martins used polynomials of high order to construct a pseudo potential. This method makes smooth and soft pseudopotentials especially for 2p valence states of the first row elements and for d valence states of the transition metals. It is defined as:

$$R_l^{pseudopotential}(\vec{r}) = R_{nl}^{all-electron}(\vec{r}) \text{ ,if } r > r_l \quad \text{A.97}$$

$$R_l^{pseudopotential}(\vec{r}) = r^l \exp(p(\vec{r})) \text{ ,if } r < r_l \quad \text{A.98}$$

where $p(\vec{r})$ is defined as:

$$p(\vec{r}) = c_0 + c_2 r^2 + c_4 r^4 + c_6 r^6 + c_8 r^8 + c_{10} r^{10} + c_{12} r^{12} \quad \text{A.99}$$

The $p(\vec{r})$ coefficients are adjusted by imposing norm-conservation, the continuity of the wave functions and their first four derivatives at $r = r_l$, and that the screened pseudopotential has zero curvature at the origin [79, 81, 93].

A.7.4. Kleinman and Bylanber Pseudopotential

Since different angular momentum states have different scattering effects, it is useful to combine the effects of the core electrons and nucleus to construct an

accurate semi-local pseudopotential. A non-local pseudopotential has the following form, in general:

$$V^{pseudopotential} = V^{local} + \sum_{l,m} |lm\rangle \delta V_l \langle lm| \qquad \text{A.100}$$

where $|lm\rangle$ refers to spherical harmonics. The local potential is the matter of choice. The semi-local potential can be written in a form that separates long and short range components. The long-range component is local and corresponds to the Coulomb tail:

$$\Delta V_l(\vec{r}) = V_l(\vec{r}) - V^{local}(\vec{r}) \qquad \text{A.101}$$

The pseudopotential can be written as:

$$V(\vec{r},\vec{r}') = V^{local}(\vec{r}) + \sum_l \Delta V_l(\vec{r}) \sum_m Y^*_{l,m}(\hat{r}') Y_{l,m}(\hat{r}) \delta(r - r') \qquad \text{A.102}$$

Kleinman-Bylander suggests that the non-local part is written as a separable potential, which transforms the semi-local potential into a non-local potential. Therefore, Kleinman-Bylander pseudopotential is a non-local one with the separable form and defined as:

$$V_{K-B}(\vec{r},\vec{r}') = V^{local}(\vec{r}) + \sum_l \Delta V_l(\vec{r},\vec{r}') \qquad \text{A.103}$$

$$V_{K-B} = V_{local} + \sum_{l,m} \frac{|\delta V_l \phi_{lm}\rangle \langle \phi_{lm} \delta V_l|}{\langle \phi_{lm} | \delta V_l | \phi_{lm} \rangle} \qquad \text{A.104}$$

where $|\phi_{lm}\rangle$ is an eigenstate of the atomic pseudo-Hamiltonian. The local component of the Kleinman-Bylander form should be the most repulsive pseudopotential component [79, 81, 93]

A.7.5. Structure Factor and Total Nuclear Potential

In a solid with different types of ions, an ionic pseudopotential is considered for every nucleus. The information about the position of the nuclei is given by the structure factor, which is calculated at the wave vector G for different types of nuclei denoted by α:

$$S_\alpha(\vec{G}) = \sum_I \exp[i\vec{G}.\vec{R}_I] \qquad \text{A.105}$$

The sum is over all the positions of all the nuclei of that type.

Summing the structure factor over all types of nuclei would give the total external potential.

References

1. E.G. Acheson; "Production of Artificial Crystalline Carbonaceous Materials"; US 492,767, patented 28th February, (1893)
2. Shubert, E. Fred, Light-Emitting Diodes, Cambridge University Press, page 1, 2003.
3. Zhe Chuan Feng, and Jian H. Zhao; "Silicon Carbide: Materials, Processing, and Devices"; Taylor & Francis Books, InC., (2004)
4. D. L. Barrett, J. P. McHugh, H. M. Hobgood, R. H. Hopkins, P. G. McMullin, and R. C. Clarke, "Growth of Large SiC Single Crystals," Journal of Crystal Growth, 128, 1, 358-362, (1993)
5. Stephen E. Saddow, Anant K. Agarwal "Advances in Silicon Carbide Processing and Applications" Artech House, INC., (2004)
6. Cree Incorporated, USA; http://www.cree.com/.
7. Dow Corning Corporation, USA; http:// www.dowcorning.com/
8. Northrop Grumman, USA; http://www.northropgrumman.com/.
9. K. Jarrendahl and R. F. Davis, SiC Materials and Devices. (Academic Press, London, 1998.
10. H. Morkoc, S. Strite, G. B. Gao, M.E. Lin, B. Sverdlov et al.; "Large bandgap SiC, IIIV nitride, and IIVI ZnSebased semiconductor device technologies"; Journal of Applied Physics, 76, 1363, 1994.
11. http://www.phys.uni-paderborn.de/~rauls/diss/thesis.pdf
12. G. L. Harris (Hrsg.), Properties of Silicon Carbide, EMIS Datareview Series 13, INSPE, (1995).

13. V. V. Afanasev, M. Bassler, G. Pensl, M. J. Schulz, and E. S. von Kamienski, " Band offset and electronic structure of SiC/SiO_2 interface"; Journal of Applied Physics 79, 3108, 1996.

14. John Rozen, Ph.D. Thesis, Vanderbilt University, 2008.

15. Carl-Mikael Zetterling, "Process technology for Silicon Carbide devices"; INSPEC, London, 2002.

16. T. Burke, K. Xie, J. R. Flemish, R. Singh, T. Podlesak, and J. H. Zhao, "Silicon Carbide Power Devices for High Temperature, High Power Density Switching Applications"; Proceedings of the Twenty-Second International Power Modulator Symposium, pp. 18-21, 1996.

17. R. C. Clarke and J. W. Palmour, "SiC Microwave Power Technologies," Proc.IEEE, vol. 90, no. 6, pp. 987-992, 2002.

18. V. V. Afanasev, M. Bassler, G. Pensl, and M. Schulz; "Intrinsic SiC/SiO_2 Interface States"; phys. stat. sol. (a) 162, 321, 1997.

19. S. T. Pantelides et al.; "Si/SiO_2 and SiC/SiO_2 Interfaces for MOSFETs–Challenges and Advances"; Materials Science Forum Vols. 527-529, pp. 935-948, 2006.

20. M. D. Ventra and S. Pantelides; "Atomic-Scale Mechanisms of Oxygen Precipitation and Thin-Film Oxidation of SiC"; Physical Review Letters, 83, 1624-1627, 1999.

21. J. Tan, M. Das, J. Cooper, and M. Melloch; "Metal-oxide-semiconductor capacitors formed by oxidation of polycrystalline silicon on SiC"; Applied Physics Letters, 70, 2280, 1997.

22. J. Knaup, P. Deak, T. Frauenheim, A. Gali, Z. Hajnal, and W. Choyke; "Theoretical study of mechanism of dry oxidarion of 4H-SiC"; Physical Review B, 71, 235321, 2005.

23. B. E. Deal and A. S. Grove "General Relationship for the Thermal Oxidation of Silicon"; Journal of Applied Physics 36, 3770, 1965.

24. S. T. Pantelides et al.; "Atomic-Scale Engineering of the SiC-SiO_2 Interface"; International Conference on Silicon Carbide and Related Materials; 338-342, 1133, 2000.

25. K. C. Chang, N. T. Nuhfer, L. M. Porter, and Q. Wahab, "High-carbon concentrations at the silicon dioxide–silicon carbide interface identified by electron energy loss spectroscopy"; Applied Physics Letters 77, 2186, 2000.

26. C. Virojanadara, L. I. Johansson; "Studies of oxidized hexagonal SiC surfaces and the SiC/SiO_2 interface using photoemission and synchrotron radiation"; Journal of Physics: Condensed Matter, 16, 1783, 2004.

27. W. Lu, L. C. Feldman, Y. Song, S. Dhar, W. E. Collins, W. C. Mitchel, and J. R.Williams; "Graphitic features on SiC surface following oxidation and etching using surface enhanced Raman spectroscopy"; Applied Physics Letter, 85, 3495, 2004.

28. J. M. Knaup, P. Deák, Th. Frauenheim, A. Gali, Z. Hajnal, W. J. Choyke; "Defects in SiO_2 as the possible origin of near interface traps in the SiC/SiO_2 system: A systematic theoretical study"; Physical Revie B 72, 115323, 2005.

29. H. Ö. Olafsson, E. Ö. Sveinbjörnsson, T. E. Rudenko, I. P. Tyagulski, I. N. Osiyuk, V. S. Lysenko; "Border traps in 6H-SiC metal–oxide–semiconductor

capacitors investigatedby the thermally-stimulated current technique"; Applied Physics Letters, 79, 24, (2001).

30. Eckhard Pippel, Jörg Woltersdorf, Halldor Ö. Ólafsson, and Einar Ö. Sveinbjörnsson; "Interfaces between 4H-SiC and SiO_2: Microstructure, nanochemistry, and near-interface traps"; Journal of Applied Physics, 97, 034302, 2005.

31. J. L. Cantin, H. J. von Bardeleben, Y. Shishkin, Y. Ke, R. P. Devaty, and W. J. Choyke; "Identification of the Carbon Dangling Bond Center at the 4H-SiC/SiO_2 Interface by an EPR Study in Oxidized Porous SiC"; Physical Review Letters, 92, 015502, 2004.

32. P. Deak, J. M. Knaup, T. Hornos, C. Thill, A. Gali, and T. Frauenheim; "The mechanism of defect creation amd passivation at the SiC/SiO_2 interface"; Journal of Physics D: Applied Physics, 40, 6242, 2007.

33. Xiao Shen, Sokrates T. Pantelides; "Identification of a major cause of endemically poor mobilities in SiC/SiO_2 structures"; Applied Physics Letters, 98, 053507, 2011.

34. M. Bassler, G. Pensl, and V. Afanas'ev; "Carbon cluster model for electronic states at SiC/SiO2 interfaces"; Diamond Relat. Mat. 6, 1472, 1997.

35. V. V. Afanas'ev, F. Ciobanu, S. Dimitrijev, G. Pensl, and A. Stesmans; "Band alignment and defect states at SiC/oxide interfaces; "Journal of Physics: Condensed Matter 16, 1839, 2004.

36. Vathulya, Vickram, Ning Wang, Dong; White, Marvin; "On the correlation between the carbon content and the electrical quality of thermally grown oxides on p-type 6H–Silicon carbide"; Appl. Phys. Lett. 73, 2161, 1998.

37. A. Koh, A. Kestle, C. Wright, S. P. Wilks, P. A. Mawby, W. R. Bowen; "Comparative surface studies on wet and dry sacrificial thermal oxidation on silicon carbide"; Applied Surface Science 174 210-216, 2001.

38. K. C. Chang, N. T. Nuhfer, L. M. Porter, and Q. Wahab; "High-carbon concentrations at the silicon dioxide-silicon carbide interface identified by electron energy loss spectroscopy"; Applied Phycics Letters, 77, 2186, 2000.

39. K. Fukuda, S. Suzuki, T. Tanaka, and K. Arai; "Reduction of interface-state density in 4H-SiC n-type metal-oxide-semiconductor structures using high-temperature hydrogen annealing"; Applied Physics Letters 76, 1585, 2000.

40. S. Wang, M. Di Ventra, S. G. Kim, and S. T. Pantelides; "Atomic-Scale Dynamics of the Formation and Dissolution of Carbon Clusters in SiO_2"; Physics Review Letter 86, 5946, 2001.

41. A. Gali, P. Deak, P. Ordejon, N. T. Son, E. Janzen, and W. J. Choyke; "Aggregation of carbon interstitials in silicon carbide: A theoretical study"; Phys.Rev. B 68, 125201, 2003.

42. Edward H Poindexter; "MOS interface states: overview and physicochemical perspective"; Semicond. Sci. Technol. 4 961, 1989.

43. C Robert Helms, Edward H Poindexter, "The silicon-silicon dioxide system: Its microstructure and imperfections"; Rep. Prog. Phys. 57, 1994.

44. K. Brower; "Source of O^{17} hyperfine broadening of the P_b resonance associated with the (111) Si-SiO2 interface"; Physical Review B 42, 11352, 1990..

45. V. V. Afanas'ev, A. Stesmans, M. Bassler, G. Pensl, and M. J. Schulz; "Comment on "Reduction of interface-state density in 4H–SiC n-type metal–oxide–semiconductor structures using high-temperature hydrogen annealing""; Applied Physics Letters, 76, 1585 .2000. Applied Physics Letters, 78, 2001.

46. K. Fukuda, S. Suzuki, T. Tanaka, K. Arai; "Reduction of Interface-Trap Density in 4H-SiC n-Type Metal-Oxide-Semiconductor Structures using High-Temperature Hydrogen Annealing"; Applied Physics letter., 76, 1585, 2000.

47. Junji Senzaki, Kazutoshi Kojima, Shinsuke Harada, Ryoji Kosugi, Seiji Suzuki, Takaya Suzuki, and Kenji Fukuda; "Excellent Effects of Hydrogen Postoxidation Annealing on Inversion Channel Mobility of 4H-SiC MOSFET Fabricated on (11 2 0) Face"; IEEE Electron Device Letters, 23, 1, 2002.

48. David J. Meyer, Nathaniel A. Bohna, Patrick M. Lenahan, and Aivars J. Lelis; "Structure of 6H silicon carbide/silicon dioxide interface trapping defects"; Appl. Phys. Lett. 84, 3406, 2004.

49. C. J. Cochrane, P. M. Lenahan, and A. J. Lelis ; "Identification of a silicon vacancy as an important defect in 4H SiC metal oxide semiconducting field effect transistor using spin dependent recombination"; Applied Physical Letters 100, 023509, 2012.

50. Tsvetanka Zheleva, Aivars Lelis, Gerd Duscher, Fude Liu, Igor Levin et al., "Transition layers at the SiO_2/SiC interface"; Applied Physics Letters 93, 022108, 2008.

51. T. L. Biggerstaff et al.; "Relationship between 4H-SiC/SiO2 transition layer thickness and mobility"; Applied Physics Letters 95, 032108, 2009.

52. C. Onnebya and C. G. Pantano; "Silicon oxycarbide formation on SiC surfaces and at the SiC/SiO2 interface"; J. Vac. Sci. Technol. A 15(3), 1997.

53. C. Radtke, I. J. R. Baumvol, and J. Morais; "Initial stages of SiC oxidation investigated by ion scattering and angle-resolved x-ray photoelectron spectroscopies"; Applied Physics Letters, Vol. 78, No. 23, 2001.

54. L.A. Lipkin, J. W. Palmour ; "Insulator Investigation on SiC Improved Reliability"; IEEE Transaction Electron Devices, 46, 1999.

55. E. H. Nicollian and J. R. Brews; "MOS (Metal Oxide Semiconductor) physics and technology"; (John Wiley & Sons, New York, 1982.

56. H. Tsuchida, I. Kamata, and K. Izumi, "Infrared Spectroscopy of Hydrides on the 6H-SiC Surface" Appl. Phys. Lett. 70, 3072, 1997.

57. H. Tsuchida, I. Kamata, and K. Izumi; "Si-H Bonds on the 6H-SiC(0001) Surface after H2 Annealing"; Jpn. J. Appl. Phys. 36, L699-L702, 1997.

58. H. Tsuchida, I. Kamata, and K. Izumi; "Infrared attenuated total reflection spectroscopy of 6H–SiC(0001) and (0001) surfaces"; J. Appl. Phys. 85, 3569, 1999.

59. P.Jamet, S.Dimitrijev, and P. Tanner; "Effects of Nitridation in Gate Oxides Grown on 4H-SiC" J. Appl. Phys., vol.90, 2001.

60. V.V. Afanas'ev; "Electronic properties of SiO_2/SiC interface"; Microelectron Eng.; 48, 241, 1999.

61. K. McDonald, M. B. Huang, R. A. Weller, L. C. Feldman, J. R. Williams, F. C. Stedile, I. J. R. Baumvol, and C. Radtke; "Comparison of nitrogen incorporation in SiO_2/SiC and SiO_2/Si structures"; Appl. Phys. Lett. 76, 568, 2000.

62. K. McDonald, R. A. Weller, S. T. Pantelides, L. C. Feldman, G. Y. Chung, C. C. Tin, and J. R. Williams; "Characterization and modeling of the nitrogen passivation of interface traps in SiO_2/4H–SiC'; Journal of Applied Physics 93, 2719, 2003.

63. K. McDonald, L. C. Feldman, R. A. Weller, G. Y. Chung, C. C. Tin, and J. R. Williams; "Kinetics of NO nitridation in SiO2/4H-SiC"; Journal of Applied Physics, 2257, 2003.

64. Dai Okamoto, Hiroshi Yano, Kenji Hirata, Tomoaki Hatayama, and Takashi Fuyuki; "Improved Inversion Channel Mobility in4H-SiC MOSFETs on Si Face Utilizin Phosphorus-Doped Gate Oxide"; IEEE Electron Device Letters, 31, 7, 2010.

65. Dai Okamoto, Hiroshi Yano, Tomoaki Hatayama, and Takashi Fuyuki; "Removal of Near-Interface Traps at SiO_2/4H–SiC Interfaces by Phosphorus Incorporation"; Applied Physics Letters, 96, 203508, 2010.

66. Fabien Devynck, Audrius Alkauskas, Peter Broqvist and Alfredo Pasquarello, "Energy levels of candidate defects at SiC/SiO_2 interfaces", AIP Conf. Proc. 1199, 108 (2010).

67. Fabien Devynck, Alfredo Pasquarello, "Semiconductor defects at the 4H-SiC(0001)/SiO_2 interface"; Physica B 401–402 556–559 (2007).

68. S. Potbhare, N. Goldsman, G. Pennington; "Numerical and experimental characterization of 4H-silicon carbide lateral metal-oxide-semiconductor field-effect transistor"; Journal of Applied Physics, 100, 044515, 2006.

69. S. Potbhare, N. Goldsman, G. Pennington, A. Lelis, J. McGarrity; "A quasi-two-dimensional depth-dependent mobility model suitable for device simulation for Coulombic scattering due to interface trapped charges" Journal of Applied Physics, 100, 044516, 2006.

70. S. Potbhare, N. Goldsman, A. Lelis, "High Temperature High Field Numerical Modeling and Experimental Characterization of 4H-SiC MOSFETs", Proc. of ISDRS 2007, College Park, MD, 2007.

71. S. Potbhare, N. Goldsman, A. Lelis, J. M. McGarrity, F. B. McLean; "A physical Model of High Temperature 4H-SiC MOSFETs"; Transactions on Electron Devices, 55, 8, 2008.

72. S. Potbhare, N. Goldsman, A. Akturk, M. Gurfinkel, A. Lelis, J. Suehle; "Energy- and Time Occupation in 4H-SiC MOSFETs"; IEEE Transactions on Electron Devices, 55, 8, 2008.

73. S. Potbhare, N. Goldsman, A. Lelis, “Modeling and Characterization of a 4H-SiC DMOSFET”, MRS Spring 08 Workshop, San Francisco, CA, 2008.

74. Akturk, Akturk, Neil Goldsman, Siddharth Potbhare,and Aivars Lelis; “High field density-functional-theory based Monte Carlo: 4H-SiC inpact ionization and velocity saturatuion”; Journal of Applied Physics 105, 033703, 2009.

75. Paolo Giannozzi et al., QUANTUM ESPRESSO: a modular and open-source software project for quantum simulations of materials Journal of Physics: Condens. Matter 21, 395502, 2009.

76. John P. Perdew, Kieron Burke, and Matthias Ernzerhof; “Generalized Gradient Approximation Made Simple”; Physical Review Letters 77, 18, 3865-3868, 1996.

77. A.D. Becke, "A new mixing of Hartree-Fock and local density-functional theories". Journal of chemical physics, 98, 1372, 1993.

78. J. Kohanoff and N.I. Gidopoulos, Stephen Wilson; “Density Functional Theory: Basics, New Trends and Applications”; Volume 2, Part 5, Chapter 26, Handbook of Molecular Physics and Quantum Chemistry; Stephen Wilson; John Wiley & Sons, Ltd, Chichester, 2003.

79. M. C. Payne, M. P. Teter, D. C. Allan, T. A. Arias, and J. D. Joannopoulos; “Iterative Minimization Techniques for ab initio Total Energy Calculations”; Rev. Mod. Phys. 64, 1992.

80. Wolfram Koch, Max C. Holthausen; “A Chemist’s Guide to Density Functional Theory”; Wiley-VCH.

81. Richard M. Martin: "Electronic Structure; Basic theory and Practical Methods; Richard M. Martin"; Cambridge University Press; 2004.

82. Mike Finnis; "Interatomic Forces in Condensed Matter"; Oxford University Press; 2003.

83. Robert G. Parr, Weitao Yang; "Density-Functional Theory of Atoms and Molecules"; Oxford University Press.

84. Klaus Capelle; "A Bird's-Eye View of Density-Functional Theory"; available at: http://arxiv.org/pdf/condmat/0211443.pdf

85. J. Kohanoff and N.I. Gidopoulos; "Density Functional Theory: Basics, New Trends and Applications"; Vol 2, Part 5, Chapter 26, pp 532–568; Handbook of Molecular Physics and Quantum Chemistry; Stephen Wilson; John Wiley & Sons, Ltd, Chichester.

86. Stefan Kurth, John P. Perdew; "Role of the exchange-correlation energy: Nature's glue"; International Journal of Quantum Chemistry; 77, 5, 814 – 818, 2000.

87. J. P. Perdew, K. Burke, and Y. Wang, "Generalized gradient approximation for the exchange-correlation hole of a many-electron system," Physical Review. B, 54, 16533-39, 1996.

88. J. Tau, J. P. Perdew, V. N. Staroverov, and E. Scuseria, "Climbing the Density Functional Ladder: Nonempirical Meta–Generalized Gradient Approximation Designed for Molecules and Solids"; Phys. Rev. Lett. 91, 146401 (2003).

89. W. Jones, N. H. March; "Theoretical Solid State Physics"; Wiley and Sons, Dover Publications, 1973.

90. S. M. Sze, Physics of Semiconductor Devices; Second Edition; John Willey & Sons, NewYork, 1981.

91. David S. Sholl, Janice A. Steckel; “Density Functional Theory, A Practical Introduction”; John Wiley & Sons, 2009.

92. H. J. Monkhorst, J. D. Pack; “Special points for Brillouin-Zone”; Physical Review B, 13, 12, 5188-5192, 1976.

93. C. Fiolhais, F. Nogueira, M. Marques; “A Primer in Denisty Funational Theory”; Speinger 2003.

94. John P. Perdew, Matthias Ernzerhof and Kieron Burke; "Rationale for mixing exact exchange with density functional approximations" J. Chem. Phys. 105 (22): 9982–9985, 1996.

95. F. Bechstedt, R. Del Sole; “Analytical treatment of band-gap underestimates in the local-density approximation”; Physical Review B, 38, 7710-7716, 1988.

96. A. P. Sutton; “Electronic Structure of Materials”; Oxford Science Publications, 1993.

97. S. Wang, S. Dhar, S.-R. Wang, A. C. Ahyi, A. Franceschetti, J. R. Williams, L. C. Feldman, and S. T. Pantelides,: “ Bonding at the SiC-SiO_2 Interface and the Effects of Nitrogen and Hydrogen”; Physical Review Letters, 98, 026101, 2007.

98. Fabien Devynck, Feliciano Giustino, Peter Broqvist, and Alfredo Pasquarello; “Structural and electronic properties of an abrupt 4H-SiC(0001)/SiO_2 interface model: Classical molecular dynamics simulations and density functional calculations”; Physical Review B 76, 075351, 2007.

99. P. Kackell, B. Wenzien, F. Bechstedt; “Electronic properties of cubic and hexagonal SiC polytypes from ab initio calculations”; Physical Review B, 50, 15, 1994.

100. C. Persson, U. Lindeffelt; “Relativistic band structure calculation of cubic and hexagonal SiC polytypes”; Journal of Applied Physics, 82, 11, 1997.

101. A. Bauer, J. Krausslich, P. Kuschnerus, K. Goetz, P. Kackell, F. Bechstedt; “High-precision determination of atomic positions in 4H-, and 6H-SiC crystals”; Materials Science and Engineering B61-62, 217-220, 1999.

102. R. T. M. Ummels, P. A. Bobbert, and W. van Haeringen; “Ab initio quasiparticle energies in 2H, 4H, and 6H SiC”; Physical Review B, 58, 11, 1998.

103. G. Pennington, N. Goldsman; “Simulation of electron transport in (0001) and (110) 4H-SiC inversion layers”; Journal of Applied Physics, 106, 063701, 2009.

104. G. Pennington, N. Goldsman; “Empirical pseudopotential band structure of 3C, 4H, and 6H SiC using transferable semiempirical Si and C model potentials”; Physical Review B, 64, 045104, 2001.

105. N. T. Son, C. Persson, U. Lindefelt, W. M. Chen, B. K. Meyer, D. M. Hofmann and E. Janzén; “Cyclotron Resonance Studies of Effective Masses and Band Structure in Silicon Carbide: Advanced Texts in Physics”; Part IV, 437-460, 2004.

106. http://www.xcrysden.org/

107. L. Patrick, W. J. Choyke, and D. R. Hamilton, "Luminescence of 4H SiC, and Location of Conduction-Band Minima in SiC Polytypes," *Phys. Rev.*, vol. 137, no. 5A, pp. A1515-A1520, 1965.

108. W. J. Choyke and L. Patrick, "Absorption of Light in Alpha SiC near the Band Edge," Physical Review., vol. 105, no. 6, pp. 1721-1723, 1957.

109. D. Volm, B. K. Meyer, and D. M. Hofmann, M. Chen, N. T. Son, C. Persson, U. Lindefelt, O. Kordina,† E. So¨rman, A. O. Konstantinov, B. Monemar, and E. Janze´n; "Determination of the electron effective-mass tensor in 4H SiC"; Physical Review B, 53, 23, 1996.

110. W. R. L. Lambrecht, S. Limpijumnong, S. N. Rashkeev, and B. Segall, "Electronic Band Structure of SiC Polytypes: A Discussion of Theory and Experiment," Physica status solidi (b), 202, 1, 5-33, 1997.

111. S. T. Pantelides, Walcr A. Harrison, "Electronic structure, spectra, and properties of 4:2-coordinated materials. I. Crystalline and amorphous SiO_2 and GeO_2"; Physical Review B, 13, 6, 1976.

112. James R. Chelikowsky and M. Schlüter; "Electron states in α-quartz: A self-consistent pseudopotential"; Phys. Rev. B 15, 4020–4029, 1977.

113. Angelo Bongiorno, Alfredo Pasquarello, Mark S. Hybertsen, and L.C. Feldman; "Transition Structure at the Si(100)-SiO_2 Interface"; Physical Review Letters, 90, 18, 2003.

114. T. Ouisse; "Electron Transport at the SiC/SiO_2 Interface"; Physica Status Solidi A 162, 339, 1997.

115. G. Y. Chung, C. C. Tin, J. R. Williams, K. McDonald, M. Di Ventra' S. T. Pantelides, L. C. Feldman, and R. A. Weller, “Effect of nitric oxide annealing on the interface trap densities near the band edges in the 4H polytype of silicon carbide”; Applied Physics Letters, 76, 1713, 2000.

116. V. V. Afanas'ev and A. Stesmans; “Interfacial Defects in SiO2 Revealed by photon Simulated Tunneling of Electrons”; Physical Review Letters, 78, 2437-2440, 1997.

117. Hikaru Kobayashi, Takeaki Sakurai, and Masao Takahashi; “Interface states at SiO_2/6H-SiC(0001) Comparison between dry and wet oxidation interfaces observed by x-ray photoelectron spectroscopy measurements under bias: Comparison between dry and wet oxidation”; Physical Review B 67, 115305, 2003.

118. H.Ö. Ólafsson, Einar Ö. Sveinbjörnsson, T.E. Rudenko, V.I. Kilchytska, I.P. Tyagulski, I.N. Osiyuk; “A Study of the Shallow Electron Traps at the 4H-SiC/SiO_2 Interface”; Materials Science Forum, 433-436, 547, 2003.

119. Reinhold Schorner, P. Friedrichs, D. Peters, and D. Stephani; “Significantly Improved Performance of MOSFET’s on Silicon Carbide Using the 15R-SiC Polytype”; IEEE Eelectron Device Letters, 20, 5, 1999.

120. V.V. Afanas'ev, A. Stesmans, and C.I. Harris, "Observation of carbon clusters at the 4H-SiC/SiO_2 interface"; Mater. Sci. Forum 264-268, 857-860, 1998.

121. L.A. Lipkin and J.W. Palmour; “Improved Oxidation Procedures for Reduced Si02/SiC Defects”; Journal of Electronic Materials, Vol. 25, No. 5, 1996.

122. Lenahan, P. M. Dressendorfer, P. V.; “Paramagnetic Trivalent Silicon Centers in Gamma Irradiated Metal-Oxide-Silicon Structures”; Appl. Phys. Lett. 49, 348, 1986.

123. Ligia Gheorghita; “Passivation Kinetics at Semiconductor Interfaces: Interaction of hydrogen with GaAs surfaces and Si/SiO_2 interfaces”; LAP LAMBERT Academic Publishing, 2011.

124. P. Jamet and S. Dimitrijev; “Physical properties of N_2O and NO-nitrided gate oxides grown on 4H SiC”; Applied Physics Letters, 79, 3, (2001).

125. Hui-feng Li, Sima Dimitrijev, H. Barry Harrison, and Denis Sweatman; “Interfacial characteristics of N_2O and NO nitrided SiO_2 grown on SiC by rapid thermal processing”; Appl. Phys. Lett. 70, 2028, 1997.

126. Sima Dimitrijev, Hui-feng Li, H. Barry Harrison, and Denis Sweatman; “Nitridation of Silicon-Dioxide Films Grown on 6H Silicon Carbide”; IEEE Electron Device Letters, 18, 5, 1997.

127. V. V. Afanas’ev, A. Stesmans, F. Ciobanu, G. Pensl, K. Y. Cheong and S. Dimitrijev; “Mechanisms responsible for improvement of 4H–SiC/SiO2 interface properties by nitridation”; Applied Physics Letters, 82, 4, 2003.

128. C. Virojanadara and L. I. Johansson; "Studies of NO on 4H-SiC(0001) using Synchrotron Radiation"; J. Phys. Condens. Matter 16, 3435, 2004

129. Hui-feng Li, Sima Dimitrijev, Denis Sweatman, H. Barry Harrison, Philip Tanner, and Bill Feil; " Investigation of nitric oxide and Ar annealed SiO2/SiC interfaces by x-ray photoelectron spectroscopy"; Journal of applied Physics 86, 4316, 1999.

130. Y.K. Sharma, A.C. Ahyi, T. Issacs-Smith, X. Shen, S.T. Pantelides, X. Zhu, L.C. Feldman, J. Rozen, J.R. Williams; "Phosphorous passivation of the SiO2/4H–SiC interface"; Solid-State Electronics 68, 103–107, 2012.

131. L. Torpo, M. Marlo, T.E.M. Staab, and R. M. Nieminen, "Comprehensive ab initio study of properties of monovacancies and antisites in 4H-SiC"; J. Phys.: Condens. Matter, 13, 6203–6231, 2001.

132. Zywietz, J. Furthmuller, and F. Bechstedt; "Vacancies in SiC: Influence of Jahn-Teller distortions, spin effects, and crystal structure"; Physical Review B 59, 23, 1999.

133. M. Bockstedte, A. Mattausch, and O. Pankratov, "Ab initio study of the annealing of vacancies and interstitials in cubic SiC: Vacancy-interstitial recombination and aggregation of carbon interstitials"; Physical Review B 69, 235202, 2004.

134. Michel Bockstedte, Adam Gali, Alexander Mattausch, Oleg Pankratov, and John W. Steeds; "Identification of intrinsic defects in SiC:

Towards an understanding of defect aggregates by combining theoretical and experimental approaches”; Physica Status Solidi (b) 245, 7, 1281-1297, 2008.

135. T. Wimbauer , B. K. Meyer, A. Hofstaetter, A. Scharmann , H. Overhof ; “Negatively charged Si vacancy in 4H SiC: A comparison between theory and experiment”; Physical Review B 56, 7384–7388, 1997.

136. W. Shi, D. H. Zhang, H. Q. Zheng, S. F. Yoon, C. H. Kam and A. Raman; “Effects of arsenic beam equivalent pressure on InGaAsP grown by solid source molecular beam epitaxy with continuous white phosphorous production”; Journal of Crystal Growth, 197, 89-94, 1999.

137. Keun-Soo Kim, Seog-Young Yoon, Won-Jae Lee, Kwang Ho Kim Surface morphologies and electrical properties of antimony-doped tin oxide films deposited by plasma-enhanced chemical vapor deposition Surface and Coatings Technology, 138, 229-236, 2001.

138. B. Hornetz, H-J. Michel, J. Halbritter; “ARXPS studied of SiO_2-SiC interfaces and oxidation of 6H SiC single crystal Si-(001) and C-(001) surfaces”; J. Mater. Res. 9, 3088, 1994.

139. F. Amy, L. Douillard, V. Yu. Aristov, P. Soukiassian ; “Oxynitridation of cubic silicon carbide (100) surfaces”; Applied Physics Letters, 75, 21, 1999.

140. J. Bernhardt, J. Schardt, U. Starke, and K. Heinz; “Epitaxially ideal oxide-semiconductor interfaces: Silicate adlayer on hexagonal (0001) and $(000\bar{1})$ SiC surfaces”; Applied Physics Letters 74, 1084, 1999.

141. T. Shirasawa, K. Hayashi, S. Mizuno, S. Tanaka, F. Komori K. Nakatsuji, and H. Tochihara; "Epitaxial seilicon oxynitride layer on a 6H-SiC(0001) surface"; Physical Review Letters, 98, 136105, 2007.

142. Ryszard Buczko, Stephen J. Pennycook, and Sokrates T. Pantelides; "Bonding Arrangements at the Si-SiO2 and SiC-SiO2 Interfaces and a Possible Origin of their Contrasting Properties"; Physical Review Letters, 84, 5, 2000,

143. B. Hornetz, H.-J. Michel, and J. Halbritter; "Oxidation and 6H-SiC-SiO_2 interfaces"; J. Vac. Sci. Technol. A 13, 767, 1995

144. G. V. Soares, C. Radtke, I. J. Baumvol, and F. C. Stedile; "Morphological and compositional changes in the SiO2/SiC interface region induced by oxide thermal growth"; Applied Physics Letters, 88, 041901, 2006.

145. Cesar R. S. da Silva, Joao F. Justo, and Ines Pereyra; "Crystalline silicon oxycarbide: Is there a native oxide for silicon carbide?", Applied Physics Letters, Vol. 84, No. 24, 2004.

146. Qiang Wang, C. G. Pantano, and J. F. Annett; "Ab initio Calculation on Atomic Structure and Charge Transfer of Silicon Oxycarbide (SiO_xC_y) at the SiC/SiO_2 Interface"; physica status solidi (b) 216, 909, 1999.

147. Shunsuke Muto, Hiroshi Sugiyama, Tomohiko Kimura and Tetsuo Tanabe; "Structure of an Oxygen-Related Defect Complex in SiC Studied with Electron Energy-Loss Spectroscopy" Japanese Journal of Applied Physics Vol. 43, No. 3, 2004, pp. 1076–1080, 2004.

148. C. Jacoboni, L. Reggiani; "The Monte Carlo method for the solution of charge transport in semiconductors with applications to covalent materials"; Reviews of Modern physics, Vol. 55, No. 3, 1983.

149. M. Lundstorm; "Fundamental of Carrier Transport"; Cambridge University Press, 2000.

150. M. Hjelm, H.-E. Nilsson, A. Martinez, K. F. Brennan, and E. Bellotti, "Monte Carlo study of high-field carrier transport in 4H-SiC including band-to-band tunneling" J. Appl. Phys. 93, 1099, 2003.

151. R. Mickevicius and J. H. Zhao; "Monte Carlo study of electron transport in SiC"; J. Appl. Phys. 83, 3161, 1998.

152. I A. Khan and J. A. Cooper; "Measurement of High-Field Electron Transport in Silicon Carbide"; IEEE Trans. Electron Devices 47, 269, 2000.

153. A. Gali, D. Heringer, P. Dea´k, Z. Hajnal, Th. Frauenheim, R. P. Devaty, and W. J. Choyke; "Isolated oxygen defects in 3*C*- and 4H-SiC: A theoretical study"; Physical Review B 66, 125208, 2002.

154. S. Potbhare, A. Akturk, N. Goldsman, A. Lelis, S. Dhar, A. Agarwal; "Effect of Band-edge Interface Traps and Transition Region Mobility on Transport in 4H-SiC MOSFETs"; Materials Science Forum 645-648 (2010) 975.

155. V. Tilak, K. Matocha, G. Dunne; "Interface Trap and Mobility Characterization of Silicon Carbide MOSFET Inversion Layers" Materials Science Forum, 616-617, 2009.

156. S. Potbhare, A. Akturk, N. Goldsman, A. Lelis, S. Dhar, A. Agarwal; "Effect of Band-edge Interface Traps and Transition Region Mobility on Transport in 4H-SiC MOSFETs"; Materials Science Forum 645-648 (2010) 975.

157. V. Tilak, K. Matocha, G. Dunne; "Interface Trap and Mobility Characterization of Silicon Carbide MOSFET Inversion Layers" Materials Science Forum, 616-617, 2009.

158. K.K, Hung, P.K. Ko, C. Hu, Y.C. Cheng, "A unified model for the flicker noise in metal-oxide-semiconductor field-effect transistors", IEEE Trans. Electron Devices, vol. 37, n. 3, pp. 654-665, 1990.

159. Mohan Vamsi Dunga," Nanoscale CMOS Modeling; available at: http://www.eecs.berkeley.edu/Pubs/TechRpts/2008/EECS-2008-20.html, March 3, 2008.

160. N. Arpatzanis, et.al, "Experimental investigation of noise in 4H-SiC p^+-n-n^+ junctions"; Semi. Sci. and Tech., 21, 591-593, 2006.

161. S.L. Rumyantsev, et.al, "Low frequency noise in 4H-SiC BJTs", Semi. Sci. and Tech., 19, 950-952, 2004.

162. Gudjón I. Gudjónsson, Fredrik Allerstam, Einar Ö. Sveinbjörnsson, Hans Hjelmgren, Per-Åke Nilsson, Kristoffer Andersson, Herbert Zirath, Thomas Rödle, and Rik Jos; "Design and Fabrication of 4H-SiC RF MOSFETs"; IEEE Transactions on Electron Devices, 54, 12, 2007.

163. D. Alok, E. Arnold, R. Egloff, J. Barone, J. Murphy, R. Conrad, and J. Burke; “4H-SiC RF Power MOSFETs”; IEEE Electron Device Letters, 22, 12, 2001.

164. A. Van der Ziel, "Noise: Sources, Characterization, Measurement", Englewood Cliffs, NJ: Prentice-Hall, 1970

165. M.J. Kirton and M.J. Uren, "Noise in solid-state microstructures: A new perspective on individual defects, interface states and lowfrequency (1/f) noise", Advances in Physics vol. 38, pp. 367-468, 1989.

166. Mark Hansen; “Achieving Accurate On-Wafer Flicker Noise Measurements through 30 MHz”; Cascade Microtech, Inc.; available at: www.cascademicrotech.com.

167. F. N. Hooge, T. G. M. Kleinpenning, and L. K. J. Vandamme; “Experimental studies on 1/f noise”; Rep. Prog. Phys., 44, 1981. Printed in Great Britain

168. Zhong Yuan Chang; Willy M C Sansen; “Low-noise wide-band amplifiers in bipolar and CMOS technologies”; Boston : Kluwer Academic Publishers, 1991.

169. L. K. J. Vandamme; “Noise as a Diagnostic Tool for Quality and Reliability of Electronic Devices”; IEEE Transactions on Electron Devices, 41, 11, 1994.

170. Mark Hansen; “Achieving Accurate On-Wafer Flicker Noise Measurements through 30 MHz”; Cascade Microtech, Inc.; available at: www.cascademicrotech.com.

171. J. B. Johnson, “The Schottky effect in low frequency circuits”; Physical Review, 26, 71-85, 1925.

172. W. Schottky; “Small-shot effect and flicker effect”; Physical Review, 28. , pp. 74-103, 1926.

173. Christensson S, LundstroÈm I, Svensson; “Low frequency noise in MOS transistors, I. Theory”; Solid-State Electron. 11, 797-812, 1968.

174. E. Simoen, C. Claeys, "On the flicker noise in submicron silicon MOSFETs", Solid-State Electron., 43, 865-882, 1999.

175. R. Q. Hood, M. Y. Chou, A. J. Williamson, G. Rajagopal, R. J. Needs, W. M. C. Foulkes; “Quantum Monte Carlo investigation of exchange correlation in silicon”; Physical Review Letters, 78, 17, 28, 1997.

176. A. Krasheninnikov; “ Introduction to electronic structure simulations pseudo-potentials”; available at: http://tfy.tkk.fi/~asf/physics/lectures/PDF/lect8.pdf